THE UNIVERSITY OF CHICAGO

MOLECULAR SIMULATION OF ION CONTAINING SOFT MATERIALS FOR SUSTAINABILITY APPLICATIONS

A DISSERTATION SUBMITTED TO

THE FACULTY OF THE PRITZKER SCHOOL OF MOLECULAR ENGINEERING

IN CANDIDACY FOR THE DEGREE OF

DOCTOR OF PHILOSOPHY

BY

CHUTING DENG

CHICAGO, ILLINOIS

DECEMBER 2023

I dedicate this dissertation to my parents, Fulu and Xiaoling, and my brother, Chuhuan.

TABLE OF CONTENTS

LIST OF FIGURES

LIST OF TABLES

ACKNOWLEDEMENTS

My PhD journey has been significantly influenced by the kindness, guidance, and trust of many individuals. I am profoundly appreciative of the opportunities to meet, collaborate, and learn from them.

Foremost, I express my heartfelt gratitude to my parents for their unwavering belief in my pursuit of this academic adventure in the first place. To my brother, who filled my days with laughter and joy. Even from afar, during my five years in a foreign country, their constant love and support have become my pillars of strength, encouraging me to be courageous, resilient, kind, and honest.

My gratitude goes to my advisor, Professor Juan de Pablo, whose mentorship and unwavering support have significantly shaped my academic and personal growth. I deeply appreciate the trust you've placed in me, and I find myself incredibly fortunate to have had the chance to explore numerous research opportunities simultaneously. This truly broadened my experience and prompted me to grow as a scholar. Working alongside you and observing your scholarly approach have been invaluable, teaching me the courage to embrace ambitious challenges, the optimism for the outcome, and the patience throughout the journey.

I feel blessed to have met and worked with many inspiring and generous individuals in the de Pablo group. I have so much gratitude to give to Dr. Ashley Guo, Dr. Michael Webb, and Dr. Nick Jackson, who guided me through all the intricate details in the field, until I could set up my own simulations. Your patient guidance and encouragement have molded me into a meticulous researcher as well as a supportive mentor. I want to express my gratitude to Dr. Heyi Liang and Dr. Riccardo Alessandri for our countless meaningful discussions. Your expertise in coarse-graining and intermolecular interactions truly broadened my knowledge and always inspired my

research. I also want to thank Dr. Joan Montes de Oca, Dr. Elizabeth Lee, Dr. Gustavo Perez-Lemus, and Dr. Pablo Zubieta, who offered their valuable expertise in advanced sampling and helped me troubleshoot. I am grateful to have learned from outstanding polymer physicists, Dr. Artem Rumyantsev, Dr. Phil Rauscher, Dr. Joshua Mysona, and Dr. Ludwig Schneider, who helped me refine my research questions. Viviana Palacio-Betancur and Aria Coraor, I truly appreciate your generous advice that helped me navigate my PhD study. Mentoring and collaborating with talented individuals later in my journey have been a true privilege. I would like to thank Maria Ley Flores, Sarah Chen, Karim Al Zahabi, and Ge Sun, whose dedication has made the journey rewarding and enjoyable.

My PhD experience wouldn't be complete without my collaborators. I am especially grateful for the support from my committee members and collaborators here at Pritzker School of Molecular Engineering (PME), Prof. Matthew Tirrell, Prof. Paul Nealey, and Prof. Shrayesh Patel. It is truly a privilege and pleasure to have maintained our collaboration throughout my entire PhD journey. Over the past five years, you have supported me and taught me perspectives that I couldn’t have gained otherwise. I especially appreciate your willingness to take on the computational perspective with me and shared insights from both angles. In the first half of my research, I am grateful to have worked with Dr. Whitney Fowler, whose leadership and creativity truly made our project enjoyable. I feel especially fortunate to have partnered with Dr. Daniel Sharon and Dr. Peter Bennington to work on polymer electrolytes, who are not only exceptionally kind collaborators but also top experts in the field. Our discussions have always been inspiring and enlightening. I would also like to thank Dr. Regina Sánchez-Leija and Ben Ketter, who later joined the project and added a new dimension to it. Outside PME, it has also been a pleasure to collaborate with prof. Mark Ediger and Dr. Kushal Bagchi from University of Wisconsin-Madison, Dr. Dean

DeLongchamp and Dr. Thomas Ferron from NIST, and Dr. Daeyeon Lee, Dr. Raymond Gorte, and Tian Ren from University of Pennsylvania. Our rewarding collaborations has significantly enriched my PhD experience. I would also like to express my gratitude to Heather Crews, Lisa Vonesh, Rovana Popoff, David Taylor, and Laura Rico-Beck for their behind-the-scenes support, which has made my PhD journey safe and enjoyable.

Finally, my cohorts and friends have been invaluable company. During graduate school, they shared countless joy and memories with me. I am especially thankful to Elise Chen, Hongyi Zhang, Jonathan Salmerón-Hernández, Fabian Byléhn, Jiachong Chu, Yang Li, Wen Chen, Wen Zhuang Yiheng Wu, and Cheng Zhang, who cheered me on with warmness and humor. I am also fortunate to have Celia Xu as my roommate from high school and now in Chicago, who shared the hardest pandemic time with me. Thank you all for the support and shared memories that have made this journey memorable and fulfilling.

ABSTRACT

Macromolecular soft materials offer tremendous versatility and design possibility to achieve novel functionalities for sustainability goals. They can be engineered to sequester ions from wastewater to combat pollution and recover elemental resources, or to transport ions for use as electrolytes in rechargeable batteries. Within these materials, the intricate interplay between chemically specific interactions and macromolecular entropy poses design challenges across various length scales. In this dissertation, diverse molecular simulation tools are employed to gain structural and dynamical insights. Supported by experimental evidence, these insights help advance the design of these materials.

In the first past of this dissertation, atomistic molecular dynamic simulations are combined with various free energy methods to investigate self-assembled peptide amphiphile micelles that selectively capture and reclaim phosphate ions from water. Chapter 2 reports a prototype material that selectively captures and releases phosphate controlled by a pH trigger. Simulations identified the significance of chain flexibility and binding entropy as design factors. In Chapter 3, we examine these design elements using multi-component micelles and apply them to propose a *de novo* micelle design. In the second part, we focus on uncovering fundamental lithium-ion transport behavior in nonhomogeneous solid polymer electrolytes, using multiscale molecular dynamics simulations combined with network analysis. Chapter 4 focuses on graft solid polymer electrolytes to elucidate the role of polymer architecture on lithium-ion transport. The investigation reveals heterogenous dynamical and ion solvation behaviors along the grafted side chains. Chapter 5 examines the impact of monomeric mixing on lithium-ion transport by comparing a blend polymer electrolyte with a block copolymer counterpart. A graph-based transport model is proposed to quantify this effect. Chapter 6 builds upon our knowledge about graft architecture and monomeric

mixing to characterize polymer electrolytes grafted with mixed polarity side chains, where entropic penalty, rather than polarity, dictates the solvation behavior of lithium ions. In Chapter 7, we summarize our findings and discuss a few interesting directions for future research.

CHAPTER 1

INTRODUCTION

Macromolecular soft materials offer tremendous versatility and design possibility in achieving novel functionalities. They can be engineered to achieve desirable nanostructures through self-assembly processes, while retaining selectivity, specificity, and precision at the molecular level. One example of such material is peptide amphiphile micelles, which consist of peptides conjugated to aliphatic tails. These biomimetic materials combine the nanostructures of self-assembled amphiphiles surfactants with the precise functions of bioactive peptides. Another example is copolymers, which consist of covalently bonded monomers of diverse chemistries. The nanostructure and local interactions are dictated by a complex interplay between the polymer architecture and the monomer chemistry. The diverse nanostructures and customizable functionalities of these materials enable a wide range of applications from drug delivery, nanofabrication, to battery electrolytes. This dissertation presents new insights into the use of macromolecular soft materials for two sustainability goals, clean water and clean energy. First, we explore design of a biomimetic material based on peptide amphiphile micelles to combat the growing issue of excess phosphate pollution in wastewater. Subsequently, we examine solid polymer electrolytes with varying architectures and monomer chemistries, aiming to deconvolute the design elements for higher performing electrolytes in solid state lithium-ion batteries.

1.1 Phosphate Recovery Using Biomimetic Binding Materials

1.1.1 Motivation and Background

Biological binding has been demonstrated for its precision and selectivity[1]. Grounded in the fundamental principles of inter- and intra-molecular interactions, this precise functionality can also be harnessed to design novel, biomimetic synthetic materials that precisely recognize and

reversibly sequestrate specific molecules[2]. These aqueous materials are potential solutions to pressing environmental challenges regarding resource reclamation and pollution removal from wastewater. Several studies have attempted to recover from wastewater valuable resources[3,4] and toxic chemicals. [5–7]

In this context, phosphate is chosen as the reclamation target out of two motivations. First, phosphate is a prime target for many reclamation technologies due to the urgent scarcity and water pollution challenges. As an essential elemental resource in food production, nonrenewable phosphate reserves are projected to deplete in 50 to 100 years. [8–10] Meanwhile, excess phosphate from wastewater and agricultural runoffs accumulates in natural water bodies, causing severe eutrophication and algae blooms that destroy natural ecosystems.[8,11] Because the natural phosphate cycle takes hundreds of years to transform the excess phosphate back into phosphate minerals, novel technology that accelerate the phosphate recycling process is necessary. Second, phosphate is one of most studied and well-understood binding targets in biology. Selective binding to phosphate occurs almost every energy-consuming biological process.[12–14] Knowledge of phosphate-binding mechanism and peptide sequence databased have become widely available, through extensive studies of native phosphate-binding proteins (PBPs) and the designs of their synthetic derivatives.[2,15]

Practical application of emerging bio-inspired resource reclamation technologies would require a versatile material platform, where the recognition, capture, and release of the target molecule are reversible, reliably controllable, and robust over cycles of use. The biomimetic prototype material considered here consists of peptide amphiphile micelles, which combine the precision of biological binding with the structural tunability of self-assembly.

1.1.2 Peptide Amphiphiles and Self-Assembled Micelles

Peptide amphiphiles are a class of synthetic molecules, in which peptides are conjugated to hydrophobic alkyl chains. Above the critical micelle concentration (CMC), they spontaneously self-assemble into a variety of functional nanostructures, where the alky tails are pointed towards the core and the peptide headgroups are solvated by the aqueous environment.[16–19] The self-assembled morphology is determined by a characteristic parameter known as the packing parameter,[20] which empirically summarizes various types of intermolecular interactions, including the hydrophobic interactions of the alkyl tails, hydrogen bonding among the peptide segments, and electrostatic repulsions among charged amino acids. To achieve a desired morphology, the design of a peptide amphiphile is often divided into four chemical features.[16] The molecule starts with a hydrophobic domain (region 1), which is typically a long alkyl chain. This alkyl chain is connected to a short peptide sequence that promotes intermolecular hydrogen bonding (region 2). Region 3 consists of charged amino acids that enhance the solubility in water and can be designed to be pH or salt-responsive. Finally, region 4 is the bioactive epitome presented to interact with the environment.

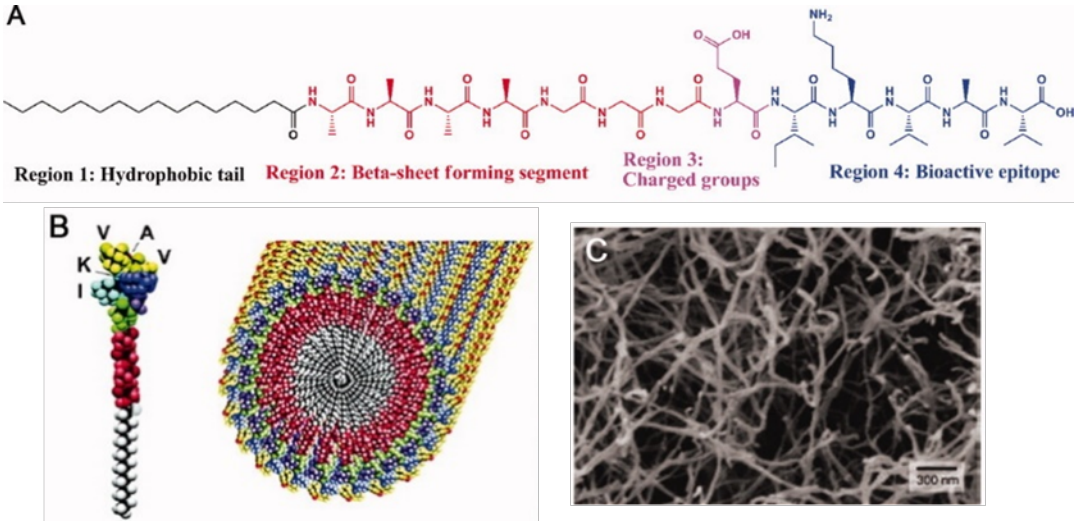

Figure 1.1. Typical design of a PA molecule and the self-assembly of PA molecules into nanofibers. (A) Molecular structure of a representative PA with four rationally designed chemical entities. (B) Molecular graphics illustration of an IKVAV-containing PA molecule and its self-assembly into nanofibers. (C) Scanning electron micrograph of the IKVAV nanofiber network formed by adding cell media (DMEM) to the PA aqueous solution. Adapted from ref.16.

The modular molecular design enables precise control over multiple length scales. For instance, hydrogen-bonding amino acids in region 2 tend to grow β-sheets along an axis, which promotes the formation of 1D cylindrical micellar fibers instead of spherical micelles. [21,22] These fibers can form an entangled, dense suspension that provides desirable mechanical property suitable for the phosphate reclamation application.[23] Furthermore, the self-assembly process is reversible and reproducible, which allows the material to refresh after use cycles. Given ample opportunities for sequence and nanostructure manipulation, PAMs will be a straightforward and promising platform to design protein-inspired materials for molecule recognition and sequestration.

1.1.3 Natural and Synthetic Phosphate Binding Sequences

The incorporation of peptide headgroups makes PAs an ideal platform to harness and engineer the selective ion capture-and-release activities found in many natural biological processes. The selective binding of phosphate is a ubiquitous phenomenon in energy-consuming biological

processes. Numerous studies have investigated binding sequences and binding mechanisms in PBPs[13,24,25] and in isolated peptides. [2,26] Comparative studies of PBPs attributed the ability to bind phosphate to a common motif, denoted as the P-loop, that has the amino acid sequence GXXXXGKS/T,[12] where X can be any amino acid. The P-loop motif is later extended to the Walker A motif[15], which includes an alpha helix before and a beta sheet after the P-loop motif. It was also reported that non-P-loop protein sequences could also exhibit remarkable selectivity towards phosphate. [1]

A P-loop motif is believed to bind phosphate through electrostatic attraction, hydrogen bonding, and nest conformation. A typical nest cavity consists of a conformation motif of RL or LR, where R and L represent consecutive dihedral angles along the amino acid backbone. However, the P-loop motif is believed to adopt an LRLR compound nest motif so that it accommodates the phosphate with sufficient volume and favorable hydrogen bond angles. [13,27] The formation of such compound nest relies on the flexibility of the glycine residue, which allows for a turning point at the end of the preceding alpha helix.[24] Along the compound nest, the amino acid backbone forms a series of hydrogen bonding with the phosphate. Additionally, the lysine residue contains a positively charged amine that attracts and stabilizes the phosphate.

To engineer the P-loop motif for realistic applications, studies have isolated the Walker A motif[15] and the P-loop motif[2] to assess their abilities to bind phosphate. A synthetic, freestanding hexapeptide (SGAGKT), inspired by the P-loop motif, has been reported to bind inorganic phosphate in a pH-controlled manner.[2] The binding mechanism of the free-standing hexapeptide seems to differ from that in PBPs. A follow up simulation study shows that the hexapeptide does not have a well-defined binding nest, and it instead shows a more dynamics binding effect with multiple bound structures that can rapidly interchange.[26] Therefore, when incorporating the P-loop

motif into a novel material platform, it should be noted that the native binding mechanism may not necessarily translate. Meanwhile, new mechanisms beyond electrostatic attraction, hydrogen bonding, and nest conformation, could potentially emerge to provide new opportunities for optimization.

This dissertation bridges the studies of phosphate-binding sequences and self-assembling biomaterials to design phosphate binding materials based on peptide amphiphile micelles. Because the bioactive functionality and the assembled nanostructure are highly coupled and jointly dependent on the headgroup peptide sequences, a strategically designed peptide sequence must simultaneously facilitate stable assemblies and demonstrate effective functionalities. In this regard, molecular simulations serve as invaluable tools to first supplement existing experiments with molecular level explanations, and then lead experiments by providing insights for the design of optimal sequences.

1.1.4 Binding Free Energy Calculation Methods

The selectivity and affinity of protein binding is a result of complicated energy exchanges among the protein, ligand, water, and spectating ions. The Gibbs free energy is the most important thermodynamics quantity that describes the driving force of binding.[28–30] The free energy of binding, ΔG, can be partitioned into enthalpic (ΔH) and entropic contributions ($-T\Delta S$). The binding enthalpy mainly reflects changes in potential energy due to the formation of noncovalent interactions such as hydrogen bonds, van der Waal contacts, and other electrostatic interactions. The entropic term accounts for the change in the degrees of freedom for water to arrange around the solutes and for the protein and ligand to translate in the system and adopt different internal conformations.

Calculation of binding free energies is a non-trivial task for computational studies. The challenge lies in the difficulty to sufficiently sample an extremely large conformation space. Since the likelihood of finding the system in a state is exponentially related to the inversed free energy of that state, binding processes that involve high energy barriers along the transition pathways present even greater sampling challenges. To overcome these difficulties, a wide range of free energy methods have been developed.[31–37] Any of these methods involve applying biased potentials or forces to facilitate sampling on a flattened free energy landscape and correcting for the bias afterwards. For instance, in Adaptive Biasing Force Sampling (ABF), a continuously updated biasing force is added to the equations of motion, eventually leading to uniform sampling on a flat energy surface.[33] Free energy landscapes can be subsequently reconstructed by directly integrating the averaged biased force applied. ABF is widely employed for free energy calculations because its underlying concept intuitively aligns with the that of potential of mean force (PMF) and it does not require prior knowledge of the free-energy landscapes. For a detailed algorithm and mathematical proof, the reader is referred to Ref.33. Another widely used free energy method is umbrella sampling (US),[37] where harmonic biasing potentials are strategically placed along a proposed transition pathway. Free energy profile will be reconstructed post-simulation using the histograms of sampled conformations.[36] In this dissertation, both ABF and US methods will be applied to compute the free energy associated with phosphate binding processes.

1.2 Solid Polymer Electrolytes

1.2.1 Background and Motivations

Technologies of affordable, safe, and efficient energy storage are essential for advancing a sustainable future. High-energy-density secondary batteries will drive progress in the fields of portable electronics, battery-powered transportation, and grid-scale storage of renewable

energy.[38–40] As the best-known, state-of-the-art secondary battery, lithium-ion batteries (LIB) have been widely used in portable electronics. An LIB typically consists of a graphite anode and a transition-metal-oxide cathode that reversibly intercalates lithium, coupled internally by a lithium ion-conducting electrolyte.[38,41,42] However, their further applicability in the domains of battery-powered transportation, and grid-scale storage of renewable energy would require even higher energy density beyond the theoretical limit. In this regard, researchers have sought to explore lithium metal batteries (LMB), in which the conventional graphite anode is replaced with metallic lithium. [41,43] The use of metallic lithium, however, introduces a serious safety risk that significantly hinders commercial applications of LMB. It tends to cause nonuniform lithium metal deposition on the anode, which can grow into dendrites that short the battery.[44]

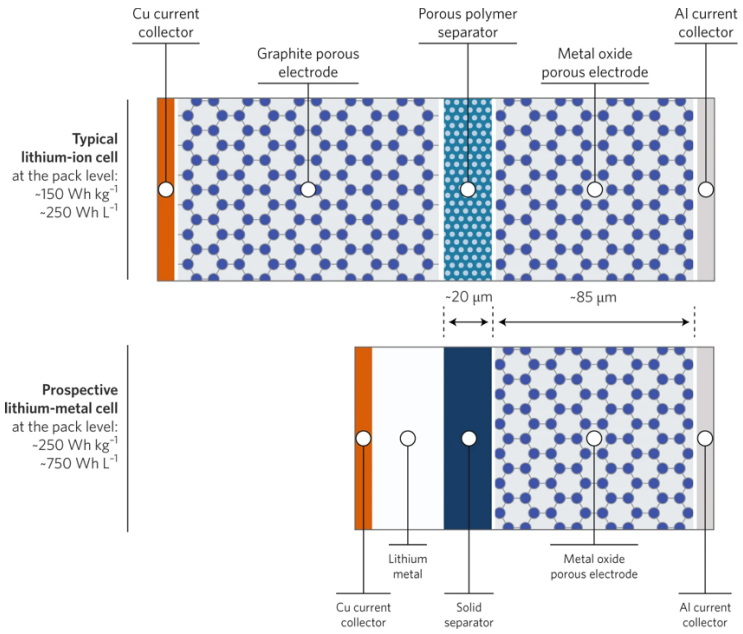

Figure 1.2. Repeat layers of a typical lithium-ion cell and one conception of a lithium metal cell, adapted from ref.43. The lithium metal cell contains a solid separator and a dense layer of metallic lithium, showing increased gravimetric and volumetric energy densities.

One of the bottlenecks lies in the development of electrolyte technologies. While LIB employs liquid electrolyte consisting of lithium salt dissolved in a mixture of organic solvents,

LMB may require solid state electrolytes with sufficient mechanical strength that suppresses Li metal dendrite growth.[44] A promising solution has emerged with the discovery of alkali-metal salt-doped poly(ethylene oxide) (PEO) as an electrolyte material,[45] paving the way for lithium salt-doped solid polymer electrolytes (SPE). Compared to other solid-state electrolytes such as ceramics, SPEs offers numerous advantages.[46,47] They are inherently safe, electrochemically stable, thermally stable, and compatible to open systems. Moreover, they can be processed and recycled at lower cost. However, many SPEs face the challenge of unsatisfactory ionic conductivity at ambient temperatures. Although the ionic conductivity of PEO/salt mixtures can reach as high as 10^{-3} S cm^{-1} at elevated temperature, the conductivity drops dramatically as PEO crystalizes at 60°C.[47,48] Since PEO must operate in its rubbery state to achieve reasonable conductivity, it does not provide sufficient mechanical strength required for true solid-state battery applications. Therefore, to overcome this inherent trade-off between mechanical strength and ionic conductivity has been a central focus in this field.

1.2.2 Ion Transport Mechanisms in SPEs

Using PEO and PEO-based polymers as examples, studies have sought to reveal the structural, dynamical, and mechanistic picture of Li^+ transport in SPEs, which help establish fundamental design principles for SPEs. For an SPE to conduct, the cations and anions must disassociate in the polymer matrix and move in opposite directions. To facilitate the solvation, the cation-polymer interaction should overcome the lattice energy of the cation and anion.[49,50] Meanwhile, the polymer host should have a sufficiently strong dielectric strength to screen the electrostatic attraction between cations and anions.[51,52] Taking PEO as an example, numerous theoretical studies suggest that it solvates Li salts by forming stable complexes with Li^+, where each Li^+ is typically coordinated by four to seven ether oxygen atoms from one or two polymer chains.[50,53,54] The

mobility of solvated ions, evidenced by several theoretical and experimental works, is intrinsically coupled to polymer dynamics, and therefore the glass transition temperature (T_g) of the polymer.[55,56] A series of simulation studies by Borodin and coworkers suggested three primary contributions for Li^+ transport: (a) intrachain hopping along the polymer backbone, (b) interchain hopping from one segment to another, and (c) cooperative motion of Li^+ with short polymer chains, also known as vehicular diffusion.[50,53,54,57] Intrachain (a) and interchain (b) hopping are also referred to as fluctuation-driven diffusion, since the hopping of a cation from one site to another is mediated by the segmental motions that cause fluctuations away from the lowest free-energy configuration of the current cation-polymer complex, ultimately leading the cation towards sites of lower free energy. At high molecular weight, vehicular diffusion is suppressed due by chain entanglement,[58] such that conductivity is dominated by fluctuation-driven diffusion.

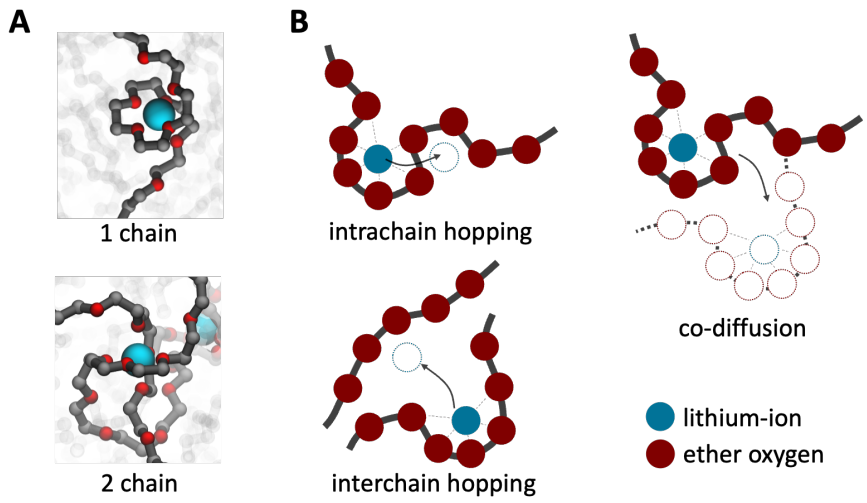

Figure 1.3. Solvation environment of lithium-ion in salt-doped PEO. (A) MD simulation snapshots of typical 1-chain and 2-chain solvation configurations. (B) schematic of three primary lithium transport mechanisms in salt-doped PEO.

Knowledge of ion transport in SPEs obtained from PEO-based examples serve to guide researchers towards new SPE materials that overcome the limitations of PEO. One strategy is to accelerate segmental dynamics by disrupting the polymer crystallinity and/or lowering the T_g.

Researchers have pursued this avenue by using plasticizing additives,[59–61] introducing comonomers into the PEO backbone,[62,63] and employing nonlinear polymer architectures.[64–67] Others explored monomer chemistries to search for new solvation moieties[68–72] and transport mechanisms.[73–76] Studies in this regard show that the connectivity[77] of these Li^+ solvation moieties is crucial for hopping events to take place. From there, the concept of solvation site connectivity arises as a simulation-derived metric that quantifies the proximity of Li^+ solvation sites and relates this feature to ionic conductivity.

1.2.3 Copolymer Electrolytes

In copolymers, monomers of different chemistries are covalently connected in a wide range of architectures, such as blocked, grafted, stared, and crosslinked, to name a few. Similar to peptide amphiphile micelles, these materials have the potential to combine functionalities from a wide range of available chemistries and allows for modularized optimization, offering opportunities to resolve existing issues of SPEs.

Combed or branched SPEs have been extensively explored to prevent crystallization[49,64] and introduce new functionalities.[78] Among a wide range of side chain- and backbone- chemistries explored, poly (oligoethylene oxide) methacrylate (POEM) stood out due to its superior room temperature conductivity compared to PEO.[79] The synthetic flexibility of its polymethacrylate backbone, combine with click chemistry for side chain grafting, enables sequence-controlled attachment of additional other functional side chains to address various shortcomings.[80–85] For instance, tethering counterions of Li^+ to the side chains enable the material to behave as single-ion conductor, significantly improving the transference number.[86]

Phase-separated, nanostructured SPEs offer a way to circumvent the tradeoff between conductivity and mechanical strength.[87] Binary linear block copolymers (BCP) are commonly

explored for this purpose, since the conducting and supporting domains can be optimized independently. The microphase separation is dictated by the Flory-Huggins interaction parameter χ_{AB}, which describes the incompatibility between the components. At high χ_{AB} or low temperature, the strong segregation drives the copolymer to self-assemble into ordered nanostructures such as lamellar, cylindrical, or spherical morphologies.[88] BCP such as polystyrene-block-poly(ethylene oxide) (PS-b-PEO) self-assembles into periodic lamellar morphology with PS domains that exhibit below-T_g mechanical modulus and PEO domains that can solvate and transport ion.[89–91] Another study with salt-doped polystyrene-block-poly(oligo-oxyethylene methacrylate) (POEM-b-PS) reveals that the PS domain dramatically improved the mechanical strength with minimal impact on conductivity.[80,92,93]

The interfaces between nanodomains are influenced by segregation strength[91,94] and monomer sequence.[80] In many block copolymer electrolytes (BCE), the addition of salt increases the segregation strength, resulting in a sharper interfacial region between dissimilar domains.[91,95] On the other hand, a gradient composition profile at the transition regions, referred to as tapering, leads to a wider interfacial region.[80] Studies of tapered PS-b-POEM systems conclude that the widened interfacial region improves ion transport by lowering the T_g and accelerating segmental dynamics.[80] Yet another study suggests that this improvement results from favorable parametric conditions.[96] Nonetheless, these findings collectively suggest the potential for enhancing material properties via manipulating nanodomain interfaces. To address these challenges and gain valuable insights for BCE designs, significant theoretical work is anticipated to provide a consistent and fundamental picture of ion transport at interfaces.

1.3 Outline of the Dissertation

This dissertation presents insights into the design of two soft material systems interfacing with ions. Within them, the coupling between chemically specific interaction and macromolecular entropy presents us design challenges across length scales. We employ diverse molecular simulation tools to address these challenges, providing molecular-level insights to explain and guide experiments.

We start by developing a novel class of protein-inspired capture-and-release materials for recycling resources on the nanoscale. These peptide amphiphile-based materials incorporate a protein-inspired binding mechanism directly into the self-assembled material network. The energetics and mechanisms of phosphate-binding to freestanding and self-assembled peptide amphiphiles are assessed using atomistic molecular dynamics and various free energy methods. In Chapter 2, we demonstrate a prototype of single-component peptide amphiphile micelles that can sequester, release, and reclaim phosphate using a stimuli-responsive pH trigger. This material can efficiently sequester and release phosphate for multiple reuse cycles, and simultaneously demonstrating selectivity over nitrate and nitrite. Our simulations reveal that, at high pH, the binding conformation of the peptide becomes constrained in the dense micelle corona, such that phosphate is expelled when it otherwise would be preferentially bound. Conversely, at neutral pH, this dense structure employs multi-chain binding to further stabilize phosphate when it would otherwise be unbound, opening opportunities to engineer higher-order conformational binding design into this controllably packed corona.

In Chapter 3, we explore the potential of multi-chain binding by studying multi-component micelles, where chain packing in the corona can be controlled by composition. Molecular dynamics simulations uncover two new design elements of flexibility and gain of entropy in these

protein-analogous synthetic materials, which may not be accessible in traditional proteins. We then translate these new design factors to create *de novo* peptide sequences that can bind phosphate independently of protein-derived sequence or conformation. Overall, this work demonstrates that traditional conformational restrictions in protein binding can be replaced and repurposed in multi-component peptide amphiphile synthetic materials, opening up opportunities for enhanced protein-mimicking design in the future.

Then, we proceed to study lithium-ion transport in solid poly(ethylene oxide)-based electrolytes, using multiscale molecular dynamics simulations combined with network analysis. A series of simulation work were conducted to evaluate the impact of a few material attributes on Li^+ transport, including polymer architecture, interfacial monomer mixing, mixed side-chain functionality, and monomer sequence. In Chapter 4, comparative study of PEO and POEM elucidates the role of polymer architecture on Li^+ transport. The analysis reveals heterogenous dynamical and ion solvation behaviors along the grafted side chains, with Li^+ preferentially solvated near the side chain ends. The transport of Li^+ is found to be directly coupled to the dynamics of these solvating segments, rather than the material-averaged dynamics. The localized Li^+ solvation leverages the accelerated segmental dynamics of side chain ends to enhance the transport of Li^+.

In Chapter 5, a blend polymer electrolyte is compared with a block copolymer counterpart to examine the impact of monomeric mixing on Li^+ transport. Although these two materials show identical local Li^+ solvation environment, their slight difference in the degree of mixing leads to a distinct variation in the clustering and connectivity of solvation sites at length scales between 5 and 10 Å. A graph-based model is proposed to quantify this feature and its impact on long-range Li^+ transport.

Chapter 6 combines knowledge about graft architecture and monomeric mixing to explore polymer electrolytes grafted with mixed polarity side chains. We find that entropic penalty, rather than polarity, dictates the solvation behavior of Li^+. Additionally, we explored the effect of functional group sequence by comparing a random copolymer and a block copolymer at fixed composition. In the random copolymer, the relatively diffuse interfaces allow for the formation of hybrid solvation sites that facilitate Li^+ transport.

Finally, the findings and contributions are summarized in Chapter 7. these results are summarized, and a few interesting future research directions are discussed.

I SEQUESTRATION OF PHOSPHATE IONS IN PEPTIDE AMPHIPHILE MICELLES

CHAPTER 2

PROOF OF CONCEPT: DESIGNING SINGLE-COMPONENT PEPTIDE AMPHIPHILE MICELLE FOR PHOSPHATE CAPTURE

This chapter is modified and reprinted with permission from Fowler, W. C.; Deng, C.; Griffen, G. M.; Teodoro, O. T.; Guo, A. Z.; Zaiden, M.; Gottlieb, M.; de Pablo, J. J.; Tirrell, M. V. Harnessing Peptide Binding to Capture and Reclaim Phosphate. *J. Am. Chem. Soc.* **2021**, *143*, 4440–4450. https://pubs.acs.org/doi/10.1021/jacs.1c01241.

2.1 Abstract

With rising consumer demands, society is tapping into wastewater as an innovative source to recycle depleting resources. Novel reclamation technologies have been recently explored for this purpose, including several that optimize natural biological processes for targeted reclamation. However, this emerging field has a noticeable dearth of synthetic material technologies that are programmed to capture, release, and recycle specified targets; and of the novel materials that do exist, synthetic platforms incorporating biologically inspired mechanisms are rare. We present here a prototype of a materials platform utilizing peptide amphiphiles that has been molecularly engineered to sequester, release, and reclaim phosphate utilizing a stimuli-responsive pH trigger, exploiting a protein-inspired binding mechanism that is incorporated directly into the self-assembled material network. This material is able to sequester and controllably release phosphate for multiple cycles of reuse, and it is selective over nitrate and nitrite. We have determined by simulations that the binding conformation of the peptide becomes constrained in the dense micelle

corona at high pH such that phosphate is expelled when it otherwise would be preferentially bound. However, at neutral pH, this dense structure conversely employs multi-chain binding to further stabilize phosphate when it would otherwise be unbound, opening opportunities for higher-order conformational binding design to be engineered into this controllably packed corona. With this work, we are pioneering a new platform to be readily altered to capture other valuable targets, presenting a new class of capture and release materials for recycling resources on the nanoscale.

2.2 Introduction

As critical resources are being unsustainably depleted while the global demand increasingly rises, society is turning towards wastewater as a new source for reclaiming valuable products or toxic chemicals,[5–7,97] including rare metals,[4] critical fertilizer ingredients,[98] and pharmaceutical products.[3,99] Our ability to harvest these, however, is limited by several infrastructural, societal, and technological challenges.[97] In particular, the emerging field of resource reclamation lacks versatile materials that are molecularly engineered to recognize, capture, and release their targets in a controllable and practical manner.

A promising design scheme in this endeavor is to exploit the inherent ability of proteins to specifically recognize, bind, and release their target molecules and incorporate this function into a tunable synthetic material. Natural abilities of phosphate-processing organisms have been harnessed in their raw form to reclaim phosphorus,[100] including the prokaryotic processes of enhanced biological phosphorus removal or eukaryotic technologies such as floating algae farming. A challenge for these technologies is that of grappling with complex operating conditions required for optimized resource reclamation.[98,100–103] On a larger scale, engineered wetlands systems have also been employed to reclaim nutrients, but thus far they have not gained momentum in use due to a limited resource return rate.[101] Since these technologies employ organisms in their

raw form, they face the innate restrictions imposed by the organism's metabolism, thereby restricting opportunities for optimization. This unique biological sequestering ability could be fully realized if it were intentionally designed into a synthetic materials platform. However, attempts to develop a hierarchically driven, biomimetic materials design scheme for resource capture and release have been limited.

A strategic target compound for development of a prototype capture-and-release material is phosphate, a commodity widely targeted by other technologies in addition to those described above. [10,98,100–107] This limited resource is an essential ingredient in many fertilizers,[108,109] but at its current rate of extraction, it is projected to be expended in 50 to 100 years.[9] Paradoxically, this highly coveted resource is also being discarded in large amounts in agricultural runoff streams, thereby causing severe eutrophication and vastly disrupting natural ecosystems.[11] An effective, capture-and-release material could be strategically employed to target and recover phosphate from where it is detrimental and reinsert it where it is depleted yet greatly needed.

In this work, we present a prototype of a novel materials platform that relies on self-assembled peptide amphiphiles to controllably capture, release, and reclaim phosphate through a pH-responsive trigger, exploiting the natural binding ability of proteins. Peptide amphiphiles (PAs) consist of a short peptide sequence "headgroup" conjugated to a hydrophobic "tail" that causes spontaneous self-assembly into micelles in water. The PAs can be precisely designed and synthesized to feature multiple functional "building block" segments,[110,111] such as protein-derived binding amino acid sequences that are systematically displayed upon assembly in the micelle coronae,[19] or segments to promote protein secondary structure conformations in the headgroup,[112] a well-known critical component in biological binding. Indeed, PAs have previously harnessed this specific targeting ability of biological molecules for use in targeted drug delivery[113,114] and

cell adhesion,[115] making this platform well-positioned to transition in application towards specified targeting of selected resources. In fact, PAs have recently been studied for macromolecular harvesting of proteins,[116] which exploits similar concepts but could have differences in its practical implementation due to molecular size and transport phenomena. Our material design is easily accomplished through use of well-studied, sequence-specific synthesis techniques to produce environmentally benign materials, an advantage over other novel capture and release materials such as metal organic frameworks that have complex synthetic routes, can be toxic, and are unstable in water.[117–119]

In addition to exploiting advantages in synthesis and targeted binding, we also leveraged the unique material characteristics of PAs, showing the importance of control over multiple length scales. In our work, the micelle architecture of PA spontaneous self-assembly was tuned according to well-studied strategies to direct the PAs towards self-assembly into wormlike micelles that form an entangled, dense suspension.[23] This network hosts a multitude of phosphate-binding sites on its exposed surfaces and provides a physical structure through which phosphate-rich water can flow, capturing the phosphate ions on the strands of the network. The ions can later be controllably released by a pH trigger. The self-assembled network thereby inherently offers a practical means to reclaim this valuable resource. To develop the proposed materials and gain a mechanistic understanding of the molecular processes through which phosphate is captured, we have relied on molecular simulations of the molecules and self-assembled structures of interest. Although the initial prototype will target phosphate, the versatility and breadth of PAs positions us to modify peptide binding sequences to target, sequester, and reclaim, with potentially high avidity and selectivity, a large number of other valuable resources such as heavy metals, pharmaceuticals, or

bioplastics, with the potential to truly become a modular materials platform for wastewater resource recovery.

2.3 Methods and Materials

2.3.1 Experimental Methods

Synthesis and Purification of Peptide Amphiphile Micelles and Micelle Preparation Procedure. Two peptide sequences (GGGSGAGKT and SGAGKTSSSGGK(dde-protected)-GGHHHSGAGKT) were synthesized on 0.25 mmoles of rink amide resin (Novabiochem) through standard FMOC solid phase peptide synthesis using an automated Prelude X Benchtop Synthesizer (Protein Technologies, Tuscon, AZ, USA). For each coupling step, the FMOC protecting group was first removed from the resin using 20% piperidine in dimethylformamide (DMF). Separately, the amino acid was activated with N,N,N',N'-Tetramethyl-O-(1H-benzotriazol-1-yl)uranium hexafluorophosphate (HBTU) and N,N-Diisopropylethylamine (DIPEA) in a molar ratio of 1:4:3.95:8 of resin: amino acid: HBTU: DIPEA. The activated amino acid cocktail was then added to the deprotected resin and then allowed to mix to conjugate.

After the amino acid couplings were completed, each peptide was then coupled with a palmitic acid tail. For the GGGSGAGKT peptide, the palmitic acid was simply conjugated to the deprotected glycine N-terminus. For the SGAGKTSSSGGK(dde-protected)GGHHHSGAGKT peptide, the palmitic acid was conjugated to the side chain of the 10^{th} residue lysine, ensuring first that the FMOC protecting group on the 1^{st} residue serine was not removed in the standard coupling procedure. The deprotecting cocktail for the dde-protecting group of the lysine was prepared by dissolving 1.8 mmol $NH_2OH.HCl$ and 1.35 mmol Imidazole in 5 mL N-Methyl-2-pyrrolidone (NMP), sonicating until dissolved. Just before adding the solution to the resin, Dichloromethane (DCM) was added in a 1:5 DCM to cocktail by volume proportion. The cocktail was then added

to the resin and the solution was shaken for 3 hours to deprotect the side chain lysine. The solution was drained and washed with DCM and DMF. The palmitic acid was coupled to this free amine using the standard coupling cocktail described previously. After palmitic acid coupling, the FMOC of the serine was deprotected with 20% piperidine in DMF to leave a positively charged N-terminus.

After drying the resin under nitrogen, the peptide amphiphiles were then cleaved from the resin using a 95:2.5:2.5 by volume trifluoroacetic acid: triisopropylsilane: MilliQ water cleavage cocktail for 2 hours while shaking. The cleaved peptide amphiphiles were then precipitated through dropwise addition of the cleavage solution in a 50:50 by volume hexanes: -80 ºC diethyl ether solution. The peptide amphiphiles were dried under nitrogen and dissolved in water.

The peptide amphiphiles were purified using reverse-phase HPLC (Prominence, Shimadzu, Columbia, MD, USA) on a C8 column (Waters, Milford, MA, USA) at 50 ºC using acetonitrile and water with 0.1% formic acid as gradient mobile phases. The molecular weight of the products in the HPLC fractions were characterized by MALDI-TOF mass spectral analysis (Biflex III, Bruker, Billerica, MA, USA). The product-verified fractions were lyophilized and stored as powders at -20 ºC. The purity was analyzed using a similar gradient method on an Agilent 6130 LCMS system in the University of Chicago's Mass Spectrometry Facility, using a Waters column, C8, XBridge, 4.6 mm × 150 mm, 5 μm particle size, and 130 Å pore size. The purity was calculated by integrating the area under the peaks during the elution time and dividing the area of the product peak by the area of all peaks, excluding peaks that were artifacts of the method. The purity was confirmed to be greater than 95% for both PAs.

Finally, the PA micelles were fabricated through dissolving the lyophilized powder in MilliQ water at the desired concentration, heating at 70 ºC for 1 hour on a mechanical shaker, and

letting the solution cool down and equilibrate at room temperature for at least 2 hours before experimental use.

Critical Micelle Concentration (CMC) Determination. The CMC was calculated by marking an increase of fluorescence intensity, corresponding to an increased micelle concentration, of a dissolved dye that fluoresces in the presence of hydrophobic micelle cores. To execute this experiment, 1,6-diphenyl-1,3,5-hexatriene (DPH) dye was dissolved in tetrahydrofuran at a concentration of 100mM and then diluted in water to a final concentration of 1 μM. Each PA was dissolved in 1 μM DPH solution and serially diluted by half to range from 0.001 μM to 1000 μM, performed in triplicates for each PA. The dilutions were allowed to equilibrate for one hour while covered with aluminum foil at room temperature. They were then transferred to a 96-well plate in triplicates to minimize instrument error. Their fluorescence intensity was measured using a Tecan Infinite 200 plate reader (Mannedorf, Switzerland) with an excitation wavelength of 360 nm and an emission wavelength of 430 nm. The data were plotted with a log-transformed concentration and fit with two linear lines of best fit, one corresponding to the zero-slope portion and one fitting the data with increased fluorescence intensity. The CMC was identified as the intersection of these two fitted lines, approximating the inflection point of increased fluorescence intensity.

Negative-stain Transmission Electron Microscopy (TEM) Imaging. Carbon film 200 mesh copper grids were glow discharged with a Gatan Solarus plasma cleaning system for 30 s. They were then loaded with 3.5 μL of PAs for 1 minute, and then the excess was removed through blotting with filter paper. The grids were negatively stained with 0.75% uranyl formate for 45 s, blotted off to remove excess stain, and then were allowed to air dry before imaging. All transmission electron microscopy (TEM) imaging was performed on either the FEI Tecnai TF30 300 kV TEM (Hillsboro, OR, USA) or the FEI Tecnai Spirit 120 kV TEM (Hillsboro, OR, USA).

The images were processed and measured digitally using ImageJ software, and the average dimensions were calculated from a sample size of at least 10 micelles.

Molybdenum Blue Assay for Analyzing Phosphate in Solution. To determine the amount of phosphate in solution, a spectrophotometric assay referred to as the molybdenum blue reaction was employed, which emits a blue color linearly proportional to the amount of phosphate present in solution. The reaction involves the following steps:

$$PO_4^{3-} + 12\ MoO_4^{2-} + 27\ H^+ \rightarrow H_3PO_4(MoO_3)_{12} + 12\ H_2O \quad (1)$$

$$H_3PMo(VI)_{12}O_{40} + \text{reductant} \rightarrow [H_4PMo(VI)_8Mo(V)_4O_{40}]^{3-}. \quad (2)$$

The first step consists of the reaction between phosphate, ammonium molybdate, and acid, producing a product that is then reduced in the second step to produce the final blue-colored product. Our procedure was modified from previous molybdenum blue assay designs.[120,121] For our procedure, the following reagents were prepared: 0.10 M ammonium molybdate (VI) tetrahydrate (ACS reagent, Acros Organics) in MilliQ water, 10%wt thiourea (99+%, for analysis, Acros Organics) in MilliQ water, 0.9 M sulfuric acid, and Na_2HPO_4 anhydrous (Fisher Scientific) in water at two concentrations of 1mM and 250 ppm phosphate. To conduct the assay for the calibration curve samples, 5 µL of ammonium molybdate, 10 µL of thiourea, and 5 µL of sulfuric acid were added in that order to 230 µL of a phosphate-containing solution with a concentration ranging from 0 to 50 ppm in MilliQ, diluted from the 250 ppm phosphate stock. Note that the reaction is catalyzed by acid, so the acid was added last and the time was recorded at this step to designate the start time of the reaction. The solution was vortexed and allowed to react for 45 minutes. Slightly before the reaction was completed, 75 µL of the molybdenum blue reaction solution was transferred in triplicates to a 96-well clear round-bottom plate. This was injected into a Tecan Infinite 200 plate reader (Mannedorf, Switzerland) so that it would be ready to be

characterized precisely at the 45-minute mark. The spectrophotometric absorbance was measured at a wavelength of 700 nm and averaged between the three samples to minimize measurement error. The ammonium molybdate and phosphate stock solutions were recreated biweekly, to account for their shorter shelf life.

Each time this method was employed to derive the phosphate concentration of an unknown solution, a calibration curve with three samples of known phosphate concentration (0, 25, and 50 ppm) was created. A new curve was created each time to account for small fluctuations in absorbance depending on the age of reagents or time allowed to react. The data were fit with a linear line of best fit and were used the calculate the phosphate concentration of the unknown sample. The curve was rejected and recreated if the R-squared value was less than 0.99.

Analysis of pH-Dependent Phosphate Binding. The binding experiments consisted of combining PA and PO_4 solutions, adjusting the pH, physically separating the PA micelles from the solution with unbound phosphate, and analyzing the phosphate concentration of the filtrate. To perform a single measurement pH-dependent binding experiment, 62.5 µL of 1 mM Na_2HPO_4 stock was combined with 62.5 µL of a PA solution in MilliQ at a predetermined concentration to achieve the desired molar ratio of PA binding unit: PO_4, with a final phosphate concentration of 0.5mM for all binding experiments. Because C_{16}SGKGHhex has two binding units per molecule and C_{16}GGGhex only has one, the concentration of C_{16}SGKGHhex was half that of C_{16}GGGhex to achieve the same molar ratio to phosphate. Upon combining the solutions, the pH was adjusted to the desired pH condition using minimal 0.25 M HCl and 0.25 M NaOH, vortexting between additions, and the pH was measured using a Fisher Scientific Accumet XL500 pH/ISE/Conductivity Benchtop Meter (Vernon Hills , IL, USA) and a Fisherbrand Accumet Micro Glass Mercury-Free Combination Electrode. Upon reaching the target pH, the PA/PO_4 solution

was centrifuged at 9000 g^{-1} for 2 minutes to collect any viscous PA material that had accumulated on the side of the container, then transferred to a 1mL disposable pipette and filtered using a 13 mm 0.22 µm GHP Acrodisc syringe filter, collecting the filtrate sans PA in another vial. 75 µL of the filtrate was withdrawn and analyzed using proportional volumes of the spectrophotometric assay reagents (1.63 µL ammonium molybdate, 3.26 µL thiourea, and 1.63 µL sulfuric acid) and adhering to the rest of the assay protocol. For pH 2, 10, and 11 samples, the amount of added 0.25M NaOH and HCl for pH adjustment was recorded per sample, and the pH of each of the calibration point samples was adjusted to the same pH using an equivalent proportional volume of the NaOH and HCl that was added to the binding sample. The phosphate concentration of the assay sample was calculated using the calibration curve generated with each sample. The original phosphate concentration of the filtrate was then determined by accounting for the volume of the added spectrophotometric reagents which diluted the reading. This was repeated in duplicates or triplicates for each pH condition.

Analysis of Kinetics of Binding. This experiment was conducted similarly to the single measurement pH dependent binding experiments, but the total volume was increased to account for multiple samples being withdraw and multiple measurements taken. The total volume was calculated according to the following scheme: 125 µL * (number of samples) + 200 µL, with the last term ensuring that enough sample was retained. A solution of 5:1 ratio of C_{16}GGGhex to PO_4 at the desired volume was prepared such that the final concentration of PO_4 was 0.5 mM. The pH of the solution was adjusted using minimal HCl and NaOH to the desired pH condition. At each time point, beginning from the moment the desired pH was attained, the pH of the sample was recorded using Hydrion pH paper and 125 µL of solution was withdrawn, filtered, and analyzed as described previously.

Analysis of Selectivity over Nitrate and Nitrite. Samples were prepared in MilliQ in molar ratios of 1:1:1:1, 2:1:1:1, and 3:1:1:1 of PA:PO_4:NO_3:NO_2 equivalent to 10 ppm PO_4. The pH was adjusted and measured as previously described, and the solutions were mixed for 30 minutes to ensure the samples reached equilibrium in the more dilute regime. The samples were filtered as previously described to partition out the PA, and the filtrate was analyzed using ion chromatography.

Ion chromatography was preformed using a Thermo Scientific Dionex ICS-5000+ equipped with a Dionex AS-DV autosampler and using a Dionex IonPac AS22 column (Product No 064141, Thermo Scientific, California, USA). The analysis was run using an eluent of 4.5 mM Sodium Carbonate and 1.4 mM Sodium Bicarbonate (Product No 063965 from Thermo Scientific, California, USA) and a Dionex AERS 500 Carbonate 4 mm Electrolutically Regenerated Suppressor (Product No 085029 from Thermo Scientific, California, USA).

Analysis of Cycles of Capture and Release. The capture and release method was designed to simulate usage conditions of filtration through a packed bed reactor, collecting the released phosphate at designated release intervals. To simulate this, a 520 µL solution of C_{16}GGGhex and PO_4 was prepared in a 5:1 ratio such that the final concentration was 0.5 mM. To capture the phosphate, the pH was adjusted to pH 6 as described previously and left to equilibrate in a shake plate at 200rpm for 30 minutes. 500 µL of this solution was transferred to the filter compartment of an Amicon Ultra 0.5 mL 3K MWCO centrifugal filter and centrifuged for 4 minutes at 9,000 g^{-1}. This filtrate was analyzed using the spectroscopic assay as described previously. A new reclamation vial was switched out, and the retained PA was then washed with 200 µL Milli-Q water 6 times, centrifuging each time at the previous conditions, to ensure all unbound phosphate was removed from the dense PA suspension. The PA material was then recovered by inverting the

filter compartment and collecting in a new collection vial by centrifuging at 1,000 g^{-1} for 10 minutes, or until all sample was recovered.

To perform the phosphate release and reclamation, 100µL of Milli-Q water was added to the filtration compartment and vortexed until well mixed with the PA. The now more dilute PA solution was transferred to a new binding analysis vial, and the total volume transferred was recorded. The volume of the recovered solution was raised to 480 µL using Milli-Q water, and the pH was adjusted to the desired release pH as previously described and left to equilibrate in a shake plate at 200rpm for 30 minutes. The amount of added acid and base was recorded. Upon reaching the target pH, Milli-Q water was added to reach a final volume of 500 µL. The released phosphate was then collected by transferring the solution to a centrifugal filter and centrifuging at 9,000 g^{-1} for 4 minutes. This filtrate was then analyzed using the spectrophotometric assay, adjusted for pH as previously described. The PA solution was washed as previously described. To prepare the solution for a recapture process, phosphate was added to the solution based on the amount of retained phosphate ions in the material as determined from the assay to obtain a 5:1 ratio of PA:PO_4 at a 0.5 mM concentration of PO_4 and a final volume of 500 µL. The solution was adjusted to pH 6, and the process was repeated as many times as desired.

Analysis of the Effect of NaCl on Binding and the Molybdenum Blue Assay. Samples were prepared in a 5:1 ratio of C_{16}GGGhex:PO_4 and varying NaCl concentrations such that the final PO_4 concentration was 0.5 mM and the final NaCl concentrations ranged from 2 µM to 40 µM. The samples were then adjusted to pH 6, filtered, and analyzed as described previously. To assess whether increased NaCl influences the reading of this assay, molybdenum blue calibration curves were constructed with varying amounts of NaCl added to match the final NaCl concentrations

tested in the binding experiments. These curves were then compared to a standardized curve with no NaCl added.

2.3.2 Simulation Model and Force Field Parameters

Atomistic Model. The simulations used the GROningen MAchine for Chemical Simulations (GROMACS) package[122] and the ABF enhanced sampling methods implemented in SSAGES.[123] The PAs were modeled using the CHARMM forcefield[124] and water was modeled using the TIP3P model.[125] Custom force field parameters used for phosphate ions are listed in Table 2.1, Table 2.2, Table 2.3, and Table 2.4. The Lorentz-Berthelot mixing rule was used for unlike non-bonded interactions involving phosphate atoms. Nonbonded interactions were calculated using a 12 Å cutoff distance. Long-range electrostatic interactions were handled using fast smooth Particle-Mesh Ewald (SPME)[126] with a 0.12 nm Fourier spacing. Covalent bonds involving hydrogens were constrained using the LINCS algorithm.[127] All simulations were integrated using the leap-frog algorithm with a 2-fs timestep. All temperature-coupling used was Nosé–Hoover thermostat with a time constant of 0.1 ps used to maintain the temperature at 300 K.

Phosphate Force Field Parameters. Atom types in phosphate were assigned in the following way. In $H_2PO_4^-$, the phosphate atom is PMHP; the unprotonated oxygen atom is OPMH; OHMH and HOMH are the hydrogen atoms and the protonated oxygen atoms, respectively. In HPO_4^{2-}, the phosphate atom is PDHP; the unprotonated oxygen atom is OPDH; OHDH and HODH are the hydrogen atoms and the protonated oxygen atoms, respectively.

The nonbonded interactions include Lennard-Jones interactions and Coulombic interactions. For atoms i and j, their nonbonded interaction is:

$$u_{nb}(r_{ij}) = 4\epsilon_{ij}\left[\left(\frac{\sigma_{ij}}{r_{ij}}\right)^{12} - \left(\frac{\sigma_{ij}}{r_{ij}}\right)^{6}\right] + \frac{q_i q_j}{4\pi\varepsilon_0 r_{ij}}, \quad (2.1)$$

where r_{ij} is the separation distance between atoms i and j, σ_{ij} is the Lennard-Jones diameter, σ_{ij} is the Lennard-Jones interaction strength, ε_0 is the vacuum permittivity. q_i and q_j are the partial charges of atoms i and j. See Table 2.1 for nonbonded interaction parameters.

Table 2.1. Nonbonded interaction potential parameters for phosphate atoms.

atom	m (amu)	σ_{ii} (nm)	ϵ_{ii} ($\frac{\text{kJ}}{\text{mol}}$)	q (e)
PMHP	30.974	0.3296	0.6904	1.17
OPMH	15.999	0.2494	0.418	-0.91
OHMH	15.999	0.2672	0.418	-0.72
HOMH	1.008	0.04	0.192	0.28
PDHP	30.974	0.3296	0.6904	1.2
OPDH	15.999	0.2494	0.418	-0.78
OHDH	15.999	0.2494	0.418	-0.66
HODH	1.008	0.04	0.192	0.34

The 1-2 bonded atoms interact via a harmonic bonding potential in the form:

$$u_{bond}(r_{ij}) = \frac{k_{bond}}{2}\left(r_{ij} - {r_{ij}}^{(0)}\right)^2, \tag{2.2}$$

where r_{ij} is the separation distance between atoms i and j, k_{bond} is the force constant and ${r_{ij}}^{(0)}$ is the equilibrium bond length. The bonding interaction parameters are listed in Table 2.2.

Table 2.2. Bonding potential parameters for phosphate atoms.

bond	${r_{ij}}^{(0)}$(nm)	k_{bond} ($\frac{\text{kJ}}{\text{mol·nm}^2}$)
PMHP-OPMH	0.154	485344
PMHP-OHMH	0.167	198322
OHMH-HOMH	0.0965	456056
PDHP-OPDH	0.154	485344
PDHP-OHDH	0.167	198322
OHDH-HODH	0.0965	456056

The 1-2-3 bonded atoms interact via a harmonic bending potential in the form:

$$u_{bend}(\theta_{ijk}) = k_{bend}(\theta_{ijk} - {\theta_{ijk}}^{(0)})^2, \quad (2.3)$$

where k_{bend} is the force constant, θ_{ijk} is the angle between united atoms i, j, and k, and ${\theta_{ijk}}^{(0)}$ is the equilibrium angle. The bending interaction parameters are listed in Table 2.3.

Table 2.3. Bending potential parameters for polymer atoms.

Angle	${\theta_{ijk}}^{(0)}$(deg)	k_{bend} ($\frac{\text{kJ}}{\text{mol}\cdot\text{rad}^2}$)
OPMH-PMHP-OPMH	114.23°	1004
OPMH-PMHP-OHMH	104.1°	827.6
PMHP-OHMH-HOMH	107.9°	836.8
OPDH-PDHP-OPDH	120°	1004
OPDH-PDHP-OHDH	108.7°	827.6
OHDH-PDHP-OHDH	102.9°	827.6
PDHP-OHDH-HODH	107.9°	836.8

The torsional potentials for 1-2-3-4 bonded united atoms take the form:

$$u_{tors}(\phi_{ijkl}) = k_{\phi}[1 + \cos(n\,\phi_{ijkl} - {\phi_{ijkl}}^{(0)})] \quad (2.4)$$

where k_{ϕ} is the coefficient and ϕ_{ijkl} is the dihedral angle defined by atoms i, j, k, and l. n is the integer multiplicity and ${\phi_{ijkl}}^{(0)}$ is a refence dihedral angle. The torsional interaction parameters are listed in Table 2.4.

Table 2.4. Bending potential parameters for polymer atoms.

Dihedral	${\phi_{ijkl}}^{(0)}$(deg)	k_{ϕ} ($\frac{\text{kJ}}{\text{mol}}$)	n
OPMH-PMHP-OHMH-HOMH	0°	1.26	3
OHDH-PDHP-OHDH-HODH	0°	1.26	3
OPDH-PDHP-OPDH-HODH	0°	1.26	3
HODH-OHDH-PDHP-OPDH	0°	1.26	3

2.3.3 Simulations of Phosphate Binding to a Single-Chain.

Simulation Protocols. For the unbiased molecular dynamics simulations, a single C_{16}GGGhex chain and a single phosphate ion were placed in a cubic box (7 nm side length). At each pH condition, the phosphate ion was initialized at 9 different starting positions relative to the PA. For each replica, 20 ns of simulation under NVT ensemble in vacuum was performed to obtain a PA-phosphate bound structure. Then the system was solvated in water and a 10-ns NVT simulation for equilibration. Subsequently, another 10-ns MD trajectory under NVT ensemble was collected for analysis.

For ABF advanced sampling, two distance CVs identified in the cluster analysis, d_{SGAGKT} and d_{GGG}, were used to describe single-chain binding. Specifically, d_{SGAGKT} is defined as the distance between the center of mass of the phosphate and the center of mass of the following atoms:{Backbone N on 8GLY, backbone N on 9LYS, sidechain N on 9LYS, backbone N on 10THR, sidechain O on 10THR}. d_{GGG} is defined as the distance between the center of mass of the phosphate and the center of mass of the following atoms:{Backbone N on 2GLY, backbone N on 3GLY, O on 3GLY, backbone N on 5SER, and sidechain O on 5SER}. Note that the C_{16} region was counted as the first residue, and the following GGGSGAGKT peptide corresponded to residues 2-10. Each CV was bound within the interval [0.05 nm, 2.0 nm] and divided into 50 bins. Each ABF simulation used 4 parallel walkers under NVT ensemble. Restraints were placed foreach CV at values of 0.0 nm and 2.5 nm with a spring constant of 500 kJ mol^{-1} nm^{-2} to ensure that the configurations explored remained in the CV space of interest. For each ABF bin, a minimum visit of 400 was required before forces are estimated. ABF was carried out and output monitored at intervals of 40 ns until the free energy features no longer changed between the two most recent outputs, resulting in 240 ns total simulation time per walker for both pH conditions.

Cluster Analysis. Cluster analysis was employed to identify the most frequently occurring PA-phosphate bound configurations. At each pH condition, snapshots from all nine trajectories were first rotationally and translationally aligned based on the peptide coordinates. Then the aligned snapshots were analyzed using the GROMACS cluster tool, using the gromos clustering algorithm[128] with a cutoff of 0.27 nm. The snapshots are clustered based on the peptide coordinates.

2.3.4 Simulations of Phosphate Binding to a Peptide Amphiphile Micelle.

Starting Configuration. The starting configuration for the PAM simulation was generated using a procedure in existing literature.[129] Briefly, nine PA molecules were packed in the *x*-*y* plane with the C_{16} tail pointing inwards, with 40° angle between adjacent chains. Then 24 layers were stacked in the *z*-direction with 20° offset and 5 Å distance between layers, resulting 216 PAs in total in the simulation box. Forty phosphate ions were inserted at random positions avoiding position overlap with the PA molecules. The simulation box was 16 nm in *x* and *y* direction (periodic) and 12 nm in *z* direction (non-periodic). The simulation box was solvated using the GROMACS solvate tool. Sodium (Na^+) or chloride (Cl^-) ions were added to neutralize the system.

Simulation Protocol. The starting configuration was energy-minimized using a steepest descent algorithm with a force tolerance of 10 kJ mol^{-1} $nm^{-1}$and a step size of 0.01 nm. The minimized configuration was then equilibrated under NVT ensemble for 4 ns. During this NVT simulation, for each PA chain, the position of the first carbon atom (closest to the micelle center) was restrained using a harmonic potential with a spring constant of 1000 kJ mol^{-1} nm^{-1} in each direction. Subsequently, the position restraint was removed, and the system was simulated for 50 ns under NPT ensemble, where the pressure in the *x*-*y* direction and the pressure in the *z* direction were coupled independently. For each direction, the pressure was maintained at 1.0 bar using Berendsen barostat with a time constant of 1.0 ps. Figure 2.5C displays the time evolution of the solvent

accessible surface area (SASA) over the total 50-ns NPT trajectory, in which the SASA are shown to stabilize by 30 ns. As a result, the last 20 ns of MD trajectory was used for analysis.

Analysis. For hydrogen bond (H-bond) analysis, the GROMACS hbond tool was used to identify H-bonds formed between PA chains and phosphate ions. The H-bond criterion used a distance cutoff of 0.35 nm and an angle cutoff of 30°. Note that the GROMACS hbond tool uses the hydrogen-donor-acceptor angle instead of the donor-hydrogen-acceptor angle. The SASA was computed using the GROMACS sasa tool.[130] The entire micelle was selected for the SASA calculation.

2.4 Results and Discussion

2.4.1 Design of the Peptide Amphiphile Prototype Material

With strategic design from the molecular level up, each PA molecule can be individually tuned to dictate its bulk self-assembled and phosphate binding properties (Figure 2.1). Here, we designed two different molecules to evaluate, denoted C_{16}GGGhex and C_{16}SGKGHhex, each consisting of three key design regions intended to optimize both functionalities: (1) producing wormlike micelles to create an entangled network and (2) optimizing phosphate binding performance. Each of these molecules was synthesized using FMOC solid phase peptide synthesis with precise monodisperse control and promise in scalability.[131]

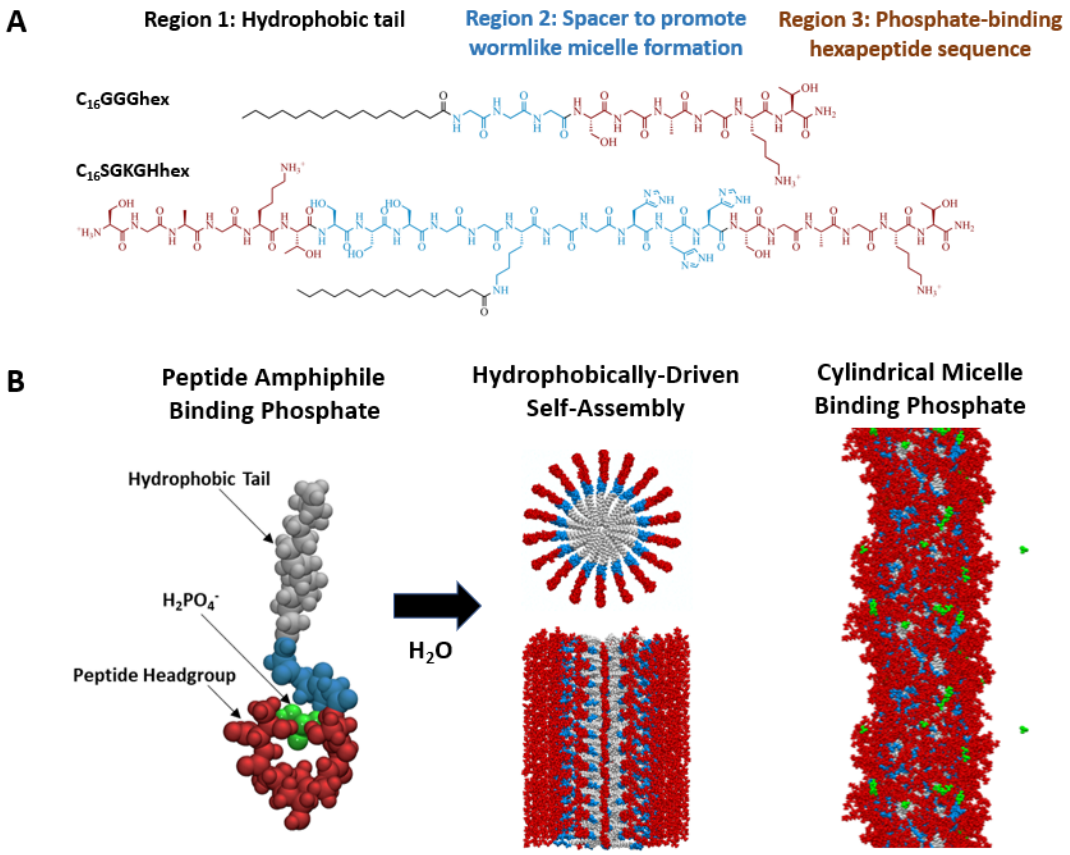

Figure 2.1. (A) PAs denoted C_{16}GGGhex andC_{16}SGKGHhex. (B) Simulation snapshots of C_{16}GGGhex. On the left, an individual PA binds to a phosphate ion in the peptide headgroup through utilizing the P-loop mechanism of hydrogen bonds of the peptide backbone and nested cavity promoted by the side chain lysine. When submerged in water, the PAs spontaneously self-assemble into a micelle to shield the cores from the aqueous solution (middle). The PA micelle binds to phosphate in the corona (right).

The critical binding moiety of our material platform (Region 3) is the protein-derived phosphate-binding sequence that protrudes into the aqueous environment, coating the surface area of the entangled wormlike micelle network with readily accessible binding sites for phosphate. The phosphate binding of proteins has been thoroughly studied in other works,[15,25] but here we extract a specific well-known sequence to molecularly engineer a new system for targeted harvesting of phosphate in a self-assembled network. The binding sequence we chose, namely SGAGKT, is taken from the P-loop motif which is common in phosphate-binding proteins. It consists of a sequence of GXXXXGK[S,T], where X is any amino acid residue and the final

residue is either serine or threonine.[12] The P-loop motif stabilizes the phosphate group of proteins, commonly of ATP or GTP, by creating a nest around the phosphate of hydrogen bonds from the amines in the P-loop backbone and utilizing the positively charged lysine side chain, as depicted in Figure 2.1. We selected this specific SGAGKT hexapeptide binding sequence because it was a commonly repeated motif among myosin-heavy chains, as opposed to other P-loop sequences that had more variation between proteins,[12] and it was previously synthesized and found to bind phosphate in a pH-dependent manner.[2,132]

Equally essential to our material design is Region 1 of the PA, the "tail" which drives the PAs to self-assemble according to the hydrophobic effect, driving the hydrophilic peptide "headgroup" to be systematically displayed to the environment in the micelle corona. For both molecules, we selected the tail to be palmitic acid (C_{16}) for its use in previous systems that adopted a wormlike micellar assembly. [133]

Finally, we incorporated Region 2 of our PAs, which we call the "spacer" here, for two purposes: i) to extend the binding moiety further into the aqueous solution and thus make the binding pocket more accessible, and ii) to produce intramolecular hydrogen bonding that in turn induces wormlike micelle formation, the desired architecture for our entangled material design. For the latter purpose, we tested two designs. The "GGG" in the name C_{16}GGGhex corresponds to three glycine residues between the tail and the binding sequence, which have been shown previously to produce hydrogen bonded beta sheets that encourage the assembly into a wormlike micellar structure.[22] Similarly, the "SGKGH" notation for C_{16}SGKGHhex corresponds to serine, glycine, and histidine residues on either side of the lysine, whose side chain amine is used to construct the branched PA junction through its direct conjugation to the tail. This double-headed branched design, without the hexapeptide, was previously shown to promote crosslinked, self-

supported gelation at pH > 6.5 due to hydrogen bonding between the hydroxyl groups of the serine residues and the deprotonated imidazole side chains of the histidine residues. It was chosen here with the intent to further increase the robustness of our entangled wormlike micelle network through these engineered physical crosslinks. Thus, by keeping PA design Regions 1 and 3 constant, we could directly evaluate the impact of each strategy for hydrogen bonding in Region 2 on the two overall design aims of (1) producing a robust wormlike micelle network and (2) optimizing phosphate binding performance.

2.4.2 Experimental Analysis of Assembly and Phosphate-Binding Properties

To characterize our capture-and-release material, we first analyzed the self-assembly properties of the PAs. To begin, we measured the critical micelle concentration (CMC), that is, the concentration at which the PAs begin to self-assemble. The CMCs were 8.43 μM and 130.1 μM for C_{16}GGGhex and C_{16}SGKGHhex, respectively (Figure 2.10). These values are in the expected range for PA molecules, but this ten-fold difference is noteworthy and is explained by the packing parameter, *P*, for these amphiphilic molecules. *P* relates the chemistry of the molecule, most notably the area of the headgroup, to the packed self-assembled state (see section 2.6 for further discussion).[20] In our binding materials, the lower CMC value of C_{16}GGGhex is advantageous because it corresponds to a lower concentration of unimer PAs in solution when the system is assembled above the CMC. To minimize the ratio of unimer to assembled micelle and to ensure that we are always working with assembled materials, we conducted all future experiments at a concentration of PA at least 10 times greater than the value of the CMC, unless otherwise noted.

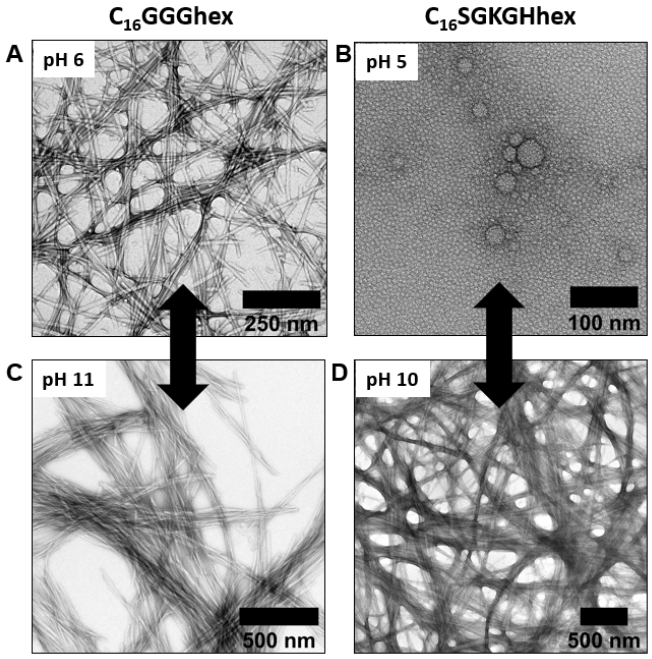

Figure 2.2. TEM images of C_{16}GGGhex and C_{16}SGKGHhex at neutral and high pH values. Both systems exhibit a reversible pH micelle transition when switching from neutral/acidic to high pH. C_{16}GGGhex clumps together at high pH, while C_{16}SGKGHhex assembled into spheres at pH 5 and clumped wormlike micelles at high pH.

We performed negative stain transmission electron microscopy (TEM) to visualize the micellar architectures and calculate the length scales of the micelle assemblies. For each system, we see a pH dependence of micelle formation. For C_{16}GGGhex, we observe entangled wormlike micelles with an average diameter of 11.5 nm that extend tens of microns in length at neutral pH (Figure 2.2A).[134] This is the desired micelle architecture for our capture and release material to provide a solid support through which phosphate-rich solution can flow. At high pH (Figure 2.2C), we observe that the wormlike micelles cluster together. This phenomenon is likely due to the lysine side chain being deprotonated, resulting in assemblies that are less soluble and then stabilize through aggregation. This pH-dependent aggregation is reversible (Figure 2.15). Overall, C_{16}GGGhex is well-suited to form a dense suspension for the retention and release of phosphate.

For C_{16}SGKGHhex, we also observe reversible pH dependence on micelle formation. At pH 5 and below, C_{16}SGKGHhex assembles into spherical micelles with a diameter 7.2 nm (Figure 2.2B), but by pH 10, it has transitioned into wormlike micelles that are also clumped together and extend for tens of microns (Figure 2.2D). This transition from sphere to wormlike micelles has been noted previously for pH-dependent materials.[135,136] For C_{16}SGKGHhex, the effective headgroup area decreases when the histidine imidazole groups are deprotonated at high pH, reversibly pushing the assembly to be most stabilized as wormlike micelles. Overall, this PA micelle platform showcases the unique tunability of small molecular variations on microscale properties, and though it does not produce the desired entangled network for the full pH range, it will allow us to determine how this micelle shape transition affects binding.

2.4.3 Analysis of Fundamental Phosphate-Binding Properties

We evaluated and compared the phosphate binding functionality of the two PA micelles. We employed a spectrophotometric assay to quantify phosphate binding which emits a blue color linearly proportional to the amount of phosphate in solution.[120,121] To perform the binding process, we combined the phosphate and PA at the desired concentrations, adjusted the pH using minimal HCl and NaOH, physically separated the PA from the unbound phosphate in solution, and then performed the spectrophotometric assay on the filtrate containing unbound phosphate. The PO_4 feed concentration was chosen to be 0.5mM (47.5ppm) for all experiments to simulate a comparable phosphate concentration to that of municipal wastewater influent streams.[137] For this preliminary fundamental testing, we evaluated the phosphate binding dependence on three factors: (i) the pH of the solution, (ii) the ratio of the hexapeptide binding unit to phosphate, and (iii) length of time permitted to bind.

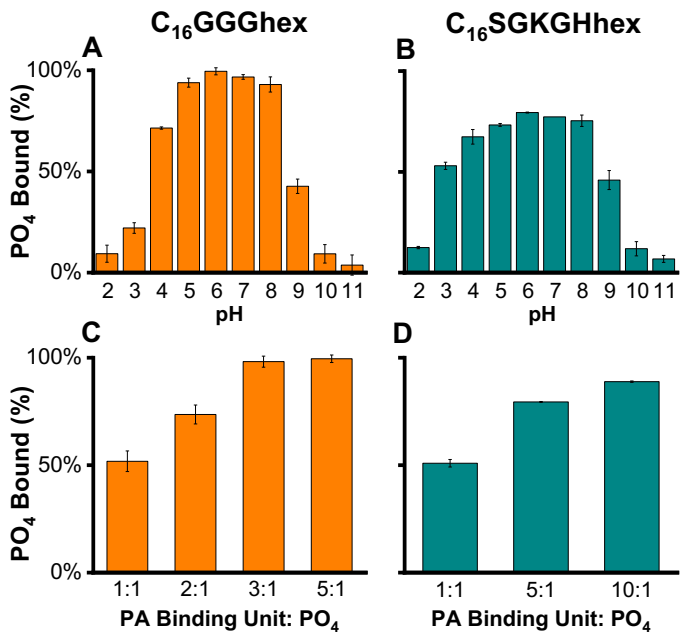

Figure 2.3. (A-B) pH-dependent phosphate binding of the PA micelles (A) C_{16}GGGhex and (B) C_{16}SGKGHhex at a molar ratio of 5:1 PA binding unit: PO_4 and a PO_4 feed concentration of 0.5 mM (47.5 ppm). For C_{16}GGGhex, essentially 100% of phosphate (within measurement error) was bound to the micelle at pH 6, representing the ideal "capture" conditions, while only 5% and 10% of PO_4 was bound at pH 2 and 10, respectively, becoming ideal "release" conditions. For C_{16}SGKGHhex, a similar trend of maximum and minimum binding was observed, although complete binding was not achieved. (C-D) Phosphate binding at pH 6 when the ratio of PA binding unit: PO_4 was varied while keeping the concentration of PO_4 constant at 0.5 mM. (C) For C_{16}GGGhex, 92% and 100% of binding were achieved at a ratio of 3:1 and 5:1 PA binding unit: PO_4, respectively. (D) For C_{16}SGKGHhex, only 89% binding was achieved even when the ratio was increased to 10:1.

The results in Figure 2.3 depict how phosphate binding depends on pH and the ratio of binding unit to phosphate. For both C_{16}GGGhex and C_{16}SGKGHhex, the optimal phosphate binding occurs at pH 6, with minimal binding occurring at low and high pH extremes. Intuitively, as the ratio of PA to phosphate increases, the amount of captured phosphate in solution also increases. C_{16}GGGhex achieved phosphate capture of 92% and 100% at pH 6 and a molar ratio of 3:1 and 5:1 PA binding unit to phosphate, respectively. Comparatively, C_{16}SGKGHhex only achieved 79% binding at identical 5:1 ratio conditions. Additionally, increasing the ratio further to 10:1 did not achieve the complete phosphate capture as exhibited by C_{16}GGGhex. The superior

performance of C_{16}GGGhex places this material on par to meet the strict phosphate effluent limits, which can be as low as 0.1 mg/L of phosphorus.[101]

The kinetics experiments (see Figure 2.18) demonstrated that C_{16}GGGhex sequestered and released phosphate within seconds to minutes of reaching the target pH, and the material maintains its unbound or bound state as long as the pH remains constant. This rapid succession between capture and release states eliminates any need for equilibrating binding time, an additional process design advantage. In light of these binding results, we chose to continue additional characterization only for the superiorly performing PA micelle, C_{16}GGGhex, at a ratio of 5:1 PA:PO_4 with a capture pH of 6 and two potential release pH's of 2 and 11.

The superior binding ability of C_{16}GGGhex over C_{16}SGKGHhex illuminates three interesting binding implications. First, it appears that binding is notably impacted by the entire PA molecule design, even though both designs utilize the same binding moiety. Second, binding is not maximized by increasing charged interactions. C_{16}SGKGHhex has a +6 charge at neutral pH (from 3 histidines, 2 lysines, and 1 amine N-terminus), while C_{16}GGGhex only has a charge of +1. Nevertheless, C_{16}GGGhex achieves maximal binding of the anion, presumably from superiorly employing the P-loop binding mechanism for targeted capture. Third, binding is achieved by both spherical and wormlike micelle architectures, with no notable differences in performance. C_{16}SGKGHhex transitions from spheres to worms, but the binding profile follows a comparable trend as C_{16}GGGhex.

The most notable implication, however, was that the binding properties appear to be significantly impacted by the self-assembled state of the PAs compared to unassembled hexapeptides not conjugated to a tail. Contrary to the results of our micelle material, namely maximal binding at pH 6 and minimal binding as pH increases, previous experimental studies of

the free peptide observed the opposite, with highest phosphate binding at high pH and minimal binding at and below pH 6.[2] A simulation study on the same peptide, in its lysine-protonated, zwitterionic state, confirmed that binding with HPO_4^{2-} is favored over H_2PO_4.[26] Moreover, as the pH rises above the pK_a of lysine sidechain at 10.5, Bianchi et al. observed that the unprotonated lysine side chain had an important role in wrapping around the phosphate to stabilize the bound complex. These works combined indicate that both protonation states of the free hexapeptide stabilize HPO_4^{2-} by forming a nested cavity and incorporating the side chain, performing the P-loop mechanism for phosphate binding.

We hypothesize that the assembled structure induces a pH shift in the binding trigger, fundamentally altering the capture and release functionality of the peptide. This is supported by the results of our simulations. The TEM images at high pH for both PAs already alluded to an intriguing macroscopic phenomenon, namely the spontaneous bundling of wormlike micelles correlated to deprotonation of lysine, that could feasibly impact phosphate binding. We propose that while the free peptide is unconstrained and able to adopt any conformation to stabilize binding of the phosphate ion at the full pH range, the peptide in our system, which already is more constrained in the micelle, becomes even more confined as pH rises and approaches the pK_a of lysine. As the lysine charges in the headgroup are neutralized and no longer repel each other, the micelle headgroup collapses and thereby eradicates any conformational freedom that previously allowed the free peptides to sequester the phosphate ions. The collapse of micelle coronae is later quantitatively confirmed by our simulations. Therefore, although previous results show that high pH is the optimal binding state for this peptide, our self-assembled micelle system distorts the peptide binding conformation within each micelle, eliminates further conformational freedom by

the micelles collapsing together upon each other, and fundamentally alters the binding ability at high pH.

Interestingly, we do not simply observe zero binding at the full pH range, as would be expected in light of the collapsed micelle morphology at high pH; instead, we see a pH shift of binding. Whereas other systems observed decreased-to-no binding below pH 6, we observe pH 6 as our maximal binding condition, with binding occurring in decreased efficacy until reaching pH 2. As our simulation results later confirm, phosphate is bound at this pH condition by the densely packed, positively charged headgroup in the micelle corona that attracts and conformationally stabilizes the negatively charged $H_2PO_4^-$ through nested hydrogen bonding. Not only is this binding pH shift induced by peptide aggregation scientifically intriguing and useful for informing future material designs, but it also has beneficial implications for resource reclamation. It is much more convenient to operate the phosphate collection conditions near the equilibrium pH of the system, which rests around neutral pH, and to perform the release conditions at the more unstable pH extremes, compared to vice versa. Overall, this system proved to capture phosphate completely and release phosphate at low and high pH values within minutes, while maintaining reversible structural stability to facilitate practical phosphate reclamation, which we were positioned to evaluate next.

2.4.4 Simulation Analysis of Phosphate-binding to Phosphate Amphiphile

To investigate the nanoscale mechanisms for the pH shift, we applied unbiased molecular dynamics (MD) simulations and the adaptive biasing force (ABF) enhanced sampling method[33,123] to study phosphate binding of both the unimer and self-assembled C_{16}GGGhex at pH 6 and 11. The pH states are represented by the differing protonation states of the phosphate ion and the PA lysine sidechain, with pH 6 consisting of phosphate as $H_2PO_4^-$ and a protonated lysine amine, and

pH 11 consisting of phosphate as HPO_4^{2-} and a deprotonated lysine amine. We studied the unimer PA first to determine whether the molecular alterations of the PA were the cause of the pH binding shift. Then we tested the assembled micelle system to further examine how binding is impacted by a dense, assembled peptide environment.

Compared to the free hexapeptide with natural C and N termini, the hexapeptide in the PA is conjugated with three additional glycine residues on the N terminal and is amidated on its C terminal, which could likely disrupt binding behavior compared to that of the free peptide. To determine this, we screened the bound PA-phosphate structures using unbiased MD. For each pH condition, 9 unbiased MD trajectories with different starting configurations were collected. Snapshots were collected every 10 ps for a total of 9009 snapshots for each pH condition. The snapshots were rotationally and translationally aligned by the peptide coordinates and were subsequently analyzed using the GROningen MAchine for Chemical Simulations (GROMACS) cluster tool.[122,128] The unbiased MD information was later used to define collective variables (CVs) to describe the system dynamics, which were then used in ABF enhanced sampling simulations to study the thermodynamics of binding at each pH condition.

For each pH condition, the phosphate interacted with the PA through various mechanisms, with the top five most commonly observed clusters presented in Figure 2.4A. At pH 6, phosphate was found to be bound only in the third cluster and unbound in the other clusters shown. In contrast, at pH 11, the phosphate was bound by C_{16}GGGhex in all of the top five most common clusters, but the binding was stabilized at multiple locations, some of which included the GGG spacer in addition to the hexapeptide. In regards to observing the proposed P-loop mechanism of binding, we identified several clusters at both pH's in which the phosphate was surrounded by a 3-pronged "claw" formed by the hexapeptide backbone and its lysine side chain. This is consistent with the

previously studied “nested cavity” P-loop mechanism for binding. These results agree with previous characterizations in that the hexapeptide prefers to bind phosphate at high pH rather than at low pH, and indicate that the physics built into our models are consistent with past reports for single molecules.

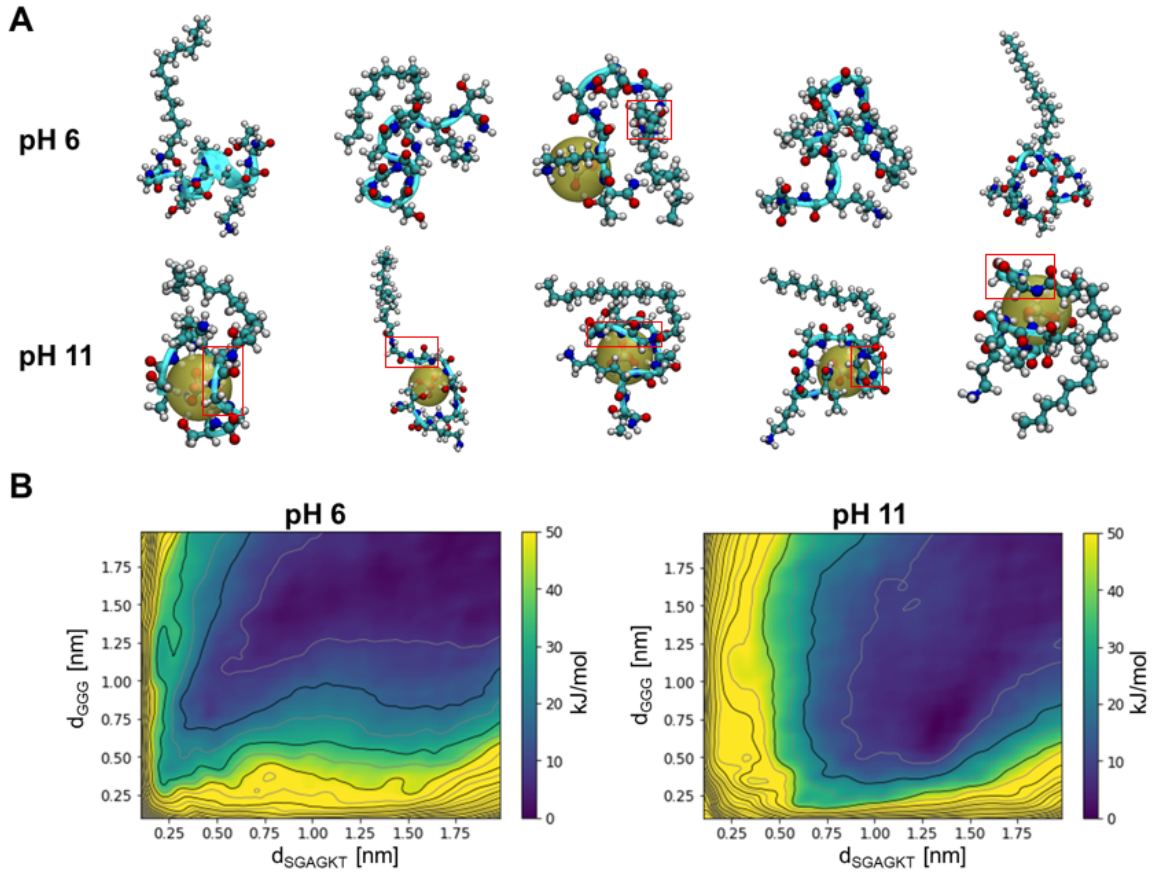

Figure 2.4. Single-chain binding simulations of C_{16}GGGhex show that binding is preferred at pH 11. (A) Snapshots of the top five populated clusters obtained in unbiased MD simulations. Populations of clusters decrease from left to right. The snapshots reveal the GGG spacer (boxed in red) and hexapeptide are the two major regions of phosphate binding along the PA chain. (B) Free energy surface obtained via ABF sampling for single-chain PA binding to one phosphate. At pH 6, free energy is lowest for the unbound state (upper right corner). At pH 11, a bound state at d_{SGAGKT}=1.34nm, d_{GGG}=0.74nm is preferred with a binding free energy of -2.8 kJ/mol.

These snapshots also highlight that the spacers, incorporated into the molecular design to tune the micellar architecture, are not passive participants in binding but rather play an active role in stabilizing the phosphate. To qualify this phenomenon further, we calculated free energy

surfaces in terms of two distance CV's to characterize binding of the unimer PA to phosphate: (1) d_{SGAGKT}, distance from the phosphate to the center of the 3-prong SGAGKT binding pocket; and (2) d_{GGG}, distance from the phosphate to the center of the GGG binding region (additional details provided in 2.3.3). We used these two CVs to perform ABF simulations to calculate the free energy landscape of one phosphate ion binding to a unimer PA at each pH condition. The results are shown in Figure 2.4B.

Our simulations confirm that phosphate is unbound at pH 6 and that it binds to the unimer PA utilizing the GGG spacer in addition to the hexapeptide. For pH 6, the free energy minimum, corresponding to the most stable binding state, is located at the top right corner of the free energy surface. This location corresponds to a phosphate ion far from both binding regions of the PA, simply stable in aqueous solution, suggesting that C_{16}GGGhex fails to sequester phosphate at pH 6. At pH 11, however, a minimum is found at d_{SGAGKT}=1.34, d_{GGG}=0.74 with a free energy difference of -2.8 kJ/mol with respect to the unbound state. This free energy minimum occurs at low d_{GGG} values, suggesting that interaction with the GGG linker is important for phosphate binding to the PA at pH 11. The free energy results confirm the finding that, unlike phosphate-binding to the SGAGKT hexapeptide, phosphate-binding to this PA exhibits more flexible binding structures, where the bound phosphate can interact with both the spacer and hexapeptide regions.

2.4.5 Simulation Analysis of Phosphate binding to Peptide Amphiphile Micelle

Having verified that the molecular alterations did not shift the pH binding conditions of the unimer PA, we simulated a micelle system to probe how the densely packed self-assembled environment impacts binding. We used unbiased MD simulations to characterize the phosphate binding behaviors of the micelle at an approximate PA:PO_4 ratio of 5:1. For each pH condition, 40 phosphate and 216 PA chains were simulated in water. Sodium (Na^+) or chloride (Cl^-) ions were

added to neutralize the simulation box. The last 20-ns of the 50-ns MD trajectory under an isothermal-isobaric ensemble were used for analysis (details in 2.3.2). The simulated micelle was periodic along its cylindrical axis, which is aligned in the z-direction.

Our micelle simulations confirm the experimental shift in binding pH that is induced when the PA molecules systematically self-assemble. We corroborated this simulated binding shift using three complementary approaches: a histogram analysis of the radial distance of the phosphate to the micelle core, a potential of mean force (PMF) estimation, and a hydrogen bond (H-bond) analysis. Visually, we observe in Figure 2.5A two top-down snapshots of the simulated system, depicting the majority of phosphate ions being bound at pH 6, while most phosphate ions were unbound at pH 11. The visual analysis was further corroborated using a histogram of the radial distance of the phosphate ions to the micelle core (Figure 2.5B). These distances were then compared to the distance to the possible PA binding sites that were observed in the single-molecule PA analysis, namely the hexapeptide and the GGG spacer. Indeed, at pH 11, the distance of the phosphate to the center of the micelle was not localized anywhere, signifying an unbound state. But for pH 6, the majority of phosphate ions were located at the same distance from the core as the hexapeptide sequence, confirming localized binding to the hexapeptide.

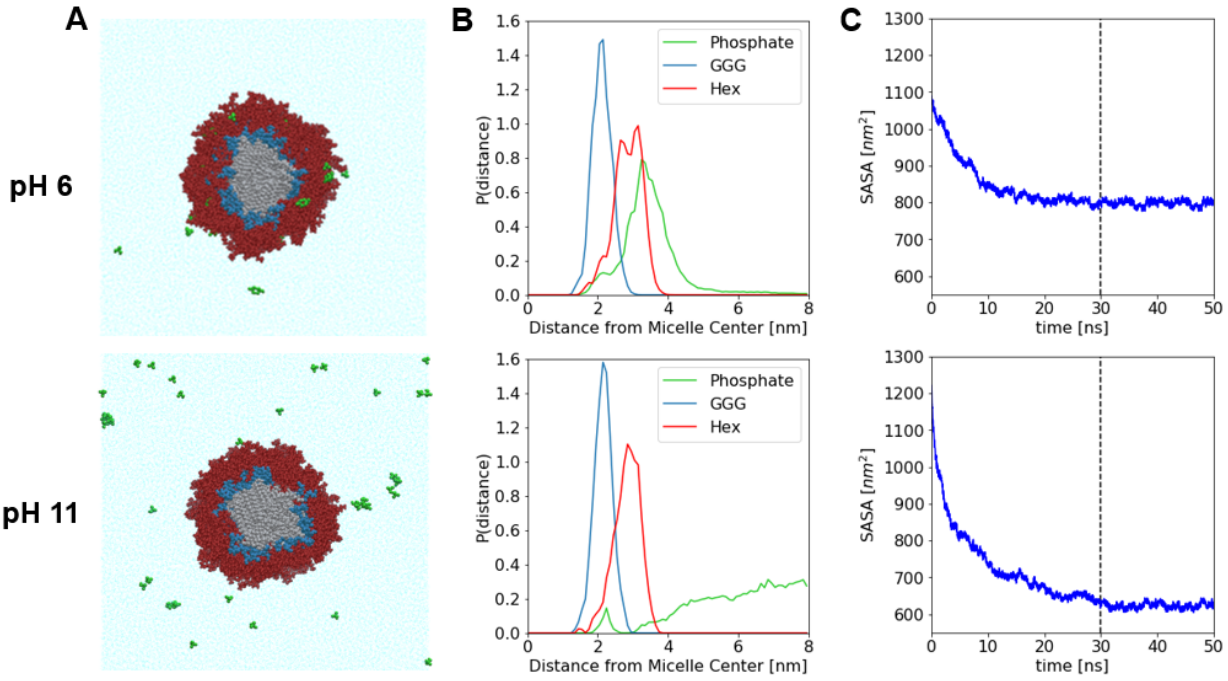

Figure 2.5. Simulations of phosphate binding to the C_{16}GGGhex micelle at pH 6 and 11. (A) Top-down snapshots of the simulated micelles at the end of the production run. (B) Normalized histograms of radial position from the micelle central axis for different components in the systems. The GGG spacer is noted as 'GGG' and the SGAGKT hexapeptide as 'Hex' in the legend. (C) Solvent-accessible surface area (SASA) of the micelle as a function of simulation time. The dash lines indicate the start of the time-averaging interval. The average SASA values are 798 ± 9 $nm^2$and 623 ± 8 nm^2 at pH 6 and 11, respectively.

The potential of mean force (PMF) offers insight into the free energy of binding of phosphate to the micelle compared to the unimer PA, with a lower free energy signifying a more stabilized bound state. The PMF along the radial CV was estimated by computing the Boltzmann inversion on the corresponding probability distribution via the equation $PMF(r) = kTln(P(r))$, where k is the Boltzmann constant and T is the temperature. Here, the PMF was computed as a function of distance from the micelle center, and $P(r)$ is the normalized histogram of the radial position of phosphate ions. From the PMF results (Figure 2.21), we estimated that the PMF for a phosphate to bind to the micelle at pH 6 was -11.7 kJ/mol, which is lower by a factor of four than the binding free energy for phosphate binding to a single PA at pH 11 (-2.8 kJ/mol). Interestingly,

this result highlights that binding at pH 6 in the assembled state is even more stabilized compared to binding to the unimer PA at pH 11.

Finally, an H-bond analysis was performed to quantify the binding percentage of phosphate to the micelle at both pH states. We define the binding percentage to be the percent of time that a phosphate forms at least one H-bond with the micelle, averaged over the simulation time and phosphate samples. This was found to be 59% and 0.4% at pH 6 and 11, respectively. Though the simulated binding percentage at pH 6 is lower than the experimental measurement of complete capture, these values qualitatively capture the significant difference between binding performances at pH 6 and 11.

Having quantified that the pH shift is in fact occurring, we probed the fundamental reason for why. For pH 11, we noted two phenomena that caused this decrease in binding, one pertaining to a per-molecule analysis and the other pertaining to a newly emergent and noteworthy bulk property. The per-molecule insight was derived from the radial histogram data. When binding did occur at pH 6 (Figure 2.5B), we observed that GGG no longer interacted with the phosphate in the assembled state, even though previously GGG played an active role in stabilizing phosphate as a unimer PA, especially for pH 11. It is likely that the densely packed corona prohibited the phosphate from penetrating deep enough into the corona to fully utilize the additional hydrogen bonds of the GGG backbone. With these key components of binding now inaccessible in the micelle state, phosphate was unable to be bound and stabilized at high pH.

Second, we were motivated by the TEM images of clustered PA micelles (Figure 2.2C) to probe how the lysine side chain deprotonation influences binding according to a bulk micellar mechanism. As discussed previously, the micelle was apparently teetering on the edge of insolubility, so simply approaching the pK_a and deprotonating a small fraction of lysine amines

causes to micelles to clump together. To quantify the impact of this phenomenon on binding, we relied on the solvent-accessible surface area (SASA) for the entire micelle to measure the extent of headgroup presentation to the aqueous environment, and thereby to the phosphate ions. Using the GROMACS SASA tool,[130] the time-averaged SASA was found to be 798 ± 9 and 623 ± 8 nm^2 at pH 6 and 11, respectively. These results suggest that the deprotonation of lysine leads to a statistically significant decrease in micellar surface area, and with that a decrease in access to binding sites. Thus, as more of the lysine amines become deprotonated, the micelle corona gradually collapses and expels more and more phosphate, corresponding to the decreased binding in Figure 2.3A as pH rises. The simulated system of all deprotonated lysine amines shows this to the extreme, when the micelle is fully collapsed and phosphate is completely expelled or "squeezed" out of the micelle. Thus, compared to a unimer PA, under assembled conditions, phosphate is no longer able to penetrate the even denser micellar headgroup, and binding becomes impossible, explaining the first part of the pH shift.

To understand the increase in binding stability at pH 6, we utilized data from the H-bonding analysis. In the assembled system, we observed multiple chains involved in binding to stabilize the phosphate in the headgroup in the densely packed corona (Figure 2.22). The multi-chain binding behavior is a direct result of the PA micelle assembly, where multiple binding opportunities are simultaneously presented to the phosphate ions. This result is also corroborated by our ratio of PA:PO_4 experiments (Figure 2.3C), which elucidated that multiple chains per phosphate were necessary to achieve complete bulk phosphate capture. This binding mechanism is not available for a single peptide, nor has it been previously remarked on in single-chain binding studies, presenting an additional advantage of this self-assembled binding system where increased binding stability is introduced.

2.4.6 Selectivity Over Nitrate and Nitrite

With knowledge of the fundamental binding properties, we experimentally evaluated the selectivity of C_{16}GGGhex to bind to phosphate in the presence of competing oxyanions, probing the molecular recognition of this material. We chose nitrate and nitrite as the competing anions since those would be the primary competitors in agricultural runoff streams that are rich in these three fertilizer components.[101] In our experiments, we introduced equimolar amounts of nitrate, nitrite, and phosphate to systems with 1x, 2x, and 3x molar excess of C_{16}GGGhex at pH 6, equivalent to 10 ppm phosphate. The results are shown in Figure 2.6.

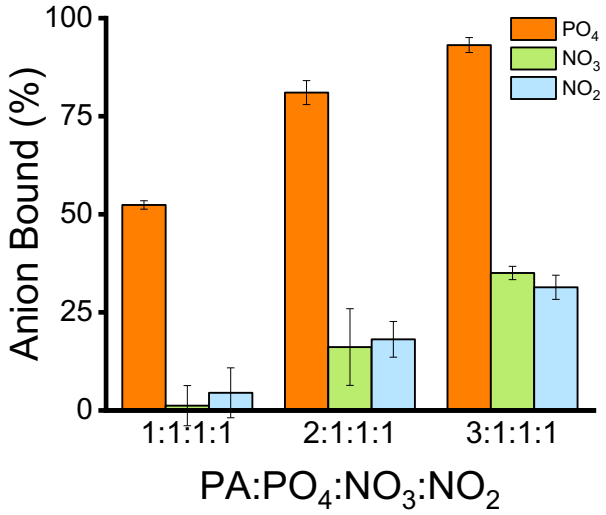

Figure 2.6. Selectivity results for C_{16}GGGhex at pH 6 with molar ratios equivalent to 10 ppm phosphate. Phosphate is bound more than nitrate and nitrite in all cases. In the case of equimolar PA to phosphate, C_{16}GGGhex binds 52% of the phosphate present and less than 5% of nitrate and nitrite, exhibiting excellent selectivity in these conditions. As the concentration of PA increases, C_{16}GGGhex begins to bind to nitrite and nitrate in a linearly increasing trend, while still binding phosphate most.

In all cases, we observe that C_{16}GGGhex binds to phosphate significantly more than to either of the competing oxyanions. In the 1:1:1:1 case, C_{16}GGGhex binds less than 5% of nitrate and nitrite but is still able to sequester 52% of phosphate, consistent with its binding performance without competing ions (see Figure 2.3C). Thus, at this lower concentration of PA, we observe

excellent selectivity and see C_{16}GGGhex performing its designed-in molecular recognition functionality. As we increase the amount of PA in the system, C_{16}GGGhex continues to bind phosphate aligned with the previously observed amounts in Figure 2.3C, but it discriminates phosphate less, following a linear trend of binding increasing amounts of nitrate and nitrite up to 35% and 31%, respectively. This trend could be indicative of the molecular-recognition P-loop being less exclusively employed to capture phosphate through the signature selective nested cavity formation. Instead, C_{16}GGGhex is likely indiscriminately binding nitrite and nitrate by electrostatic attraction to the positively charged lysine, whose abundance increases as the PA concentration increases. It could also be that the densely packed corona prohibits the peptides from adopting the molecular-recognition P-loop nested cavity formation as readily, decreasing its designed-in means to select only phosphate. However, because we do not simply observe proportionate binding of anions in each case but rather observe a linear binding trend that ends in nearly zero binding of competitors, a strong case can be made for P-loop molecular recognition in the 1:1:1:1 conditions.

While these preliminary results present opportunities for optimizing exclusive binding to phosphate even with excess binding sites present, we nonetheless observe molecular preference for phosphate in all cases, with particular success in discriminating between phosphate and its competitors with equimolar amounts of binding sites and phosphate. To harken back to our previous findings in considering routes for optimization, the unique multi-chain binding observed in our micelle simulations presents an intriguing starting point, specific to the versatility PA micelles, to design increased molecular selectivity in future rounds of synthesis.

2.4.7 Cycles of Capture and Release

Finally, we evaluated the capture, release, and reclamation functionality of this material, as well as its durability upon cycles of reuse, providing valuable information for the practical phosphate reclamation potential of our material platform. We sequentially adjusted the pH from 6 to the acidic or basic release pH, collecting and analyzing the filtrate at each step. After filtration at the release pH, we added phosphate to re-achieve a starting concentration of 50 ppm, as calculated from the phosphate concentration of the filtrate.

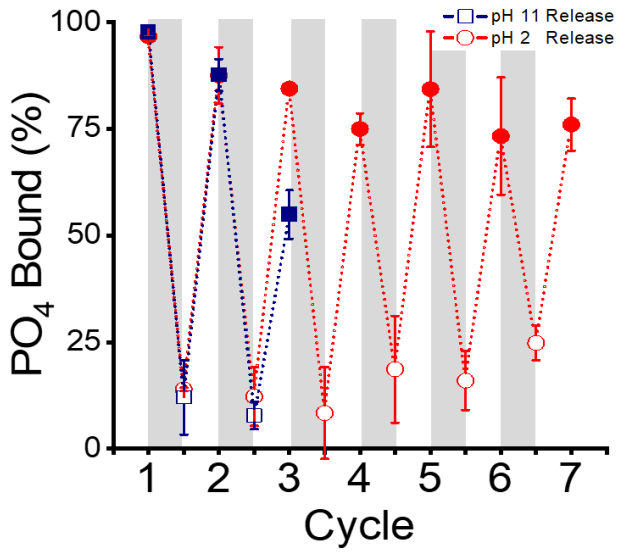

Figure 2.7. Capture and release results for C_{16}GGGhex. The filled-in markers represent the pH 6 capture condition, while the open markers represent the release condition of either pH 2 or 11. The gray rectangle depict the release step from pH 6 to either pH 2 or 11. The material demonstrates an ability to reversibly capture and release phosphate for both the release pH 2 and pH 11. For the pH 11 release condition, the material becomes unable to rebind nearly half of the present phosphate after 3 cycles. It was noted that the solution turns notably cloudy, highlighting how the PA aggregation at high pH likely contributed to a decreased ability to rebind phosphate. For the pH 2 release condition, the material could rebind greater than 73% of phosphate and release up to 75% of phosphate for up to 7 cycles, becoming the superior release condition.

The cycles of capture and release data in Figure 2.7 demonstrate that our material does indeed perform sequential binding and release, and it also highlighted interesting material properties at pH 11. For pH 2 triggered release, the material was able to expel and rebind phosphate

for up to the 7 cycles tested, rebinding up to 73% each time and releasing up to 75%. The capture and release performance both diminish as the number of cycles increases, which could be a function of increased time required to achieve equilibrium after successive cycles, highlighting the potential for optimization of this process. The material using a pH 11 triggered release, on the other hand, exhibited a sharp decrease in ability to rebind after only 3 cycles, binding only 55% of the added phosphate in solution. Since this performance was markedly worse, we ceased performing further cycles under this release condition after this point. We believe that this trend is occurring due to the clumping of micelles observed at high pH, which was visually supported by a significant increase in cloudiness of the sample after successive cycles. Thus, it appears that the fundamentally altered binding ability at pH 11, as observed in the simulation results, also negatively impacts the functionality of the material when operating repetitively at these basic release conditions. The decrease in binding for both systems could also be due to loss of unimer PAs upon wash steps. This loss could be averted by locking the assemblies through internal covalent crosslinks, a straightforward design change that has been employed previously,[111] which could increase the robustness and recyclability of the PA micelle network.

In summary, these data demonstrate that our material is capable of successive capture and release of phosphate, as opposed to remaining permanently bound like many adsorbents,[138–140] with promise for further process optimization. More broadly, they highlight the feasibility of using an entangled wormlike micelle structure with phosphate binding units coating the fibers to practically catch, retain, and separate out the phosphate from water, an advantage over the free-floating peptides which would be difficult to partition out from the solution.

2.5 Conclusion

We have designed, synthesized, and characterized a prototype of a materials platform to capture and reclaim phosphate, utilizing self-assembled peptide amphiphiles that easily incorporate specific protein-inspired binding sequences to molecularly recognize their specific targets. These peptide amphiphile wormlike micelles form a dense entangled suspension that becomes a solid support for straightforward collection of phosphate in response to a pH trigger. The PA material C_{16}GGGhex sequestered 100% of phosphate at pH 6 and released up to 75% at pH 2 for up to seven cycles. C_{16}GGGhex also was found to selectively bind to phosphate over nitrate and nitrite. Detailed atomistic simulations with advanced sampling confirm that the assembled state of the material fundamentally alters the pH binding functionality compared to the free peptide, shifting the maximal binding conditions from pH 10.5 to 6 due to the micellar headgroup becoming conformationally constrained at high pH, thereby expelling the phosphate. At pH 6, simulations indicate that unimer PAs do not bind phosphate, but they are able to do so via multi-chain binding when assembled into a micelle. Our simulations serve to highlight the important role of PA packing in phosphate binding behavior and suggest a new multi-chain phosphate-binding mechanism that is unique to PA micelles, reminiscent of the tertiary structure adopted by proteins for targeted binding. These findings indicate that PA packing in micelles is an important design factor, thus opening up a new avenue of relying upon multi-chain binding motifs for the design of selective ion-sequestering materials.

This work represents a first step in our aim to incorporate protein-inspired design into a tunable synthetic material for practical resource reclamation from wastewater. Since this material platform so naturally incorporates protein-inspired binding sequences, we are positioned to easily modify the binding sequence to target a wide array of other valuable resources in wastewater.

Overall, if proven to be scalable and cost-effective, this novel materials platform could potentially provide a paradigm shift in materials development for specific capture and reclamation for wastewater.

2.6 Additional Experimental Results and Discussions

2.6.1 Mass Spectroscopy Verification using Matrix-Assisted Laser Desorption-Ionization – Time of Flight (MALDI-TOF)

The theoretical molecular weight for C_{16}GGGhex is 928.10 g/mol. The main peak in the purified HPLC fraction is 950.698 (Figure 2.8A). An artifact of this technique is that a sodium ion commonly adheres to the molecule in the place of a hydrogen atom upon ionization, making the detected mass larger than the mass of the molecule. After subtracting the molecular weight of a sodium ion (22.99 g/mol) and adding back the mass of the hydrogen atom it replaced, the confirmed molecular weight of C_{16}GGGhex is 928.72 g/mol. Similarly, for C_{16}SGKGHhex, the theoretical weight is 2288.55 g/mol. After subtracted the mass of sodium and adding the mass of hydrogen, the confirmed molecular weight of C_{16}SGKGHhex is 2287.37 g/mol (Figure 2.8B).

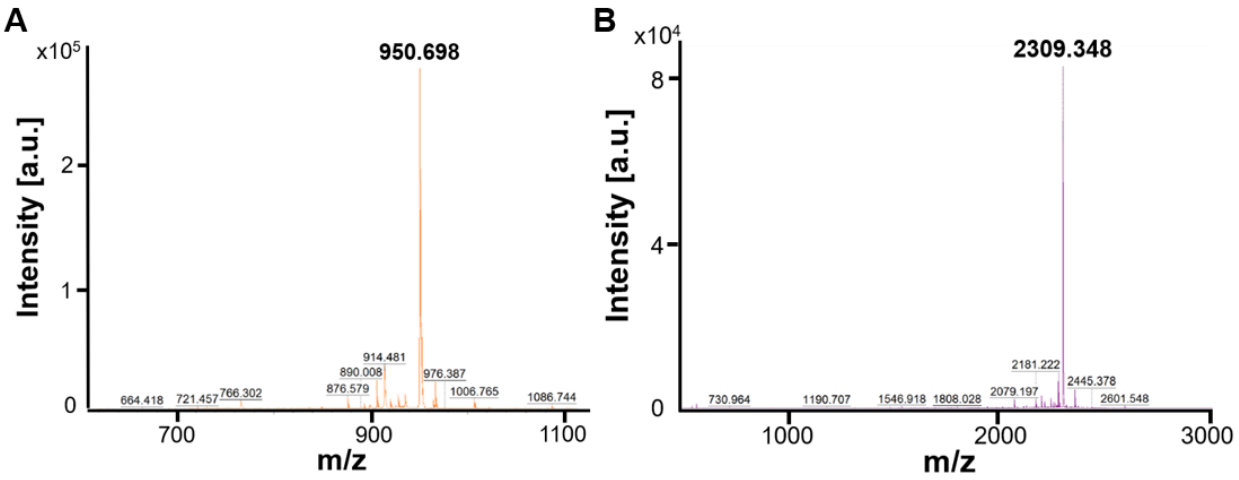

Figure 2.8. The mass spectra for (A) C_{16}GGGhex and (B) C_{16}SGKGHhex after purification from HPLC.

2.6.2 Purity Analysis using Liquid Chromatography – Mass Spectroscopy (LC-MS)

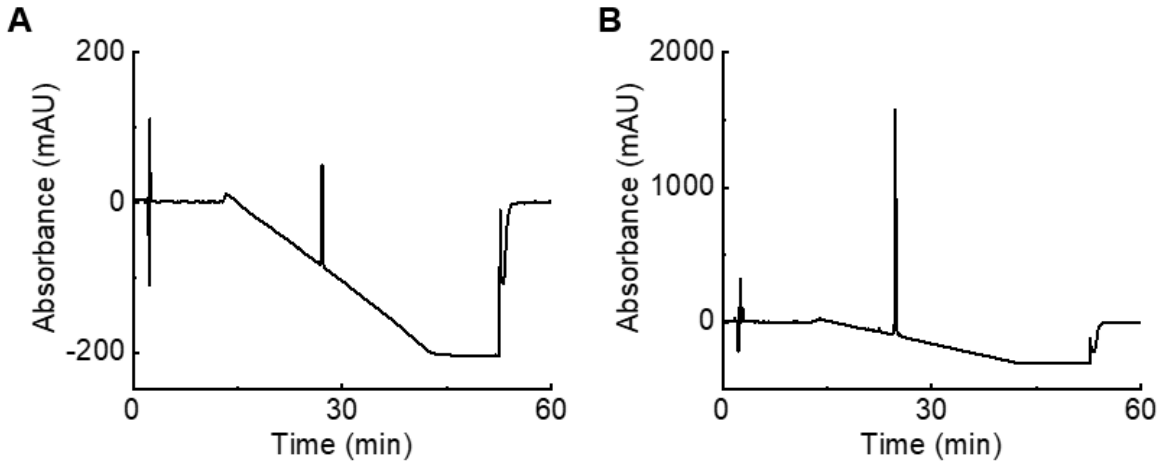

Figure 2.9. LC-MS chromatograph of (A) C_{16}GGGhex and (B) C_{16}SGKGHhex at 220 nm. The product elutes in the center peak for each plot. The purities were calculated to be (A) 96.5% and (B) 97.3%.

Table 2.5. LC-MS Chromatogram peak table for C_{16}GGGhex

Peak #	Ret. Time [min]	Area [mAU*s]	Height [mAU]	New Area [%]
1	7.075	17.42218	1.10176	1.81%
2	26.603	16.72878	1.79469	1.74%
3	**27.115**	**929.08282**	**134.86389**	**96.45%**
Total		19711.92	1744.347	100.00%

Table 2.6. LC-MS Chromatogram peak table for C_{16}SGKGHhex

Peak #	Ret. Time [min]	Area [mAU*s]	Height [mAU]	New Area [%]
1	15.06	71.84814	3.26691	0.36%
2	16.16	50.0343	3.10221	0.25%
3	17.457	16.36457	2.35443	0.08%
4	18.007	5.32924	1.11091	0.03%
5	18.234	33.99007	1.75981	0.17%
6	19.27	28.48297	4.28034	0.14%
7	19.704	12.98752	2.0538	0.07%
8	19.964	16.9283	2.95362	0.09%
9	20.449	30.83108	2.91836	0.16%
10	22.018	6.64445	1.70828	0.03%
11	22.312	5.37997	1.35502	0.03%
12	22.411	58.5399	15.22104	0.30%
13	22.538	63.15965	14.43723	0.32%
14	23.886	14.48648	1.14472	0.07%

Table 2.6. LC-MS Chromatogram peak table for C_{16}SGKGHhex, continued.

15	**24.728**	**1.92E+04**	**1668.184**	**97.30%**
16	25.306	42.21921	7.38365	0.21%
17	25.446	12.94693	2.46567	0.07%
18	25.702	28.63228	4.45938	0.15%
19	26.481	8.51018	1.46951	0.04%
20	28.191	8.36704	1.13123	0.04%
21	29.378	15.93975	1.58721	0.08%
Total		19711.92	1744.347	100.00%

The confirmed purity of C_{16}GGGhex was 96.45%, and the confirmed purity of C_{16}SGKGHhex was 97.30%.

2.6.3 Critical Micelle Concentration (CMC)

The CMC is calculated as the inflection point of the fluorescence intensity beginning to increase, which occurs in the presence of hydrophobic cores (Figure 2.10). The CMCs were 8.43 μM and 130.1 μM for C16GGGhex and C16SGKGHhex, respectively. The ten-fold difference in CMC values can be explained by the packing parameter for surfactant molecules.[20] The packing parameter *P* evaluates the most stable degree of curvature at the tail-headgroup interface of the micelle using the ratio $P = v/al$, where (v) and (l) are the volume and maximum extended length of the tail, respectively, and (a) is the area of the headgroup at the interface. For C_{16}SGKGHhex, the (a) area of the headgroup is much larger due to the double-sided headgroup, causing each PA molecule to face more steric constraints in its ability to self-assemble, corresponding to the higher CMC. C_{16}SGKGHhex is also much more hydrophilic than C_{16}GGGhex with more than double the number of amino acids in the headgroup, further stabilizing the individual PA molecules in an unassembled state.

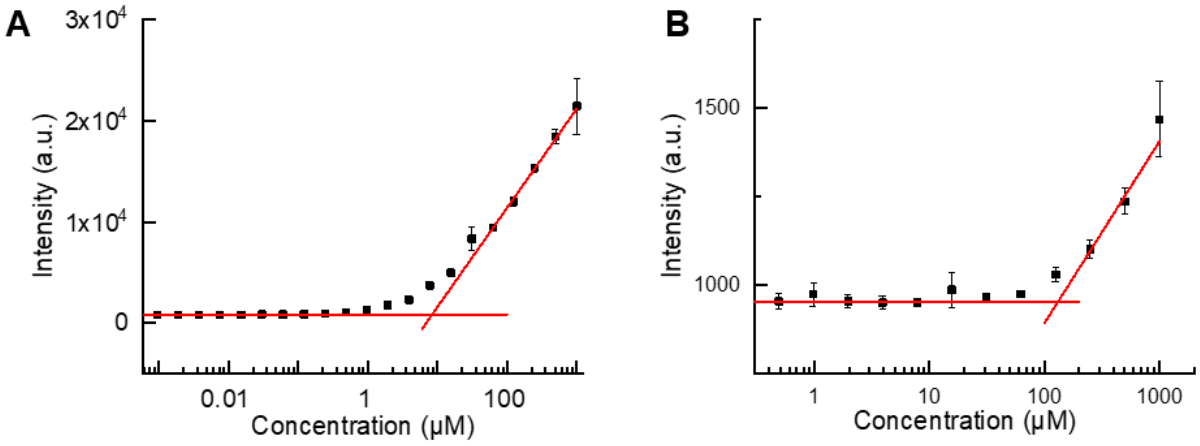

Figure 2.10. The CMC plots of (A) C_{16}GGGhex and (B) C_{16}SGKGHhex.

2.6.4 Additional Negative-Stain Transmission Electron Microscopy (TEM) Imaging

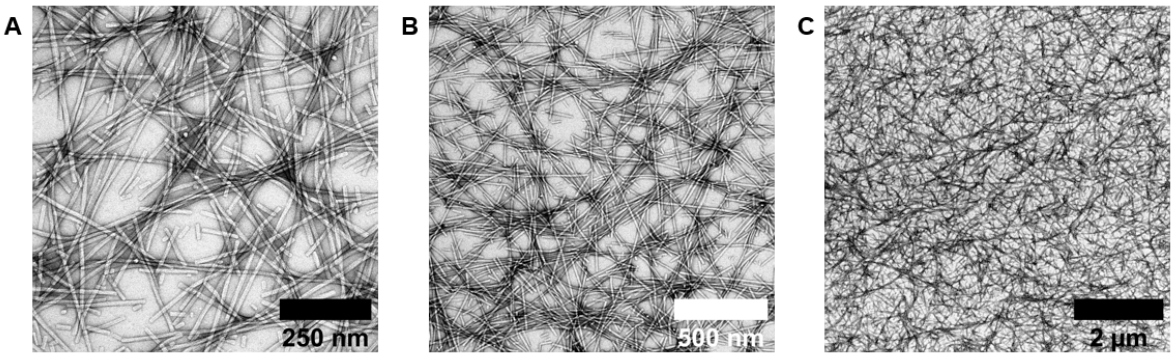

Figure 2.11. C16GGGhex at pH 2 forms extended wormlike micelles.

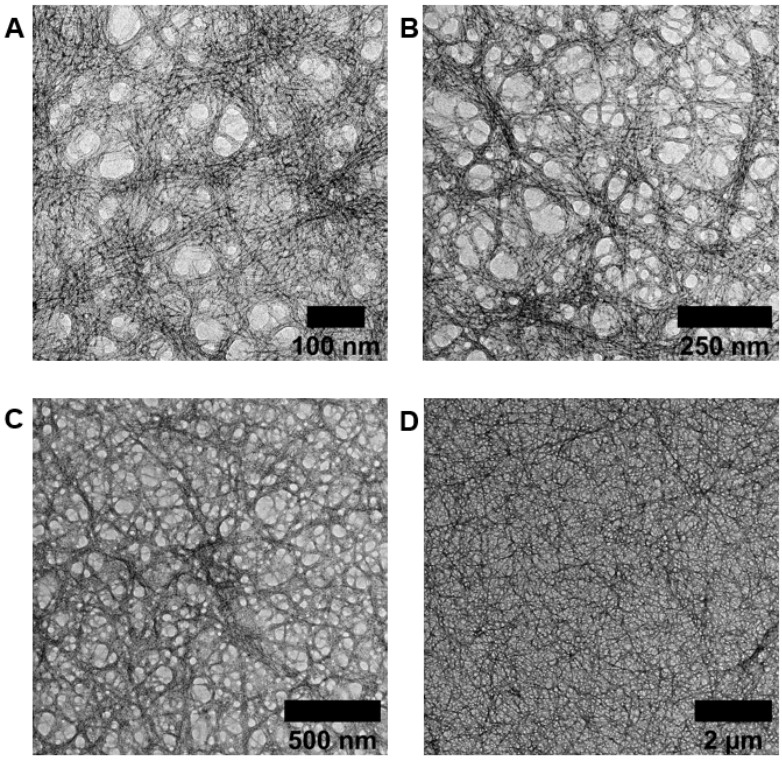

Figure 2.12. C_{16}GGGhex at pH 6 forms extended wormlike micelles.

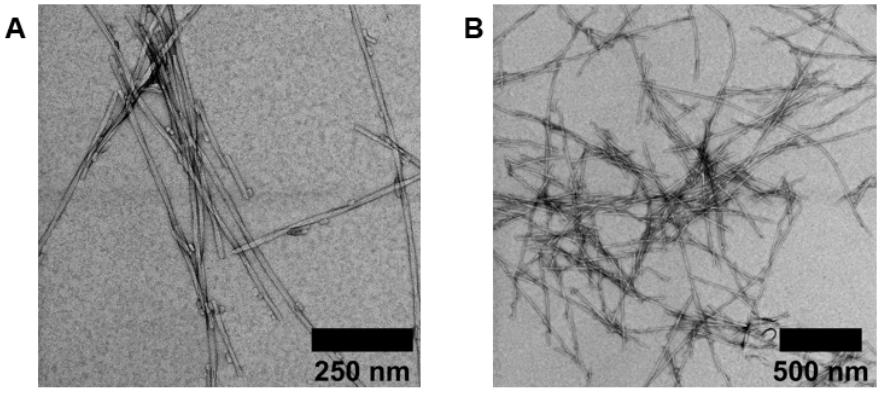

Figure 2.13. C_{16}GGGhex at pH 10 forms wormlike micelles that begin to clump together.

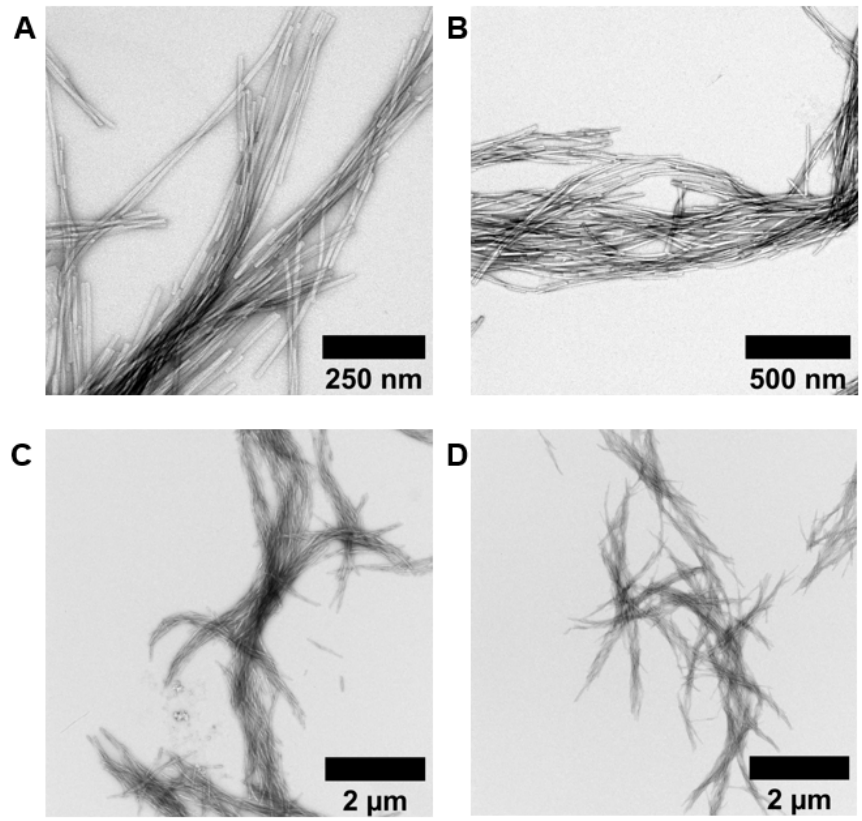

Figure 2.14. C_{16}GGGhex at pH 11 forms wormlike micelles that heavily clump together.

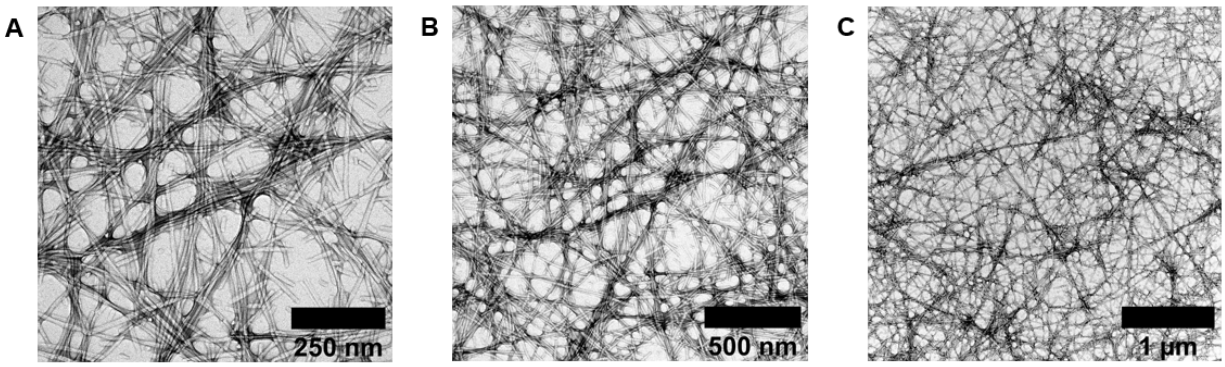

Figure 2.15. C_{16}GGGhex at pH 6 after one cycle of capture and release at pH 11 demonstrates that the declumping of the micelles is reversible.

For C_{16}SGKGHhex in Figure 2.16, this transition at high pH to wormlike micelles from spherical micelles can be understood in terms of the packing parameter discussed above. At low

pH, the histidines are protonated, repelling each other and effectively increasing the area of the headgroup, pushing the packing parameter below the 1/3 value corresponding to spherical micelles to accommodate the larger steric hindrance. Upon deprotonation and a subsequent decrease in headgroup area at high pH, the assembly becomes more stabilized as wormlike micelles and approaches the 1/2 packing parameter value corresponding to the wormlike micelles seen in Figure 2.16.

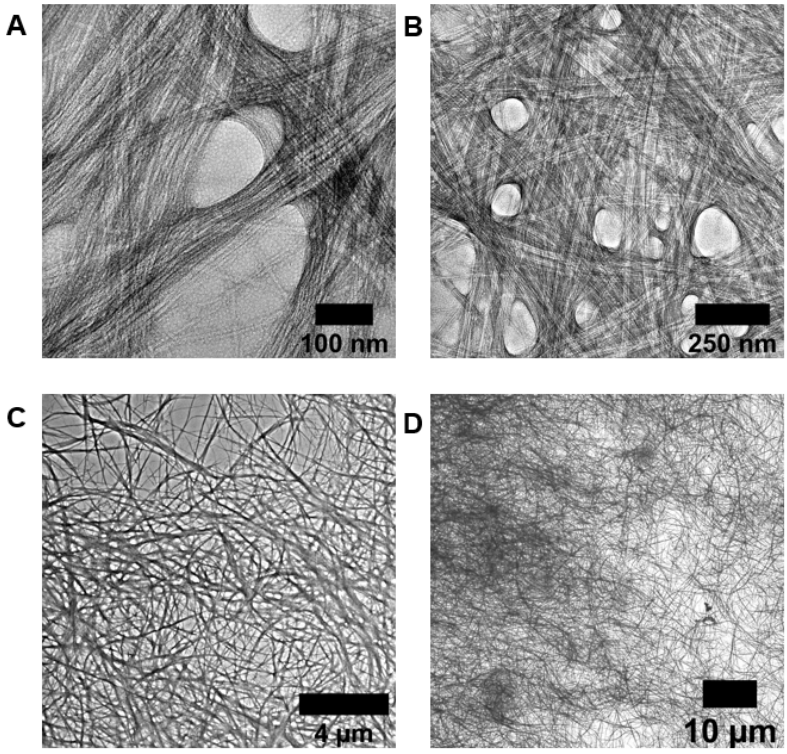

Figure 2.16. C_{16}SGKGHhex at pH 10 forms extended wormlike micelles that clump together very thickly.

2.6.5 Spectrophotometric Molybdenum Blue Assay

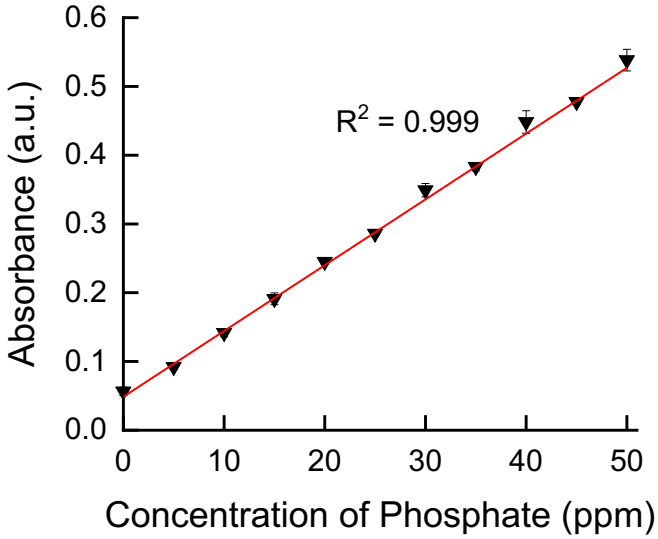

Figure 2.17. Confirmation of a linear trend using the spectrophotometric molybdenum blue assay. As concentration of phosphate in solution increases, the absorbance increases with very reliable accuracy.

2.6.6 Analysis of Kinetics of Binding

The kinetics data shown in Figure 2.18 demonstrated that C_{16}GGGhex sequestered and released phosphate within seconds to minutes of reaching the target pH, corresponding to the time it requires to promptly filter the suspension and evaluate the phosphate content. Additionally, the material maintains its unbound or bound state as long as the pH remains constant, up to the two hours that we tested.

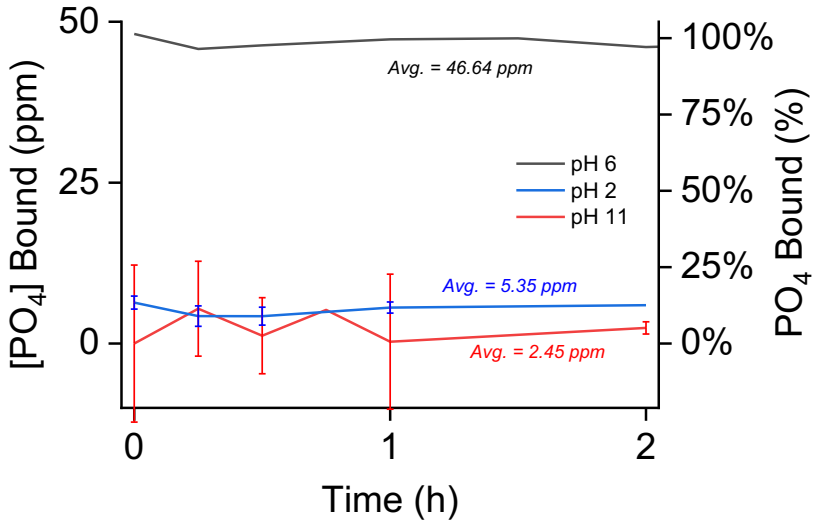

Figure 2.18. The phosphate binding concentrations and percentages measured over time at the three pH values of 6, 2, and 11. Phosphate is captured at pH 6 and unbound at pH 2 and 11 over the two hours measured.

2.6.7 Effect of Increased NaCl on Binding and the Molybdenum Blue Assay

As more NaCl is added to binding experiments of C_{16}GGGhex at pH 6, the amount of phosphate binding noticeably decreases (Figure 2.19). This phenomenon could explain the slight decrease in binding after multiple cycles of capture and release as the pH was repeatedly altered, if for example the wash steps between cycles did not completely wash out all NaCl and the concentration NaCl gradually accumulated in the sample as the number of cycles increases. This effect of decreased hexapeptide binding by an increase in NaCl concentration was also observed by Zhai, et al.[132]

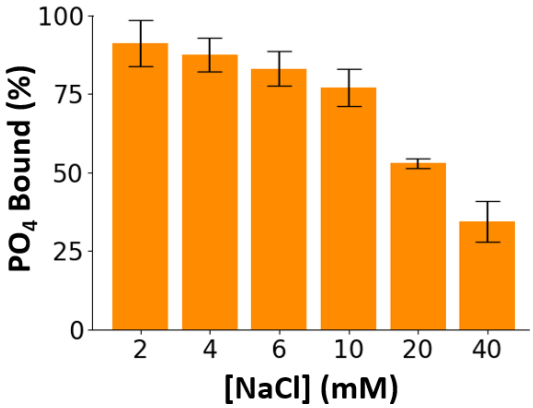

Figure 2.19. Binding experiments of C_{16}GGGhex at pH 6 at a 5:1 ratio of PA:PO_4 and varying final solution concentrations of NaCl.

We also investigated whether these higher concentrations affected the spectrophotometric assay to confirm that the observed decrease in binding was not an artifact of the assay (Figure 2.20). As the concentration of NaCl increases in the spectrophotometric calibration curves, the fitted lines do not noticeably vary or follow any noticeable trend, implying that added NaCl does not affect the spectrophotometric readings at these concentrations.

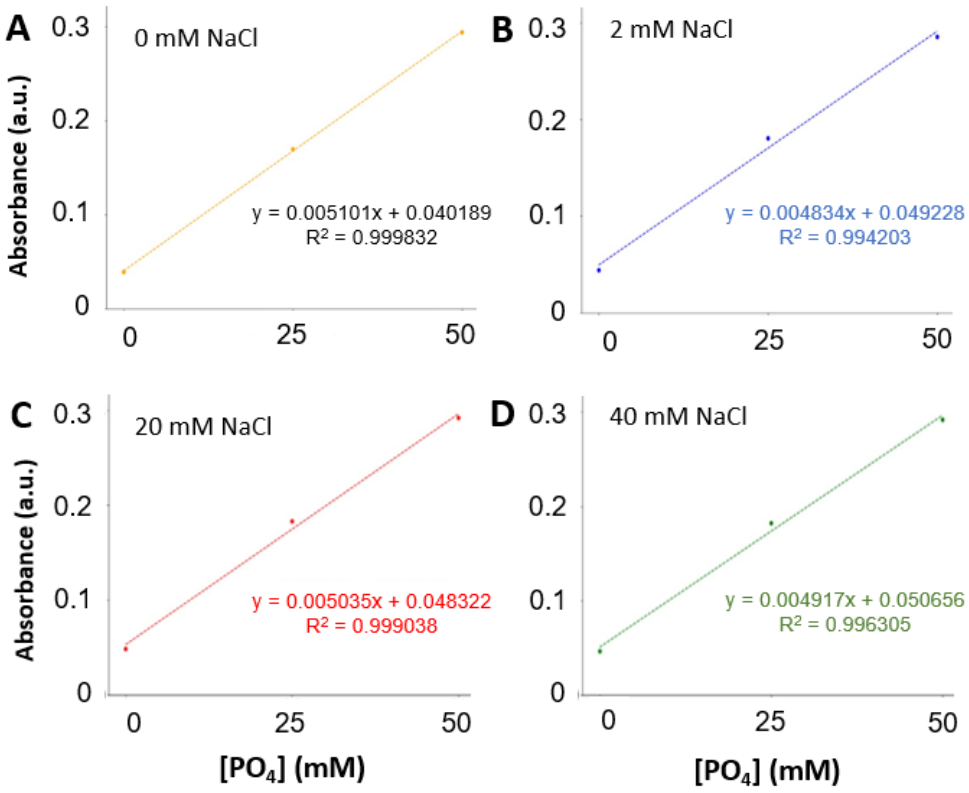

Figure 2.20. Spectrophotometric calibration curves constructed with increasing amounts of added NaCl, from (A) 0 mM NaCl, (B) 2 mM NaCl, 20 mM NaCl, and (D) 40 mM NaCl.

Even though we confirmed that binding is impacted by increased NaCl, the impact for our material is relatively small at the pH extremes. Table 2.7 details the average final concentration of added HCl and NaOH in order to achieve pH 2, 6, and 11 for our binding systems. The release conditions of pH 2 and 11 require concentrations of HCl and NaOH that fall in the range that would impact binding, both near 4 mM of added HCl or NaOH. However, this approximately 12% decrease in binding at pH 6 does not match the roughly 90-95% unbound phosphate at these extremes (Figure 2.3). Thus, we confirm that NaCl interference is not the cause of the observed near zero binding at pH 2 and 11.

Table 2.7. Average final concentrations of added HCl and NaOH to achieve the final solution pH

Final pH	[HCl] (mM)	[NaOH] (mM)
2	3.6±0.2	0

Table 2.7. Average final concentrations of added HCl and NaOH to achieve the final solution pH, continued.

6	0	0.2±0.1
11	0	4.6±0.2

2.7 Additional Simulation Results and Discussion

2.7.1 Estimated Potential of Mean Force for Phosphate Micelle Binding

From the phosphate-micelle simulation at pH 6, we estimated the potential of mean force (PMF) profile as a function of separation distance between phosphates and the micelle center. The PMF is obtained *via* the equation $\mathrm{PMF(r)} = \mathrm{kTln(P(r))}$. The PMF profile shown is relative to the PMF at the distance of 8 nm, which corresponds to the unbound state. The PMF shows a minimum at a phosphate-micelle separation distance of approximately 3.5 nm. The PMF difference between this minimum and the unbound state is -11.6 kJ/mol.

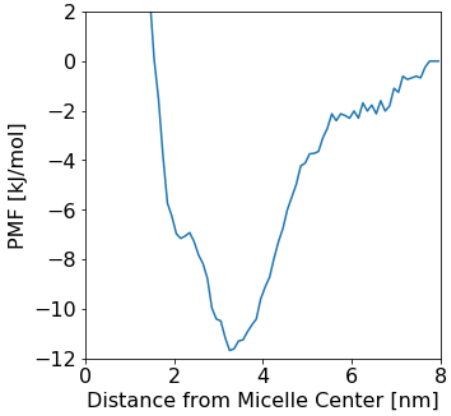

Figure 2.21. PMF as a function of the separation distance between phosphates and the micelle central axis. The result is obtained at the condition pH 11 and PA:PO_4 = 5:1.

2.7.2 Representative Snapshot of Multi-chain Binding

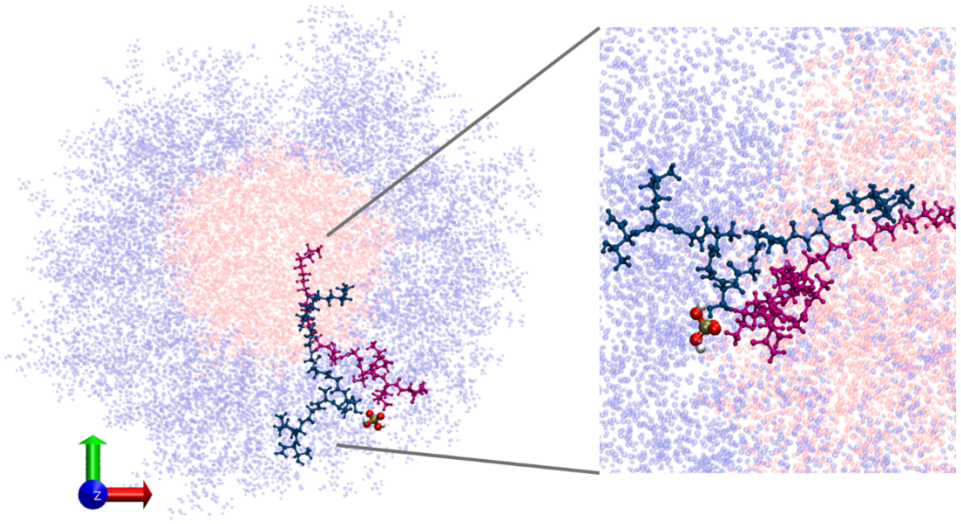

Figure 2.22. Representative snapshot of Multi-chain Binding from phosphate-micelle simulation at pH 6. The hydrophobic core is shown in red and the corona is shown in blue. The two different PA chains interacting with the phosphate is shown in dark blue and magenta, respectively.

CHAPTER 3

DESIGNING MULTI-COMPONENT PEPTIDE AMPHIPHILE MICELLES FOR PHOSPHATE CAPTURE

3.1 Abstract

The unique and precise capabilities of proteins are unmatched in their specificity and range of application. Effective mimicking of protein-binding offers enticing potential to direct their abilities towards useful applications, but it is nevertheless quite difficult to realize this characteristic of protein behavior in a synthetic material. Here, we design, synthesize and evaluate experimentally and computationally a series of multi-component phosphate-binding peptide amphiphile micelles to derive design insights into mimicking protein binding in synthetic materials. By inserting the Walker A P-loop binding motif into this peptide synthetic material, we successfully translate the protein-binding design parameters of hydrogen-bonding and electrostatic interaction to bind phosphate completely and selectively in this highly tunable synthetic platform. In this densely arrayed peptide environment, we use molecular dynamics simulations to identify an intriguing mechanistic shift of binding that is inaccessible in traditional proteins, introducing two corresponding new design elements of flexibility and gain of entropy in protein-analogous synthetic materials. We then translate these new design factors to *de novo* peptide sequences that bind phosphate independent of protein-extracted sequence or conformation. Overall, this work reveals that traditional complex conformational restrictions of binding by proteins can be replaced and repurposed in a multi-component peptide amphiphile synthetic material, opening up opportunities for future enhanced protein-mimicking design.

3.2 Introduction

Proteins perform remarkable functions using highly sophisticated molecular interactions and conformations, inspiring attempts to realize their functionality in tunable synthetic materials[141–143] for applications such as targeted drug delivery,[144] biomimetic scaffolding,[115,133,145] or reclamation and purification efforts.[107,146] However, adequately translating protein binding to synthetic counterparts is highly nontrivial. To date, various synthetic designs have been engineered to recapture protein binding potential, including employing peptides[107,142–144,147,148] or peptoids[146,149]; utilizing unconjugated binding motifs[15,26,132] or tethering them to a larger construct;[107,145,148] and either extracting a pre-identified protein-binding motif[2,132] or identifying a new motif through combinatorial[149] or computational screening[15,150]. Nevertheless, further study of synthetic binding mechanisms is merited so that future evolutions of materials can more fully realize proteins' sophisticated specificity and performance.

To study how protein binding can best be translated into a synthetic material, both a well-characterized protein-binding motif and a strategic material platform must be chosen. The Walker A P-loop motif[12,151] is an apt choice for several reasons. First, it is a simplified motif. Its sequence is GXXXXGK(S,T), where X is any amino acid, and its binding interactions largely depend on an isolated sequence and localized conformation rather than a complex tertiary structure, simplifying synthetic mimicry. Second, its native binding mechanism within phosphate-binding proteins (PBPs) has been highly characterized over decades of research.[12,15,24,26,132,152] The P-loop binds to phosphate through three factors—adopting a nested cavity conformation,[13,153,154] stabilizing phosphate through hydrogen bonds in the amide backbone, and utilizing a positively charged amino acid (AA) residue. This well-established understanding of binding in its native state will allow one to compare directly which binding features are adequately translated and which become

altered. Third, there have been preliminary synthetic studies verifying that its phosphate binding capabilities can be retained outside of the protein. [2,26,132]Lastly, if the P-loop is properly translated to a synthetic platform, it could have intriguing applications in resource recovery,[9,108] phosphate sensing,[155] or medical treatment of diseases corresponding excess phosphate concentration in the blood. [156]

This P-loop binding motif can readily be translated into a strategic material framework. One promising synthetic construct, peptide amphiphile (PA) micelles or "protein-analogous" micelles (PAMs),[19] is especially well-suited for a rational protein-mimicry mechanistic study. PAs consist of a peptide conjugated to a hydrophobic tail that spontaneously self-assemble in water, displaying the peptide binding motif in precise concentration to target ligands. Importantly, PAs are highly tunable in key protein-mimicking design components: precise amino acid (AA) control is achieved through sequence-specific synthesis[23,157]. Their supramolecular assembly architecture[19] and composition[158,159] is tuned through programable intermolecular interactions of multiple components, and their secondary structure within the peptide "headgroup" can be tailored through well-studied design principles of peptide interaction.[112,160,161] PA micelles have recently been designed to extract protein-derived sequences to bind to phosphate selectively over nitrate and nitrite for multiple cycles, [162] as well as monoclonal antibodies,[116] showcasing the translatable nature of protein binding to this platform. In addition to its promise as a useful material, we can also learn from this material how the binding mechanism of proteins is altered when rationally translated into a synthetic material.

To realize protein functionality in synthetic materials, we must first understand how binding functionality translates and then use that information to optimize synthetic design. In this work, we evaluated a series of rationally designed multi-component PA micelles to (1) identify

binding mechanistic shifts that occur from a single phosphate-binding peptide to a dense array of phosphate-binding peptides assembled in a micelle, (2) distill our findings into generalized design principles, and (3) translate the design principles towards *de novo* design of phosphate-binding peptides. By employing complementary experimental and molecular dynamics simulation methods, we uncover new binding contributors unique to synthetic material platforms that overcome the limitations of complex tertiary and quaternary conformations required for traditional *in situ* protein binding. Overall, this work redefines essential features required to translate protein functionality into a deployable material, motivating optimized protein-mimicking design in future synthetic materials in PA micelles and beyond.

3.3 Results and Discussion

3.3.1 Peptide Amphiphile Design Scheme

To mimic protein binding adequately in synthetic PA micelles, one must first review the mechanism that proteins employ in their native state to determine which features must be replicated in the synthetic construct. Over decades of study, proteins of vastly different size and function have been found to specifically and reversibly bind using three complementary contributors: hydrogen bonds (H-bonds), electrostatic charge stabilization, and the formation of a localized secondary structure. In the Walker A P-loop in phosphate-binding proteins (PBPs), NH and OH H-bonds along the backbone of an AA sequence play essential roles in binding various forms of phosphate.[154,163] Since the positioning of H-bonds is reliant on a delicate trivariate balance of covalent, electrostatic, and van der Waals interactions, slight changes in the AA sequence or the secondary structure of a protein or peptide can significantly alter its binding behavior and even its physiochemical properties.[164] Cooperating in tandem with H-bonds, the presence of positively charged AAs—particularly arginine, with the guanidinium group and lysine —have been observed

in many proteins as especially crucial for anion capture in contexts where limited H-bond stabilization is available from other residuals. [13,24,165] Lastly, the P-loop employs the secondary structure of a compound LRLR nest to bind phosphate. L and R correspond to predetermined dihedral backbone angles, and a single LR "nest" consists of three NH groups in a peptide backbone oriented to create a cavity to bind negatively-charged ligands.[13,154,166] Many small polypeptide AA sequences have been shown to form similar H-bond nest formations when extracted from larger proteins,[154] revealing their predisposition towards adopting this conformation even when isolated from their native environment. Harnessing these insights, in our previous work we successfully mimicked protein-binding of phosphate using PA micelles by harnessing a LRLR-nested P-Loop motif, Ser-Gly-Ala-Gly-Lys-Thr, extracted from ATP-binding proteins. However, the relative impact of each of these three contributors has not been explored, limiting possible design insights.

Here, a series of multi-component peptide amphiphile micelles were designed (Figure 3.1) to isolate the relative contributions of conformation, hydrogen bonding, and electrostatic attraction on peptide binding of phosphate in a PA micelle, utilizing a dual experimental and computational approach. This rational design was informed by a key insight derived from our previous work, namely that the phosphate ions were stabilized through hydrogen bonding and electrostatic attraction from multiple peptide chains in the micelle corona, reminiscent of tertiary binding.[162] However, in this high-density environment of the peptide micelle corona, the peptide binding motifs were hypothesized to be conformationally constrained, and the protein-derived LRLR nested cavity conformation could be inhibited.

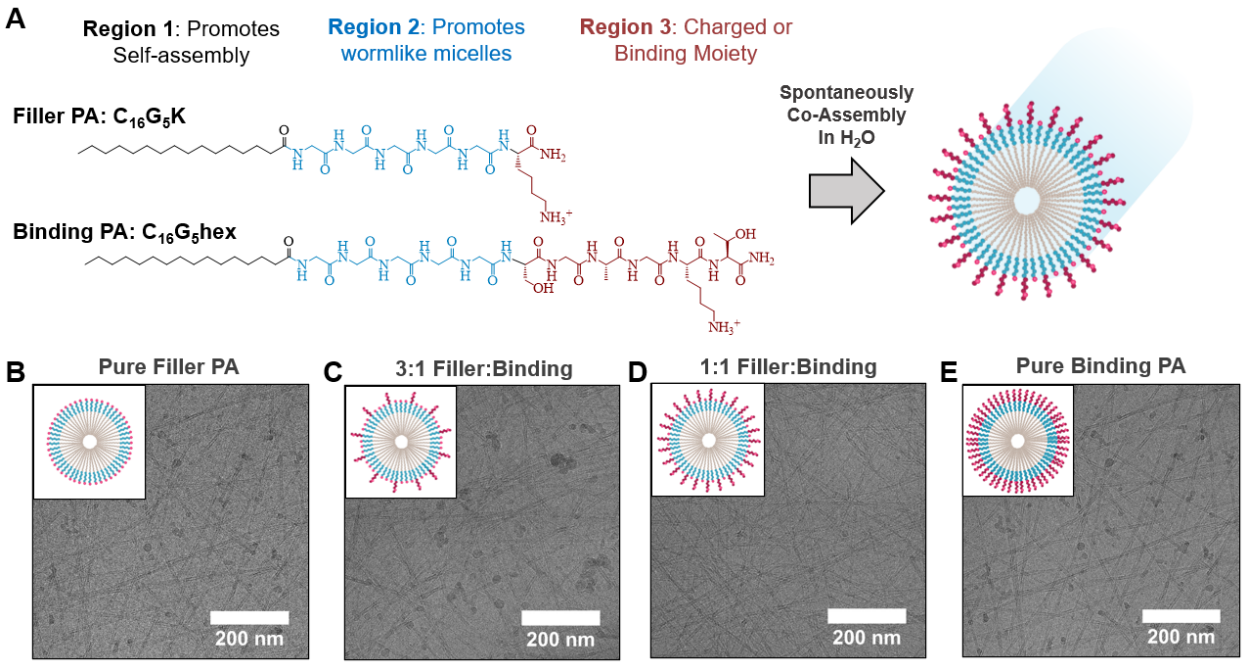

Figure 3.1. (A) Molecular structures of the Filler PA and the Binding PA that feature three building block regions, which spontaneously co-assemble into a micelle in water due to the hydrophobic effect. (B) Cryo-TEM images of the four PA systems with varying ratios of Filler PA to Binding PA, which reveal extended wormlike micelles for all systems.

We aimed to reinsert the protein-derived conformation into the system design by sequentially decreasing the density of the peptide binding motifs in the micelle corona, making the motifs less conformationally constrained. We hypothesized that increasing the conformational freedom of the phosphate-binding motifs would further optimize phosphate binding, allowing the protein-analogous micelle to more closely mimic the nested conformation characteristic of P-loop binding.

Multi-component PA systems are well poised to evaluate this. The peptide density can be precisely tuned by spontaneous co-assembly of a Binding PA and a Filler PA into multi-component supramolecular structures at predetermined compositions. Here, we designed a series of four PA micelle systems using both components, with the composition of Binding PA sequentially reduced by half from 100% to 50% to 25%. A pure Filler PA system was also evaluated as a control for

non-sequence-specific binding. A similar design scheme was used by Cui and co-workers. They designed a two-component PA micelle to bind to monoclonal antibodies, and they found that decreased composition of the binding moiety corresponded to increased antibody capture.[116]

Each PA was designed with tunable "building block" regions with individualized function.[23,141] The Binding PA, denoted $C_{16}G_5$hex (Figure 3.1A), is derived from the prototype phosphate-binding PA micelle with a nearly identical design.[162] Region 1 is a hydrophobic tail required to facilitate self-assembly. Region 2 is a five-glycine spacer region that promotes wormlike micelle formation,[22] which is the desired micelle architecture to create an entangled network of PA micelles to capture and release phosphate. The number of glycine residues was increased from three to five in this study to further extend the binding motif into the environment and access greater conformational freedom, as well as increase the solubility of the Filler PA counterpart. Region 3 is the protein-derived P-loop hexapeptide binding moiety, SGAGKT, that has previously been shown to bind phosphate.[2,132,162] The Filler PA, denoted $C_{16}G_5K$, has identical Regions 1 and 2 to ensure that it homogenously co-assembles with $C_{16}G_5$hex. The binding moiety in Region 3 is substituted with a lysine residue, which was required for solubility.

We synthesized the PAs using FMOC solid phase synthesis and purified them to greater than 95% purity (Figure 3.8). All PAs were found to self-assemble into wormlike micelles using cryogenic transmission electron microscopy (cryo-TEM) imaging (Figure 3.1B-E) with similar dimensions, which will allow for direct comparison between systems.

3.3.2 Experimental Phosphate-Binding Results by Multi-Component Peptide Amphiphile Micelles

The phosphate-binding abilities of the multi-component PA micelles were evaluated at key conditions derived from our previous study. In that work, phosphate was nearly completely bound

at pH 6 and a molar ratio of 3:1 PA:PO, with simulations revealing that two to three PA chains were always required to bind. In our re-engineered multi-component design, we wanted to determine if we could achieve higher binding at lower ratios of Binding PA to PO_4 if the nested cavity conformation was employed, which would also provide further insight into binding mechanisms. Thus, we evaluated phosphate binding at pH 6 at ratios of 1:1, 2:1, and 4:1 PA:PO_4. Here the PA is total PA, rather than Binding PA, to keep the PA concentration constant across all systems tested. These ratios nicely complement the Binding PA multi-component compositions and would easily facilitate a direct per-molecule binding analysis. For example, a 4:1 PA:PO_4 ratio for the 3:1 Filler:Binding system would have a 1:1 ratio of binding motif to phosphate. In our previous work, we also described how phosphate-binding in the micelle at high pH was restricted due to a "squeezing" effect of the micelle corona when the amine lysine side chain was deprotonated at high pH, which is contrary to phosphate binding trends of the free hexapeptide.[2,132] Thus, we evaluated binding at pH 10 and 11 again here to determine if a decreased density of the micelle corona would mitigate this squeezing effect and replenish the ability to bind at high pH.

The phosphate binding performance of the four PA systems is shown in Figure 3.2. The results are surprising, revealing similar binding trends across all four systems for each pH or ratio condition. At pH 6, we observe essentially complete binding of phosphate at 4:1 ratio of PA:PO_4 for all systems, with incomplete binding at lower ratios. These PA:PO_4 ratio trends are consistent with our previous work. We also see similar trends across pH conditions as in our previous study, namely that binding was still prohibited at pH 10 and 11 but maximized at pH 6. The only noticeable difference between systems is that there is marginally higher binding for the Pure Filler PA and the 1:1 Filler:Binding PA systems at pH 6 and 1:1 ratio of PA:PO_4, which bound nearly

50% of the phosphate compared to 25%. Interestingly, selectivity over nitrate and nitrite is also retained for all four PA systems, as shown in Figure 3.10.

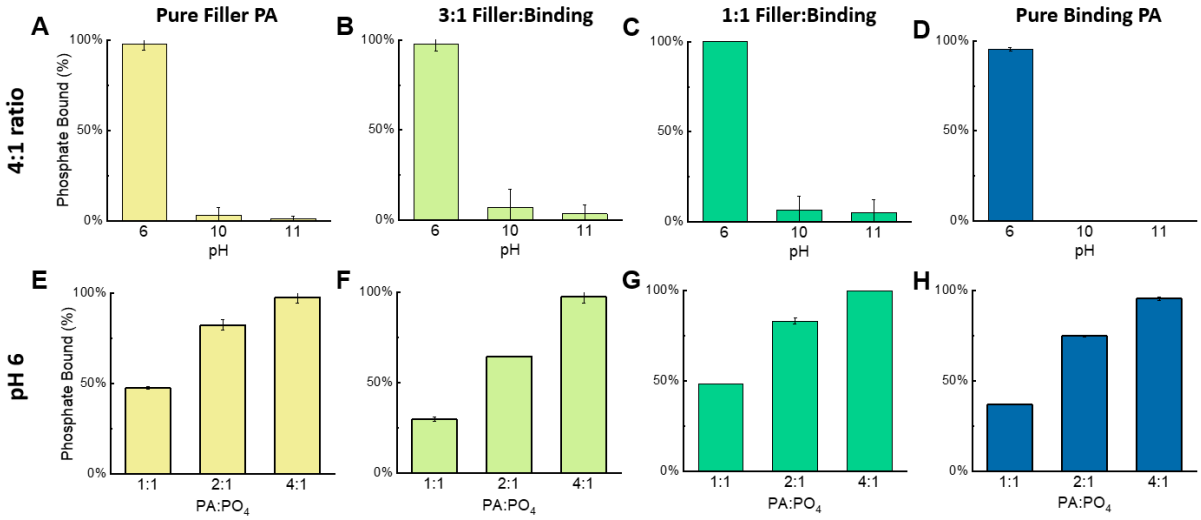

Figure 3.2. Phosphate-binding results of the multi-component micelle systems. (A-D) Phosphate-binding performance of each PA system at a 4:1 ratio of PA_{total}:PO_4 and pH conditions of 6, 10, and 11. (E-H) Phosphate-binding performance at pH 6 of increasing ratios of PA_{total}:PO_4. The binding trends are nearly identical across all systems, contrary to expectations.

These unexpected results lead to several conclusions. First, as the density of the phosphate-binding motif decreases from 100% to 50% to 25%, there is no noticeable effect on binding, suggesting that increased conformational freedom of the unit in this design does not correlate with more efficient 1:1 binding of phosphate. What is more surprising is that the trend remains intact even for the pure Filler PA system, which was designed to be a control system. The P-loop sequence-specific binding motif was unexpectedly not required to selectively bind phosphate, suggesting that the P-loop associated nested cavity conformation may not be needed to bind phosphate but that other binding factors exert a larger influence. We also determined that binding at high pH is not re-established as the density is reduced. To understand these results, we turned to molecular dynamics simulations to deconvolute the influence of H-bonds, charge, and

conformation in each of the four PA designs and to probe the molecular-level interactions of binding in a synthetic, densely arrayed supramolecular material.

3.3.3 Molecule Dynamics (MD) Simulation Results

Using molecular dynamics (MD) simulations, we aimed to (i) verify that simulations matched experimental results, (ii) probe why binding occurred in the PA micelle independent of P-loop sequence specificity, considering binding by both a unimer PA and a PA micelle, and (iii) derive new design insights for mimicking protein binding from these unexpected yet illuminating findings.

To compare with experimental results and verify our simulation setup, we performed unbiased MD simulation for the multi-component PA micelles at pH 6 and 11, with the Filler PA composition *X* varying from 0% to 100% at a 25% interval. As *X* increases, the reduced crowding in the corona is hypothesized to improve the presentation of the P-loop binding motifs. As introduced in our previous work, the pH 6 condition consists of protonated lysine amine and $H_2PO_4^-$ and the pH 11 condition consists of neutral lysine amine and HPO_4^2. The experimental protonation states for pH 10 are more ambiguous, as the lysine amine is thought to partially deprotonate before $H_2PO_4^{2-}$ does, due to a shift in the lysine pK_a in the densely packed charged environment. Therefore, we use the protonation state consisting of a protonated lysine amine and HPO_4^{2-} to represent an idealized binding condition that allows us to obtain useful design insight.

The PA micelle binding results are shown in Figure 3.3 at the three protonation conditions. We measured the extent of binding as the probability for a phosphate ion to form *n* hydrogen bonds with the micelle, where *n*=0 implies that the phosphate is unbound. Overall, the results agree with the experiments. We find that binding is stronger at pH 6 than at pH 11, as in experiments. The binding performance remains unchanged as the Filler PA gradually replaces the Binding PA, with

the Filler PA-only system exhibiting effective phosphate binding that is comparable to the Binding PA-only counterpart. The same trend is observed at each protonation condition. The binding results are accompanied by representative snapshots of the phosphate-micelle complexes taken at the end of the production run to visualize binding (Figure 3.3b). Overall, the snapshots indicate that the Filler and Binding PA are uniformly mixed in the multi-component micelle. At each pH condition, the phosphate binding visually appears to remain constant across all compositions tested. We note that at pH 6, while the snapshots agree with our experiments and show that most, if not all, phosphates are bound, the extent of binding is somewhat underestimated by the hydrogen-bonding measure, where roughly 40% of the phosphate ions are labeled unbound. This is because H_2PO^{4-} are found to form clusters (Figure 3.11), and as the clusters bind to the micelle, only some of its members form hydrogen bond with the micelle. The phenomenon of spontaneous clustering for phosphate has been previously reported.[167] At the optimized condition, each phosphate (HPO_4^{2-}) binds strongly to the micelle as individual ions, with most of them forming more than three hydrogen bonds.

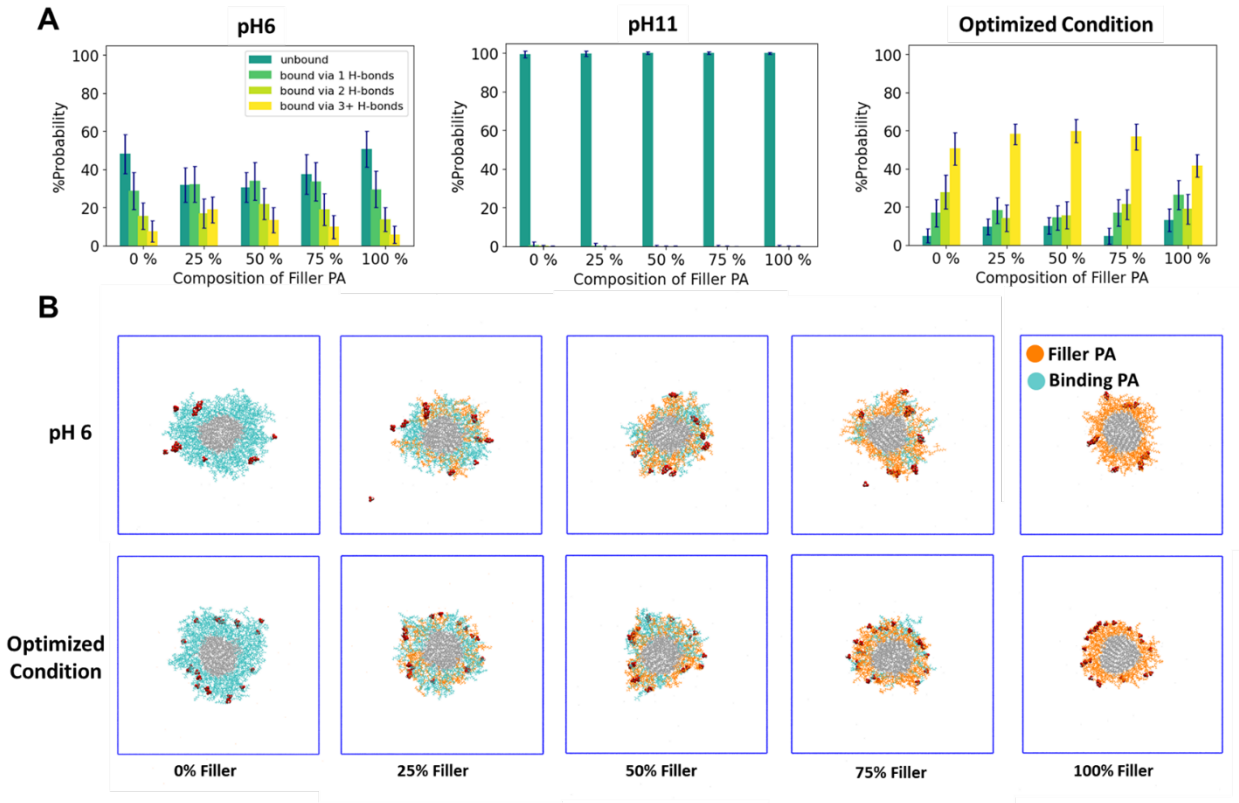

Figure 3.3. Simulated phosphate-binding results of the multi-component micelle systems. (A) Phosphate-binding performance as measured by extent of hydrogen-bonding. The Filler PA composition is varied from 0% to 100% at 25% increments. A pH of 6 is represented by protonated lysine ε- ammonium group and $H_2PO_4^-$. A pH of 11 is represented by neutral lysine ε-amino group and HPO_4^{2-}. The optimized condition contains protonated lysine ε-ammonium group and HPO_4^{2-}. The error bar comes from 22 phosphate ions in a single simulation. (B) Representative snapshots of the micelle cross-section at pH 6 and at the optimized condition. Under each protonation condition, the snapshots are arranged as a function of Filler PA composition. The C_{16} hydrophobic core is shown in grey, phosphates are shown in red, Filler PA are shown in orange, and Binding PA are shown in cyan.

Next, we consider why we observe binding across systems independent of composition or P-loop. To do this, we analyze binding mechanisms of both the unimer PAs and the assembled PAs. Studying the Filler PA as a unimer allows us to determine if the phosphate-binding functionality of the non-sequence-specific Filler PA arises at the single-molecular level or can only be achieved by micelle assembly.

To study unimer PA binding, we employed MD simulations with the adaptive biasing force (ABF) sampling method to obtain the free energy surfaces describing the binding of a unimer PA to a phosphate. The free energy results are shown in Figure 3.4, evaluated at the three pH conditions. Informed by our previous work, the free energy surfaces are constructed in terms of two distance CV's. d_1 denotes the distance from the phosphate to the center of the region-3-moiety (SGAGKT for Binding PA and K for Filler PA), and d_2 denotes the distance from the phosphate to the center of region 2. At pH 6 and for both Binding PA and Filler PA systems, the free energy difference between the bound state and the unbound states is below 5 kJ/mol, indicating no strong preference to bind. While it is enthalpically favorable for the oppositely charged phosphate and PA to form a charge-neutral complex, such enthalpic gain is offset by a comparable loss of entropy. Similar comments have been made for the free-standing, zwitterionic hexapeptide.[26] We observe a similar preferred unbound state at pH 11 for both PAs, since neither enthalpic nor entropic driving force is present to facilitate binding.

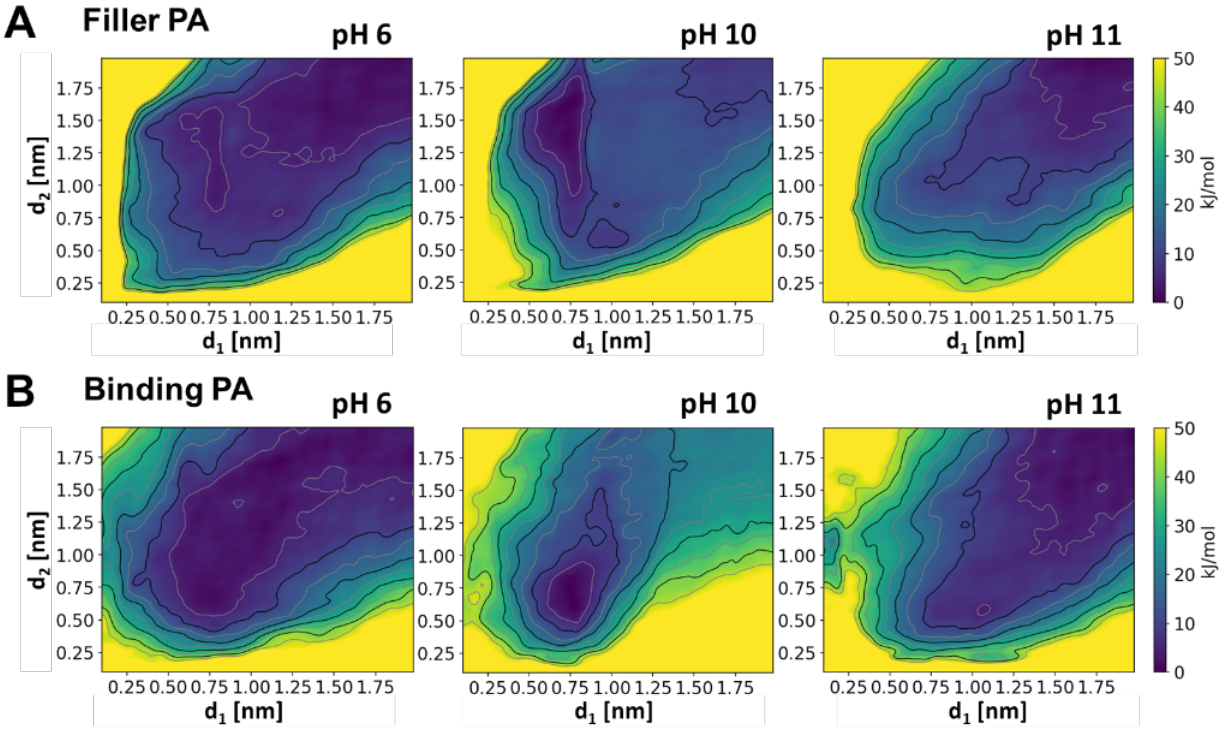

Figure 3.4. Free energy surface for a unimer (A) Filler PA ($C_{16}G_5K$) and (B) Binding PA ($C_{16}G_5$hex) binding to a phosphate. The free energy difference between two adjacent contour lines is 5kJ/mol. The free energy is described in terms of two distance CV's. d_1 denotes the distance from the phosphate to the center of the region-3-moiety (SGAGKT for Binding PA and K for Filler PA), and d_2 denotes the distance from the phosphate to the center of the region 2, allowing one to determine a phosphate location that is stabilized or bound to a peptide. For each system, the free energy surface is close to converged and obtained at the end of 400-ns of ABF biased simulation. At pH 10, there is a local minimum that indicates that phosphate binds for both the Filler PA and the Binding PA.

At pH 10, the Binding PA shows a favorable binding with free energy between -20 and -25 kJ/mol, with is very close to the binding free energy estimated experimentally for the free-standing hexapeptide (-4±0.1 kcal/mol).[2] The free energy surface for the Filler PA also shows a minimum for the bound state, with an energy difference of ~ 5kJ/mol. For both systems, the wide free energy wells for bound states suggest that the overall bound structures are not fully constrained, but instead can freely adopt different conformations. Overall, the free energy surface suggests that the phosphate is bound exclusively to the charged lysine side chain, while the flexible

G_5 linker aids to wrap around the phosphate in many different ways. While both systems show relatively flexible binding provided by the G_5 region, the bound state of Binding PA is better-defined and deeper, suggesting that the P-loop provides a stronger binding and leads to a specific bound conformation.

The single-chain simulations confirm the functionality of the P-loop. More importantly, however, they reveal that phosphate binding can also be realized by combining electrostatic attraction from the protonated lysine amine and flexible accommodation from the G_5 region. The finding provides us with an alternative route to access and engineer the phosphate-binding functionality. The self-assembled micelle system is one way to harness such an alternative binding route. As the PAs self-assemble, the functional peptide headgroup become dramatically condensed at the micelle corona. The rise in concentration can potentially amplify the access to the alternative binding route since a phosphate will be able to simultaneously interact with multiple lysine amine sites and flexible G_5 segments, neither of which are required to pre-organize into specific conformations.

Finally, we move to the third aim of the MD study: deriving design insights from the altered binding mechanism in this synthetic platform. So far, both experimental and simulated observations suggest an overall improvement in binding performance as PA unimers self-assemble into micelles. At pH 6, while as a unimer, neither Binding PA nor Filler PA shows preferential binding; as micelles, they exhibit nearly complete binding. At pH 10, while the Binding PA unimer exhibits stronger binding than the Filler PA, the binding performance as micelles remains constant at all compositions. The remaining question lies in explaining why the binding performance improves in micelle systems.

Informed by the unimer binding results, we hypothesize that the multi-component micelle systems can have two phosphate binding routes, one relying on the P-loop motif, and the other utilizing one or more positively charged lysine amine tails. To understand how each contributes to phosphate binding under different circumstances, we start by examining the dihedral conformation for the P-loop sequence, and then characterize how and where the phosphates are mostly bound on the micelle. Our Ramachandran plots (Figure 3.12) show that, in the micelle systems, the P-loop motif tends to adopt a particular dihedral conformation that resembles an LRL compound nest. The G_5 region shows a typical glycine dihedral distribution, meaning the Filler PA does not adopt any nest conformation. However, since the binding performance is found to be constant regardless of the presence of nests, we employ a second analysis to determine whether, and if so to what extent, the compound nests are indeed employed to bind phosphate. Figure 3.13 presents the statistics for the bound location along the peptide sequence at pH 6 and at the optimized protonation condition. Under both conditions, over 50% of the total hydrogen bonds are contributed by the G_5 linker domain, lysine residue, and amidated C-termini, which are the common domains present in both Binding PA and Filler PA. This binding contribution resembles the alternative binding route utilized by the Filler PA unimer for phosphate binding. The rest of the hydrogen bonds are contributed by the remaining P-loop hexapeptide (excluding lysine and amidated C-termini) that is unique to the Binding PA. As Filler PA composition increases, the contribution from the P-loop motif diminishes and becomes substituted by that from the common domains. The result confirms that the alternative binding route, discovered from the unimer's binding behavior, continues to function in the micelle. It also shows that the compound nest formed at the P-loop is not the predominant binding location for phosphate, which consistently explains why phosphate-binding performance is independent of the presence of nests. As Filler PA

composition increases, the gradual transition from P-loop contributed binding to charged lysine amine-contributed binding aligns with our hypothesis that the alternative binding route takes over the phosphate binding as Filler PA becomes the majority.

Another point of discussion is that the alternative binding route is amplified in the micelle, which could be the main reason for the overall improved binding in the micelle. To evaluate this idea, we categorized the binding environment of a phosphate ion into binding motifs, where a motif of *x*-*y* denotes that the phosphate is bound by *x* Binding PA and *y* Filler PA. Figure 3.5A reports the percent population of the five most-observed binding motifs. We used data obtained at the optimized condition for better statistics and informative insights. Similar trends are observed from the results at pH 6 (Figure 3.14). In this analysis, bound phosphates are found to adopt diverse binding motifs with comparable probability. Among them, multi-chain binding motifs, such as 0-2, 1-1, 2-0, and 1-2, contribute significantly. Representative snapshots for the prevalent multi-chain binding route seen in the 50% Filler PA system are included in Figure 3.5B-D. We also notice that in this system, despite the symmetric composition, popular motifs are predominantly contributed by Filler PA. The mismatch (or shift) between the stoichiometry in binding motifs and the composition shows that the alternative binding route, once amplified by multi-chain binding, becomes more favorable than the P-loop binding route.

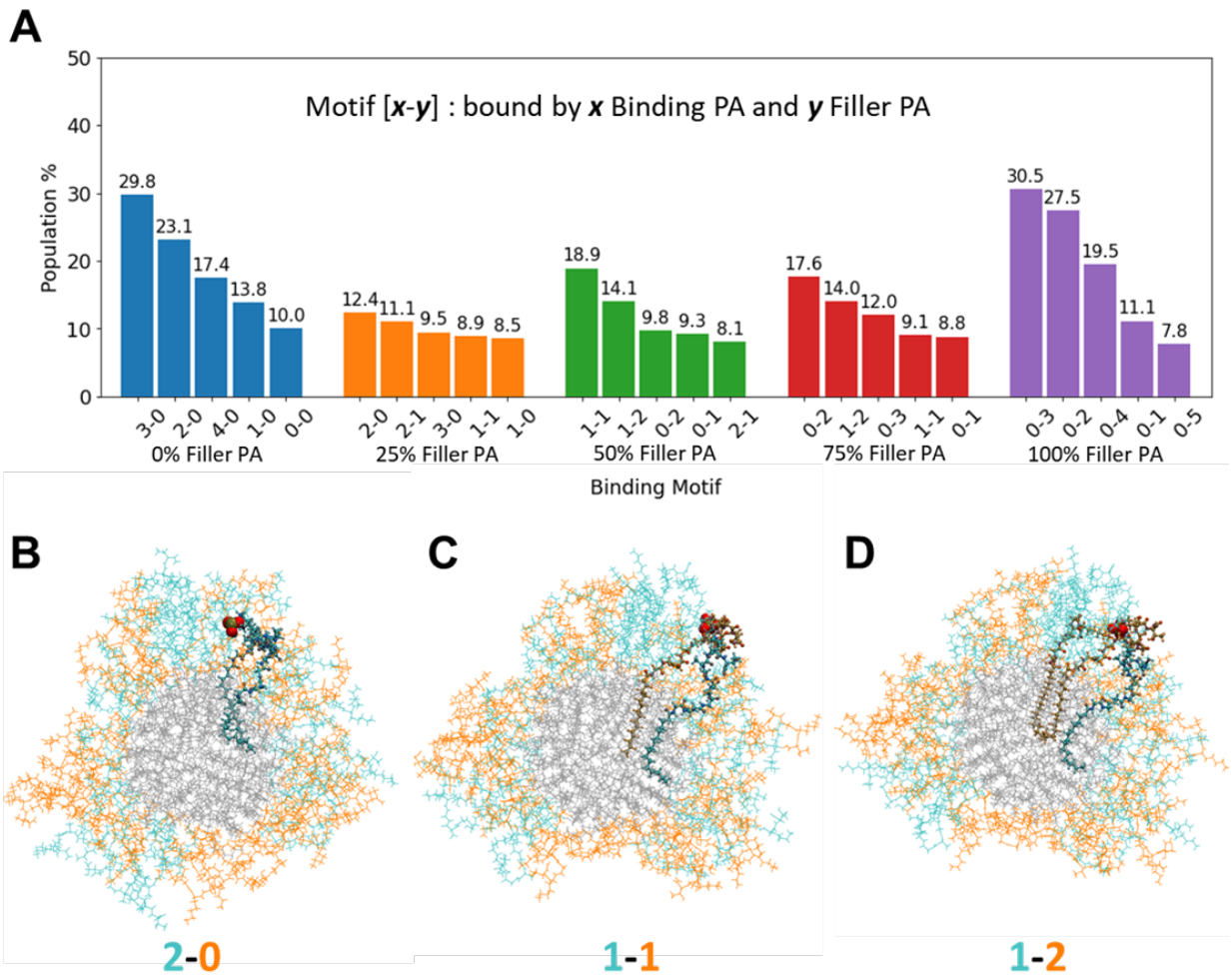

Figure 3.5. Population and snapshots of top phosphate binding motifs. (A) The population of top five most-observed binding motifs at the optimized protonation condition. The Filler PA composition is varied from 0% to 100% at 25% increments. The binding motif of a phosphate ion is denoted as *x*-*y*, where *x* refers to the number of Binding PA bound to the phosphate, and *y* refers to the number of Filler PA bound to the phosphate. The numeric population for each motif is printed on top of the bar. (B-D) Representative snapshots for the (B) 2-0, (C) 1-1, and (D) 1-2 multi-chain binding motifs at 50% Filler PA composition, optimized protonation condition. The snapshots are taken along the micelle cross-section. The C_{16} hydrophobic core is shown in grey, phosphates are shown in red, Filler PAs are shown in orange, and Binding PAs are shown in cyan.

The binding motif analysis points us to an important free energy contribution—the loss of entropy associated with molecular binding. As seen in the unimer binding simulation at pH 6, the favorable enthalpic gain is offset by the entropy loss, resulting in an overall zero binding free energy favor. For multi-chain binding in micelle, the enthalpic gain is amplified, as there will be

more pairs of electrostatic interactions. Meanwhile, the entropy loss is minimized for multi-chain binding for two reasons. First, the micelle can accommodate the phosphate via a diverse range of interchangeable binding motifs. Second, each binding motif also includes numerous degenerate states, because a PA in the motif can be indistinguishably substituted by another neighboring PA of the same kind. As a result, increased enthalpic gain and minimized entropic loss both act to improve phosphate binding to micelles as compared to the unimer counterpart.

In sum, we determined that the protein-analogous micelle, binding is retained but the binding mechanism shifts from native proteins. Certain factors remain consistent, namely H-bonding and electrostatic attraction. But in this platform, the design element of a conformationally constrained nested cavity is disregarded in favor of a new factor unique to this synthetic platform, namely that of minimized entropy loss through the flexibility of multi-chain binding conformation using non-specific residues. This intriguing design element aligns with recently published work, where flexibility is introduced as a critical design factor in engineered protein binding.[168] Their flexible protein is selectively bound to unfavorable metals by adopting previously inaccessible conformations in the native protein. This PA platform intrinsically accesses this feature to selectively bind to phosphate, making it an intriguing platform to optimize in future rounds of design.

3.3.4 Case Study: Evaluating Design Principles through Single-Peptide Binding of Phosphate

We are poised to translate these design insights and physical principles to engineer *de novo* peptide sequences to determine if we can mimic the protein binding of phosphate without the predetermined conformational restrictions that are characteristic of protein binding. To engineer *de novo* peptide sequences for phosphate binding, we designed a series of simplified motifs to manipulate the effects of hydrogen bonding, electrostatic interaction, and chain flexibility. We

chose only to build the motifs using glycine and lysine residues, as those were the only residues necessary to achieve binding in the Filler PA. We also wanted to isolate more precisely the individual molecular mechanistic binding principles, so we switched material platforms from the highly interactive peptide micelle corona to a polystyrene-polyethylene-peptide Tentagel resin system that has been used to characterize single-peptide binding.

Using glycine and lysine residues, we constructed five peptide motifs. The first was a single lysine (K) residue, to determine if binding could be achieved by a single charge alone, without significant hydrogen bond contributions. The other four motifs varied two design variables: (i) charge number, through controlling the number of lysine residues, and (ii) charge spacing and their corresponding conformational freedom, adjusted through the number of glycine residues that spaced the lysine residues. From these guiding principles, the four synthesized sequences were KGK, KGGK, KGKGK, and KGGKGGK. Their phosphate binding performance is shown in Figure 3.6 at pH 6 and 1:1, 2:1, 4:1, and 8:1 peptide:PO_4 molar ratios, all at a phosphate concentration of 10 ppm.

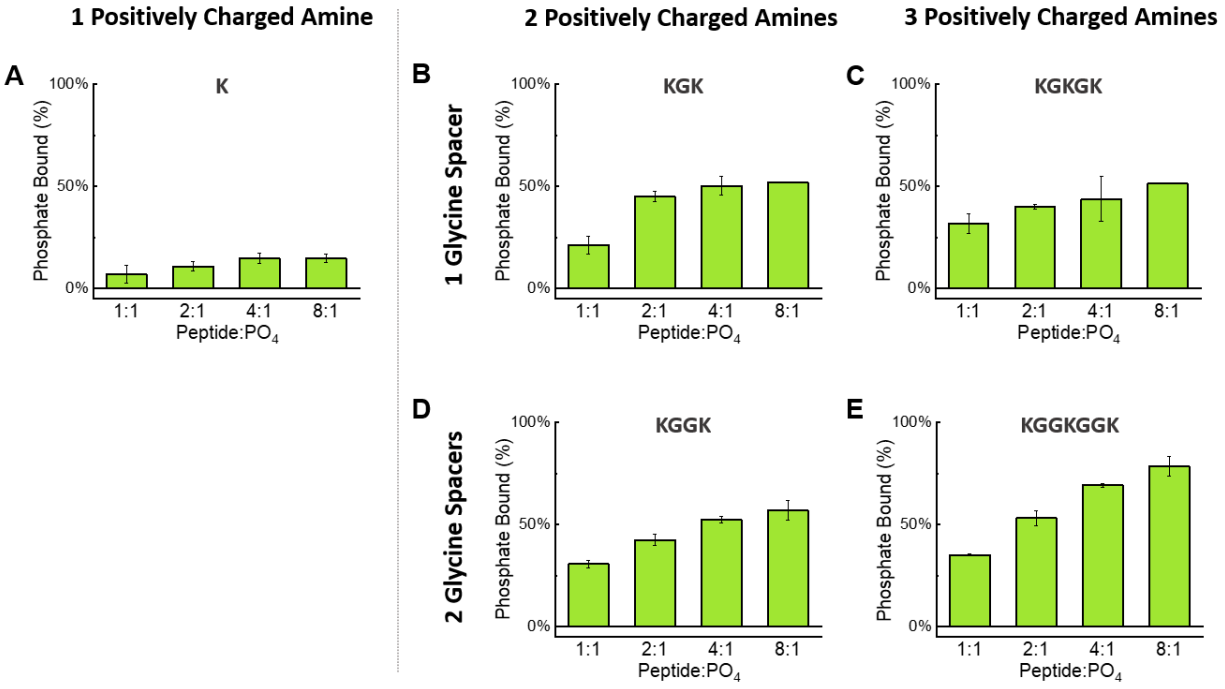

Figure 3.6. Phosphate-binding results of five single-peptide motifs, (A) K, (B) KGK, (C) KGKGK, (D) KGGK, and (E) KGGKGGK, at pH 6, 10 ppm PO4, and 1:1, 2:1, 4:1, and 8:1 peptide:PO4 molar ratios.

Significantly, the phosphate-binding results demonstrate that binding can be achieved by *de novo* peptide systems. All systems excluding the K system bound phosphate to a noteworthy degree as the ratio of peptide increased. The KGK, KGGK, and KGKGK systems all performed similarly, with roughly half of the phosphate bound at 4:1 and 8:1 ratios of peptide to phosphate. KGGKGGK bound the highest percentage of phosphate at 78%±4.8% for an 8:1 ratio of peptide:PO4. The K system shows minimal binding, indicating that a single charge alone is insufficient to bind to phosphate. None of the systems achieved 100% binding of phosphate at the ratios tested.

The *de novo* systems also offer a valuable conformational design insight towards synthetic mimicking of protein-binding. Comparing KGKGK to KGGKGGK, we see that increased spacing and conformational freedom between charges promote higher binding performance, aligning with

our newly derived flexibility design factor. Binding in these systems is similarly likely correlated to entropy maximization of the chains, where chains are not forced to adopt a specific constrained conformation to bind, but rather can bind through multiple flexible binding factors. The flexible PA micelle and the KGGKGGK systems are better poised to adopt a favorable binding conformation than the other three more rigid counterparts.

Despite not achieving complete binding in these single-peptide resin systems, we were nevertheless able to demonstrate that synthetic binding sequences can still be employed to bind to phosphate. This intriguing result indicates that we no longer need to be limited to protein-derived sequences and particular tertiary and quaternary structures to mimic protein binding. While these systems present a reduced design approach, we are positioned to translate these features and principles to more sophisticated sequences and systems in the effort to engineer precise biomimetic materials.

3.4 Conclusion

In this work, we determined that complete and selective binding by peptides can be achieved independent of sequence when facilitated by the densely packed, highly flexible micelle peptide corona environment. This micelle platform has the unique advantage of presenting a high density of adaptable hydrogen bonding donors that can readily adopt the conformation necessary to bind to phosphate. While proteins must rely on adopting a specific conformation to bind, the protein-analogous micelle can adapt more readily to achieve binding conformations within the headgroup that utilize both charge and hydrogen bond donors. We started out the study with two well-established design parameters—hydrogen bonding and charge—and identified the importance of entropy maximization and flexibility of the binding moieties, offering insight into how conformational freedom can affect functionality in synthetic materials. Ion capture mechanisms

that take advantage of highly flexible binding cites and the associated increase in entropy are often non-accessible in naturally occurring proteins, which must resort to a highly constrained conformation to bind. These results make the peptide micelle platform highly intriguing for future rounds of protein-inspired binding design, presenting a high concentration of highly flexible and tunable binding contributors in one local environment. Finally, we demonstrated that *de novo* phosphate-binding peptide sequences can be engineered from these design principles, opening an intriguing opportunity for biomimetic materials to overcome the highly complex binding mechanisms of proteins to outperform them through informed engineered design.

3.5 Methods and Materials

Synthesis of Peptide Amphiphile Micelles and PS-PEG-Peptide Resin Systems

Two peptide sequences (GGGGGK and GGGGGSGAGKT) were synthesized on 0.25 mmoles of rink amide resin (Novabiochem) through standard FMOC solid phase peptide synthesis using an automated Prelude X Benchtop Synthesizer (Protein Technologies, Tuscon, AZ, USA). For each coupling step, the FMOC protecting group was first removed from the resin using 20% piperidine in dimethylformamide (DMF). Separately, the amino acid was activated with N,N,N',N'-Tetramethyl-O-(1H-benzotriazol-1-yl)uranium hexafluorophosphate (HBTU) and N,N-Diisopropylethylamine (DIPEA) in a molar ratio of 1:4:3.95:8 of resin: amino acid: HATU: DIPEA. The activated amino acid cocktail was then added to the deprotected resin and then allowed to mix to conjugate. After the amino acid couplings were completed, the deprotected glycine N-terminus was then coupled with a palmitic acid tail.

After drying the resin under nitrogen, the peptide amphiphiles were then cleaved from the resin using a 95:2.5:2.5 by volume trifluoroacetic acid: triisopropylsilane: MilliQ water cleavage cocktail for 2 hours while shaking. The cleaved peptide amphiphiles were then precipitated

through dropwise addition of the cleavage solution in a 50:50 by volume hexanes: -80 ºC diethyl ether solution. The peptide amphiphiles were dried under nitrogen and dissolved in water.

The peptide amphiphiles were purified using reverse-phase HPLC (Prominence, Shimadzu, Columbia, MD, USA) on a C8 column (Waters, Milford, MA, USA) at 50 ºC using acetonitrile and water with 0.1% formic acid as gradient mobile phases. The molecular weight of the products in the HPLC fractions were characterized by MALDI-TOF mass spectral analysis (Biflex III, Bruker, Billerica, MA, USA). The product-verified fractions were lyophilized and stored as powders at -20 ºC. The purity was analyzed using a similar gradient method on an Agilent 6130 LCMS system in the University of Chicago's Mass Spectrometry Facility, using a Waters column, C8, XBridge, 4.6 mm × 150 mm, 5 μm particle size, and 130 Å pore size. The purity was calculated by integrating the area under the peaks during the elution time and dividing the area of the product peak by the area of all peaks, excluding peaks that were artifacts of the method. The purity was confirmed to be greater than 95% for both PAs.

The PS-PEG-Peptide systems were synthesized on 0.25 mmoles of TentaGel® S NH2 Resin (90 μm) for the following peptide sequences: K, KGK, KGGK, KGKGK, and KGGKGGK. The synthesis protocol was identical to that of the rink amide resin systems, with the exception that a double coupling step was performed for each amino acid to ensure complete conjugation. The peptides were not cleaved from the resin. After the coupling steps were completed, the resin was rinsed with dichloromethane, dried under nitrogen, weighed on an analytical balance, and submerged in MilliQ water to reach the desired molar concentration of peptide given the loading (mmol/g) of the TentaGel resin.

Micelle Fabrication Procedure

The multi-component PA micelles were fabricated to ensure homogenous mixing of both PA components in each micelle. To do this, the purified single-component PAs were lyophilized, and the lyophilized powder was dissolved in hexafluoroisopropanol (HFIP), which is a good solvent for PAs that does not promote hydrophobically driven self-assembly into micelles. The PA-in-HFIP solutions of each PA were combined to achieve the desired ratio and molar concentration. The HFIP was evaporated until nitrogen flow, leaving behind a thin film. The film was dissolved in MilliQ water at the desired concentration, heated at 70 ^{o}C for 1 hour on a mechanical shaker, and left to equilibrate to room temperature before experimental use.

Critical Micelle Concentration (CMC) Determination

The CMC was calculated by marking an increase of fluorescence intensity, corresponding to an increased micelle concentration, of a dissolved dye that fluoresces in the presence of hydrophobic micelle cores. To execute this experiment, 1,6-diphenyl-1,3,5-hexatriene (DPH) dye was dissolved in tetrahydrofuran at a concentration of 100mM and then diluted in water to a final concentration of 1 μM. Each PA was dissolved in 1 μM DPH solution and serially diluted by half to range from 0.05 μM to 500 μM μM, performed in triplicates for each PA. The dilutions were allowed to equilibrate for one hour while covered with aluminum foil at room temperature and then were transferred to a 96-well plate. Their fluorescence intensity was measured using a Tecan Infinite 200 plate reader (Mannedorf, Switzerland) with an excitation wavelength of 360 nm and an emission wavelength of 430 nm. The data were plotted with a log-transformed concentration. The CMC was identified as the concentration at which the fluorescence value is greater than that of 20% above the zero-slope baseline region.

Cryogenic Transmission Electron Microscopy (Cryo-TEM) Imaging

Cryo-TEM samples were flash-frozen in liquid ethane onto Quantifoil R1.2/1.3 grids (copper, 200 mesh; Q210CR1.3, EMS, Hatfield, PA) using a Vitrobot Mark IV (FEI, Hillsboro, OR). Grids were imaged at 300kV accelerating voltage on a Titan Krios (Thermo Scientific, Hillsboro, OR). The images were processed and measured digitally using ImageJ software.

Analysis of pH-Dependent Phosphate Binding

Samples were prepared in MilliQ water in molar ratios of 1:1, 2:1, and 4:1 of Peptide:PO_4, equivalent to 10 ppm PO_4 using a Na_2HPO_4 salt. The pH was adjusted to the desired pH condition using minimal HCl and NaOH, and the pH was measured using a Fisher Scientific Accumet XL500 pH/ISE/Conductivity Benchtop Meter (Vernon Hills , IL, USA) and a Fisherbrand Accumet Micro Glass Mercury-Free Combination Electrode. Upon reaching the target pH, the solution was filtered using a 13 mm 0.22 μm GHP Acrodisc syringe filter to separate the unbound anions from the PA-anion bound complexes. The filtrate was analyzed using ion chromatography using a Thermo Scientific Dionex ICS-5000+ equipped with a Dionex AS-DV autosampler and using a Dionex IonPac AS22 column (Product No 064141, Thermo Scientific, California, USA). The analysis was run using an eluent of 4.5 mM Sodium Carbonate and 1.4 mM Sodium Bicarbonate (Product No 063965 from Thermo Scientific, California, USA) and a Dionex AERS 500 Carbonate 4 mm Electrolutically Regenerated Suppressor (Product No 085029 from Thermo Scientific, California, USA). The experiments were performed in duplicate for each condition.

Simulation Methods

Atomistic Model. The simulations used the GROningen MAchine for Chemical Simulations (GROMACS) package[122] and the ABF enhanced sampling methods implemented in SSAGES.[123] The PAs were modeled using the CHARMM forcefield[124] and water was modeled using the TIP3P model.[125] Custom force field parameters used for phosphate ions are described in

our previous work.[162] The Lorentz-Berthelot mixing rule was used for unlike non-bonded interactions involving phosphate atoms. Nonbonded interactions were calculated using a 12 Å cutoff distance. Long-range electrostatic interactions were handled using fast smooth Particle-Mesh Ewald (SPME) with a 0.12 nm Fourier spacing.[126,127] Covalent bonds involving hydrogens were constrained using the LINCS algorithm. All simulations were integrated using the leap-frog algorithm with a 2-fs timestep. All temperature-coupling used was Nosé–Hoover thermostat with a time constant of 0.1 ps used to maintain the temperature at 300 K.

Simulations of PA Unimer. The simulation protocol for unimer phosphate binding from ref. 162 is adopted exactly for Filler PA and Binding PA. The two distance CVs used in this work are defined as the following. For Binding PA, d_1 is defined as the distance between the center of mass of the phosphate and the center of mass of {the main chain heavy atoms of SGAGKT and the ε-amino N in lysine}. For Filler PA, d_1 is defined as the distance between the center of mass of the phosphate and the center of mass of the main chain heavy atoms and the ε-amino N in the lysine residue. d_2 is defined as the distance between the center of mass of the phosphate and the center of mass of the main chain heavy atoms of the GGGGG linker. Readers are referred to ref. 162 for detail settings for ABF sampling. Each ABF simulation was carried out with 4 walkers and output was monitored at intervals of 40 ns until the free energy features no longer changed between the two most recent outputs, resulting in 400 ns total simulation time per walker for each pH condition.

Starting Configuration of Multi-Component Micelle. Protocol to generate starting configurations for multi-component micelles is adapted from ref.129. First, nine PA molecules were packed in the x-y plane to form a layer, with the C_{16} tails pointing inwards, and with 40° angle between adjacent chains. To achieve a target composition, a probabilistic criterion was used

to initialize the identity of each PA. For example, to achieve a Filler PA fraction of 0.25, a random number *R* was generated for each PA. The corresponding PA would be initialized as a Filler PA if $R<0.25$. Then, 10 multi-component layers were independently generated and stacked in the z-direction. Phosphate ions were subsequently inserted at random positions avoiding position overlap with the PA molecules. At an PA_{total}:PO_4 ratio of 4:1, each simulation box contains 90 PA chains and 22 phosphate ions. The simulation box was 16 nm in *x* and *y* and 5 nm in *z*. After solvation, sodium or chloride ions were added to neutralize the system.

Simulations of Multi-component Micelles. The starting configuration was first energy-minimized and subsequently equilibrated under NVT ensemble for 4 ns. During the equilibration, harmonic position restraint was applied to the first carbon in the C_{16} group. Subsequently, the position restraint was removed, and the system evolved under NPT ensemble. Anisotropic barostat was used so that the pressure in the *z* direction was coupled independently from that in the *x*-*y* direction. The pressure was maintained at 1.0 bar using Berendsen barostat. The total simulation time was 150 ns for the system. Trajectories collected during the final 50 ns were used for analysis.

Hydrogen Bonding Analysis. The GROMACS hbond tool was used to identify H-bonds formed between PA chains and phosphate ions. The H-bond criterion used a donor-acceptor distance cutoff of 0.38 nm and a hydrogen-donor-acceptor angle cutoff of 45°.[169] Visual Molecular Dynamics (VMD) was used for trajectory visualization.[170]

3.6 Additional Experimental Results and Discussion

Mass Spectroscopy Verification and Purity Analysis using Liquid Chromatography–Mass Spectroscopy (LC-MS).

After purification of the peptide amphiphiles on high performance liquid chromatography (HPLC), the collected fraction containing the purified product was analyzed using LC-MS. The

chromatographs (Figure 3.7) and the mass spectra of the eluted peak (Figure 3.8) indicate that the syntheses were successful (see Table 3.1). The purification achieved greater than 95% purity for both samples (Table 3.2 and Table 3.3).

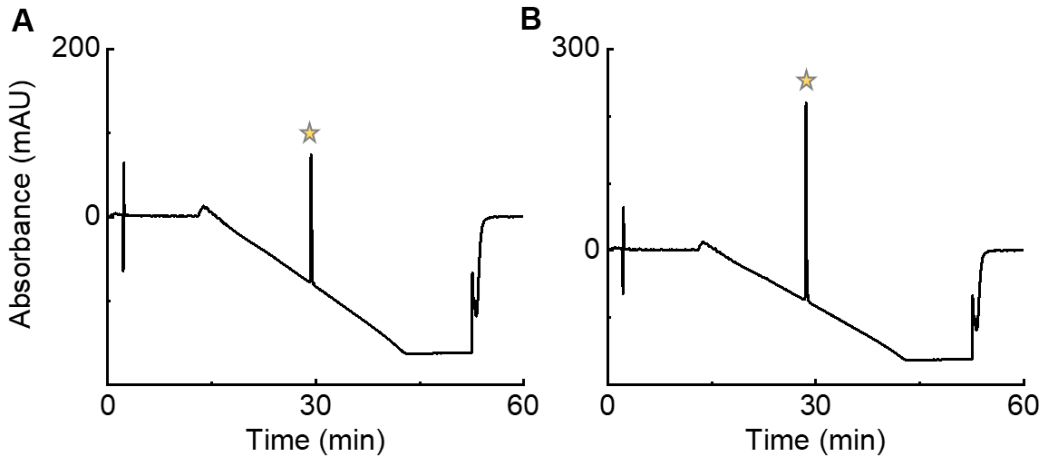

Figure 3.7. LC-MS chromatograph at 220 nm UV absorbance of (A) $C_{16}G_5K$ and(B) $C_{16}G_5$hex. The product elutes in the center peak for each plot.

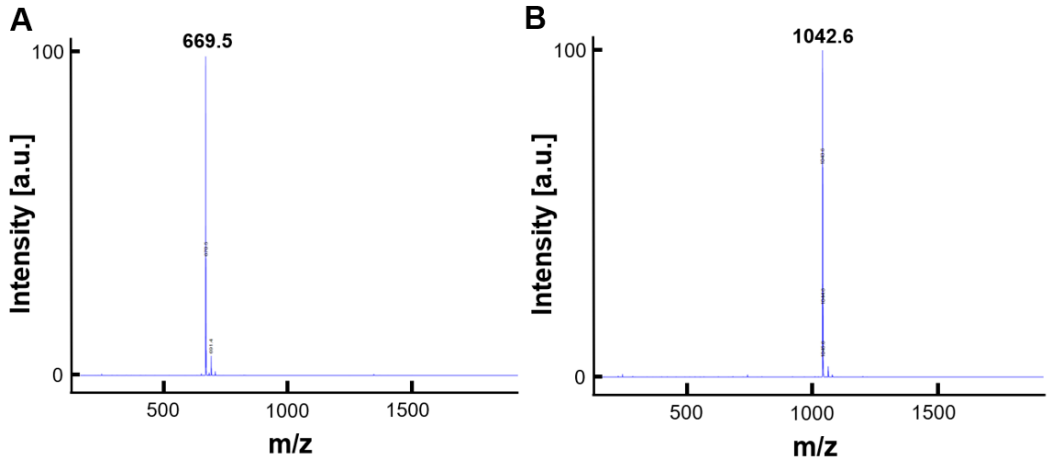

Figure 3.8. The mass spectra at the LC-MS center peak for (A) C16G5K and (B) C16G5hex.

Table 3.1. Theoretical and Experimentally Measured Molecular Weights of Three Peptide Amphiphile (PA) Samples

Sample	Theoretical Molecular Weight (g/mol)	Experimentally Measured Molecular Weight on LC-MS (g/mol)
$C_{16}G_5K$	668.8	669.5
$C_{16}G_5$hex	1042.2	1042.6

Table 3.2. LC-MS Chromatogram peak table for C16G5K

Peak #	Ret. Time [min]	Area [mAU*s]	Height [mAU]	Area [%]
1	14.24228001	30.97977257	1.652881622	2.2%
2	16.94313431	12.77208042	1.306900024	0.9%
3	29.30536842	1386.741699	152.6833344	96.5%
4	29.697752	6.706115246	1.231860876	0.5%
Total		1437.199667	156.8749769	100%

Table 3.3. LC-MS Chromatogram peak table for $C_{16}G_5$hex

Peak #	Ret. Time [min]	Area [mAU*s]	Height [mAU]	Area [%]
1	14.38019	9.962159	1.059084	0.4%
2	14.80785	25.19563	1.346974	1.0%
3	15.5501	28.60013	2.50615	1.2%
4	17.6879	19.15074	1.238985	0.8%
5	28.58741	2364.111	294.5662	96.6%
Total		2447.02	300.72	100%

The confirmed purities of $C_{16}G_5K$ and$C_{16}G_5$hex are 96.5% and 96.6% respectively. This was calculated according to the area of each peak that eluted during the solvent gradient change from water with trifluoroacetic acid to acetonitrile. The area of the peak corresponds to the amount of that product present in the sample.

Critical Micelle Concentration (CMC).

The CMC was calculated as the concentration at which fluorescence begins to increase by greater than 20% above the zero-slope baseline region. This increased fluorescence occurs when 1,6-diphenyl-1,3,5-hexatriene (DPH) dye partitions into hydrophobic cores, indicating micelle formation (Figure 3.9). The CMCs were 2.0 μM and 1.0 μM for C16G5K and C16G5hex, respectively.

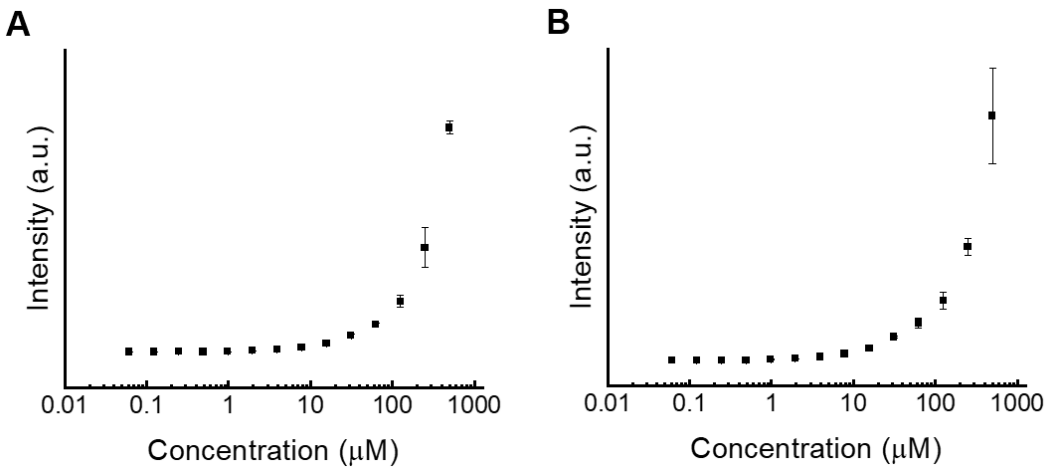

Figure 3.9. The CMC plots of (A) C16G5K and (B) C16G5hex.

Selectivity Results of Multi-Component PA Micelles.

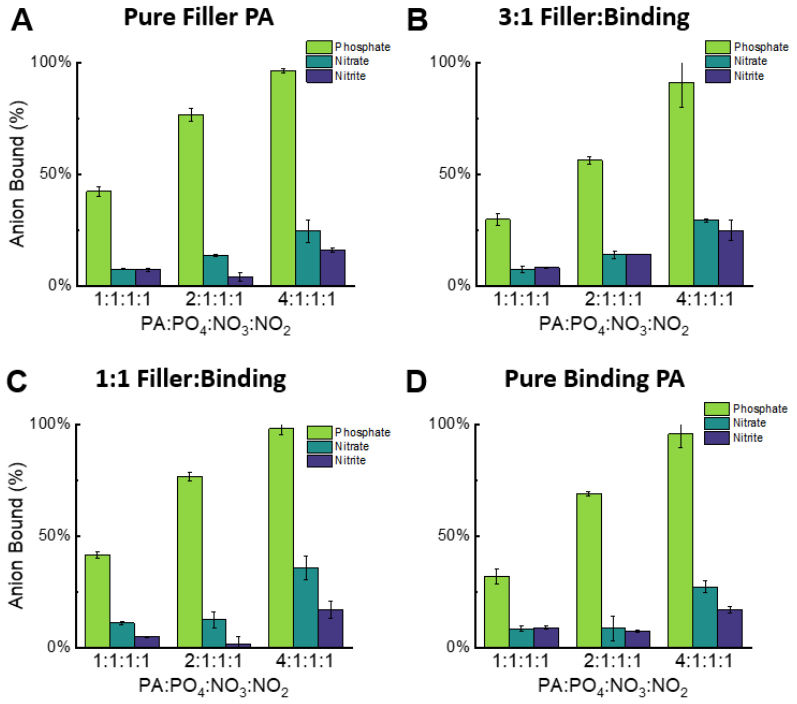

Figure 3.10. Selectivity phosphate-binding results over nitrate and nitrite of four PA micelle systems at pH 6. The phosphate concentration is 10 ppm and the molar ratios of PA:PO4:NO3:NO2 evaluated were 1:1:1:1, 2:1:1:1, and 4:1:1:1. The performance across the systems shows similar trends.

3.7 Additional Simulation Results and Discussion

Snapshot for Phosphate Clustering.

At pH 6, the phosphates are observed to form clusters. We provide here a representative snapshot showing the structure of a cluster, and the hydrogen bonding forming among itself and with surrounding waters. A similar hydrogen-bonding scheme is previously reported.[167]

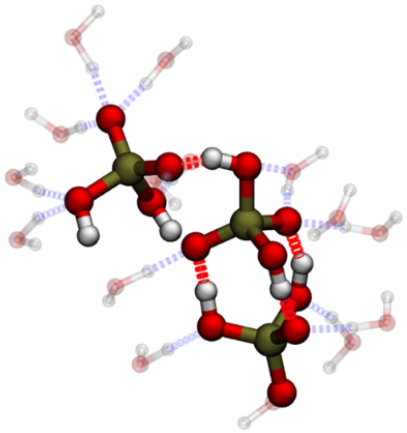

Figure 3.11. Example of a 3-phosphate cluster with surrounding water. Phosphorus atoms are brown, oxygen atoms are red, and hydrogen atoms are white. Hydrogen bonds within the cluster are shown as red dashed bonds, and hydrogen bonds between water and the cluster are shown as blue dashed bonds. To qualify for hydrogen bonds, the donor-acceptor distance is less than 0.3 nm and the donor-H-acceptor angle is less than 20 degrees.

Ramachandran Plots for Binding PA in Micelle

We computed the backbone dihedral conformations for the SGAGKT hexapeptide (P-loop motif) in the Binding PA. The results are obtained at pH6 and at optimized protonation conditions. The composition is 80% Binding PA and 20% Filler PA. We select the 80%-20% composition to show the conformation of Binding PA in the presence of Filler PA, while still providing good statistics. The same analysis was performed for all compositions at both protonation conditions. The qualitative trend is the same across compositions.

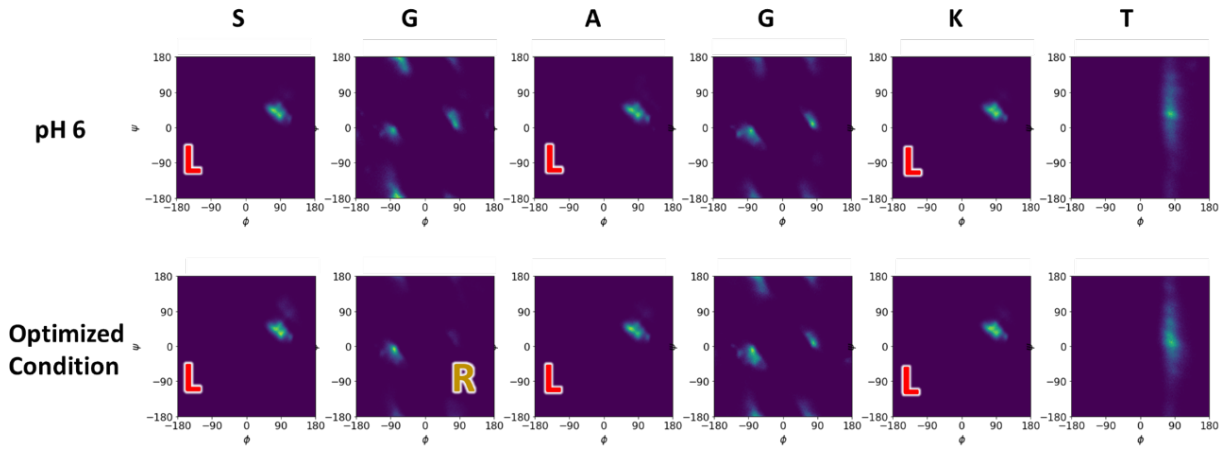

Figure 3.12. Ramachandran plots for the SGAGKT hexapeptide domain in Binding PA in mixed micelle. The nest R and nest L conformations are qualitatively assigned based on the highlight locations.

Hydrogen-Bonding at Different Micelle Locations.

Hydrogen bonds formed between phosphates and the micelle are categorized based on their location micelle. We used five categories to differentiate different contributions to phosphate binding: the “LINKER” refers to the flexible G5 domain; the “TER” refers to the amidated cap at the C-termini; the “HEX-LYS” and “G5K-LYS” refer to the lysine residues in Binding PA and Filler PA, respectively; and “HEX-BB” refer to the SGAGKT hexapeptide. Note that the lysine and amidated C-termini are excluded from the “HEX-BB” category. The first four categories are commonly present in Binding PA and Filler PA, whereas the last category, “HEX-BB”, is unique to Binding PA. The percentages plotted measure the relative importance of each category in phosphate binding.

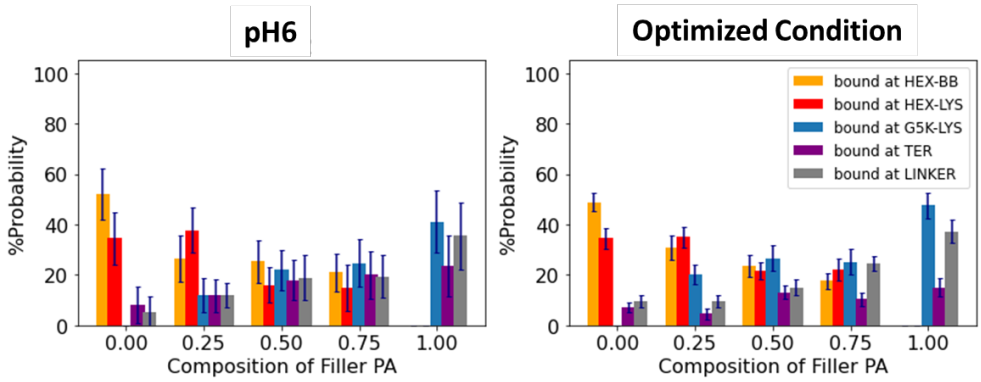

Figure 3.13. Percentage of hydrogen bonds contributed by different locations in the micelle. The error bars are from averaging over 22 phosphate ions in a single simulation.

Binding Motif Analysis at pH 6.

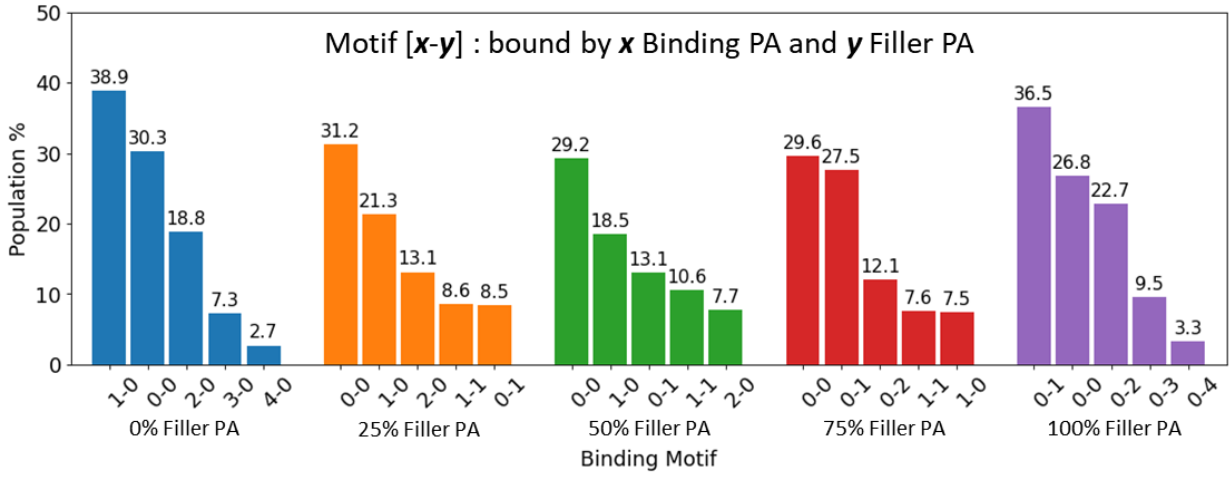

Figure 3.14. The population of top five most-observed binding motifs at the optimized protonation condition.

II TRANSPORT OF LITHIUM IONS IN POLYMER ELECTROLYTES

CHAPTER 4

ROLE OF MOLECULAR ARCHITECTURE MOBILITY ON ION TRANSPORT IN POLY(ETHYLENE OXIDE)-BASED POLYMER ELECTROLYTES

This chapter is modified and reprinted with permission from Deng, C.; Webb, M. A.; Bennington, P.; Sharon, D.; Nealey, P. F.; Patel, S. N.; de Pablo, J. J.. Role of Molecular Architecture on Ion Transport in Ethylene oxide-Based Polymer Electrolytes. Macromolecules 2021, 54, 5, 2266–2276. https://pubs.acs.org/doi/abs/10.1021/acs.macromol.0c02424.

4.1 Abstract

This work aims to develop a detailed mechanistic understanding of the role of a graft polymer architecture on lithium ion (Li^+) transport in poly(ethylene oxide)-based polymer electrolytes. Specifically, we compare Li^+ transport in poly(ethylene oxide) (PEO) versus poly(oligo oxyethylene methacrylate) (POEM) polymers doped with lithium bis(trifluoromethanesulfonyl) (LiTFSI) salts, using both experimental electrochemical characterization and molecular dynamics (MD) simulations. Our results indicate that POEM exhibits a range of relaxation processes that cannot be interpreted solely in terms of glass-transition temperature (T_g) effects. Due to its side-chain architecture, the segmental relaxation of POEM is nonuniform across ether oxygens (EOs) and shows a more pronounced sensitivity to temperature above T_g compared to PEO. Moreover, POEM also exhibits a nonuniform Li^+ coordination behavior, in which Li^+ is primarily solvated by two different chains in POEM, compared to a single chain in PEO. Li^+ transport in POEM occurs *via* two events with distinct characteristic times: a fast intrachain hopping along side chains

and a slow interchain hopping between side chains. Taken together, the relaxation processes and ion transport mechanisms identified in POEM provide useful insights into design of more effective solid polymer electrolytes.

4.2 Introduction

Since the original discovery of poly(ethylene oxide) (PEO) as an ion-conducting electrolyte solvent,[45] solid polymer electrolytes (SPEs) have grown to represent a promising class of electrolyte systems for safe, stable, and cost-effective battery technologies.[49] However, practical implementation of SPEs in Lithium-ion (Li^+) batteries is in part limited by their low ionic conductivity at room temperature.[47] Lithium (Li) salt-doped PEO, an archetypal SPE system, can exhibit conductivities as high as 10^{-3} S cm^{-1} at elevated temperatures, which is adequate for use as a battery electrolyte.[47] That conductivity, however, is temperature-dependent and reduced considerably near room temperature (by as much as four orders of magnitude[47,48,171] due to crystallization of the polymer. Moreover, if one simply extrapolates the conductivity of amorphous PEO to room temperature, the conductivity remains insufficient for practical applications.

Molecular dynamics (MD) simulations have been used extensively in efforts to develop SPEs that overcome some of the drawbacks of PEO, and have helped identify design principles and fundamental structure–function relationships.[50,53,54,66,72,77,89,90,172–180] Previous MD studies have shown that ion transport in SPEs occurs *via* three principal mechanisms: (i) intrachain hopping along the polymer backbone, (ii) interchain hopping from one segment to another, and (iii) codiffusion with short polymer chains (<10,000 g mol^{-1}).[47,49,177,179] In particular, the intrachain and interchain motions between solvation sites have been found to be intrinsically coupled to polymer motion,[54,72,77,177,178,181] ion–polymer coordination, [72] and the connectivity of available ion solvation sites.[77,179,182] Guided by some of the design factors discovered to date, strategies to

improve room-temperature lithium-ion conductivity include disrupting polymer crystallinity, lowering the glass-transition temperature (T_g), and optimizing solvation-site connectivity. Introducing plasticizing additives such as nanoparticles[183,184] and ionic liquids[185] has also improved transport. In parallel, various monomer chemistries have been explored with the aim of facilitating ion transport based on the aforementioned mechanisms, *i.e.*, by altering ion–polymer coordination and solvation-site connectivity.[71,75,77,179,182]

Another promising strategy is to incorporate additional ether oxygens as short side chains, which would inhibit polymer crystallization, provided that relatively short side chains are used.[66,81,186] Such architecture could also allow for a separate optimization of the backbone and side-chain properties and offer a wider palette of available chemistries.[187–196] Past experimental work has shown that single-ion conducting behavior and improved transference numbers can be achieved by attaching anions to the side chains.[197] To date, the majority of experimental studies of branched SPEs have focused on PEO-grafted polymethacrylates[186] and its copolymers.[64,65,80,81,92,93] Poly(oligo oxyethylene methacrylate) (POEM) is a graft polymer where a short PEO oligomer is covalently linked to the ester groups along the methacrylate backbone. POEM is believed to exhibit higher room-temperature conductivity than PEO due to its lack of crystallinity and its lower T_g.[81,186] Unlike PEO and its branched derivatives, which require anionic polymerization,[198] POEM can be synthesized *via* more synthetically flexible controlled radical polymerizations, such as atom transfer radical polymerization (ATRP) and reversible addition–fragmentation chain-transfer (RAFT) polymerization.[80,81] The synthesis approach enables random or block copolymerization with other compounds in a sequence-controlled fashion,[80] thereby providing a vast design space for POEM-based SPE systems.

Although improved ionic conductivity performance has been reported for POEM-based electrolyte systems, a detailed, molecular view of Li^+ transport in these materials is still lacking. The characterization of Li^+ transport in POEM-based SPEs has been primarily pursued experimentally; insights from simulation reports on similar molecules may not be directly applicable to POEM [66,178,199]A few accounts have considered comb-branched poly(epoxide ether) ($PEPE_5$) doped with lithium bis(trifluoromethanesulfonyl) (LiTFSI), where both the backbone and side chain consist of ether segments (Figure 4.1).[66,178] Simulations of $PEPE_5$ identified a disparity in the conformational relaxation timescales of the backbone and side chains and proposed that complexation of Li^+ with the backbone slows ionic transport.[66] In contrast to the branched $PEPE_5$, where the coordinating centers have identical chemistries, the grafted POEM material represents a more complex and richer system because the backbone and side chains no longer share the same chemistry. Although the segmental relaxation behavior found in $PEPE_5$ may be relevant for understanding POEM, whether the ester groups along the POEM backbone influence Li^+ transport or not requires additional research. Webb *et al.* explored a similar idea in a family of polyester-based SPEs, consisting of backbones and short side chains of diverse chemistries selected in a combinatorial fashion.[72] The chemical structure of a representative molecule studied in that work, referred to as polymer 3b, is shown in Figure 4.1. These authors pointed out that in SPE systems with multiple functional groups, the local solvation structures, *i.e.*, the type of chemistries involved in Li^+ coordination and the polymer chain conformations as well as the proximity of viable solvation sites, are important factors for Li^+ transport. As insightful as previous reports have been, there is still a need to collectively establish how the existence of side chains and the disparity in side-chain and backbone chemistries can impact ion solvation and transport mechanisms and whether the influence of side chain and backbone design can be decoupled from each other. To

address that need and in contrast to past studies, we focus on molecules containing short side chains, and we examine the role of functional groups, as opposed to that of side-chain architecture.

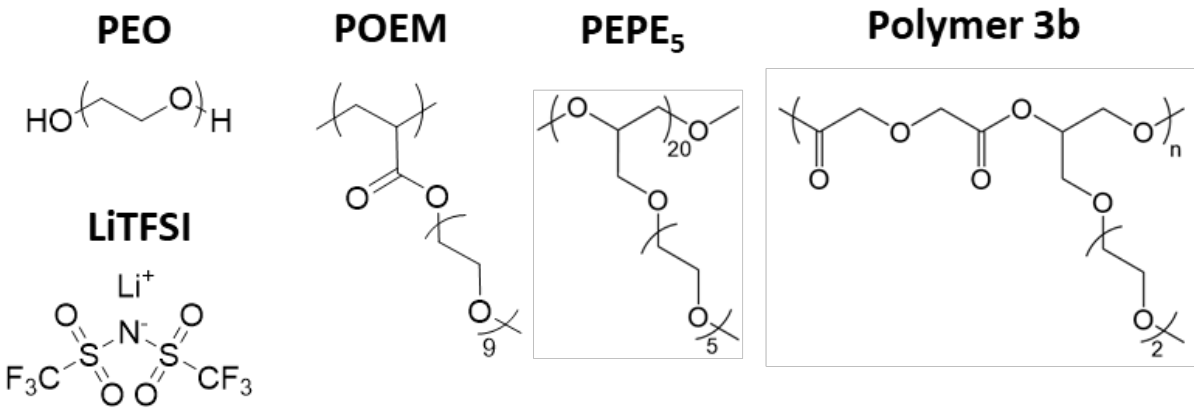

Figure 4.1. Chemical structures of LiTFSI salt and relevant polymers. PEO and POEM are studied in this study. $PEPE_5$ was studied in Ref 66. Polymer 3b was studied in Ref 72. See 4.6 for details on terminal groups.

The goal of this study is to develop a detailed mechanistic understanding of how oligoether side chains in a graft polymer facilitate Li^+ transport and how this differs from the behavior of linear polymers. Specifically, we compare Li^+ transport in PEO and POEM, each blended with LiTFSI, using a combined experimental and computational approach. Electrochemical characterization and MD simulations show excellent agreement with one another, revealing a detailed molecular picture of the role of polymer architecture on ionic conductivity and its temperature dependence. We analyze the segmental mobility and ion solvation behaviors at multiple positions along the side chain. Further analysis of Li^+ solvation environments in terms of residence times is used to explain some key differences in the transport mechanisms of Li^+ between PEO and POEM. Finally, we use our findings to propose generalized design principles for SPEs having a grafted architecture.

4.3 Methods

Materials

PEO was purchased from Polymer Source, Inc. and dried in an argon glovebox antechamber at 50 °C overnight before use. All solvents—acetonitrile (99.8%, anhydrous), toluene, dimethylformamide (DMF), tetrahydrofuran (THF), and hexanes—and 2-cyano-2-propyl dodecyl trithiocarbonate (CPDTC) were purchased from Sigma-Aldrich and used as received. LiTFSI (Sigma, battery grade, >99.95% trace metal basis) was dried at 100 °C under vacuum and stored in an argon glovebox. Azobisisobutyronitrile (AIBN, Sigma) was recrystallized in ethanol before use. Oligo(ethylene oxide) methyl ether methacrylate (OEM_9, M_n = 500 g mol^{-1}) was obtained from Sigma-Aldrich and purified of inhibitor before use by passing through a column of basic alumina.

Synthesis of POEM

POEM was prepared by RAFT polymerization according to Figure 4.7. Five grams (10 mmol) of OEM_9 monomer was placed in a round-bottom flask along with 0.17 g of (0.5 mmol) CPDTC, 8.2 mg (0.05 mmol) of AIBN, and 9.8 mL of DMF. The flask was sealed with a rubber septum, and the solution was sparged with dry N_2 for 30 min. The flask was then placed in an oil bath at 70 °C for 20 h, after which it was quenched in an ice water bath. The crude reaction mixture was concentrated under vacuum and then diluted with THF. The polymer was then precipitated from 10-fold excess hexanes. This purification process was repeated three times. Purified polymer was then dried in a vacuum oven to a constant mass and then further dried under high vacuum for 24 h before storing in an argon glovebox. The number-averaged molecular weight M_n and polydispersity index (PDI) are listed in Table 4.1.

Table 4.1. Properties of PEO and POEM for Simulation and Experiment.

	experiment			simulation	
	$\langle M_n \rangle$ (kDa)	polydispersity index (PDI)	T_g (K)	M_n (kDa)	Fictive T_g (K)[a]

Table 4.1. Properties of PEO and POEM for Simulation and Experiment, Continued.

PEO	20	1.10	223 K	147	262 ± 3 K
POEM	17.7	1.13	216 K	155	2502 K

[a]The standard deviation arises from two independent samples and the selections of fitting ranges for glassy and liquid regions (see 4.6 for details).

Polymer Electrolyte Solution Preparation

Polymer solutions were prepared inside of an argon glovebox by dissolving polymer in either pure acetonitrile or a mixture of acetonitrile and toluene (50/50 v/v). Solutions were heated to 50 °C to help facilitate dissolution of the polymer and then were left stirring overnight. LiTFSI in acetonitrile solutions was prepared in the same manner. Polymer electrolyte solutions were prepared by blending polymer and salt solutions at an appropriate volumetric ratio to obtain a ratio of $r = 0.05 = [\text{LiTFSI}]/[\text{EO}]$.

Characterization

Size Exclusion Chromatography (SEC). Size exclusion chromatography (SEC) measurements were conducted on a Shimadzu Prominence high-performance liquid chromatograph system with THF as the eluent at a flow rate of 1 mL min^{-1}. Separation was achieved using two PLgel MIXED-D columns (Agilent) maintained at ambient temperature. The differential refractive index signal was collected using a Wyatt Optilab T-rEX differential refractometer (λ = 658 nm). Online multiangle light scattering (MALS) measurement was performed using a Wyatt DAWN HELEOS II light scattering detector. Weight-averaged molecular weight and dispersity were determined by MALS using the previously reported refractive index increment for POEM in THF ($dn/dc = 0.073$ mL g^{-1}).[200]

Differential Scanning Calorimetry (DSC). Calorimetric T_g values of neat polymers and polymer electrolytes were determined by DSC using a TA Instruments Discovery 2500 DSC.

Sample pans were prepared in the glovebox by drop casting solutions, heating at 65 °C until dry, and then repeating until 5–10 mg of material was in the pan. The pans were then hermetically sealed before removing from the glovebox to avoid any water adsorption before DSC measurement. Samples were conditioned at 135 °C followed by three cycles of cooling to −85 °C and heating to 135 °C at a scan rate of 10 °C min^{-1}. T_g is reported as the inflection point of the heat flow thermograms taken from the third heating curve.

Ionic Conductivity Measurements. Ionic conductivity was determined by electrochemical impedance spectroscopy (EIS) of polymer electrolyte thin films using interdigitated electrodes (IDEs), as described previously.[201] Briefly, electrolyte solutions were spin cast onto IDEs with geometric parameters $N = 160$ electrodes, $l = 1$ mm of electrode overlap, $w = 2$ μm electrode width, and $d = 8$ μm interelectrode distance. Polymer film height (h) was determined by casting an identical film on a Si wafer and performing ellipsometry (J.A. Woollam alpha-SE ellipsometer). The films were approximately 70 nm thick. EIS measurements were performed on a custom heating stage inside of a nitrogen glovebox using a Gamry 600+ potentiostat. Impedance was measured from 1 MHz to 1 Hz, and the resulting impedance spectrum was fitted to an appropriate equivalent circuit. The extracted film resistance was then used to determine the conductivity by eq. 4.1. All conductivity data are reported as the average of three samples, with error bars representing the standard deviation.

$$\sigma = \frac{d}{R_f(N-1)lh} \tag{4.2}$$

Simulation

For PEO and POEM, a single, long polymer chain with approximately 10,000 interaction sites was employed; the use of a single chain has been adopted in past simulation studies of SPEs

to eliminate the codiffusion of Li^+ with the polymer chain, thereby highlighting the hopping mechanisms that underlie Li^+ transport.[77] The polymers are represented by united atoms, using an adapted TraPPE-UA force field[202–204] that was previously validated to match the density of PEO.[205] The bond stretching spring constants were adopted from generalized CHARMM bonding parameters.[124] Li^+ and $TFSI^-$ are represented by a compatible all-atom model.[59,206] A cutoff radius of 12 Å with van der Waals tail correction was used for short-range nonbonded interactions. Long-range electrostatics were handled using the particle–particle particle–mesh solver[207] with 10^{-4} accuracy.

All simulations were conducted using the LAMMPS package[208] using a velocity Verlet integrator with a 1 fs timestep. Temperature is controlled in NVT simulations using the Nosé–Hoover thermostat with a damping parameter of 100 fs. For NPT simulations, pressure is controlled using the Nosé–Hoover barostat with a damping parameter of 1000 fs. Additional details of the simulation procedures and force field parameters are included in 4.6.

4.4 Results and Discussion

4.4.1 Reduced Li^+ Transport in POEM

The chemical structures of the polymer electrolyte systems considered here are shown in Figure 4.1. POEM repeat units are atactic and have nine ether oxygen (EO) units per side chain. In both experiments and simulations, LiTFSI salt was added to the polymers at a ratio of r = [Li]/[EO] = 0.05. In polyether-based electrolytes, the ionic conductivity and the rate of ion hopping among solvation sites are intrinsically coupled to the segmental dynamics of the polymer matrix.[53,54,77,177,181] In particular, the Vogel–Fulcher–Tammann (VFT) equation has been used to directly relate conductivity to T_g,[80,182,209,210] a common proxy for characterizing segmental dynamics. Table 4.1 lists the T_g values determined *via* DSC and the corresponding fictive

temperatures, which serve as a simulated counterpart for T_g, in PEO and POEM. Additional details on the estimation of fictive temperatures are provided in 4.6. Both simulated and experimental results indicate that POEM has lower T_g than PEO. Note that the absolute value of the simulated fictive temperatures is higher than the corresponding experimental values due to the fast cooling rates employed in simulations.[72]

To mitigate the effects of disparate segmental mobilities between PEO and POEM, the dynamic properties are compared at fixed reduced temperatures ($T - T_g$). Figure 4.2A presents the experimentally determined ionic conductivity of PEO and POEM across a range of temperatures above their respective T_g values. At elevated temperatures, POEM exhibits a lower conductivity than PEO (approximately a factor of two). As temperature decreases, a rapid drop in PEO conductivity is observed, starting 100 K above T_g. This behavior can be attributed to PEO crystallization, which typically happens at about 333 K.[48] At room temperature, POEM has higher conductivity than PEO, as previously reported in the literature.[186] To assess ion diffusion in simulations, we examine the mean-squared displacements (MSDs) of Li^+ in PEO and POEM. The results are shown in Figure 4.2B at various temperatures above their respective fictive temperatures ($T - T_g$ = 50, 150, and 250 K). As shown in Figure 4.2B, although Li^+ does not reach the diffusive regime over the time interval over which the MSD is computed, one can appreciate that Li^+ mobility is slower in POEM than in PEO at all reduced temperatures, which is consistent with our experimental conductivity measurements. In contrast to MSDs at $T - T_g$ = 150 and 250 K, the MSD at $T - T_g$ = 50 K suggests that Li^+ is mostly restricted to their local solvation environment at timescales below 1 ns. In experiments, PEO crystallizes when the temperature is below $T - T_g$ = 100 K; crystallization is not observed in our simulations, likely because our simulations do not reach the timescales required for crystallization to occur.

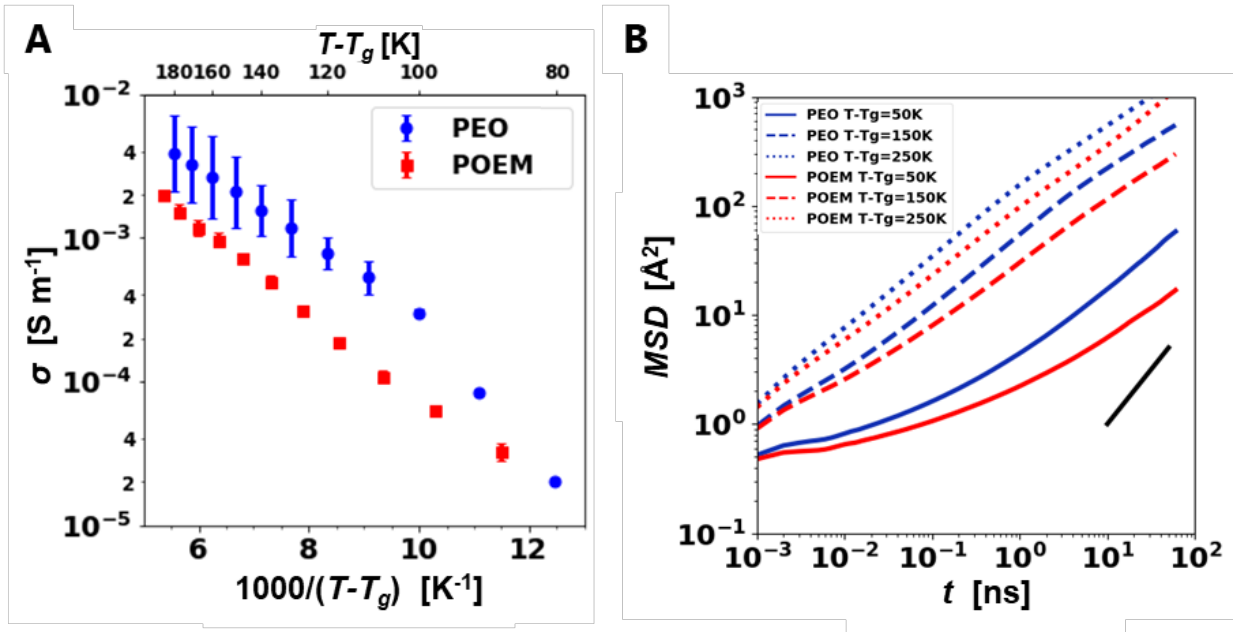

Figure 4.2. Characterization of temperature-dependent ion mobility in PEO and POEM. (A) Experimentally determined temperature-dependent conductivity for $r = 0.05$ electrolytes. (B) Simulated MSD of Li^+ in PEO and POEM at fixed reduced temperatures for $r = 0.05$ electrolytes. The MSD was computed using up to 50 from 120 ns trajectories. The black segment represents a guideline with unit slope.

4.4.2 Heterogenous Li^+ Solvation Behaviors in POEM Due to Graft Architecture

To understand how Li^+ is transported in the material, we begin by characterizing the Li^+ solvation environment. Figure 4.3 presents an analysis of the solvation environment of Li^+ from simulations at $T - T_g = 150$ K. Pair radial distribution functions (RDFs) are computed to characterize the compositions and sizes of solvation shells around Li^+. Figure 4.3A,B shows that the sizes and compositions of the first solvation shells of Li^+ are similar for PEO and POEM. The radius of the first solvation shell is determined to be ca. 3.25 Å. Additionally, the carbonyl oxygen and ester oxygen in the methacrylate groups along the POEM backbone barely affect the solvation environment of Li^+ within 5 Å. Similar observations have been reported for polyester electrolytes.[72] In both plots, the first peaks of Li–O (ether) and Li–O (TFSI) RDFs occur at approximately 1.95 Å, indicating that the first solvation shell consists primarily of EOs and oxygen

atoms from the TFSI anions. The location of the first Li–O (ether) peak is consistent with previous reports.[72,77] In each system, the second peak occurs at approximately 4.5 Å. The first peaks in the Li–O (ester) and Li–O (carbonyl) RDFs occur at approximately 5 and 6 Å, respectively, both beyond the radius of the first solvation shell. Based on the size and composition of the Li^+ first solvation shells identified in Figure 4.3A,B, it is possible to further analyze the solvation shell structures and motifs. Figure 4.3C,D presents snapshots of two prominent Li^+ coordination structures observed in simulations: Li^+ coordinated to a single chain with six contiguous EOs and Li^+ coordinated to two chains, each with three contiguous EOs. The conformations corresponding to each coordination motif agree with those reported before.[50,54,72] The ion-solvating single chain generally adopts a helical conformation, while in the two-chain case, the polymer chains adopt a crisscross conformation. Here, we find that the two types of coordination structures are also found in POEM, which adopts very similar conformations to those found in PEO.

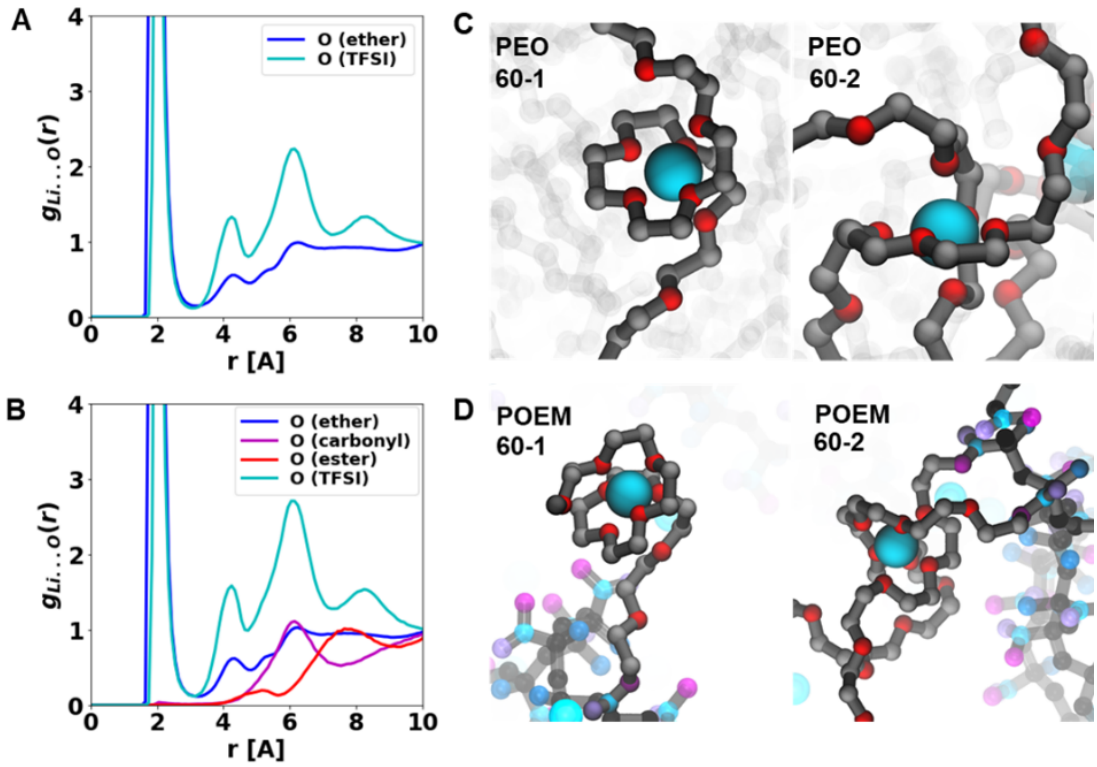

Figure 4.3. Solvation shell compositions and structures in PEO and POEM. Radial distribution functions between Li^+ and oxygen atoms in (A) PEO and (B) POEM at 150 K above T_g. Note that the RDFs are normalized by the concentration of each oxygen type, so the relative heights of the peaks do not necessarily relate to the composition. Representative snapshots for major Li^+ coordination motifs in (C) PEO and in (D) POEM. In panels (C) and (D), the Li^+ atoms are colored cyan, EO atoms are red, and carbon atoms are black. In POEM (panel D), carbonyl oxygens are purple and ester oxygens are magenta; only the side chains involved in solvation are shown, while their neighboring side chains are omitted. The coordination motif in panels (C) and (D) is defined by the counts of different types of oxygen atoms present in the first solvation shell of Li^+ and the number of coordinating chains. The two digits refer to the number of EO atoms and the number of oxygen atoms in the TFSI anion, respectively. The digits following the dash refer to the number of coordinating chains. For example, 60-2 indicates a motif with six EO from two different chains and zero oxygens from TFSI anions. Two oxygens are considered contiguous if they are separated by fewer than two monomers. The presence of each TFSI molecule is treated as a chain.

Although the graft architecture does not alter the chemical makeup and chain conformation of the local Li^+ solvation shell, further analyses of Li^+ coordination motifs and solvation-site connectivity reveal quantitative differences between PEO and POEM. Figure 4.4A presents a breakdown of the population distribution of the Li^+ coordination motifs identified in simulations.

These are categorized based on the number of EO atoms, number of oxygen atoms from TFSI anions, and the number of chains that directly coordinate Li^+; since RDFs show that the ester and carbonyl oxygens along the POEM backbone participate only minimally in ion solvation, they are not used to categorize coordination motifs. In both systems, Li^+ atoms are typically surrounded by 5–6 oxygens, as reported in the literature studies. [50,54,72,175] The major difference between PEO and POEM lies in the relative population of single-chain solvation motifs [60-1] and two-chain solvation motifs [60-2]. Although Figure 4.3C shows that [60-1] and [60-2] motifs adopt the same conformation in PEO and POEM, they arise with different frequencies. In PEO, Li^+ atoms are primarily solvated by six contiguous EOs from the same chain, whereas in POEM, they are more likely to be solvated by oxygens from two different chains. The probabilities that an EO participates in a six-contiguous or a three-contiguous Li^+-solvating sequence have been reported to be similar in PEO at moderate salt concentrations ([Li]/[EO] = 1/15) and high temperatures (450 K).[50] Since each two-chain binding requires two three-contiguous EO segments, a naïve calculation would indicate that single-chain binding is roughly twice as prevalent as two-chain binding in PEO, as shown in Figure 4.4A. For the two-chain binding motif to dominate, as observed in POEM, the three EO segments should be much more prevalent than six EO segments for ion solvation. The varying ion binding behaviors of EOs along POEM side chains appear to explain the abundance of two-chain coordination in POEM.

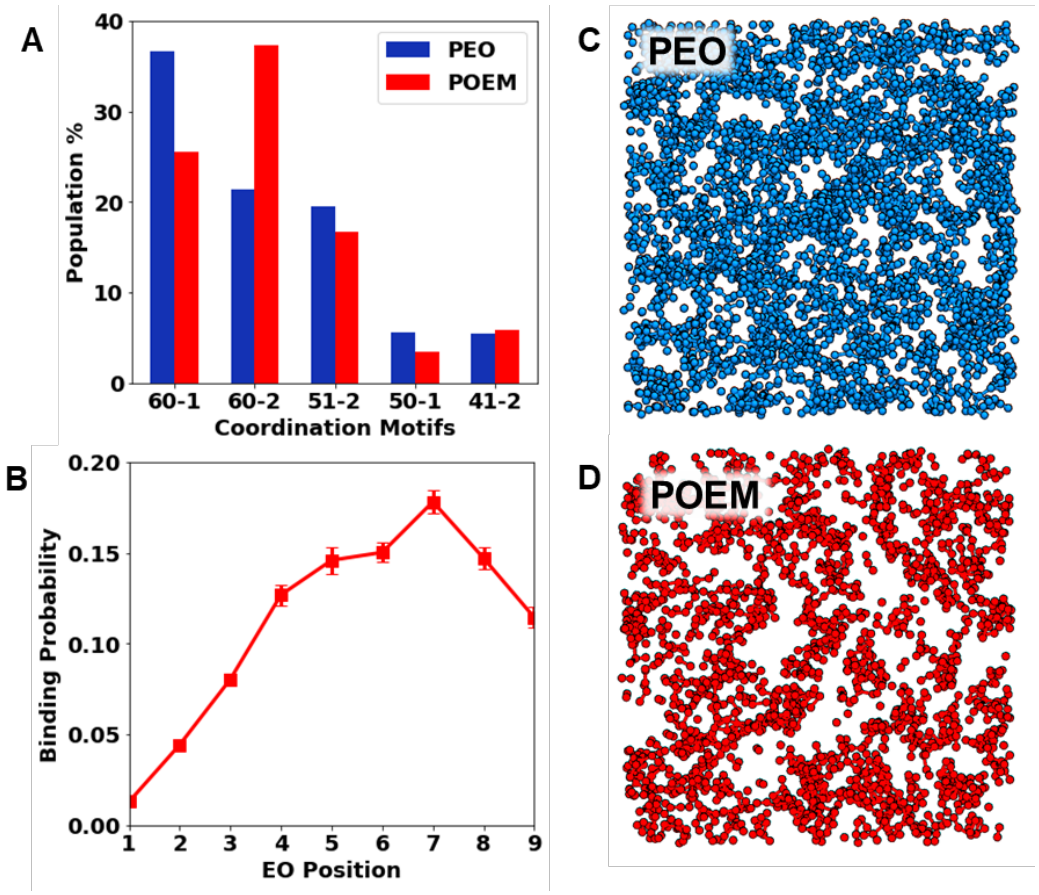

Figure 4.4. Solvation behavior and reduced solvation-site connectivity in PEO and POEM. (A) Population of Li^+ coordination motifs in PEO and POEM at $T - T_g = 150$ K. Only the five most abundant coordination motifs are shown. (B) Binding probability of EOs to Li^+ as a function of the position along a POEM side chain. (C, D) Representative configuration of possible solvation sites in (C) PEO and (D) POEM.

Figure 4.4B presents the Li^+ binding probability of EOs at each position along the POEM side chains. By categorizing the ion-solvating EOs based on their side-chain position, the Li^+ binding probability can be decomposed into the probability of finding an ether O at a particular side-chain position among all of the ion-solvating EOs. Our results indicate that EOs at positions 4–7 participate more frequently in ion solvation compared to those at positions 1–3 and at the chain ends. These findings contrast with past work, which reported that the binding probability decreases monotonically along the side chain in branched $PEPE_5$.[66] This observation was attributed to the fact that Li^+ solvation was most likely to occur in the middle of the chain[50] where there are more

permutations to form contiguous six or three EO solvating segments. In POEM, the EO side chains are grafted onto a backbone that does not contribute to solvation. As a result, for POEM, the maximal solvation probability is instead located in the middle of the side chain. In contrast to linear PEO or branched $PEPE_5$, the ion solvation probability profile along grafted side chains in POEM leads to fewer permutations of six EO solvating segments. Instead, it gives rise to the prevalence of three EO solvating segments and two-chain binding motifs.

Apart from the local solvation environment, the relative proximity of possible solvation sites is also important for Li^+ transport. The concept of solvation-site connectivity has been shown to provide a useful metric to explain differences in Li^+ transport once the effects of segmental mobility are accounted for, which is commonly achieved by correcting for temperature relative to T_g.[77,179,182,211] For consistency, we adopt the same definition and computational procedures to quantify solvation-site connectivity as those employed in previous works.[77,179] The possible solvation sites are defined as the centroid of a set of five or more EOs that are each within 3.7 Å from the centroid. Based on the solvation shell composition found in Figure 4.3A,B, ester oxygens and carbonyl oxygens are excluded when searching for possible solvation sites. We compute a solvation-site connectivity metric as $\kappa = e^{-\langle r_{nn} \rangle}$ (see ref 77 and 4.6 for details) where $\langle r_{nn} \rangle$ is the average nearest-neighbor distance among possible solvation sites; this metric is expected to be proportional to a characteristic hopping rate in a given material. Figure 4.4C,D provides a representative snapshot of possible solvation sites identified in each polymer using this procedure, 150 K above T_g. One can appreciate visually that the solvation sites are more densely distributed in PEO than in POEM. The connectivity κ is found to be $(1.3 \pm 0.14) \times 10^{-3}$ for PEO and $(7.0 \pm 1.2) \times 10^{-4}$ for POEM. This gives rise to a connectivity ratio $\frac{\kappa_{POEM}}{\kappa_{PEO}}$ of 0.55 ± 0.11 at a temperature of 150 K above T_g; solvation-site connectivity results at other temperatures are available in 4.6.

This analysis suggests that POEM forms a less connected solvation site network and that the relative difference in solvation-site connectivity between POEM and PEO is essentially temperature-independent.

4.4.3 Gradient Segmental Mobility in POEM

Figure 4.3 and Figure 4.4 compare structural properties in PEO and POEM at a single temperature; Figure 4.5 examines the temperature dependence of dynamical quantities relevant to Li^+ transport. Figure 4.5A presents the ratio between Li^+ MSD in PEO and that in POEM at three reduced temperatures; for reference, the ratio of solvation-site connectivity between PEO and POEM is also shown. Since Figure 4.2B shows that the motion of Li^+ is not yet diffusive, the ratio of MSD only approximates the diffusivity ratio; this quantity is essentially the ratio of apparent diffusivities, which converge to the true diffusivity in the long-time limit.[77] The position of the dashed lines corresponds to the time-invariant connectivity ratios at the corresponding relative temperatures. If the effect of segmental mobility is accounted for by correcting for T_g, the connectivity ratio should provide a reasonable estimate of the MSD ratio at each temperature. However, Figure 4.5A shows that this is not the case. Although the MSD ratio of POEM to PEO is below unity at all reduced temperatures, consistent with connectivity ratios being also below unity, the asymptotic values of the MSD ratios vary with temperature, while the connectivity ratios remain constant within the uncertainty of our results. In particular, the MSD ratio and connectivity ratio only agree at $T - T_g = 150$ K. Compared with the expected relative ion mobility based on solvation-site connectivity, the transport of Li^+ in POEM is lower at $T - T_g = 50$ K and higher at $T - T_g = 250$ K.

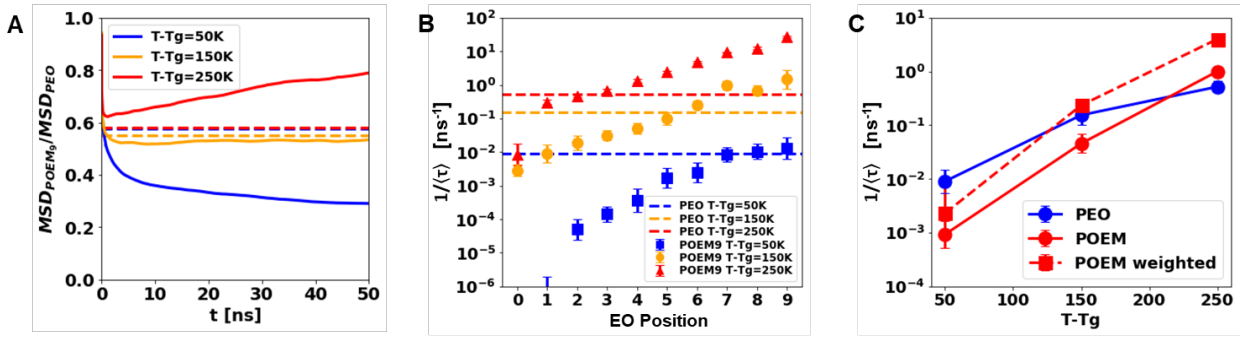

Figure 4.5. Position-dependent relaxation and ion solvation properties of side-chain EOs. (A) Normalized MSD of Li^+ in POEM at fixed $T - T_g$. The dashed lines are ratios of solvation-site connectivity at different temperatures. (B) $1/\langle\tau\rangle$ extracted from BVAFs as a function of the EO position along the POEM side chain at three fixed $T - T_g$ values. The dashed lines are inverse relaxation times ($1/\langle\tau\rangle$) for all EOs in the PEO system at various relative temperatures. An EO position of 1 refers to the EO that is closest to the backbone. The EO position of "0" refers to the $1/\langle\tau\rangle$ calculated for the C–C bonds along the backbone. (C) Average $1/\langle\tau\rangle$ in PEO and POEM and effective $1/\langle\tau\rangle$ for POEM as a function of $T - T_g$. For average $1/\langle\tau\rangle$ values (solid series), a single BVAF is calculated for all EOs in the system. The effective $1/\langle\tau\rangle$ shown by the dashed series refers to a weighted average over separate $1/\langle\tau\rangle$ for each EO position along the POEM side chains. Additional information is provided in 4.6.

To understand why the observed relative ion transport performance deviates from that expected from the solvation-site connectivity at high and low reduced temperatures, we use the bond vector autocorrelation function (BVAF) to directly characterize the local dynamics of the polymers. This function quantifies how rapidly a vector connecting two bonded atoms decorrelates from its initial orientation. In this study, BVAFs are computed for C–O (ether) bonded pairs. Based on the comb architecture of POEM, the EO atoms are analyzed separately based on their position along the side chain. For PEO, the BVAF is computed for all C–O (ether) bonded pairs, and the results are then fitted using a stretched exponential function of the form $\mathrm{BVAF}(t) = e^{-(t/\tau)\beta}$; the mean relaxation time $\langle\tau\rangle$ of a stretched exponential decay is then computed as $\langle\tau\rangle = (\beta/\tau)\Gamma(\beta^{-1})$, where τ is the characteristic relaxation time and β, the stretching parameter, measures the heterogeneity of relaxation processes present in the system. We use the inverse mean relaxation time, $1/\langle\tau\rangle$, as a measure of segmental mobility. Figure 4.5B shows the inverse mean relaxation

times extracted from the BVAF of C–O (ether) bonded pairs at each side-chain position in POEM and compares them to their averaged counterpart in PEO. Unlike T_g, which only provides a single comparison of segmental dynamics between PEO and POEM, the analysis of BVAFs reveals a more nuanced and complicated relaxation behavior in POEM, which is likely governed by two major effects. First, the segmental dynamics varies along the POEM side chain. The relaxation times of different EOs in POEM span approximately three orders of magnitude from the backbone to the side-chain end. A gradient of segmental mobility along side chains has also been reported in other comb architecture polymers.[66] The increased segmental mobility close to the side-chain tail is likely due to the chain ends exploring more free volume. Second, the temperature dependence of segmental dynamics is more pronounced in POEM than in PEO. As temperature increases, the segmental mobility of EOs increases more dramatically in POEM than in PEO. In fact, the mobility of PEO EOs is comparable to that of the fastest ones in POEM at low temperature and comparable only to that of the slowest ones in POEM at high temperatures. It is also worth noting that a drastic change in POEM backbone segmental dynamics is observed as temperature decreases from 150 to 50 K above T_g. Since the glass-transition temperature of PMMA is 381 K,[212] which is approximately 150 K above the T_g of PEO, such a behavior may be attributed to the glassy (below T_g) behavior of a PMMA-like backbone. Although a separate T_g for PMMA is not apparent in our DSC measurements, its nuanced effects are manifest in the BVAF.

In an attempt to summarize the complicated relaxation behavior in POEM into a single, comprehensive metric that reflects Li^+ transport performance, we introduce an effective relaxation time (τ_{eff}) for POEM of the form

$$\log \tau_{eff} = \sum_{i=1}^{9} \log\langle\tau_{EOi}\rangle \cdot P_{bind,EOi} \quad (4.2)$$

where $\langle \tau_{EOi} \rangle$ is the mean BVAF relaxation time of the i-th EO along the side chain and $P_{\text{bind, EO}i}$ is the Li^+ binding probability for the i-th EO. This weighting accounts for the finding in Figure 4.4B that the contribution of EOs to Li^+ transport depends on their position along the side chain. Weighting the EO relaxation times based on their Li^+ binding probabilities emphasizes the segmental dynamics of EOs that more frequently solvate Li^+.

Figure 4.5C compares the "average mobility", obtained in each system from a single, nondiscriminant BVAF for all EOs, with the "weighted mobility", which averages over separate BVAF relaxation times for EO positions along the POEM side chain; here, the mobilities are related to the inverse of the relaxation times. By comparing Figure 4.5A,C, one finds that neither T_g nor the average mobility effectively corrects for the effect of segmental mobility on Li^+ mobility, whereas the weighted mobility is in good agreement with the trends discussed in Figure 4.5A. At $T - T_g = 150$ K, where the alignment between the MSD ratio and connectivity ratio implies a cancellation of the segmental mobility effect, the weighted mobility of POEM is comparable to the average mobility of PEO. At $T - T_g = 50$ K, where the asymptotic value for the MSD ratio is lower than that predicted by the connectivity ratio, the weighted mobility is lower in POEM. The crossover in effective mobility as a function of temperature occurs at 250 K above T_g, at which point Li^+ mobility in POEM surpasses that expected on the basis of solvation-site connectivity.

The concept of effective segmental mobility suggests that when designing for SPEs, solely optimizing for the segmental mobility may not be sufficient. There is another layer of complexity between an increased segmental mobility and an actual improvement in ion transport performance, namely, which part of the system actively participates in the ion transport. One can appreciate that in POEM, the "active", ion-solvating EOs roughly coincide with the EOs that benefit from the

enhanced segmental mobility caused by the side-chain architecture. The methacrylate backbone, although it exhibits orders of magnitude slower relaxations, does not participate in Li^+ solvation and thereby barely affects the effective segmental mobility. As a result, at $T - T_g = 150$ K, for example, segmental mobility effects on Li^+ transport seem to be on a par between PEO and POEM, while a comparison of their average mobilities would underestimate the Li^+ transport performance in POEM.

In contrast, such synergy between relaxation and solvation behaviors in POEM is not found in the comb-branched $PEPE_5$ system. As discussed above, Li^+ was found to most likely coordinate with the slowly relaxing backbone. Therefore, although a similar increase in segmental mobility along side chains was observed, Li^+ transport in that system did not take advantage of the increased segmental mobility.[66]

4.4.4 Two Distinct Li^+ Transport Mechanisms in POEM

Apart from the difference in solvation-site connectivity and the position-dependent Li^+ binding probability shown in Figure 4.4, the population of coordination motifs is also an important factor for Li^+ transport. As pointed out in previous works, the abundancy of single-chain solvation motifs in PEO is associated with enhanced intrachain ion hopping.[72,177] To characterize how a difference in ion solvation motifs influences ion hopping mechanisms, past literature reports have relied on detailed analyses of various autocorrelation functions of the ion coordination environment (CACF).[213–216] Here, we compute the CACF for Li^+ to quantify the characteristic time for a Li^+ to escape from its current coordination environment. In this study, the CACF is defined as

$$\mathrm{CACF}(t) = \langle \frac{|S(t) \cap S(0)|}{|S(0)|} \cdot 1_{[\text{hopping mechanism}]} \rangle, \tag{4.3}$$

where S(t) denotes the set of atoms present in the first solvation shell of a Li^+, $\cap$ refers to the intersection operator, |...| is the cardinality of the set, 1[...] is the indicator function, and $\langle ... \rangle$ denotes

an ensemble average over time origins and Li^+ instances. Two types of conditions are used for the indicator function. In the first calculation, the average includes decorrelation of solvation environments due to any type of hopping mechanism. The second calculation highlights the decorrelation of the ion solvation environment via only interchain hopping; the indicator function for interchain hopping is evaluated based on whether the newly associated (or disassociated) oxygen is noncontiguous with the rest of the solvation shell members. Figure 4.6 shows the resulting CACF. Overall, a comparison of the two polymer systems indicates that both hopping modes decay faster in PEO than in POEM, which is consistent with the observation that the solvation-site connectivity is higher in PEO. However, closer inspection reveals distinctive Li^+ hopping mechanisms in POEM. The CACF can be treated as a stretched exponential, which is often conceptualized as a linear superposition of simple exponential decays with different characteristic times. As discussed in 4.6, the stretching parameters, β, for POEM are 0.5 and 0.8 for overall hopping CACF and interchain hopping CACF, respectively. The corresponding β parameters in PEO are 0.3 and 0.4, respectively, which is indicative of a more heterogeneous distribution of decay modes in PEO. Such features can also be identified based on the shape of the decay curve. The interchain hopping CACF in POEM appears to be linear on a semilog plot, i.e., it suggests that interchain hopping in POEM is dominated by a single exponential decay mode. The overall hopping CACF in POEM appears to exhibit two linear regions with different slopes. The first linear region decays from 1 to 0.8 with a steep slope. The second linear region is parallel to the interchain hopping curve, decaying in the same manner as the interchain hopping CACF.

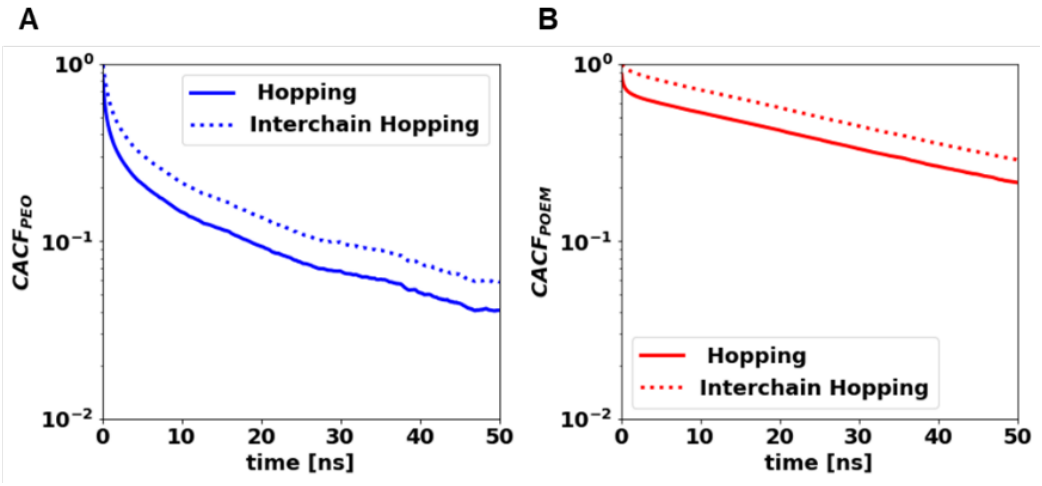

Figure 4.6. Comparison of CACF in PEO and POEM. Coordination autocorrelation (CACF) for hopping and interchain hopping in PEO and POEM at 250 K above T_g.

This result can be explained by noting that the decorrelation of ion coordination in POEM occurs through two types of events. One is the intrachain hopping along short side chains, which has a short characteristic time and makes only a small contribution to the decay. The other is interchain hopping from one side chain to another, which is associated with a longer characteristic time and has the major contribution to the decorrelation of the Li^+ solvation environment. Because the POEM backbone does not participate in Li solvation, the ion cannot migrate from one side chain to another by hopping along the backbone. Due to the side-chain architecture of POEM, these two events are distinct and occur over separate timescales. The separation of timescales and distinct decay modes are not present in the CACFs for PEO, where the concave decay reflects a superposition of a wide range of simple exponential decay modes. This can be rationalized by the fact that in PEO, the intrachain hopping of Li^+ is less limited by chain length; many types of intrachain and interchain hopping events, with a wide range of timescales, contribute to ion transport. Since distinctive ion hopping modes in POEM are a direct result of the graft architecture, there are opportunities to improve ion hopping in graft SPEs by controlling the architecture. These findings suggest that such effort can be decomposed into increasing the contribution of the

intrachain hopping and improving the rate of interchain hopping. Since the side-chain length determines the extent of intrachain hopping, varying the side-chain length could potentially increase the contribution of intrachain hopping. The rate of interchain hopping is associated with solvation-site connectivity, (18) which in graft polymers can be affected by the exclusion volume occupied by the backbone. Therefore, manipulating the backbone chemistry and graft density could potentially enhance interchain hopping.

4.5 Conclusion

In this work, Li^+ transport in PEO–LiTFSI and POEM–LiTFSI systems has been compared *via* experiments and MD simulations. Simulations and experiments both indicate that POEM exhibits slower ion transport than amorphous PEO above the crystalline melting point of the PEO (ca. 333 K). The observed relative differences in ionic conductivity cannot be adequately explained by differences in T_g or in terms of solvation-site connectivity. Instead, we find that the graft architecture of POEM leads to nonuniform, position-dependent relaxation and ion solvation behaviors along the side chain, where the relevant segmental mobility in POEM is not fully captured by its glass transition. First, in addition to confirming the previously reported observation[66] that the relaxation times span a few orders of magnitude along the side chain, we find that the segmental relaxation in POEM is much more sensitive to temperature than in PEO. Moreover, EOs along the side chain contribute differently to ion solvation. The ion solvation probability is the highest for EOs in the center of the side chain, while it drops for EOs at both ends. In contrast to the behavior of the $PEPE_5$ system, where Li^+ tends to be solvated by backbone EOs,[66] in POEM, Li^+ solvation is localized on the relatively mobile side chains instead of the slow backbone. By combining the position-dependent relaxation and ion solvation behaviors in POEM, the effect of segmental dynamics on Li^+ mobility can be quantified using an effective relaxation

time, averaged over different positions along the side chain, and weighted by the corresponding ion solvation probability. The effective relaxation time explains the discrepancy between the relative performance suggested *via* solvation-site connectivity and that characterized by the MSD ratios. This finding also suggests that the solvation-site connectivity, although first used for describing ion transport performance[77] in linear polymer systems, is also applicable for graft polymers, provided that the effect of segmental dynamics is correctly accounted for using an effective relaxation time. Importantly, when designing for SPEs, segmental mobility and effective ion solvation participation should be considered collectively.

Characterization of the solvation environment reveals that, although PEO and POEM share the same set of coordination motifs and typical coordination conformations, the population distributions of these motifs are different. In PEO, Li^+ atoms tend to be solvated by a single contiguous chain, whereas they are usually solvated by two different chains in POEM. The relative abundance of six and three contiguous Li^+-solvating EO segments is closely related to the inhomogeneous ion solvation behavior of EOs along the POEM side chains. Further analysis of the decorrelation of solvation sites shows that ion transport in POEM occurs *via* two events with distinct characteristic times. The intrachain hopping along side chains has a short characteristic time but makes a minor contribution. The interchain hopping between side chains has a longer characteristic time and is responsible for the major contribution to ion hopping. The newly acquired understanding of relaxation behavior, ion solvation behavior, and ion transport mechanisms in POEM presented here provides useful insights into the design of future SPEs. Having identified that the relaxation and ion solvation behaviors vary along the side chain, our future studies of graft SPEs will focus on side-chain length and composition as an important design parameter. Indeed, based on the ion transport mechanisms identified here, tuning side-chain length

and chemistry could potentially improve the contributions of the fast intrachain hopping, and tuning the backbone chemistry and grafting density could potentially impact the rate of interchain hopping.

4.6 Supporting Information

Synthesis of POEM$_9$

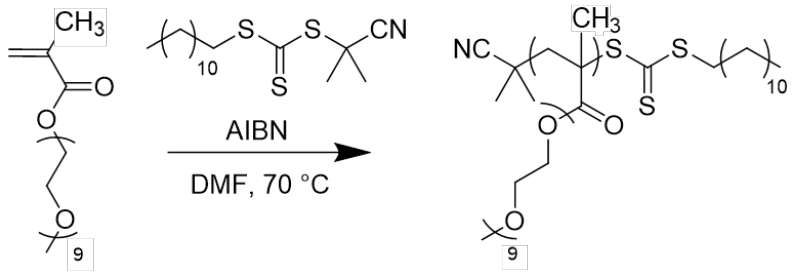

Figure 4.7. Reaction scheme for RAFT polymerization of homopolymer POEM9.

SEC Characterization

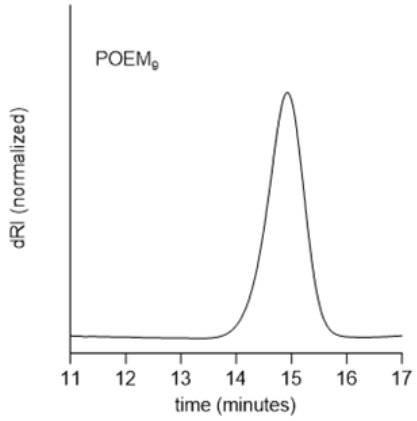

Figure 4.8. Differential refractive index (dRI) vs. elution time data taken from SEC-MALS measurements of synthesized polymers in THF. Molecular weight and dispersity are taken from this data assuming a differential refractive index of dn/dc = 0.073 mL g-1.

DSC Thermograms

Calorimetric T_g of neat polymers and polymer electrolytes were determined by DSC using a TA Instruments Discovery 2500 DSC. T_g is reported as the inflection point of the heat flow thermograms taken from the third heating curve shown in Figure 4.9.

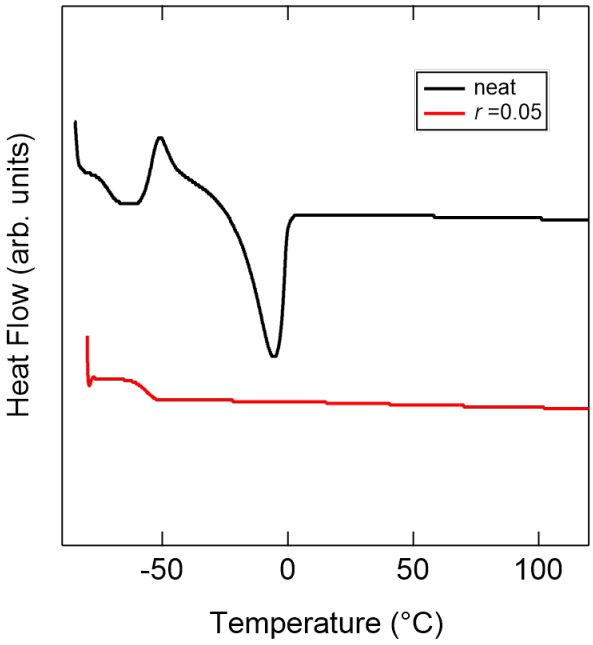

Figure 4.9. DSC thermograms of neat and r = 0.05 POEM samples. These curves represent the third heating cycle, and T_g is taken as the midpoint in the inflection in the heat flow rate.

Force Field Parameters for Molecular Dynamics Simulations

In this study, the TraPPE-UA force field[202–204] is used for all inter- and intramolecular interactions between polymer atoms. Instead of rigid bonds used in TraPPE-UA force field, the generalized CHARMM bonding parameters are used.[124] Parameters for the lithium cation are adapted from a previous simulation study.[59] Figure 4.10 provides reference labels for the different atom types in polymer for assigning the appropriate force field parameters.

United Atom Model: Terminal Groups, Tacticity, and Atom Type Assignments

The PEO chain has 3333 monomers (146.8k g mol^{-1}). The POEM chain has 300 monomers (155.4k g mol^{-1}). For PEO, the termini at both ends are methoxy end groups as noted in (OET-CE3) in Figure 4.10. For POEM, the termini at both ends are CH3 that are connected to a CT interaction site. POEM is this study is atactic. When generating the atactic POEM chain, the stereochemistry of each chiral center is randomly chosen as S or R with equal probability.

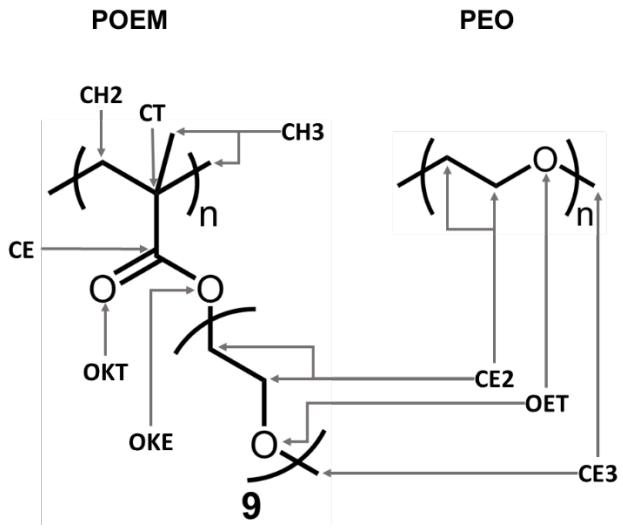

Figure 4.10. Reference labels for atom types in force field parameters.

Non-bonded Interaction Parameters

The nonbonded interactions include Lennard-Jones interactions and Coulombic interactions. For united atoms i and j, their nonbonded interaction is:

$$u_{nb}(r_{ij}) = 4\varepsilon_{ij}\left[\left(\frac{\sigma_{ij}}{r_{ij}}\right)^{12} - \left(\frac{\sigma_{ij}}{r_{ij}}\right)^{6}\right] + \frac{q_i q_j}{4\pi\epsilon_0 r_{ij}}, \tag{4.4}$$

where r_{ij} is the separation distance between atoms i and j, σ_{ij} is the Lennard-Jones diameter, ε_{ij} is the Lennard-Jones interaction strength, ϵ_0 is the vacuum permittivity. q_i and q_j are the partial charges of atoms i and j.

LJ interactions are computed with Lorentz-Berthelot mixing rules. For 1-2, 1-3, and 1-4 bonded interaction sites, the Lennard-Jones interactions are turned off. Coulomb interactions are turned off for 1-2 and 1-3 bonded interaction sites, and scaled by 0.5 for 1-4 bonded interactions. The non-bonded interaction parameters are listed in Table 4.2.

Table 4.2. Nonbonded interaction potential parameters for polymer atoms.

atom	m (amu)	σ_{ii} (Å)	ϵ_{ii} ($\frac{\text{kcal}}{\text{mol}}$)	q (e)

Table 4.2. Nonbonded interaction potential parameters for polymer atoms, continued.

CE2	14.027	3.950	0.091411	0.25
CE3	15.035	3.750	0.194746	0.25
OET	15.999	2.850	0.109296	-0.50
CH2	14.027	3.950	0.091411	0.00
CH3	15.035	3.750	0.194746	0.00
CT	12.011	6.400	0.000994	0.05
CE	12.011	3.820	0.079488	0.55
OKT	15.999	3.050	0.156989	-0.45
OKE	15.999	2.800	0.109296	-0.40

Bonding Potential Parameters

1-2 bonded united atoms interact via a harmonic bonding potential in the form:

$$u_{bond}(r_{ij}) = k_{bond}(r_{ij} - {r_{ij}}^{(0)})^2, \tag{4.5}$$

where r_{ij} is the separation distance between atoms i and j, k_{bond} is the force constant and ${r_{ij}}^{(0)}$ is the equilibrium bond length. The bonding interaction parameters are listed in Table 4.3.

Table 4.3. Bonding potential parameters for polymer atoms

bond	k_{bond} ($\frac{\text{kcal}}{\text{mol}\cdot\text{Å}^2}$)	${r_{ij}}^{(0)}$ (Å)	bond	k_{bond} ($\frac{\text{kcal}}{\text{mol}\cdot\text{Å}^2}$)	${r_{ij}}^{(0)}$ (Å)
CE2-CE2	225.0	1.54	CE2-OKE	360.0	1.41
CE2-OET	360.0	1.41	CE-CT	200.0	1.52
CE3-OET	360.0	1.41	CE-OKT	360.0	1.20
CH3-CT	225.0	1.54	CE-OKE	360.0	1.34
CH2-CT	225.0	1.54	CH2-CH2	225.0	1.54

Bending Potential Parameters

1-2-3 bonded united atoms interact via a harmonic bending potential in the form:

$$u_{bend}(\theta_{ijk}) = k_{bend}(\theta_{ijk} - {\theta_{ijk}}^{(0)})^2, \tag{4.6}$$

where k_{bend} is the force constant, θ_{ijk} is the angle between united atoms i, j, and k, and ${\theta_{ijk}}^{(0)}$ is the equilibrium angle. The bending interaction parameters are listed in Table 4.4.

Table 4.4. Bending potential parameters for polymer atoms

bend	k_{bend} ($\frac{\text{kcal}}{\text{mol·rad}^2}$)	${\theta_{ijk}}^{(0)}$ (Å)	bend	k_{bend} ($\frac{\text{kcal}}{\text{mol·rad}^2}$)	${\theta_{ijk}}^{(0)}$ (Å)
CE2-OET-CE2	60.0136	112.0	OKT-CE2-CE2	49.9782	112.0
CE2-OET-CE3	60.0136	112.0	CH2-CT-CE	62.1000	109.5
CE2-CE2-OET	49.9782	112.0	CT-CE-OKT	62.1000	125.0
CH2-CT-CH2	62.1000	109.5	CT-CE-OKE	70.1483	110.0
CH3-CT-CH2	62.1000	109.5	CH3-CT-CE	62.1000	109.5
CT-CH2-CT	62.1000	114.0	CH3-CT-CH3	62.1000	109.5
CE-OKE-CE2	62.1000	115.0	OKE-CE2-CE2	49.9782	112.0
OKT-CE-OKE	62.1000	125.0			

Torsional Potential Parameters

The torsional potentials for 1-2-3-4 bonded united atoms take the form:

$$u_{tors}(\phi_{ijkl}) = \frac{K_1}{2}[1 + \cos(\phi_{ijkl})] + \frac{K_2}{2}[1 - \cos(2\phi_{ijkl})] + \frac{K_3}{2}[1 + \cos(3\phi_{ijkl})] + \frac{K_4}{2}[1 - \cos(4\phi_{ijkl})], \tag{4.7}$$

where c_1, c_2, and c_3 are coefficients and ϕ_{ijkl} is the dihedral angle defined by atoms i, j, k, and l. The torsional interaction parameters are listed in Table 4.5.

Table 4.5. Torsional potential parameters for polymer atoms

torsion	K_1 ($\frac{\text{kcal}}{\text{mol}}$)	K_2 ($\frac{\text{kcal}}{\text{mol}}$)	K_3 ($\frac{\text{kcal}}{\text{mol}}$)	K_4 ($\frac{\text{kcal}}{\text{mol}}$)
OKE-CE2-CE2-OET	1.888000	-1.888000	0.000000	0.000000
OET-CE2-CE2-OET	1.888000	-1.888000	0.000000	0.000000
CE2-CE2-OET-CE2	2.882840	-0.650809	2.218510	0.000000
CE2-CE2-OET-CE3	2.882840	-0.650809	2.218510	0.000000
CH3-CT-CH2-CT	0.000000	0.000000	1.833350	0.000000
CH2-CT-CH2-CT	0.000000	0.000000	1.833350	0.000000
CT-CH2-CT-CE	0.000000	0.000000	1.833350	0.000000
CH3-CT-CE-OKT	-0.919280	0.229880	-0.609280	0.000000
CH2-CT-CE-OKT	-0.919280	0.229880	-0.609280	0.000000
CH3-CT-CE-OKE	0.915310	0.216840	0.609670	0.000000
CH2-CT-CE-OKE	0.915310	0.216840	0.609670	0.000000
CT-CE-OKE-CE2	9.689610	7.678560	1.387070	0.000000
CE-OKE-CE2-CE2	-2.988080	2.142010	-0.087834	0.203768
OKT-CE-OKE-CE2	-9.669740	7.376500	-1.045270	0.000000

Simulation Protocol

To prepare the starting configuration, a single polymer chain with approximately 10,000 interaction sites is initiated in a large box. The polymer chain is first relaxed under NVT ensemble at 500 K for 30 ns. Then a 20 ns NPT equilibration at 500 K and 1 bar is performed to ensure the density does not drift. The process of introduction of Li^+ is as follows: Li^+ and $TFSI^-$ ions are introduced at random positions in the equilibrated neat polymer at the designated ratio of $r = 0.05$ = [LiTFSI]/[EO]. To remove any steric clashes in the simulation cell, the system is relaxed under

NVE ensemble for 10,000 steps, where the maximum displacement of an atom is limited to 0.1 Å per step. The system is subsequently equilibrated for 15 ns under NPT at 400 K and 1 bar.

To perform simulation at each temperature, the salt-doped polymer is equilibrated at the designated temperature under NPT for 10 ns. Then the system is further equilibrated for 10 ns under NVT ensemble. In the beginning of this NVT equilibration, the box size is scaled to reflect the ensemble average density during at the last 3 ns of NPT equilibration. Then, the trajectory for analysis is collected from a 100-ns production simulation under NVT ensemble.

Fictive Temperature Determination

To determine the fictive temperature, the polymer is cooled from 400 K to 100 K at a cooling rate of 10 K/ns at 1 bar. The density is plotted as a function of temperature under NPT ensemble. Two linear segments are fitted to for the glass and liquid region respectively. The T_g is determined as the intercept of the extrapolated linear fit lines. This procedure to calculate T_g is sensitive to the fitting range of the two segments. Therefore, the end points of the fitting segments are systematically sampled in the following manner. The starting point of the glassy segment was fixed at 50 K, while the end point of the glassy segment was randomly sampled between 180 K and 200 K. Similarly, the starting point of the liquid segment was fixed at 400 K, whereas the end point of the liquid segment was sampled between 300 K and 320 K. The fitting intervals for the glassy segment and the liquid segment are randomly drawn within the sampling interval defined above, the intersections between which yield a set of T_g values. Only T_g values that fall between the end points of fitting segments are kept. The T_g calculation described above was repeated for another independent sample. For each sample, combinations of glassy and liquid fitting ranges are generated 10,000 times. The mean and standard deviation of the set of T_g values collected from

both samples are reported. Figure 4.11 includes the cooling curve and the distribution of resulting T_g values collected.

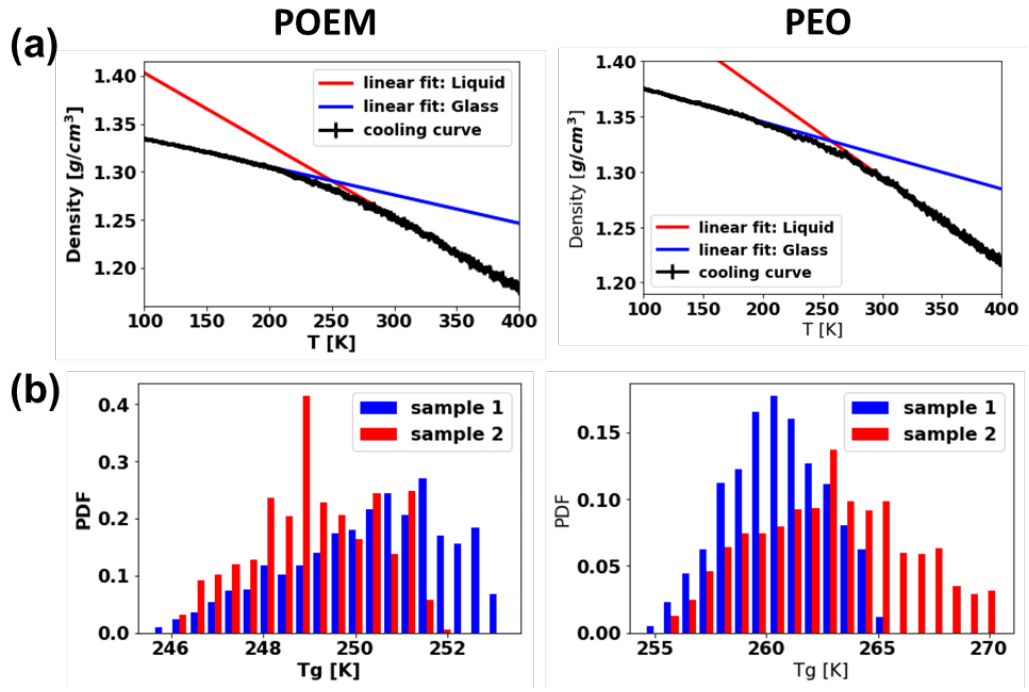

Figure 4.11. Fictive temperatures in simulations. (a) Representative density as a function of temperature. Example fitting lines for liquid and glassy regions are shown in red and blue, respectively. The fitting range for the example linear fits are [100 K,200 K] for the glassy region and [300 K,400 K] for the liquid region. (b) Normalized histograms of collected T_g values. Histograms from different samples are plotted in different colors.

Solvation-site Connectivity

The solvation-site connectivity is calculated as:

$$\kappa = e^{-\langle r_{nn} \rangle}, \tag{4.8}$$

where $\langle r_{nn} \rangle$ is the average nearest neighbor distances among possible solvation sites.[77,179] The values for solvation-site connectivity for POEM and PEO and their respective ratio are listed in Table 4.6 at each reduced temperature. The mean and uncertainty in solvation-site connectivity are obtained by averaging over 100 frames sampled from each trajectory.

Table 4.6. Solvation-site connectivity values for PEO and POEM at T-T_g = 50, 150, and 250 K.

	T-T_g = 50 K	T-T_g = 150 K	T-T_g = 250 K
κ_{PEO}	(1.8±0.19) ×10^{-3}	(1.3±0.14) ×10^{-3}	(8.9±1.2) ×10^{-4}
κ_{POEM}	(1.1±0.15) ×10^{-3}	(7.0±1.2) ×10^{-4}	(5.2±0.91) ×10^{-4}
$\frac{\kappa_{POEM}}{\kappa_{PEO}}$	0.58 ± 0.10	0.55 ± 0.11	0.58 ± 0.13

Bond Vector Autocorrelation Functions

BVAF Averaged Over All Ether Oxygens. Mean relaxation times plotted in Figure 4.3D (solid blue and red lines) are obtained by computing the first moment of the stretched exponential decay fitted to the BVAFs. In each system, this BVAF is calculated for all C-O(ether) bond vectors regardless of the EO positions. Figure 4.12 shows the original BVAFs and the corresponding stretched exponential fits.

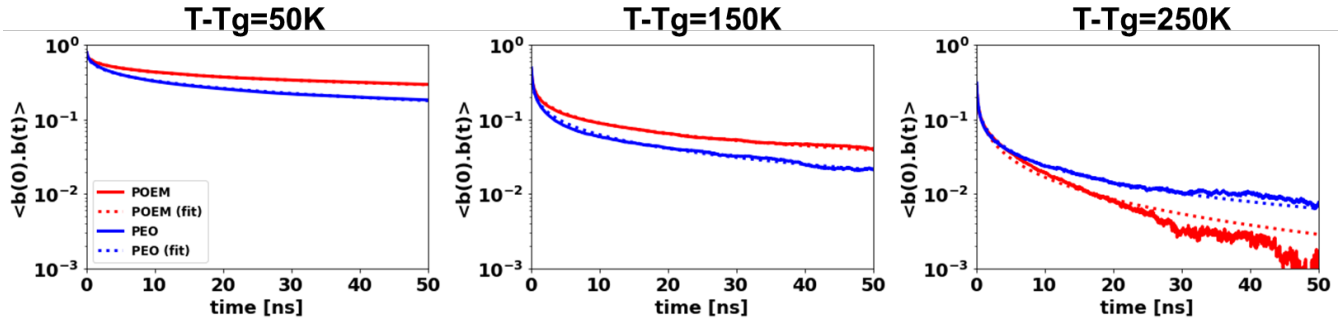

Figure 4.12: Bond vector autocorrelation functions (BVAF) for ether oxygens in PEO and POEM and corresponding stretched exponential fitting lines at fixed reduced temperatures (50 K, 150 K, and 250 K above T_g).

BVAFs of Ether Oxygens Along Sidechain. Mean relaxation times plotted in Figure 4.3B (scattered points) are obtained by computing the first moment of the stretched exponential decay fitted to the BVAFs of ether oxygens at each position along the sidechain. Figure 4.13 shows the original BVAFs. For clarity, the stretched exponential fits are omitted.

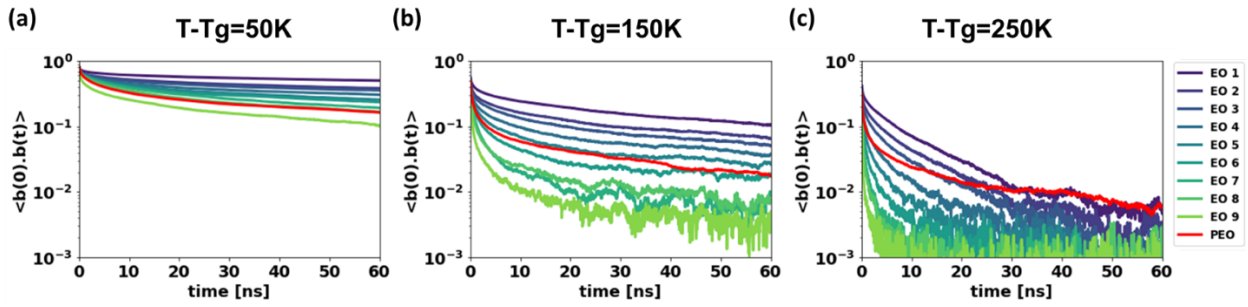

Figure 4.13: Bond rotation autocorrelation of different ether oxygen along the POEM side chains. EO 1 corresponds to the ether oxygens that are closest to the backbone. EO 9 corresponds to oxygens that are at the tail of the sidechains. For reference, the red line is the bond rotation autocorrelation function averaged over all ether oxygens in PEO system. The temperatures are 50 K, 150 K, and 250 K above T_g respectively.

Fitting Parameters for Coordination Autocorrelation Functions

Table 4.7. Stretched exponential fitting parameters for CACF

CACF	β	τ (ns)	$\langle\tau\rangle$ (ns)
PEO combined	0.33	1.38	9.0
PEO interchain	0.41	3.76	11.6
POEM combined	0.51	22.14	42.4
POEM interchain	0.82	38.22	42.7

Radial Distribution Functions in Alternative Plot Range

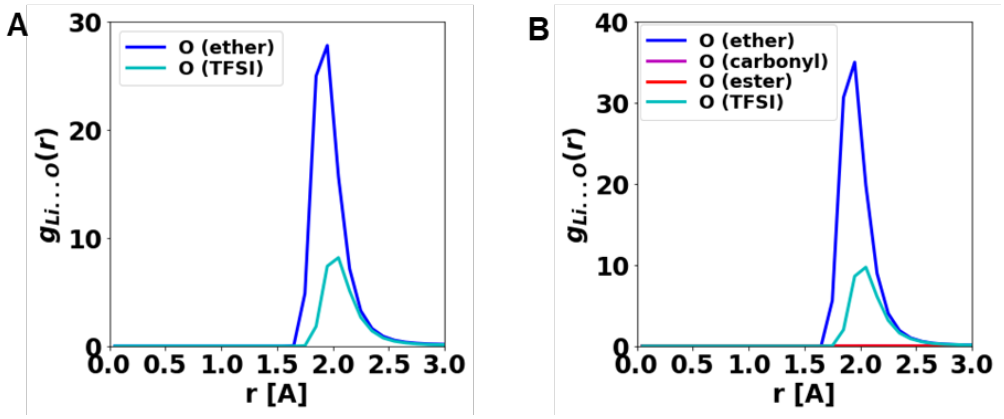

Figure 4.14. Radial distribution functions between Li^+ and oxygen atoms in (A) PEO and (B) POEM at 150 K above T_g shown. Figure 4.3A-B are plotted here with a smaller x-axis range to highlight the positions of the first RDF peaks and an extended y-axis range to highlight the magnitudes of the first PDF peaks.

Simulation Results at Lower Concentration

The PEO and POEM systems are further examined computationally at salt concentration r=0.025 (Li:EO = 1:40). Using the same T_g calculation protocol, the T_g's of PEO and POEM at r=0.025 are estimated to be 241 ± 1 K and 241 ± 2 K, respectively.

The solvation behavior analysis presented in Figure 4.15 is conducted at 150 K above T_g. The Li^+-O RDF indicate that the locations of each Li-O peaks at r=0.025 are the same as those at r=0.05 (Figure 4.3), while the magnitudes of the peaks shift upwards because at r=0.025 the RDF are normalized by a lower concentration. Figure 4.15D shows that the top five populated coordination motifs at r=0.025 are in the same order as those at r=0.05 (Figure 4.4A), where Li^+ are predominately coordinated by six EOs. In PEO, the six EOs belong to a single contiguous chain, whereas in POEM they come from two separate chains. Figure 4.15D presents the Li^+ binding probability of EOs at each position along the POEM sidechains at r=0.025. It indicates that the observed Li^+ solvating behavior is consistent between the two concentrations r=0.025 and 0.05, where Li^+ solvation is relatively localized at EOs at positions 4-7. Overall, Figure 4.15 shows that the solvation behavior at r=0.05 presented in the paper is still valid at r=0.025.

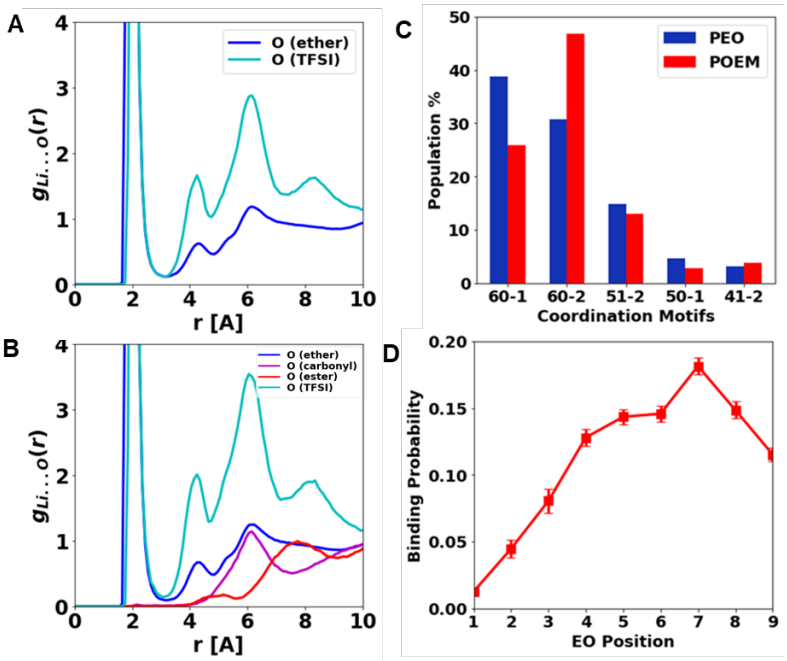

Figure 4.15. Solvation behavior in PEO and POEM at T-T_g = 150 K and r = 0.025. Radial distribution functions between Li^+ and oxygen atoms in (A) PEO and (B) POEM at 150 K above T_g. The RDFs are normalized by the concentration of each oxygen type. (C) Population of Li^+ coordination motifs in PEO and POEM. Only the five most abundant coordination motifs are shown. (D) Binding probability of EOs to Li^+ as a function of position along a POEM sidechain.

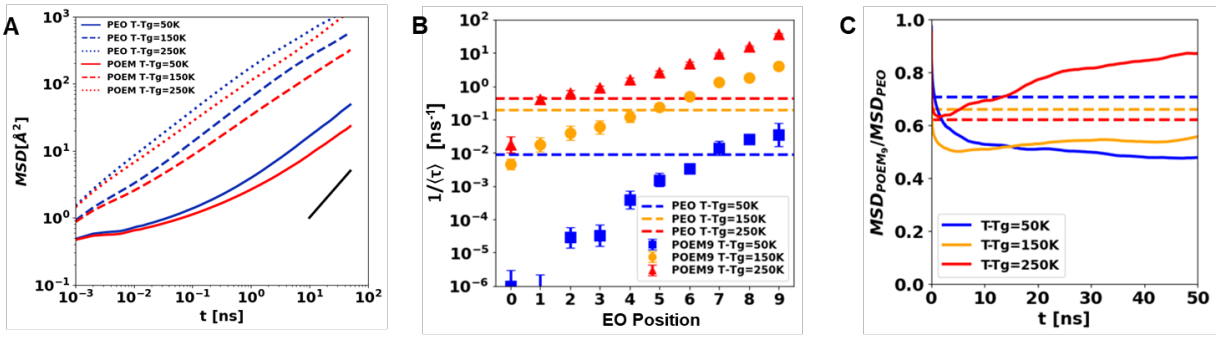

Figure 4.16. Characterization of temperature-dependent ion and chain mobility in PEO and POEM at r = 0.025. (A) Simulated MSD of Li^+ in PEO and POEM at fixed reduced temperatures for r = 0.025 electrolytes. The MSD was computed up to 50 ns using 120-ns trajectories. The black segment represents a guideline with unit slope. (B) 1/<τ> extracted from BVAFs as a function of EO position along the POEM sidechain at three fixed T-T_g. The dashed lines are inverse relaxation times (1/<τ>) for all EOs in PEO system at various relative temperatures. (C) Normalized MSD of Li^+ in POEM at fixed T-T_g. The dashed lines are ratios of solvation site connectivity at different temperatures.

Figure 4.16 compares the ion mobility and segmental dynamics between PEO and POEM at three reduced temperatures. The Li^+ mobility indicated by MSD and the chain mobilities indicated by BVAF are faster at the lower concentration of r=0.025 compared to r=0.05 presented in the paper. The position dependency of sidechain EO mobilities reported at r=0.05 is also observed at r=0.025. The comparison among relative Li+ mobility, relative chain mobilities and the relative connectivity are consistent with the case at r=0.05, except for the crossover temperature, the temperature at which Li^+ in POEM benefit from the improved chain mobility such that the Li^+ mobility starts to outperform what would be expected based on the relative connectivity. As reported in the paper, such temperature for r=0.05 is approximately 150 K above T_g. Here at r=0.025, the crossover temperature seems to fall between 150 K and 250 K above T_g. Overall, Figure 4.16 shows that the conclusions regarding Li^+ and chain mobilities at r=0.05 presented in the paper is consistent with results at r=0.025.

Simulation Results at Higher Concentration

The PEO and POEM systems are additionally examined computationally at salt concentration r=0.1 (Li:EO = 1:10). This concentration is slightly higher than the widely used concentration, r=0.085 (Li:EO~1:12), in experimental studies. The simulations are conducted at temperatures relative to T_g's obtained at r=0.05, which are noted as T_g^*'s in the following text. We believe this would still yield qualitatively reliable results.

The solvation behavior analysis presented in Figure 4.17 is conducted at 150 K above T_g^*. The Li^+-O RDF in Figure 4.17 indicate that the locations of first and second Li-EO peaks at r=0.1 are the same as those at r=0.05 (Figure 4.3). However, the third Li^+-EO peak seen at r=0.05 at approximately 6 Å is not present at r=0.1. Moreover, at r=0.1, the Li-O(carbonyl) and Li-O(ester) RDF exhibit small peaks at around 2 Å. This suggests that carbonyl oxygens and ester oxygens

start to participate in Li^+ coordination at r=0.1, a phenomenon unseen at r=0.05. These RDF suggest that at a salt concentration as high as r=0.1, Li^+ in POEM can adopt additional solvation structures that do not exist in PEO. The top five populated coordination motifs at r=0.1 are presented in Figure 4.17C. It shows that Li^+ solvation is no longer dominated by six-EO motifs. Rather, a diverse range of coordination motifs are observed, without any obviously dominant one. Additionally, there seems to be more participation from oxygens from $TFSI^-$, a reasonable observation considering the high salt concentration. Figure 4.17D presents the Li^+ binding probability of EOs at each position along the POEM sidechains at r=0.1. The distribution of binding probability is qualitatively different from results at the two lower concentrations tested, where Li^+ solvation is relatively localized at EOs at positions 4-7. At r=0.1, there is increased coordination of Li^+ by EOs that are closest to the backbone, consistent with the suggestion from RDF that carbonyl oxygens and ester oxygens start to participate in Li^+ solvation at this salt concentration. Overall, Figure 4.17 shows that at increased salt concentration as high as r=0.1, the Li^+ solvation environment is different. Most importantly, the difference in more prominent in POEM than in PEO, since there are additional Li^+ solvation structures involving ester and carbonyl oxygens apart from those involving only EOs observed at lower concentrations. The difference in solvation environment could lead to different transport mechanism at elevated salt concentrations. Li^+ transport in POEM at concentrated conditions may have very rich and diverse behavior, and thereby worth investigating.

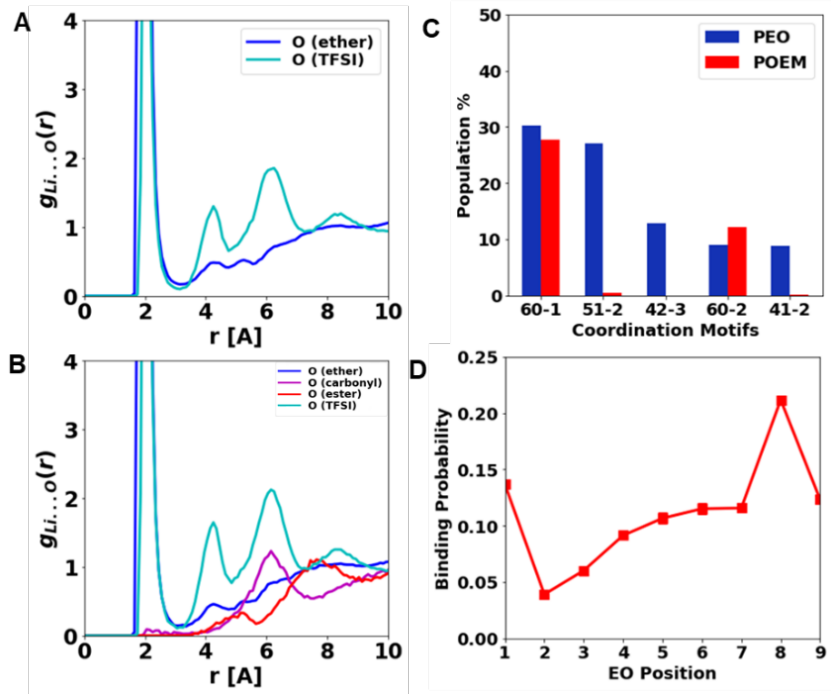

Figure 4.17. Solvation behavior in PEO and POEM at T-T_g^* = 150 K and r = 0.1. Radial distribution functions between Li^+ and oxygen atoms in (A) PEO and (B) POEM at 150 K above T_g^*. The RDFs are normalized by the concentration of each oxygen type. (C) Population of Li^+ coordination motifs in PEO and POEM. Only the five most abundant coordination motifs are shown. (D) Binding probability of EOs to Li^+ as a function of position along a POEM sidechain.

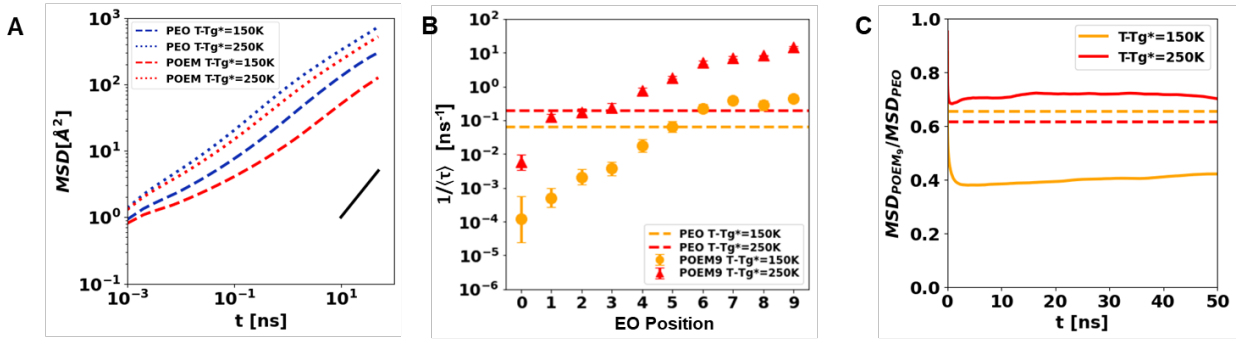

Figure 4.18. Characterization of temperature-dependent ion and chain mobility in PEO and POEM at r = 0.1. (A) Simulated MSD of Li^+ in PEO and POEM at fixed reduced temperatures for r = 0.1 electrolytes. The MSD was computed up to 50 ns using 120-ns trajectories. The black segment represents a guideline with unit slope. (B) $1/\langle\tau\rangle$ extracted from BVAFs as a function of EO position along the POEM sidechain at T-T_g^*=150 K and 250 K. The dashed lines are inverse relaxation times ($1/\langle\tau\rangle$) for all EOs in PEO system at various relative temperatures. An EO position of 1 refers to the EO that is closest to the backbone. The EO position of "0" refers to the $1/\langle\tau\rangle$ calculated for the C-C bonds along the backbone. (C) Normalized MSD of Li^+ in POEM at T-T_g^*=150 K and 250 K. The dashed lines are ratios of solvation site connectivity at different temperatures.

Figure 4.18 compares the ion mobility and segmental dynamics between PEO and POEM at two reduced temperatures. Due to the slow dynamics, the simulations are conducted only at 150 K and 250 K above T_g^*. The Li^+ mobility indicated by MSD and the chain mobilities indicated by BVAF are slower at r=0.1 compared to r=0.05 presented in the paper. Similar to results at r=0.05, sidechain EOs also exhibit a separation in relaxation time scales at r=0.1. Based on the position dependent sidechain ion binding probabilities (Figure 4.17D) and mobilities (Figure 4.18B), the effective mobility of POEM is expected to be lower than PEO at 150 K above T_g^* and higher than PEO at 250 K above T_g^*. Such result suggests that the effective chain mobilities, not T_g, can qualitatively capture the difference between relative Li^+ mobility and relative solvation site connectivity. Overall, Figure 4.18 shows that the comparison among relative Li^+ mobility, relative chain mobilities and the relative connectivity at r=0.1 is qualitatively similar as that at r=0.05. Based on the characterization of Li^+ solvation behavior at r=0.1, we expect that additional factors due to the different solvation behavior and its corresponding transport mechanism need to be considered to fully capture the complete relationship among ion mobility, polymer properties, and polymer-ion interaction. The results further suggest that at salt concentration as high as r=0.1, there might also exist ion correlation effects, which requires a more detailed representation, such as polarization force field, to model.

Comparing among the three concentrations tested, we find that as salt concentration increases, an increase in number of carriers can be offset by a decrease in Li^+ mobilities. This suggests that there exists an optimal salt concentration for the conductivity performance of the material, at which there is a balance between increased number of carriers and compromised Li^+ mobilities. Moreover, further raising the concentration to r=0.1 can qualitatively alter the Li^+ solvation environment, which has been shown to be an important factor that determines the Li^+

transport mechanisms. Overall, results at various salt concentrations presented here provide additional insights into further investigations on Li^+ transport at concentrated conditions.

CHAPTER 5

CRITICAL PERCOLATION THRESHOLD FOR SOLVATION SITE CONNECTIVITY IN POLYMER ELECTROLYTE MIXTURES

This chapter is modified and reprinted with permission from Sharon, D.; Deng, C.; Bennington, P.; Webb, M. A.; Patel, S. N.; de Pablo, J. J.; Nealey, P. F.. Critical Percolation Threshold for Solvation-Site Connectivity in Polymer Electrolyte Mixtures. *Macromolecules* 2022, 55, 16, 7212–7221. https://pubs.acs.org/doi/full/10.1021/acs.macromol.2c00988.

5.1 Abstract

Poly(ethylene oxide) (PEO)-based polymer electrolytes are often mixed with rigid, nonconductive polymers to improve mechanical strength. The suppressed conductivity of the mixture typically arises from a reduced segmental mobility and a diminished connectivity between conductive PEO sites. To decouple these two mechanisms, we compare transport in symmetric miscible blends and disordered block copolymers (BCP) of PEO and poly(methyl methacrylate) (PMMA). Because the two systems have identical physicochemical properties, differences in their conductivity directly reflect the underlying PEO network connectivity. We find that, at short distances (<5 Å), the Li^+ solvation networks are identical for the two systems; however, a distinct variation in the network connectivity arises at length scales between 5 and 10 Å. Specifically, the BCP exhibits a lower connectivity, and therefore a lower conductivity than the blend. A quantitative model is proposed that associates long-range Li^+ transport with local miscibility; the concept of network connectivity discussed here could be useful for designing polymer electrolyte systems.

5.2 Introduction

To date, the most efficient polymer hosts for lithium-ion (Li^+) transport have been based on poly(ethylene oxide) (PEO).[217] The ionic transport mechanism in PEO-lithium bis(trifluoromethanesulfonyl)imide (LiTFSI) is based on the hopping of Li^+ between solvation sites composed of five to six ether oxygens (EO).[50,54,177] The rate of hopping depends on the number of solvation sites, their connectivity, and segmental mobility.[77,218,219] To achieve a reasonable conductivity, PEO must operate in its rubbery state, above its melting temperature, and well above its glass-transition temperature.[220] This is because fast transport of Li^+ relies on fast chain motions of the polymer host, which only occur when the polymer material is in the rubbery state. Such transport improves as temperature increases. True solid-state battery applications, however, require a certain level of mechanical strength, which is believed to help suppress uncontrolled dendritic growth in Li-metal batteries.[44] A common strategy to overcome this inherent trade-off between mechanical strength and ionic conductivity has been to mix PEO with a rigid, high-T_g polymer to form a robust solid electrolyte membrane. PEO-based blends can be formed through direct mixing (PEO/X) [221–227] or by synthetic copolymerization (PEO-X),[87,228–232] where X is a rigid component (X) that provides mechanical support but does not conduct Li^+. While this mixed material could simultaneously achieve conductivity and mechanical integrity, it is often observed that improvements involve a compromise: the PEO phase within the mixture exhibits a lower ionic conductivity than the unmixed, pure material. [232–236]

The addition of a glassy, nonconductive component reduces the conductivity of the mixed PEO phase through two main mechanisms. First, the low chain mobility of the glassy polymer component is believed to slow the segmental dynamics of the PEO domains in the mixture, thereby also slowing down Li^+ transport (which is tightly coupled to the chain mobility of the host). Recent

studies have investigated how a contrast in host segmental dynamics affects the transport of Li^+ within it. Those studies considered Li^+ transport in poly(oligo-ethylene oxide) methacrylate (POEM), where flexible EO side chains are grafted onto glassy poly(methyl methacrylate) (PMMA) backbones.[218,219] Reports indicate that the glassy backbone slows down the non-ion-solvating portion of the EO side chains and that the dynamics of the ion-solvating portions of the side chain are directly correlated with Li^+ mobility. Moreover, this body of research has shown that the PMMA backbone mixed into the system neither solvates nor conducts Li^+. Instead, the very existence of nonconductive PMMA segments disrupts Li^+ transport pathways between conducting PEO sites (5–6 EO units). The "dilution" of conductive PEO segments by nonconductive polymeric components was originally identified by Mayes et al. as the second cause of lower ionic conductivity. [64]

Only recently, with the refinement of the concept of solvation-site connectivity, have attempts been made to measure the diluting effect of nonconductive components.[77] In some of these studies, the ionic conductivity of polymer electrolytes with different number and proximity of solvation sites (EO units) have been determined by means of extensive molecular dynamic (MD) simulations. The concept of solvation-site connectivity is gradually gaining favor, but questions remain about its importance relative to the effects of segmental mobility. Note that in most experimental systems, variations in the number or proximity of solvation sites lead to changes in the chemical (functional groups) and physical properties (segmental mobility) of the different electrolyte systems. As a result, quantification of the effects of solvation sites has been performed after artificially correcting for the chemical and physical disparities between the electrolyte systems. To overcome these shortcomings, in this work, we present a comparative study of

symmetric blends and copolymers, where the chemical and physical properties of the electrolyte systems are the same, but the local solvation-site connectivity is different.

More specifically, we compare two types of polymer electrolyte mixtures based on PEO and poly(methyl methacrylate) (PMMA): a miscible polymer blend and a syntactic disordered block copolymer (BCP) PEO-*b*-PMMA. The mixtures have the same compositions (50:50 wt %) and are each blended with LiTFSI salt at the same concentrations (r = [Li]/[EO] = 0.05). Note that polymer mixtures based on PEO and PMMA are a good model system to investigate the relationship between ion transport and solvation-site connectivity for several reasons. First, as demonstrated by Lodge and McLeish, PEO, and PMMA mixtures are microscopically miscible, implying that chain conformations remain unaltered after mixing and do not adopt a particular long-range order.[237,238] Second, it has been reported that PMMA as a dry homopolymer does not transport Li^+ ions. Therefore, the ionic conduction mechanism in the blend and BCP electrolytes relies on the PEO component and can be assumed to be identical to that of pure PEO. Third, as reported by Maranas et al., because the bulk segmental properties and chemical composition of the blend and BCP are identical, the only difference between the two systems should be the degree of mixing (miscibility) at length scales below 1.5 nm.[239] As a result, any changes in the ion transport behavior between them can be attributed to local changes in the connectivity of the PEO solvation-site network.

Our experimental measurements indicate that the ionic conductivity of the blend and the BCP systems is an order of magnitude lower than that of the unmixed PEO electrolyte. Furthermore, the ionic conductivity of the blend mixture is higher than that of the BCP electrolyte by a factor of 2. We propose that, in both blend and BCP systems, the presence of nonconducting PMMA near the PEO interferes with the ionic transport. Our simulation results corroborate this

view and help establish a quantitative model that considers Li^+ transport between clusters, which are a direct result of PMMA mixing into PEO. These clusters occur at length scales of 5–10 Å, which are larger than the typical size of the immediate Li^+ solvation shell. In the context of polymer electrolyte mixtures, this newly acquired understanding of molecular packing, ion solvation behavior, and ion transport mechanism could help inform future design of nonhomogeneous polymer electrolyte systems.

5.3 Materials and Methods

Materials

PEO (10 kg/mol), PMMA (11 kg/mol), and PEO-*b*-PMMA (11-11 kg/mol) were purchased from Polymer Source, Inc. and dried in an argon glovebox antechamber at 50 °C overnight before use. Acetonitrile (99.8%, anhydrous) was purchased from Sigma-Aldrich and used as received. Anhydrous LiTFSI was purchased from Sigma-Aldrich and was further dried under vacuum at 100 °C for 48 h. Polymers and LiTFSI were stored in an argon glovebox after the drying processes.

Characterization

Differential Scanning Calorimetry (DSC). Calorimetric glass-transition temperatures (Tg) of neat polymers and polymer electrolytes were determined by DSC using a TA Instruments Discovery 2500 DSC. Sample pans were prepared in the glovebox by drop-casting solutions, heating at 65 °C until dry, and then repeating until 5–10 mg of material was in the pan. The pans were then hermetically sealed before removing them from the glovebox to avoid any water adsorption before DSC measurement.

Vibrational Spectroscopy. Samples for Fourier transform infrared (FTIR) measurements were prepared on Au-coated Si substrates by spin coating. Samples were prepared inside a glovebox, annealed at 135 °C for 15 min, and sealed until immediately before measurement to

minimize water absorption. Measurements were performed using a Shimadzu IRTracer-100 spectrometer using a diamond prism for attenuated total reflection (ATR) at ambient temperature from 400 to 4000 cm–1.

Table 5.1. Characteristics of polymer electrolyte systems with LiTFSI (r = 0.05)

Characteristic	PEO	PEO/PMMA (50:50 wt. %)	PEO-b-PMMA
Mn / Kg·mol^{-1}	10.0	10.0/11.5	11.0-11.0
T_g / °C	-50	-40	-39
Structure	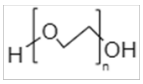	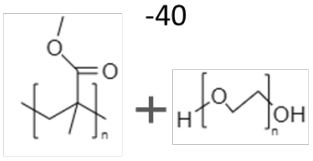	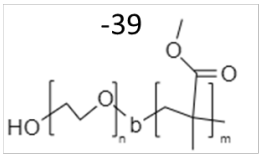

Thin-Film Conductivity Measurements. Polymer electrolyte conductivity was determined by electrochemical impedance spectroscopy (EIS) of thin films on interdigitated electrodes (IDEs) as described previously.[201] Briefly, IDEs are microfabricated by photolithography on top of thermal oxide Si wafers. Ti (5 nm) and then Au (45 nm) are deposited in the lithographically defined electrode area, and excess metal is removed by liftoff in warm *n*-methyl pyrrolidone. IDEs are designed with N = 160 electrodes, l = 1 mm of electrode overlap, w = 2 mm electrode width, and d = 8 mm interelectrode distance. Polymer electrolyte thin films were cast onto the IDEs by spin coating at 4000 rpm inside the glovebox, followed by drying on a hot plate at 70 °C before EIS measurements. Polymer film height (h) was determined by casting identical films on a Si wafer and performing ellipsometry (J.A. Woollam alpha-SE ellipsometer). Polymer films were in the range of 70–100 nm for this study. IDEs were placed on a custom heating stage in the glovebox and connected to a Gamry 600+ potentiostat by tungsten probe tips. Potentiostatic EIS was performed with an applied amplitude of 100 mV over a frequency range of 1 MHz–1 Hz. EIS data is fit to an appropriate equivalent circuit that models the physical process

of thin films IDE systems using the Gamry E-chem Analyst software, and the resulting film resistance (R_f) is used to find the conductivity (σ) by eq 1. All conductivity data are reported as the average of three samples, with error bars representing the first standard deviation.

$$\sigma = \frac{d}{R_f(N-1)lh} \tag{5.3}$$

Simulation. In this study, the TraPPE-UA force field[202–204] is used for all inter- and intramolecular interactions among polymer atoms. Compatible all-atom parameters for LiTFSI are adapted from a previous simulation study.[59,206] For all MD simulations, a cutoff radius of 12 Å with van der Waals tail correction is used for short-range Lennard–Jones (LJ) interactions. Long-range nonbonded interactions use a cutoff radius of 12 Å and are handled using the particle–particle particle–mesh solver with 10^{-4} accuracy.[207]

The simulation is performed using the LAMMPS package.[208] The trajectories are integrated using the velocity-Verlet algorithm with a 1 fs timestep. For NVT simulations, the Nosé–Hoover thermostat with a damping parameter of 100 fs is used. For NPT simulations, the Nosé–Hoover barostat with a damping parameter of 1000 fs is applied in addition to the thermostat. Additional details of the simulation procedures and force field parameters are included in 5.6.

5.4 Results and Discussion

As mentioned earlier, we examine experimentally and computationally two polymer electrolyte mixtures: (1) a miscible 50:50 wt % PEO/PMMA (10–11 kg/mol) blend electrolyte and (2) a disordered symmetric PEO-b-PMMA (11–11 kg/mol) BCP, both having a fixed LiTFSI concentration (r = [Li]/[EO] = 0.05). We begin by comparing the experimental ionic conductivity and simulated Li^+ transport of these two systems to those of a pure PEO-LiTFSI (10 kg/mol) electrolyte having the same LiTFSI concentration (Table 5.1).

EIS measurements and equivalent circuits modeling were used to determine the resistivity of the polymer electrolytes that was then converted to ionic conductivity.[201] The general assumption is that at relatively low concentrations like $r = 0.05$, majority of the TFSI anions are "free" and their motion is unaffected by the PEO conformation or coordination, whereas the Li cation is, and thus it is widely accepted to use ionic conductivity as a proxy to measure the Li^+ diffusivity. Figure 5.1a shows ionic conductivity as a function of temperature for PEO/PMMA blend, PEO-b-PMMA BCP, and PEO homopolymer electrolytes with LiTFSI ($r = 0.05$). At all temperatures, the ionic conductivity of the unmixed homopolymer electrolyte (PEO) exceeds that of the polymer mixtures by an order of magnitude. The conductivity of the disordered BCP is lower than that of the blend by a factor of two. Previous studies have shown that PMMA segments do not actively participate in the solvation or transport of Li^+;[218,219] we therefore normalize the measured ionic conductivity by the PEO-LiTFSI volume fraction to account for the reduced Li^+-conducting sites in the blend and BCP (Figure 5.1a, open symbols). Even after this normalization, the conductivities of the blend and BCP are still significantly lower than that of the unmixed PEO electrolyte. This finding implies that, while PMMA does not actively engage in the ion transport mechanism, its presence interferes with the passage of Li^+ through the PEO segments.

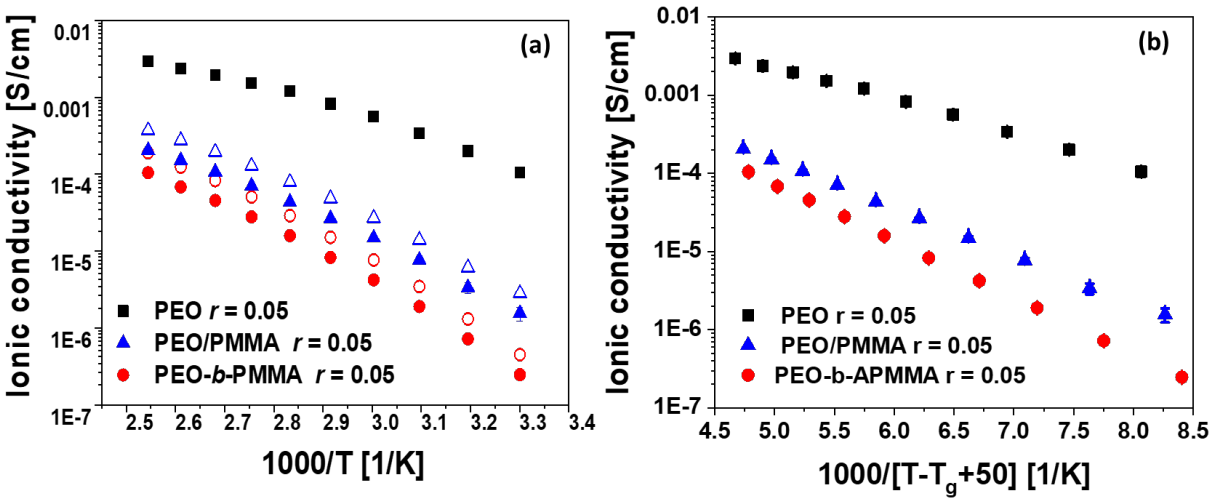

Figure 5.1. Polymer electrolyte ionic conductivity with LiTFSI (r = 0.05) as a function of (a) temperature and (b) temperature corrected by T_g ($T - T_g$ = 50). In (a), the as-measured experimental conductivities are shown as solid symbols. The open symbols for mixed polymer electrolytes represent normalized conductivities by the volume fraction of PEO.

To understand why and how the presence of inactive fragments (PMMA) affects ionic transport within the blend and BCP electrolytes, we consider the two mechanisms mentioned in the introduction. First, the incorporation of high-T_g components, such as PMMA, tends to slow down the segmental mobilities of the material, which is essential to promote Li^+ hopping in high-molecular-weight PEO-based electrolytes.[234,240] To account for the conductivity differences due to the disparities in the segmental mobility (T_g), we further present the normalized conductivities as a function of reduced temperature, $T - T_g$ (Figure 5.1b). The addition of the glassy PMMA component increases the T_g of the mixtures by 10 °C (blend) and 11 °C (BCP) with respect to the unmixed PEO-LiTFSI system. The linear increase in ionic conductivity as a function of temperature corresponds to the VTF relationship, since the ionic transport in all samples is dependent on the segmental motion of the PEO chains. More importantly, we can observe that although the differences in ionic conductivities between the mixtures and the unmixed PEO-LiTFSI decrease after the T_g correction, the change is only minor. The conductivity difference

between the blend and the BCP electrolyte is not affected by the correction either, as their T_g's are virtually identical. Overall, T_g-normalized results show that while the reduction in segmental mobility is a valid explanation, it is not the major reason for the reduced conductivities observed here for the blend and BCP systems. The explanation for the lower ionic conductivity is most likely due to the second mechanism, in which the percolating PMMA segments disrupt (dilute) the solvation-site network formed by PEO segments. To examine that hypothesis, we next characterize the local miscibility (concertation fluctuation) of these systems at a molecular level.

Note that a common approach to assess miscibility in polymer blends is to characterize the glass transition behavior. The DSC curves of both the blend and the BCP electrolytes with $r = 0.05$ LiTFSI exhibit a singular glass transition at −41 and −39 °C, respectively. Generally, a single glass transition trace in DSC measurements indicates that the blend components are miscible. The measured T_g of the polymer electrolyte blend does not agree with the calculated T_g from the Fox equation for miscible binary blends ($T_{g\text{-fox}} \approx -23$ °C). Lodge and McLeish suggested that deviations from the Fox equation are caused by changes in the local concentration of the polymer components with respect to their bulk compositions.[241,242] The origins of these changes can be intermolecular chain connectivity or concentration fluctuations.[241–243] It was also suggested that in PEO/PMMA mixtures, the PEO has a measurable influence on PMMA mobility, whereas the presence of PMMA has a minor effect on PEO mobility until the matrix contains a sufficiently high concentration of PMMA (above 90%).[244] This could explain why the T_g of our symmetric polymer electrolyte mixtures is more tilted toward the T_g of the PEO component. Our DSC measurements also reveal that such behavior is preserved after the addition of a Li salt ($r = 0.05$). To summarize, the DSC results indicate that the blend components are miscible and exhibit some asymmetry in their glass transition behavior. However, because their T_g's are essentially the same,

DSC measurements are insufficient to detect differences in local miscibility between the blend and the BCP, which might explain the difference in ionic conductivity.

While the glass transition provides a somewhat macroscopic account of polymeric blend miscibility, FTIR spectroscopy can be used to provide a measure of intermolecular interactions between the components of a mixture. Taking the spectra of the unmixed polymer components as a reference, changes in the FTIR spectra of the mixtures (such as peak decrease, shift, or broadening) can provide insights into structural changes at the molecular-level caused by the interaction or proximity between different components.[245,246] Figure 5.2 shows the FTIR spectra of the PEO/PMMA blend and the PEO-*b*-PMMA BCP, along with those of the homopolymer PEO and PMMA for different wavenumber regions. Figure 5.2a focuses on the symmetric stretching of the PEO CH_2 groups, which is represented by multiple peaks in the range 2850–2900 cm^{-1}. The PEO component in the PEO/PMMA blend does not present significant changes in the peak shape or height ratios. Conversely, the PEO-*b*-PMMA peak at 2891 cm^{-1} decreases considerably with respect to the unmixed PEO homopolymer. The same trend is observed for the characteristic CH_2 wagging vibration mode of the PEO component, where the decrease in the intensity of the sharp doublet at 1341 and 1360 cm^{-1} is more pronounced in the block copolymer sample (Figure 5.2b).[245] The PEO ether (C–O–C) vibration signature peaks between 1050–1150 cm^{-1} are presented in Figure 5.2c. The peaks at 1135 and 1057 cm^{-1} correspond to the crystalline PEO phase, while the peak centered around 1118 cm^{-1} includes both crystalline and amorphous phases. The crystalline PEO peaks in both mixtures are reduced with respect to the pure PEO; nonetheless, the decrease is more pronounced in the BCP sample. The suppression of the PEO crystalline phase by the introduction of a miscible polymer component has been well documented and can be attributed to the reduced formation of extended PEO chain crystals.[247] We found no evidence of any specific

interactions between the two polymeric components, such as hydrogen bonding between the methyl ester PMMA hydrogens and the PEO ether oxygens or the PMMA carbonyl ester and the PEO hydrogens.[239,248] Nonetheless, we can observe that the PEO natural conformation is more disturbed in the BCP, which implies that the degree of miscibility in the BCP at a molecular level is higher than that in the blend. FTIR results are in good agreement with a previous simulation study by Maranas et al., where the local miscibility was suggested to be higher for the PEO-*b*-PMMA with respect to a blend.[239] In summary, we find that both mixtures are miscible, and the degree of miscibility for the BCP is higher than for the blend.

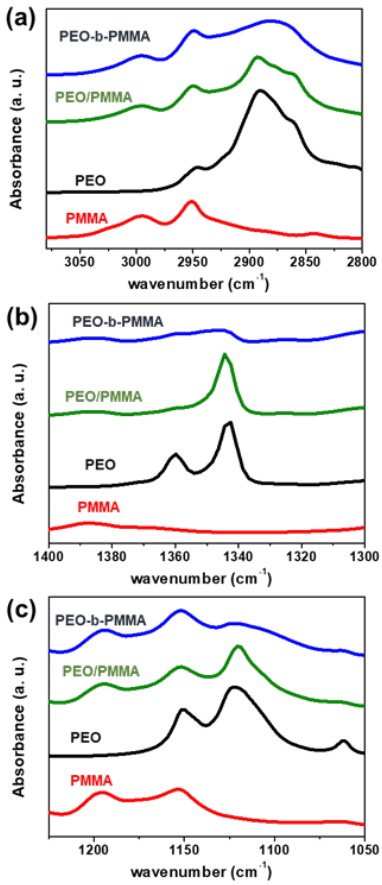

Figure 5.2. FTIR spectra of (a) CH2 stretching, (b) CH2 wagging, and (c) C–O–C vibrations in the PEO/PMMA blend, the PEO-b-PMMA BCP, PEO homopolymer, and PMMA homopolymer.

As noted above, there are two independent mechanisms by which ionic conduction in miscible polymer electrolyte mixtures can be reduced: glassy PMMA segments that slow down the PEO segmental motions, and a molecular "dilution" of the PEO fragments by the nonconductive PMMA component, leading to a disrupted EO network. In some polymer electrolyte mixtures, the overall reduced ionic transport is a combined effect of the two mechanisms. Here, however, we have shown that the segmental motion mechanism only accounts for a small portion of the difference in ionic conductivities between the mixtures and pure PEO, leading us to conclude that the dilution mechanism is the predominant contributor to the reduced ionic conductivity. In the following sections, we propose a model that helps explain the influence of the dilution effect on ionic conductivity.

Simulations of the PEO/PMMA blend and the BCP systems are particularly helpful for revealing the extent of local mixing of polymer segments and its influence on Li^+ transport. The results discussed in what follows were generated from three independent simulations at 190 K above the T_g of the corresponding system. Simulated T_g values and their calculations are included in 5.6. It is widely accepted that, in polymer electrolytes, the transport of Li^+ relies on hopping between solvation sites, either along a polymer chain or from one chain to another.[47,49] The solvation-site environment, i.e., the composition of solvation sites and the vicinity of available neighboring solvation sites, determines the hopping mechanism and the associated hopping rates.[72] We first consider the extent of miscibility via the concept of self- and effective concentrations (Figure 5.3a–c).[239,241] The self-concentration decays from unity to zero and quantifies how closely a chain packs with itself; the effective concentration of a component decays from unity to its bulk volume fraction and indicates how closely a chain packs with other chains of the same species. Our results show that PEO and PMMA chains have identical intrachain packing in the blend and

the BCP. However, the interchain packing of each component decays faster in the BCP, revealing a higher degree of intermixing in the BCP. Since the effective concentrations of PMMA and PEO decay to slightly different volume fractions (each is 50% by weight), we normalize the effective concentration to decay from unity to zero to provide a better visual comparison. The normalized results confirm the greater miscibility in the BCP relative to the blend. This finding is consistent with our FTIR measurements. A previous study reported similar inter- and intrachain packing behaviors for salt-free PEO/PMMA mixtures at a lower PEO content (20 wt %).[239] Our results extend that observation to systems that are more relevant for energy storage applications, i.e., mixtures with higher PEO content and with ions. To show how differences in polymer chain packing impact Li^+ solvation, we describe the solvation environment using the pair radial distribution functions (RDFs) between Li^+ and oxygen atoms for the PEO (ether) and PMMA (carbonyl and ester) components (Figure 5.3d–f). We find that up to a radius of 4 Å, both blend and BCP systems show all-EO coordination is contributed by the PEO component, while PMMA oxygens only participate beyond $r \approx 6$ Å. The first solvation shell composition in the mixtures is identical to that in the unmixed PEO. Note that the RDFs are normalized by the concentration of the relevant atoms, so the decreased peak height of the first EO solvation peak in homopolymer PEO results from the normalization to a higher EO concentration in that system. Overall, it is of interest to note that the addition of PMMA to the mixtures does not alter the local solvation environment.

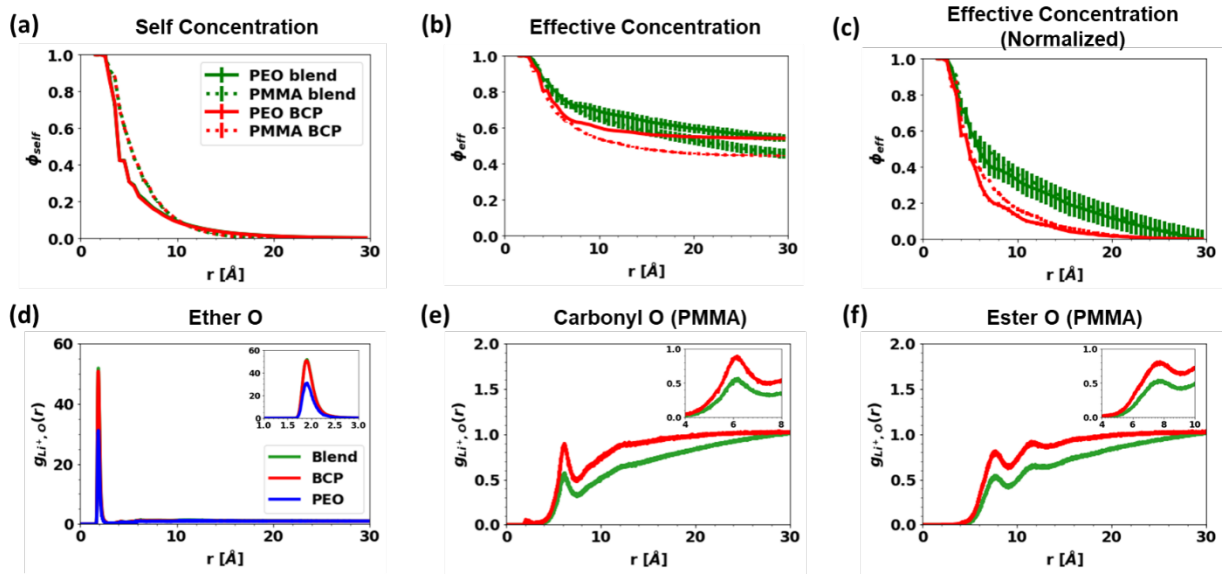

Figure 5.3. Li-oxygen radial distribution functions (RDF) for different oxygen types for the blend and BCP system. Note that the RDFs are normalized by the concentration of each oxygen type, so the relative heights of the peaks do not necessarily relate to the solvation shell composition.

Since Li^+ ions are primarily solvated by EO units in both the blend and BCP systems and in PEO, we can infer that their conductivity relies on the same ionic transport mechanism, i.e., hopping between sites formed by ether oxygens only. Therefore, the Li^+ transport models presented in what follows for miscible polymer mixtures share the same criteria for identifying viable solvation sites as used in a series of PEO-based homopolymer hosts.[72,179,218,219]

Here, we adopt the solvation-site connectivity protocol by Webb et al. but in the context of miscible polymer mixtures.[77] Specifically, a viable solvation site in a PEO-based electrolyte is defined at the centroid of a set of five or more EO atoms, each within 3.7 Å of the centroid. Figure 5.4a shows representative snapshots of viable solvation sites for the homopolymer, the blend, and the BCP electrolyte systems at a salt concentration of $r = 0.05$. Visually, both miscible mixture electrolytes appear to have fewer viable solvation sites than the unmixed PEO electrolyte. Furthermore, while solvation sites tend to organize into isolated clusters in the mixtures, they are evenly distributed in the PEO electrolyte, where they form a well-connected network. To

quantitatively compare the different systems, we compute the solvation-site connectivity defined as $\kappa = \exp(-\langle r_{nn} \rangle)$, where $\langle r_{nn} \rangle$ is the average nearest neighbor distance.[77] As shown in Figure 5.4b, the connectivity in PEO appears to be more than 3 times higher than in the blend and BCP systems. Although the difference in connectivity is less dramatic than the factor of ten difference between the conductivity of PEO and the mixed electrolyte systems, it demonstrates that the addition of PMMA suppresses Li^+ conduction mainly by diluting and disrupting the solvation-site network. Solvation-site connectivity, however, does not reveal a difference between the blend and the BCP. Recall that the blend exhibits a conductivity that is twice as large as that of the BCP.

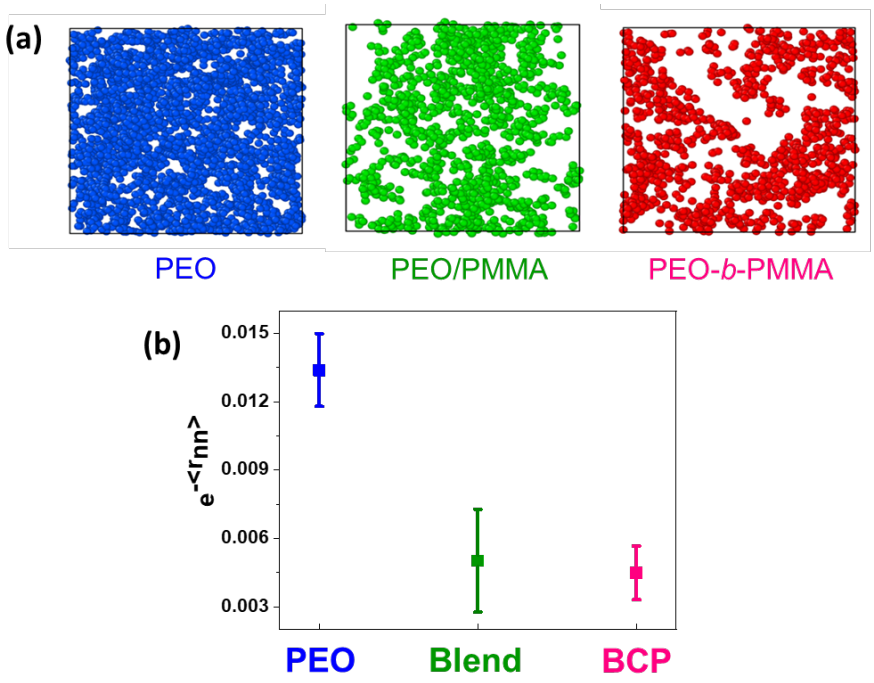

Figure 5.4. (a) Snapshots of viable solvation sites from the MD simulations. Viable solvation sites are shown as filled circles. where circle size reflects an approximate radius of 3.7 Å and the simulation boxes are approximately 60 Å in each dimension. (b) Average connectivity density for the different polymeric systems. The error bars derive from an averaging over 1000 snapshots.

We next consider the length scale at which the solvation-site connectivity describes the solvation-site network. As described here and in previous studies, the solvation-site connectivity is proportional to the characteristic hopping rate between two solvation sites separated by $\langle r_{nn} \rangle$.

The logic behind this approach originates from a transition state-like theory, where the rate or likelihood of a hopping event is inversely related to its energy barrier, which we assume to increase linearly with the distance between sites. Because the hopping rate decays exponentially as the distance increases, the connectivity metric is dominated by short-range Li^+ hopping events that occur at the length scale of the immediate solvation environment (within 5 Å), and it only incorporates limited information about how solvation sites are arranged on a larger length scale. When comparing the blend and the BCP, the immediate solvation environment is identical in the two systems, and the most critical difference between them lies in the molecular packing at length scales in the range of 5–10 Å, where miscibility heterogeneity is manifest. An effective model for ion transport in these systems must therefore highlight features of the solvation-site network at such length scales.

To better quantify the long-range connectivity of solvation sites, we first apply a percolation analysis. First, we group solvation sites into ionic conductive clusters. Under the context of ion hopping between solvation sites, we assumed that a Li^+ could hop from one solvation site to another when the distance between them is lower than a given hopping threshold d. If two sites are separated by a distance larger than the threshold, they are considered disconnected and can be defined as isolated clusters. Figure 5.5a displays representative snapshots of solvation-site clusters at a representative hopping threshold distance $d = 6$ Å. Different colors represent isolated clusters that are separated by at least 6 Å from one another. We find that, in the unmixed PEO, solvation sites form an overall connected network, where almost all solvation sites belong to the same cluster. In contrast, in the blend and the BCP systems, the solvation sites aggregate into a few isolated clusters instead of forming a single connected cluster. The BCP system appears to have more isolated clusters than the blend. To characterize how the formation of clusters disrupts

the network of solvation sites, we follow a similar idea and examine the spanning percolation probability (P_s) as a function of hopping threshold (d) to identify the critical length scale for percolation transitions. The term spanning probability defines the likelihood that a solvation-site cluster is connected across the ∼60 Å simulation box along at least one of the three Cartesian directions. Figure 5.5b presents the calculated P_s as a function of d in the unmixed PEO, the blend, and the BCP. Because P_s is averaged over 1000 frames of different fluctuating solvation-site configurations, the percolation transition in each system exhibits a smooth curve, instead of a step function, growing from zero to unity as d increases. We find that the largest difference between unmixed PEO and the mixtures occurs at approximately 4.5 Å, which is roughly the size of the second solvation shell, and therefore reflects the nearest neighbor distance. This implies that in the unmixed PEO, long-range Li^+ transport occurs as long as short-range transport, i.e., hopping from one site to its immediate neighbor, is enabled. For the mixture systems, however, this is not the case; short-range transport only allows a Li^+ to move within a cluster, but not across isolated clusters. In other words, in PEO the rate-limiting process for long-range transport is intersolvation-site transport, while in the mixtures, it is intercluster transport. A comparison of the blend and the BCP shows that their Ps differ most significantly at $d \sim 6$ Å. Recall that the local effective concentrations also exhibit the largest difference at around ∼6 Å (Figure 5.3a). Based on these findings, we attribute the greater disruption in the solvation-site network observed in the BCP to its higher degree of mixing, or lower local effective concentration of PEO units at that length scale. These results confirm that the key intermediate-range features of the underlying solvation-site network are determined by molecular arrangements at length scales of 5–10 Å and that this critical length regime is larger than that considered in the original solvation-site connectivity model. Note that the cutoff distances identified here do not correspond to previously reported ionic transport

mechanisms, but they can be used to highlight critical length scales that might affect ionic transport efficiency in mixed polymer electrolyte systems.

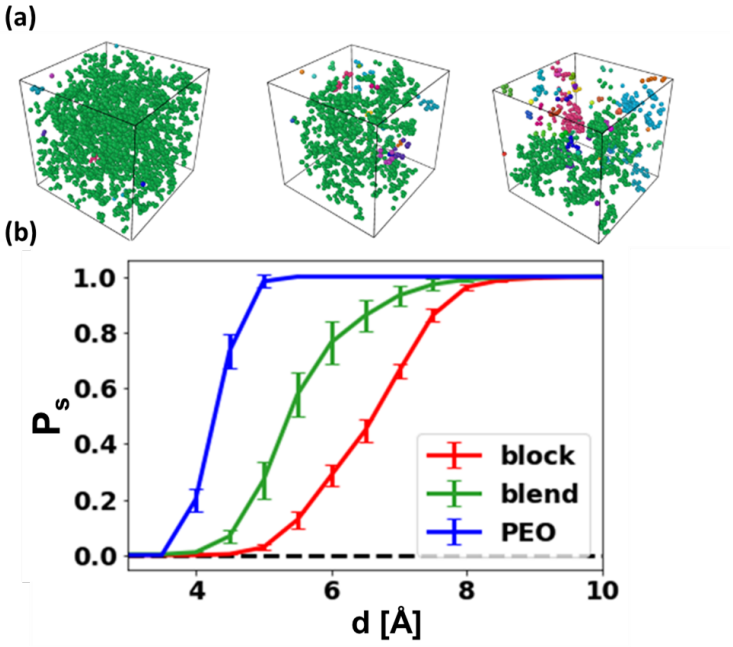

Figure 5.5. (a) Representative configurations of percolated clusters with cutoff length of 6 Å and (b) percolation probability plotted as a function of normalized edge length cutoff.

The relevance of solvation-site cluster connectivity can be better understood by introducing a different transport model. We do so by applying the Kirchoff transport index (K_T) as described by Jackson and co-workers, which was shown to be successful in quantifying charge transport in bulk organic photovoltaic materials.[249] That classical resistance theory is adapted here to analyze Li^+ transport in the solvation-site network. In a network of solvation sites, the "admittance" between two sites is related to the probability of hopping, P_{hop}, which is expressed as a function of the separation distance r, $P_{hop} \propto e^{-r}$. K_T is defined as the normalized sum of the inverse resistance distances between every pair of solvation sites. For additional details, readers are referred to Jackson et al.'s original work.[249] Figure 5.6 presents the calculated K_T for each system. We find that K_T in the blend is 2 times higher than in the BCP, which is consistent with the factor of two

reported here in their ionic conductivities. Comparing the mixtures to the unmixed PEO, K_T does not reproduce the factor of ten difference in conductivity; K_T seems to only capture the relative difference in ionic conductivity due to the degree of miscibility in the blend and BCP systems. In contrast to the solvation-site connectivity, which is solely based on nearest neighbor distances, K_T considers all possible pairwise distances between viable solvation sites and assigns to them a relative importance. This model not only considers short-range transport between neighboring sites but also accounts for the long-range transport involving Li^+ transport between solvation-site clusters. While the relative contributions from intra- and intercluster transport might not be captured quantitatively, we believe this model is useful for the analysis of transport in mixed systems.

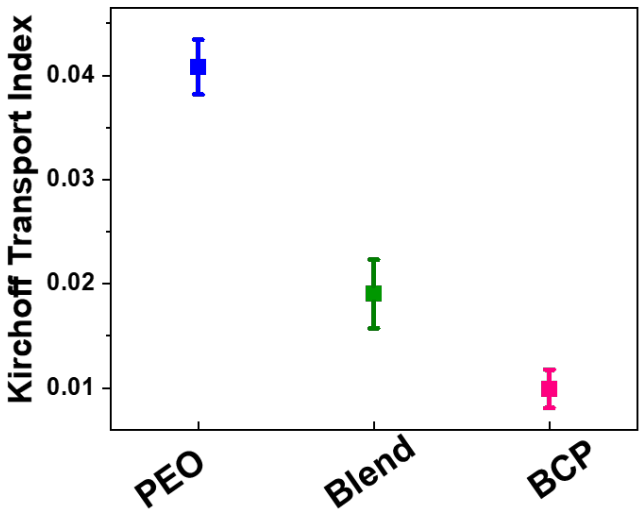

Figure 5.6. Kirchoff transport indices K_T for studied ionic transport in polymer electrolyte systems.

As noted above, this model determines resistance distances between pairs of solvation sites regardless of how far they are. However, long-range ion hopping events between clusters that are more than 6 Å apart are unlikely. Actual ion hopping events occur between neighboring solvation sites, and the transport between clusters possibly relies on their rearrangement. One should therefore evaluate the segmental dynamics, which is closely associated with the rate of

rearrangement of solvation sites and solvation-site clusters.[179] Here, we argue that for comparable chain dynamics, the time required for solvation-site rearrangement is proportional to the length scale of the rearrangement. This is the case in our study, where the segmental dynamics are comparable for the blend and the BCP systems so that differences in the spatial arrangement of solvation sites directly explain differences in conductivity. Also note that the model originally intended for electron transport assumes that the transport between nodes is much faster than the rearrangement of the network. That might not be the case for Li^+ hopping in PEO,[179] and this model merely highlights how the critical length scale of a time-averaged, static representation of solvation-site networks can be connected to the rate of Li^+ transport.

The critical length scales identified here provide a first step toward understanding Li^+ transport in polymer electrolyte mixtures. To arrive at a complete physical picture, it is necessary to also evaluate and consider the kinetics of the rate-limiting mechanisms for long-range Li^+ transport. In this work, we have shown that in PEO the intersolvation-site hopping is rate-limiting, and it depends on segmental relaxations at a length scale below 5 Å. In the blend and BCP systems, the rate-liming process is the intercluster transport, which depends on segmental relaxations at length scales in the 5–10 Å range. For these different rate-limiting processes, the need for relaxation at a larger length scale is further linked to a higher activation energy, which could manifest in a more dramatic temperature dependence. We are currently developing a time-temperature superposition principle to investigate Li^+ transport behavior for a dynamic representation of solvation-site networks. The goal is to elucidate the underlying kinetics by determining the time scale for Li^+ hopping events relative to that of solvation network rearrangement as a function of temperature.

5.5 Conclusion

The comparison of Li^+ transport in homopolymer PEO and PEO-containing polymer blends and BCP electrolytes presented here helps explain several physical processes that influence conductivity. These materials exhibit essentially identical thermophysical properties and only differ by their local concentration conditions. Experimental characterization and MD simulations reveal that the critical percolation threshold for Li^+ transport is closely associated with local miscibility features that arise at length scales in the 5–10 Å range.

Our experiments indicate that the ionic conductivity of the blend and the BCP is an order of magnitude lower than that of the unmixed PEO electrolyte. Further, the ionic conductivity of the blend is higher than that of the BCP electrolyte by a factor of two. The PMMA near the PEO interferes with ionic transport, as revealed by our observation that the BCP, which has a higher degree of miscibility than the blend, exhibits a greater reduction in ionic conductivity.

Our simulation results provide a quantitative framework to understand the proposed mechanism. Simulated effective concentrations confirm that the BCP is more homogeneous than the blend and that the miscibility difference between the two mixtures is most apparent in changes in the local concentration at length scales of 5–10 Å. The first Li^+ solvation shell in the mixtures is similar to that in the pure PEO. Between the blends and the BCP, the miscibility difference causes the Li^+ solvation environment to differ only after 6 Å. A cluster analysis confirms that the critical length scale at which the presence of PMMA near PEO can affect Li^+ transport efficiency is approximately 6 Å. The spanning probability analysis confirms that the rate-limiting process for long-range Li^+ transport is the intersolvation-site hopping (<5 Å) in PEO and intercluster transport (5–10 Å) in the mixtures. These views were further substantiated by combining a solvation-site connectivity analysis κ and introducing a Kirchoff transport index K_T to model Li^+ transport in

blends and BCP systems. The first model captures the relative conductivity difference between pure PEO and the mixed electrolytes, but it does not differentiate between the blend and the BCP. We believe this is due to different degrees of solvation-site clustering in the mixture and BCP at length scales of 5–10 Å. The second model successfully captures the nuanced conductivity difference, caused by the degree of miscibility between the two systems. The model considers Li^+ transport within and between clusters, where the latter is a direct result of PMMA mixing into PEO and occurs at length scales longer that extend beyond the typical size of the first Li^+ solvation shell. This newly acquired understanding of molecular packing, ion solvation behavior, and ion transport model in the context of polymer electrolyte mixtures could help inform future design of combined polymer electrolyte systems.

5.6 Supporting Information

Methods and Force Field Parameters for Molecular Dynamics Simulations

In this study, the TraPPE-UA force field is used for all inter- and intramolecular interactions between polymer atoms.[202–204] Instead of rigid bonds used in TraPPE-UA force field, the generalized CHARMM bonding parameters are used.[124] Compatible all-atom parameters for LiTFSI are adapted from a previous simulation study.[59,206] Figure 5.7 provides reference labels for the different atom types in polymer for assigning the appropriate force field parameters.

The simulations were performed using the LAMMPS package.[208] For all MD simulations, a cutoff radius of 12 Å with Van der Waals tail correction was used for short range Lennard-Jones (LJ) interactions. Long range non-bonded interactions were cutoff at a radius of 12 Å and were handled using the Particle-particle particle-mesh solver with 10^{-4} accuracy.[207] The trajectories were integrated using the velocity-Verlet algorithm with a 1 fs timestep. For NVT simulations, the Nosé-Hoover thermostat with a damping parameter of 100 fs was used. For NPT simulations, the

Nosé-Hoover barostat with a damping parameter of 1000 fs was applied in addition to the thermostat. **United Atom Model: Terminal Groups, Tacticity, and Atom Type Assignments**

The number of chains and number of repeat units for each system are summarized in Table 5.2. The salt concentration for all simulations is ***r*** = Li:EO = 1:20 = 0.05. For PEO segments, the termini are methoxy end groups as noted in (OET-CE3) in Figure 5.7. For PMMA segments, the termini are CH3 that are connected to a CT interaction site. PMMA is this study is atactic. When generating the atactic PMMA chain, the stereochemistry of each chiral center is randomly chosen as S or R with equal probability.

Table 5.2. Summary table of PEO homopolymer, PMMA/PEO blend and PMMA-b-PEO simulations: system composition, polymer chain lengths, and fictive temperature

System	Polymer (MW)	Number of Chains	Number of Repeat Units	r	T_f
PEO	PEO (10K)	120 PEO	30	0.05	246 ± 3 K
Blend	PMMA (10K) / PEO (10K)	60 PMMA, 60 PEO	10 (PMMA), 30 (PEO)	0.05	260 ± 4 K
BCP	PMMA(10K)-b-PEO(10K)	60	10 (PMMA)-b-30 (PEO)	0.05	275 ± 3 K

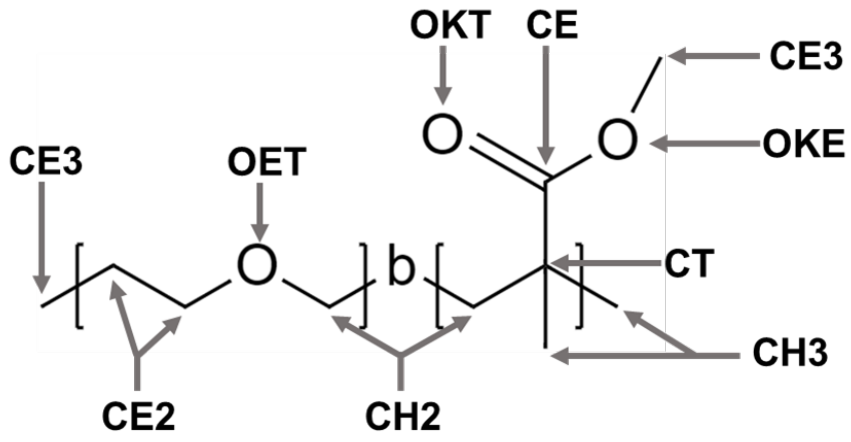

Figure 5.7. Reference labels for atom types in force field parameters.

Non-bonded Interaction Parameters

The nonbonded interactions include Lennard-Jones interactions and Coulombic interactions. For united atoms i and j, their nonbonded interaction is:

$$u_{nb}(r_{ij}) = 4\varepsilon_{ij}\left[\left(\frac{\sigma_{ij}}{r_{ij}}\right)^{12} - \left(\frac{\sigma_{ij}}{r_{ij}}\right)^{6}\right] + \frac{q_i q_j}{4\pi\epsilon_0 r_{ij}}, \quad (5.2)$$

where r_{ij} is the separation distance between atoms i and j, σ_{ij} is the Lennard-Jones diameter, ε_{ij} is the Lennard-Jones interaction strength, ϵ_0 is the vacuum permittivity. q_i and q_j are the partial charges of atoms i and j.

LJ interactions are computed with Lorentz-Berthelot mixing rules. For 1-2, 1-3, and 1-4 bonded interaction sites, the Lennard-Jones interactions are turned off. Coulomb interactions are turned off for 1-2 and 1-3 bonded interaction sites, and scaled by 0.5 for 1-4 bonded interactions. The non-bonded interaction parameters are listed in table .

Table 5.3. : Nonbonded interaction potential parameters for polymer atoms

atom	m (amu)	σ_{ii} (Å)	ϵ_{ii} ($\frac{\text{kcal}}{\text{mol}}$)	q (e)
CE2	14.027	3.950	0.091411	0.25
CE3	15.035	3.750	0.194746	0.25
OET	15.999	2.850	0.109296	-0.50
CH2	14.027	3.950	0.091411	0.00
CH3	15.035	3.750	0.194746	0.00
CT	12.011	6.400	0.000994	0.05
CE	12.011	3.820	0.079488	0.55
OKT	15.999	3.050	0.156989	-0.45
OKE	15.999	2.800	0.109296	-0.40

Bonding Potential Parameters

1-2 bonded united atoms interact via a harmonic bonding potential in the form:

$$u_{bond}(r_{ij}) = k_{bond}(r_{ij} - {r_{ij}}^{(0)})^2, \quad (5.3)$$

where r_{ij} is the separation distance between atoms i and j, k_{bond} is the force constant and ${r_{ij}}^{(0)}$ is the equilibrium bond length. The bonding interaction parameters are listed in Table 5.4.

Table 5.4. Bonding potential parameters for polymer atoms

bond	k_{bond} ($\frac{\text{kcal}}{\text{mol·Å}^2}$)	${r_{ij}}^{(0)}$ (Å)	bond	k_{bond} ($\frac{\text{kcal}}{\text{mol·Å}^2}$)	${r_{ij}}^{(0)}$ (Å)
CE2-CE2	225.0	1.54	CH2-OET	360.0	1.41
CE2-OET	360.0	1.41	CE-CT	200.0	1.52
CE3-OET	360.0	1.41	CE-OKT	360.0	1.20
CH3-CT	225.0	1.54	CE-OKE	360.0	1.34
CH2-CT	225.0	1.54	CH2-CH2	225.0	1.54

Bending Potential Parameters

1-2-3 bonded united atoms interact via a harmonic bending potential in the form:

$$u_{bend}(\theta_{ijk}) = k_{bend}(\theta_{ijk} - {\theta_{ijk}}^{(0)})^2, \quad (5.4)$$

where k_{bend} is the force constant, θ_{ijk} is the angle between united atoms i, j, and k, and ${\theta_{ijk}}^{(0)}$ is the equilibrium angle. The bending interaction parameters are listed in Table 5.5.

Table 5.5. Bending potential parameters for polymer atoms

bend	k_{bend} ($\frac{\text{kcal}}{\text{mol·rad}^2}$)	${\theta_{ijk}}^{(0)}$ (Å)	bend	k_{bend} ($\frac{\text{kcal}}{\text{mol·rad}^2}$)	${\theta_{ijk}}^{(0)}$ (Å)
CE2-OET-CE2	60.0136	112.0	OET-CH2-CT	49.9782	112.0
CE2-OET-CE3	60.0136	112.0	CH2-CT-CE	62.1000	109.5
CE2-CE2-OET	49.9782	112.0	CT-CE-OKT	62.1000	125.0
CH2-CT-CH2	62.1000	109.5	CT-CE-OKE	70.1483	110.0
CH3-CT-CH2	62.1000	109.5	CH3-CT-CE	62.1000	109.5

Table 5.5. Bending potential parameters for polymer atoms, continued.

CT-CH2-CT	62.1000	114.0	CH3-CT-CH3	62.1000	109.5
CE-OKE-CE3	62.1000	115.0	CE2-OET-CH2	60.0136	112.0
OKT-CE-OKE	62.1000	125.0			

Torsional Potential Parameters

The torsional potentials for 1-2-3-4 bonded united atoms take the form:

$$u_{tors}(\phi_{ijkl}) = \frac{K_1}{2}\left[1 + \cos(\phi_{ijkl})\right] + \frac{K_2}{2}\left[1 - \cos(2\phi_{ijkl})\right] + \frac{K_3}{2}\left[1 + \cos(3\phi_{ijkl})\right] + \frac{K_4}{2}\left[1 - \cos(4\phi_{ijkl})\right], \quad (5.5)$$

where c_1, c_2, and c_3 are coefficients and ϕ_{ijkl} is the dihedral angle defined by atoms i, j, k, and l. The torsional interaction parameters are listed in Table 5.6.

Table 5.6. Torsional potential parameters for polymer atoms

torsion	K_1 ($\frac{\text{kcal}}{\text{mol}}$)	K_2 ($\frac{\text{kcal}}{\text{mol}}$)	K_3 ($\frac{\text{kcal}}{\text{mol}}$)	K_4 ($\frac{\text{kcal}}{\text{mol}}$)
CT-CH2-OET-CE2	2.882840	-0.650809	2.218510	0.000000
OET-CE2-CE2-OET	1.888000	-1.888000	0.000000	0.000000
CE2-CE2-OET-CE2	2.882840	-0.650809	2.218510	0.000000
CE2-CE2-OET-CH2	2.882840	-0.650809	2.218510	0.000000
CE2-CE2-OET-CE3	2.882840	-0.650809	2.218510	0.000000
CH3-CT-CH2-CT	0.000000	0.000000	1.833350	0.000000
CH2-CT-CH2-CT	0.000000	0.000000	1.833350	0.000000
CT-CH2-CT-CE	0.000000	0.000000	1.833350	0.000000
CH3-CT-CE-OKT	-0.919280	0.229880	-0.609280	0.000000
CH2-CT-CE-OKT	-0.919280	0.229880	-0.609280	0.000000

Table 5.6. Torsional potential parameters for polymer atoms, continued.

CH3-CT-CE-OKE	0.915310	0.216840	0.609670	0.000000
CH2-CT-CE-OKE	0.915310	0.216840	0.609670	0.000000
CT-CE-OKE-CE3	9.689610	7.678560	1.387070	0.000000
OKT-CE-OKE-CE3	-9.669740	7.376500	-1.045270	0.000000

Simulation Protocol

To prepare the starting configuration, the polymer chains are initiated with random position and orientations in a large box. The polymer chains are first relaxed under NVT ensemble at 500 K for 30 ns. Then a 40 ns NPT equilibration at 500 K and 1 bar is performed for polymer chains to equilibrate and to ensure the bulk density does not drift. The process of introduction of Li^+ is as follows: Li^+ and $TFSI^-$ ions are introduced at random positions in the equilibrated neat polymer at the designated ratio of $r = 0.05$ = [LiTFSI]/[EO]. To remove any steric clashes in the simulation cell, the system is relaxed under NVE ensemble for 10,000 steps, where the maximum displacement of an atom is limited to 0.1 Å per step.

To perform each production simulation, the salt-doped polymer is equilibrated at the designated temperature under NPT for 10 ns. Then the system is further equilibrated for 10 ns under NVT ensemble. In the beginning of this NVT equilibration, the box size is scaled to reflect the ensemble average density during at the last 3 ns of NPT equilibration. Then, the trajectory for analysis is collected from a 100-ns production simulation under NVT ensemble.

Fictive Temperature Determination

To determine the fictive temperature, the polymer is first equilibrated for 20 ns under NPT at 450 K,1 bar and then cooled from 450 K to 100 K at a cooling rate of 10 K/ns at 1 bar. The density is plotted as a function of temperature under NPT ensemble. Two linear segments are fitted

to for the glass and liquid region respectively. The T_g is determined as the intercept of the extrapolated linear fit lines. This procedure to calculate T_g is sensitive to the fitting range of the two segments. Therefore, the end points of the fitting segments are systematically sampled in the following manner. The starting point of the glassy segment was fixed at 100 K, while the end point of the glassy segment was randomly sampled between 150 K and 200 K. Similarly, the starting point of the liquid segment was fixed at 450 K, whereas the end point of the liquid segment was sampled between 300 K and 350 K. The fitting intervals for the glassy segment and the liquid segment are randomly drawn within the sampling interval defined above, the intersections between which yield a set of T_g values. Only T_g values that fall between the end points of fitting segments are kept. The T_g calculation described above was repeated for another independent sample. For each sample, combinations of glassy and liquid fitting ranges are generated 10,000 times. The mean and standard deviation of the set of T_g values collected from both samples are reported. Figure 5.8 includes the cooling curve and the distribution of resulting T_g values collected.

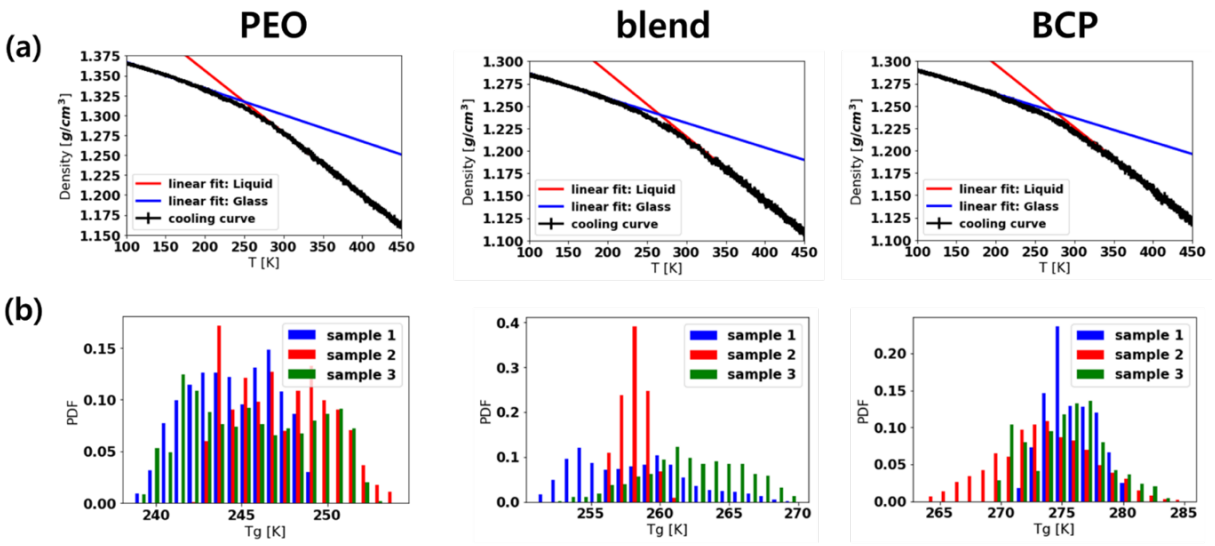

Figure 5.8. Fictive temperatures in simulations. (a) Representative density as a function of temperature for PEO homopolymer, PMMA/PEO blend and PMMA-b-PEO block copolymer, respectively. Example fitting lines for liquid and glassy regions are shown in red and blue, respectively. The fitting range for the example linear fits are [100 K,200 K] for the glassy region and [350 K,450 K] for the liquid region. (b) Normalized histograms of collected T_g values. Histograms from different samples are plotted in different colors.

Comparing Li^+ Mean Squared Displacement between Blend and BCP systems

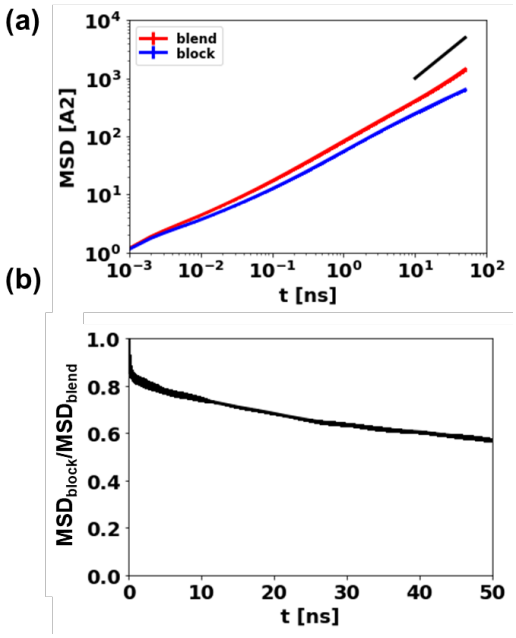

Figure 5.9. (a) Mean squared displacement of Li ion in the studied polymer mixture systems. (b) Ratio of Li ion MSD between blend and copolymer system. The result is obtained at T-T_g = 190 K.

Relaxation Times for Different Components in Polymer Mixtures

To characterize the dynamics of the systems, intermediate scattering functions were computed for EO atoms and Li^+ in three systems of interest. We believe the relaxation of these two types of atoms are critical and representative for the ion transport motions in the material. Then, α and β relaxation times are extracted by fitting the intermediate scattering function to a

$$\boldsymbol{f(x) = A_1 e^{-(\frac{t}{\tau_1})^{\beta_1}} + A_2 e^{-(\frac{t}{\tau_2})^{\beta_2}}}. \quad (5.6)$$

two-step stretched exponential decay in the form

Figure 5.10 compares the α and β relaxation times between the PMMA/PEO blend and PMMA-b-PEO systems. The relaxation times shows that at fixed T-T_g, the relaxation times of EO atoms in the systems are almost identical. The relaxation time of Li^+ is fastest in PEO homopolymer and slowest in PMMA-b-PEO. Overall, identical EO relaxation times suggest that differences in solvation site connectivity are critical for explaining the differences in ion mobility.

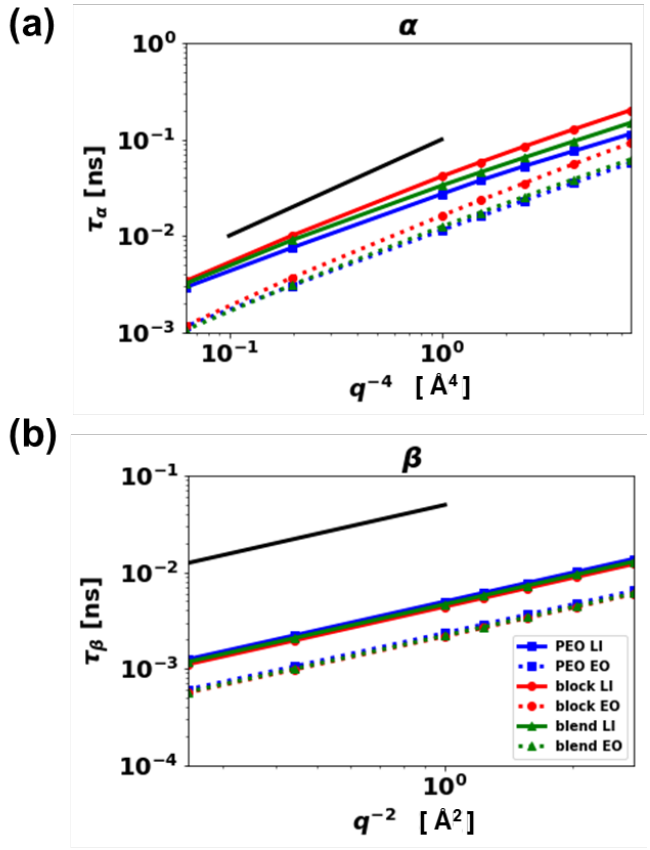

Figure 5.10. α- and β- relaxation times as a function of wavenumber q, extracted from simulated intermediate scattering function for Li^+ (solid) and ether oxygen (dashed) atoms in PEO homopolymer (blue), PMMA/PEO blend (green), and PMMA-b-PEO copolymer (red). (a) α-relaxation times. (b) β -relaxation times. The black lines are references for slope=1.

DSC Thermograms

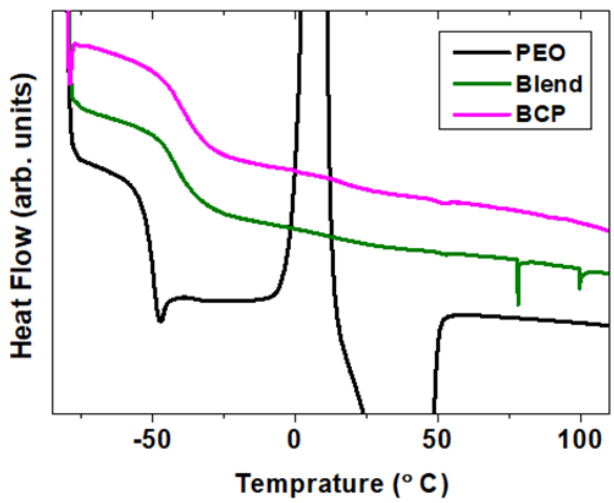

Figure 5.11. DSC thermograms of PEO, PEO/PMMA blend, and PEO-b-PMMA BCP electrolyte systems at r = 0.05. Tg is taken as the midpoint in the inflection in the heat flow rate.

CHAPTER 6

ENTROPIC PENALTY SWITCHES LI^+ SOLVATION SITE FORMATION AND TRANSPORT MECHANISMS IN MIXED POLARITY COPOLYMER ELECTROLYTES

This chapter is modified and reprinted with permission from Deng, C.; Bennington, P.; Sánchez-Leija, R. J.; Patel, S. N.; Nealey, P. F.; de Pablo, J. J.. Entropic Penalty Switches Li^+ Solvation Site Formation and Transport Mechanisms in Mixed Polarity Copolymer Electrolytes. *Macromolecules* **2023**, 56, 19, 8069–8079. https://pubs.acs.org/doi/10.1021/acs.macromol.3c00804.

6.1 Abstract

Emerging solid polymer electrolyte (SPE) designs for efficient Li-ion (Li^+) conduction have relied on polarity and mobility contrast to improve conductivity. To further develop this concept, we employ simulations to examine Li^+ solvation and transport in poly(oligo ethylene methacrylate) (POEM) and its copolymers with poly(glycerol carbonate methacrylate) (PGCMA). We find that Li^+ is solvated by ether oxygens instead of the highly polar PGCMA, due to lower entropic penalties. The presence of PGCMA promotes single-chain solvation, thereby suppressing interchain Li^+ hopping. The conductivity difference between random copolymer PGCMA-*r*-POEM and block copolymer PGCMA-*b*-POEM is explained in terms of a hybrid solvation site mechanism. With diffuse microscopic interfaces between domains, PGCMA near the POEM contributes to Li^+ transport by forming hybrid solvation sites. The formation of such sites is hindered when PGCMA is locally concentrated. These findings help explain how thermodynamic driving forces govern Li^+ solvation and transport in mixed SPEs.

6.2 Introduction

Solid polymer electrolytes (SPE) in Li-ion (Li^+) batteries must exhibit high conductivity, mechanical strength, and high transference number to achieve good cycling performance, fast charging rates, and to prevent Li dendrite growth[49,250]. Poly (ethylene oxide) (PEO) is perhaps the most widely studied polymer host for Li^+ transport to date, and past work has shown that it does not meet these three criteria[217,251]. In attempts to overcome its inherent limitations, PEO is often mixed with other materials to improve conductivity or to incorporate additional functionalities. Previous efforts have sought to blend PEO with plasticizers[184], copolymerize it with high-T_g polymers such as poly (styrene) (PS) to form a phase-separated block copolymer (BCP)[87,89,90,228,252], and copolymerize it with single-ion conductors[86]. These three strategies have been found to increase ionic conductivity, improve mechanical strength, and increase the transference number, respectively.

Studies of mixed liquid electrolytes have shown that polarity and mobility contrast can be combined to improve conductivity relative to that of the pure components[253]. These small-molecule systems typically blend a high-polarity solvent, such as ethylene carbonate (EC), with a low-viscosity solvent, such as dimethyl carbonate (DMC). The high dielectric constant of the former facilitates salt dissociation, whereas the low viscosity of the latter provides a high-mobility medium for Li^+-EC complexes to diffuse. However, achieving this synergistic coupling can be challenging in polymeric systems. This is because ion solvation and transport in mixed SPEs cannot be anticipated solely based on the individual properties of each component. Instead, it emerges from the interplay of multiple factors, such as polarity[254], chemical structure[71,72], miscibility[77,80,235,255], solvation site connectivity[219,256,257], and segmental dynamics[216,219,256], to name a few. On the one hand, in SPE, specific chemical structures can favorably solvate Li^+ despite

a relatively low polarity. Particularly, Li^+ solvation by poly- or oligo-ether motifs is found to be important in the presence of other functional groups having higher polarity. Studies have shown that in poly (oligo ethylene methacrylate) (POEM), Li^+ is primarily solvated by the ether side chains, even if the carbonyl oxygen on the backbone is more polar[219,256]. Similarly, when EC is mixed with an oligoether, the less polar oligoether chains are primarily responsible for solvating Li^+[258]. On the other hand, Li^+ transport occurs through different mechanisms in liquid electrolytes and in SPEs. In a mixed liquid electrolyte, the enhanced Li^+ transport is achieved *via* the vehicular diffusion of Li^+-solvent complexes through a low-viscosity medium[253]. In contrast, in high-molecular-weight SPEs, such vehicular diffusion is inhibited[251] and Li^+ transport occurs through discrete hopping events from one solvation site to another[72,177]. This mechanism in turn relies on both fast segmental dynamics and the connectivity of solvation sites[219,256,257], which can be altered dramatically when polymers are mixed with other components. Studies of Li^+ transport in mixed polymeric materials have been limited, and a mechanistic understanding of the underlying molecular processes is still lacking. Past reports of mixed SPE materials have typically involved a high-T_g, non-conducting polymer mixed with a rubbery ion-conducting polymer to improve the mechanical strength[80,235,239,255,259]. In those systems, the non-conducting components are found to not only slow down the segmental dynamics of the conducting component[80,96,260] but also disrupt the conducting network[235,255,259,260]. As the degree of miscibility increases, interconnected solvation sites tend to disintegrate into clusters. As a result, long-range Li^+ in those blends is often found to involve two timescales, one associated with local Li^+ hopping within a cluster, and another associated with transport between clusters upon network rearrangements[259].

Since the mechanism for Li^+ transport in polymers differs from that in liquid electrolytes, one must consider the specific chemical characteristics of an SPE when designing polarity-

mobility contrast. In this work, we build on the hypothesis that a suitable contrast of mobility and polarity in SPE systems is best achieved when the low-*Tg*, conductive PEO-based polymer is selected as the DMC analog, and a polymer containing highly polar cyclic carbonate groups is selected as the EC analog. In recent experiments from our group, the POEM / poly(glycerol carbonate methacrylate) (PGCMA) pair was shown to provide a desirable contrast of polarity and mobility[260]. Perhaps counterintuitively, experiments indicate that in LiTFSI-doped PGCMA-r-POEM, the highly polar cyclic carbonate interacts with the Li ions only minimally, and the polyether segments are responsible for Li^+ solvation. Because the presence of PGCMA suppresses chain mobility without improving ion dissociation, the overall conductivity of PGCMA-r-POEM is lower than that of the POEM homopolymer electrolyte.

To gain a better understanding of Li^+ solvation and transport in PGCMA-r-POEM, we resort to atomistic molecular dynamics (MD) simulations and compare POEM and PGCMA-r-POEM (Figure 6.1), each blended with LiTFSI salt at $r = 0.05$. We find that the slowdown of the overall chain dynamics due to PGCMA can be corrected via a simple renormalization by the T_g of the mixture. A subsequent analysis of the underlying structures reveals that Li^+ solvation by the highly polar PGCMA is rare and transient. In contrast, Li^+-ether solvation is entropically favored. This suggests that entropic penalties, which can be pronounced in SPEs, lead to fundamentally different solvation tendencies compared to those encountered in liquid electrolytes. Our findings also show that the diluting effects of PGCMA suppress inter-chain hopping by promoting single-chain solvation, thereby decreasing the efficiency of solvating oxygens for Li^+ transport. This concept is developed by studying PGCMA-b-POEM, where one can observe the formation of local compositional fluctuations or small domains. In PGCMA-b-POEM, the formation of solvating sites is further decreased with respect to that in the random copolymer; transient PGCMA-rich

regions are inactive for transport and interrupt the connectivity of solvation sites in favor of isolated clusters. More generally, the results presented in this work provide a direct characterization of how local heterogeneities and mixing influence local and long-range Li^+ transport in mixed SPEs, thereby providing useful principles for the design of new SPEs systems.

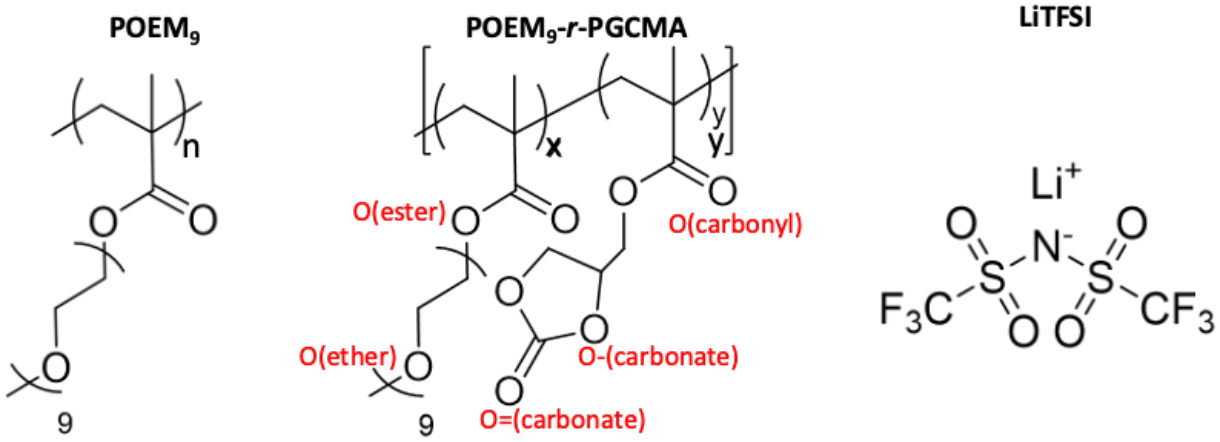

Figure 6.1. Chemical structure of POEM, POEM-*r*-PGCMA, and LiTFSI salt. Salt concentration is determined as $r = [Li^+]/([EO]+[OCOO]) = 0.05$. Different oxygen types are labeled in red.

6.3 Methods

United Atom Model and Partial Charge Assignments

The polymers considered here are represented by united atoms. For POEM units, all interaction parameters are taken from an adapted Trappe-UA force field[202–204], previously validated to match the experimental properties, including density, of PEO[205]. Li^+ and $TFSI^-$ are represented by a compatible all-atom model [59,261]. For the cyclic carbonate units, the bonded parameters and the short-range Lennard-Jones (LJ) parameters are adopted from the Trappe-UA force field[203,204,262,263] and a cyclic carbonate force field[264]. The LJ parameters of the cyclic carbonate are scaled to match the Li^+-O=(carbonate) radial distribution function[265] and densities of liquid EC and PC measured in experiments[264]. Partial charges for polymer interaction sites are refined through *DFT* calculations using a B3LYP functional and the 6-31G(d,p) basis set,

performed with the GAUSSIAN 09 program[266]. The charge fitting uses the ChElPG calculation scheme[267]. A charge scaling of 0.7 is applied to Li^+ and $TFSI^-$ as a mean-field treatment for polarization effects[268]. Detailed force field parameters, a protocol for partial charge assignment, and procedures for initial configuration generation are provided in the SI.

MD Simulation Parameters

The simulations are performed using the LAMMPS package[208]. For LJ interactions, a cutoff radius of 12 Å with Van der Waals tail correction is used. The long-range coulombic interactions use a cutoff radius of 12 Å and are handled using the Particle-particle particle-mesh solver with 10^{-4} accuracy[207]. The trajectories are integrated using the velocity-Verlet algorithm with a 1 fs timestep. For NVT simulations, the Nosé-Hoover thermostat with a damping parameter of 100 fs is used. For NPT simulations, the Nosé-Hoover barostat with a damping parameter of 1000 fs is applied in addition to the thermostat. Additional details about the simulation procedures are included in the SI.

6.4 Results and Discussion

In this section, we present simulation results that compare ion solvation tendencies and transport in LiTFSI-doped PGCMA-*r*-POEM (50 wt.%) to that in the POEM homopolymer electrolyte. Figure 6.1 shows the chemical structures and introduces the nomenclature for different oxygen types used in this study. Here the salt concentration is $r = [Li^+]/([EO]+[OCOO]) = 0.05$, under the assumption that both O(ether) and O=(carbonyl) are expected to be potential Li^+-solvating units. The rest of the Results and Discussion section is organized as follows: in the first two parts, we compare the ion-segmental dynamics and ion solvation, respectively, before and after the incorporation of PGCMA. the third part examines the implication of the altered ion solvation

tendency, due to the presence of PGCMA, on Li^+ transport mechanisms locally and over the long range.

6.4.1 Reduced Ion Mobilities

In SPEs, Li^+ conductivity is intrinsically coupled to the segmental dynamics of the polymer matrix, typically described via the Vogel-Fulcher-Tammann (VFT) equation[51,80]. This is due to the intersegmental hopping of Li^+, which is the major transport mechanism in SPEs and relies on conformational rearrangements of ion-solvating segments[177]. We first compute the fictive glass transition temperature (T_f) of PGCMA-*r*-POEM and POEM (Table 6.1). Experimentally, the addition of 40 wt.% PGCMA was reported to raise the T_g by *ca.* 50 K[260]. Consistent with experiments, the simulated T_f is increased by 37 K after 50 wt.% PGCMA is incorporated into the mixed system. To isolate any intrinsic effects of side-chain architecture and copolymer polarity, our production simulation runs are performed at a fixed temperature relative to the T_f of the mixture to account for differences in the average segmental mobility of the materials.

Figure 6.2 summarizes the simulated diffusion coefficients of ions in POEM and PGCMA-*r*-POEM at fixed temperatures above T_f. The two materials show significant differences in ion diffusion after normalizing with respect to T_f, suggesting that additional mechanisms beyond segmental dynamics and the VFT equation are involved. Figure 6.2A presents the mean squared displacements (MSD) of Li^+ for different time intervals. For time intervals below 1 ns, Li^+ motion is sub-diffusive, as indicated by a slope of less than unity on a log-log scale. At timescales greater than 10 ns, Li^+ motion is diffusive, as indicated by a unit slope. The self-diffusion coefficients of Li^+ (D_{Li}) and $TFSI^-$ (D_{TFSI}), obtained by performing a linear fit to the MSD, are reported in Figure 6.2B as a function of reduced temperature. At 50-250 K above T_f, the diffusion coefficient of Li^+ ranges between 1 and 10 $\cdot 10^{-7}$ cm^2/s. At r =0.05, which corresponds to a relatively dilute salt

concentration, the correlated motion between cations and anions is found to be negligible (Figure 6.12); the sum of D_{Li} and D_{TFSI} is therefore directly proportional to the equivalent conductivity via the Nernst-Einstein equation[177]. Figure 6.2C reports the ratios of the diffusion coefficients in PGCMA-*r*-POEM to those in POEM. At 50 and 150 K above T_f, the Li^+ diffusivity in PGCMA-*r*-POEM is reduced by 45%, and the $TFSI^-$ diffusivity is reduced by roughly 64%, leading to a drop in conductivity of approximately 60%. The simulated results for ionic diffusivity are consistent with the experimental conductivity measurements reported by Bennington et al.[260], where a 2-fold decrease was observed in PGCMA-*r*-POEM with a similar composition (58 wt. % of POEM) at a similar reduced temperature above T_g. As the temperature increases to 250 K above T_f, the reduction in ion diffusivities becomes less prominent.

The following analysis examines how the transport of Li^+ occurs in PGCMA-*r*-POEM by dissecting the local segmental motions and the solvation environment of Li^+.

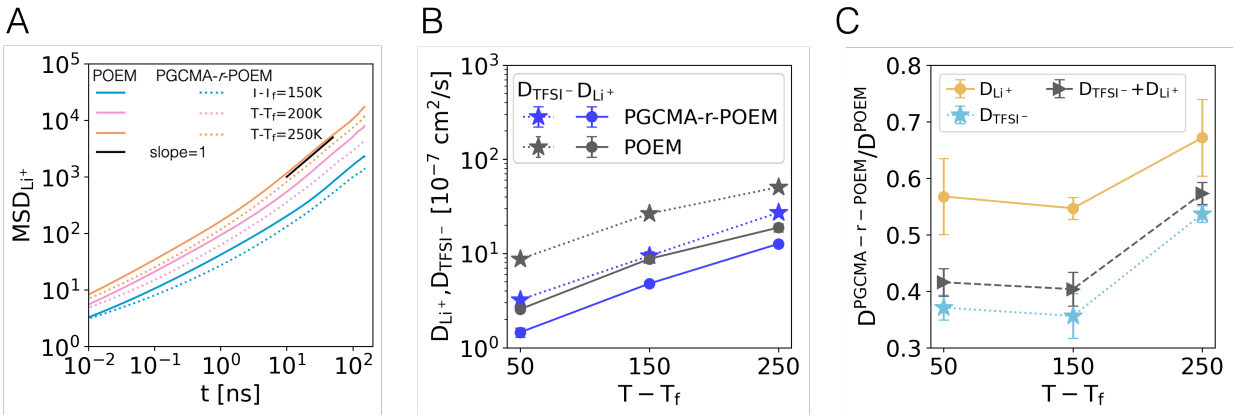

Figure 6.2. (A) Mean Squared Displacements (MSD) of Li^+ in POEM and PGCMA-r-POEM at 150 K, 200 K, and 250 K above their fictive temperature, T_f. (B) Diffusion coefficients of Li (D_{Li}) and TFSI (D_{TFSI}) in POEM and PGCMA-r-POEM. MSD between 20 ns and 120 ns are used to determine the diffusion coefficients using the Einstein relation. The error bars are estimated based on the difference in the diffusion coefficient obtained from fits over the first and second halves of the fit interval. (C) Ratio of diffusion coefficients in POEM and PGCMA-*r*-POEM. Error bars in (C) are based on propagation from (B).

6.4.2 Segmental Mobilities

Renormalizing the temperature by T_g is generally effective for explaining the effect of segmental dynamics on ionic conductivity. For systems with side-chain architectures such as POEM, however, our recent work suggests that this is not the case. In POEM, the segmental dynamics vary along the ether side chain, which incorporates the ion-solvating segments that are most critical for Li^+ transport[219,256]. Because T_f and T_g reflect the average dynamics of the entire system, they fail to provide complete information about individual relaxation modes along the ether side chain. Apart from the side chain architecture, the mixing of glassy and mobile components is also thought to affect local segmental mobility[96,239,259]. In the PGCMA-*r*-POEM copolymer, PGCMA units could conceivably slow down the segmental motions in their immediate vicinity. To examine the rate of each relaxation mode along the side chains, we compute the bond vector autocorrelation function (BVAF) for each C-O(ether) bond along the side chain[219,256]. This function quantifies how fast a vector connecting two bonded atoms becomes decorrelated from its initial orientation. Each BVAF is fitted to a stretched exponential function of the form $BVAF(t) = e^{-(t/\tau)\beta}$, whose first moment is given by $\langle\tau\rangle=(\beta/\tau)\Gamma(\beta-1)$. The inverse mean relaxation time, $1/\langle\tau\rangle$, is used to describe the local segmental mobility. Figure 6.3 compares the local segmental mobility along the side chain at three reduced temperatures. It increases with temperature as a result of faster side chains (positions 1-9), rather than more mobile backbones (position 0). At each temperature, ethers 1-3 in the random copolymer exhibit slower segmental mobility, possibly due to the presence of the PGCMA side chain, whereas ethers 4-7, the ion-solvating segments along the POEM side chain (Figure 6.13 and ref.219), exhibit similar mobilities to those observed in POEM. Overall, despite the presence of the PGCMA pendant group, the segmental mobility of the backbone and that of the ion-solvating group are identical in POEM and the RCP. Segmental dynamics can be thought

to affect ion transport at two length scales[259]. At the length scale of an immediate solvation shell (below 5A), Li^+ hopping between solvation sites is assisted by fluctuations in the local solvation structure. Beyond that scale, the long-range transport of Li^+ requires consecutive hopping events capable of traversing the solvation site network. Such a process is expected to benefit from a fast reorganization of the entire network of solvation sites[257]. The unaffected backbone relaxation after the addition of PGCMA suggests that the rate of solvation site network reorganization in the two systems is also comparable once the temperature is renormalized by T_g. To understand the origin of a factor of 2 difference in ion diffusivity between the two materials, whose local segmental mobilities are similar, we contrast their Li^+ solvation environments, including both the immediate solvation structure and the network of viable solvation sites.

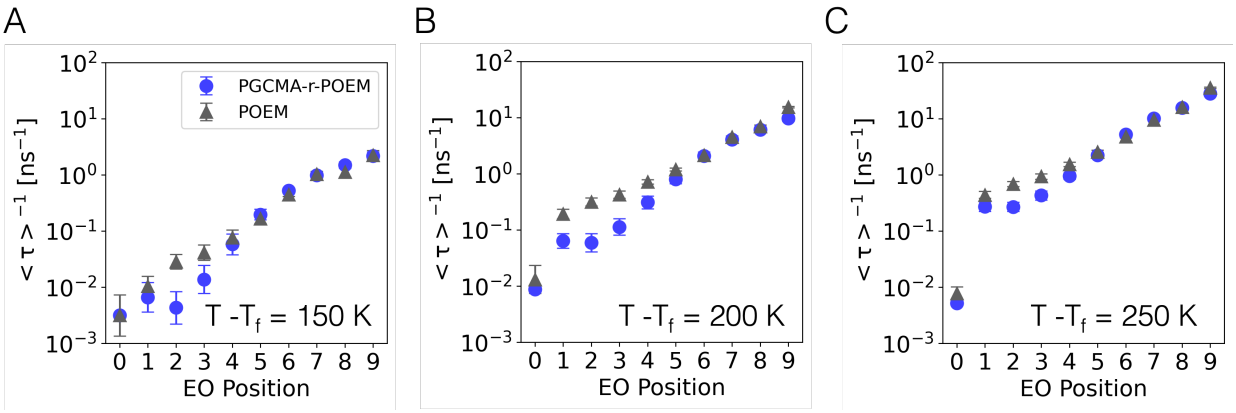

Figure 6.3. Inverse mean relaxation time extracted from BVAF for different ether oxygens along an OEM sidechain in POEM and PGCMA-*r*-POEM at (**A**) T-T_f=150 K, (**B**) T- T_f=200 K, and (**C**) T- T_f=250 K. An EO position of 1 refers to the ether oxygen that is closest to the backbone. The EO position of 0 refers to the backbone.

6.4.3 Entropic Favorability of Li+ Solvation by Ether Segments

In mixed systems with synergistic solvent polarity and mobility, the high polarity facilitates salt dissociation, and the slower mobility is minimally coupled to ion diffusion or is offset by increases in the concentration of free carriers[51,254,269]. From simulations, the dipole moment of the cyclic carbonate group is estimated to be 5.14 Debye and that of the C-O-C ethylene oxide group is

around 1.83 Debye (Figure 6.10). The added cyclic carbonate groups increase the dielectric constant from 4.83 for the POEM homopolymer to 7.85 for PGCMA-*r*-POEM. Equations used for dielectric constant are included in the SI. As has been shown in various studies, increased dielectric constant tends to reduce the correlated motion of oppositely charged ions[52,270]. Experimental studies of PGCMA-*r*-POEM, however, reveal that despite a high polarity, the cyclic carbonate group does not improve salt dissociation, and does not interact with Li^+ to any significant extent[260]. To gain insights into Li^+ solvation in these materials, we begin our analysis by computing the radial distribution function between Li^+ and different oxygen types, which we identify as potential coordinating sites. Figure 6.4A compares the sizes and compositions of the first solvation shells of Li^+ in POEM and PGCMA-*r*-POEM. In both systems, the first solvation peaks occur at around 2.0 Å, and the size of the first solvation shell, delineated by the first minimum, is determined to be *ca*. 3.25 Å. The first solvation shell consists of O(ether), O(TFSI), and O=(carbonate), each contributing differently, as indicated by their different peak heights. Additionally, we note that although the carbonyl oxygens in both the methacrylate group and the carbonate group are more polar than the O(ether), these carbonyl oxygens are absent in the first solvation shell.

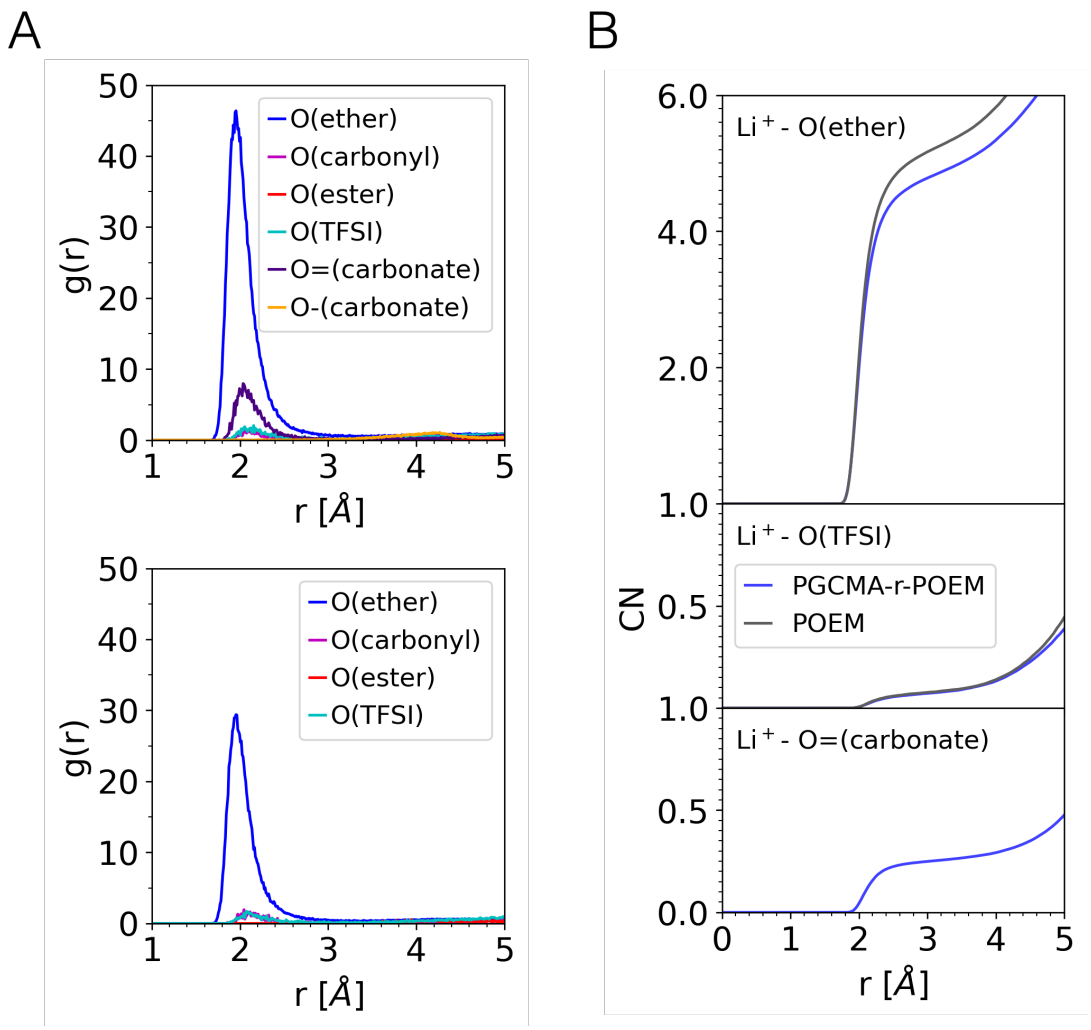

Figure 6.4. (A) Radial distribution functions between Li^+ and oxygen atoms in POEM (top) and PGCMA-*r*-POEM (bottom). (B) Coordination numbers $CN_{ij}(r)$ in POEM and PGCMA-*r*-POEM between Li^+ and O(ether) (top), O(TFSI) (center), and O=(carbonate) (bottom).The results are obtained at 150 K above T_f.

To compare the first solvation shell compositions in POEM and PGCMA-*r*-POEM, we present their coordination numbers for each type of oxygen in Figure 6.4B. In both materials, O(ether) predominately solvates Li^+ with a coordination number of around 5. However, compared to those in POEM, the Li^+-O(ether) and Li^+-O(TFSI) coordination in PGCMA-*r*-POEM both decrease by a small percentage and are replaced by Li+-O=(carbonate) coordination. The added cyclic carbonate groups, which were expected to facilitate salt dissociation, decrease the

interaction between Li^+ and $TFSI^-$ only slightly. The degree of salt dissociation depends strongly on Li^+-O(ether) interactions. In our simulations, the O=(carbonate) carries -0.5105 *e*, the O(ether) carries -0.4757 *e*, and the O(TFSI) carries -0.371 *e*, where *e* is the elementary charge. The relative contributions from O=(carbonate) and O(TFSI) are closely related to their negative partial charges in our model. Such an argument, however, is not sufficient to explain why O(ether) is the major Li^+-solvating oxygen despite its relatively low polarity. Our simulations, performed for two alternative sets of partial charge assignments, lead to similar observations and are discussed in the 6.6.

Despite the general expectation that ion dissociation is favored by high-polarity solvents, some specific chemistries have been reported to enhance solvation, even in the presence of other highly polar groups. For example, a study on polyether-polycarbonate copolymers reported that solvation by ether groups, particularly side-chain ethers, was favored over more polar carbonate groups[72]. Similar findings were observed in studies on POEM, which showed that Li^+ was exclusively solvated by ether groups, not by the more polar carbonyl oxygens of the methacrylate backbone[219,256]. Salt dissociation processes can be viewed as a competition among three thermodynamic driving forces: an unfavorable increase in enthalpy (lattice energy) from breaking up the underlying "lattice", a favorable decrease in enthalpy due to the interaction between ions and the solvent, and a favorable increase in entropy due to mixing. While high solvent polarity produces enthalpic gains, an additional entropy penalty arises in ion-polymer solvation due to several mechanisms. First, we note that entropy gains from mixing are usually small in generic polymer systems[271]. Second, there is an entropic penalty for a high concentration of dissociated ions, because they restrict the polymer conformation space by acting as crosslinking sites and by forming solvation structures with polymer segments that require specific chain conformations[50,272].

These thermodynamic driving forces for Li^+ solvation explain the respective solvation tendencies of the POEM and PGCMA units in studied materials. For PGCMA units to solvate a Li^+, approximately four cyclic carbonate side chains must orient themselves towards the Li^+. Additionally, each solvation results in four anchored carbonate side chains, leading to additional conformational restrictions. In contrast, a single POEM side chain can readily supply nine contiguous ether oxygens to solvate one Li^+. The conformational change upon Li^+ solvation is minimal, and such single-segment ether solvation does not lead to the entropic penalty associated with cross-linking. The phenomenon discussed above can be better understood via a chelating mechanism, in which a polydentate ligand is more entropically favorable than a monodentate ligand and thus has a higher affinity for the binding ion. In that context, a POEM side chain can be considered to be a polydentate ligand for Li^+, whereas a cyclic carbonate side chain is monodentate. Zhang et al. provided a similar argument for a series of glyme-LiTFSI ionic liquid electrolyte systems[273].

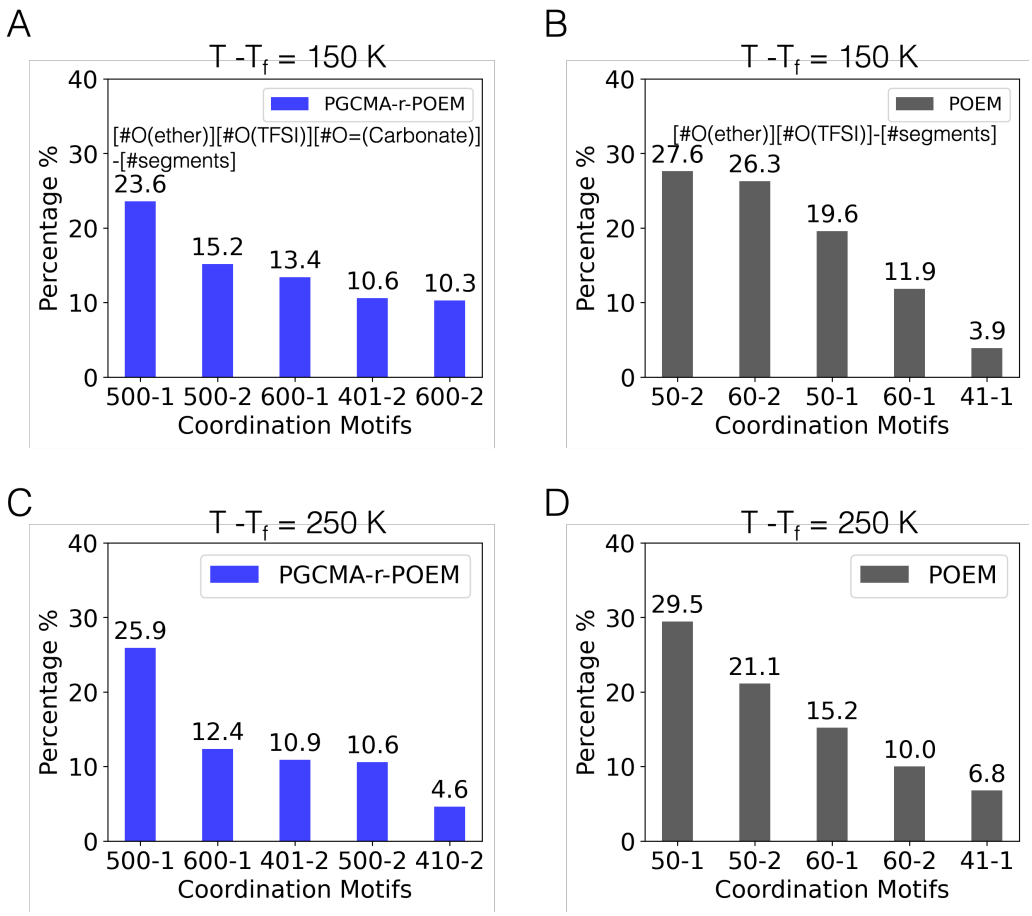

Figure 6.5. (A-B) Population of the five most abundant Li^+ coordination motifs in (A, C) PGCMA-*r*-POEM and (B, D) POEM. The simulations are at (A, B) T- T_f = 150 K and (C, D) T- T_f = 250 K. The binding motif denotes the counts of different oxygens present in the first solvation shell of Li^+ and the number of coordinating segments. For PGCMA-*r*-POEM, the first three digits refer to the count of O(ether), O(TFSI), and O=(carbonate), respectively. For POEM, the first two digits refer to the count of O(ether) and O(TFSI), respectively. The digit following the dash refers to the number of coordinating chains. For example, 401-2 in PGCMA-*r*-POEM indicates a first solvation shell consisting of four ether oxygens from one OEM side chain, zero oxygen from TFSI anions, and one oxygen from a cyclic carbonate side chain. The presence of each TFSI molecule is treated as one segment. The presence of each O=(carbonate) is treated as one segment.

The favorability of Li^+ solvation by ether molecules is further supported by the underlying populations of solvation motifs. Solvation motifs describe the immediate environment of Li^+ and include the count of each type of oxygen and the number of solvating segments. Note that the number of solvating segments is included as an important criterion for two reasons. First, it indicates the extent of cross-linking effects, and its statistics provide insights into the role of

entropic driving forces on Li^+ solvation. Second, it gives insights into the relative importance between the two major Li^+ transport mechanisms: inter-chain and intra-chain hopping[177,219]. Previous studies have shown that in POEM, intra-side chain hopping is fast but local, while long-range Li^+ transport relies on inter-side chain hopping[72,274]. Although Li^+ hopping is a dynamic process, the time-averaged statistics on single-chain solvation versus multichain-solvation can still provide helpful information about the relative importance of the two hopping mechanisms. Figure 6.5 presents the population of the five most abundant Li^+ solvation motifs in POEM and PGCMA-*r*-POEM at two temperatures. These results show that Li^+ is primarily solvated by 5-6 ether oxygens. In PGCMA-*r*-POEM, the O=(carbonate) exhibits a slightly higher affinity to Li^+ than O(TFSI) does. Two-chain solvation is more likely to occur at low temperatures, and decreases at elevated temperatures. Similarly, at a fixed temperature, two-chain solvation is more favorable in the POEM homopolymer than in the PGCMA-*r*-POEM copolymer. This highlights the impact of entropy on Li^+-ether solvation, as both temperature increase and dilution amplify the entropic contributions to the total free energy. Note that single-chain solvation is preferred over two-chain solvation as the latter forms temporary cross-links that restrict polymer conformation and lead to a higher entropic penalty. The temperature dependence of the entropic driving force explains why single-chain solvation is favored at elevated temperatures. This trend towards single-chain solvation as temperature increases is also observed in the PEO/LiI system[50]. In the context of the chelate effect, the entropic favorability of multidentate ligands allows their binding to metal ions to be more resistant to dilution. In such materials, single-chain solvation involves a single POEM side chain donating six O(ether) to a Li^+, whereas two-chain solvation involves two side chains each donating three O(ether) to the Li^+[219]. The higher number of solvating sites provided by the single side chain yields a stronger chelate. This is why single-chain solvation is favored in the

copolymer, where the addition of PGCMA segments dilutes the concentration of solvating O(ether).

The arguments presented above are also supported by past reports. For example, in a linear PEO-polycarbonate system, Li^+ is reported to be solvated mainly by the carbonate group and not by the ether segments, which are linearly copolymerized with the carbonate groups and take up only 30 mol%[275]. This is because these ether segments are frequently interrupted by carbonate units such that Li^+-ether solvation does not benefit from any entropic favorability. A separate study reported that when PGCMA-*r*-POEM is swollen with 1:1 EC: DMC solvent, Li^+ tends to be mainly solvated by the small-molecule EC solvent and only partially by the ether segments from the polymer matrix[276]. These results suggest that the interaction between Li^+ and cyclic carbonate groups varies depending on whether it is a small molecule or part of the polymer, and that solvation by the former involves a favorable entropic gain when solvating Li^+.

In contrast to liquid electrolytes, where the high polarity of EC facilitates salt dissociation, the role of cyclic carbonate groups in SPEs is less explicit. They are rarely found in the Li^+ solvation shell in PGCMA-r-POEM, but their presence dilutes the Li^+-solvating ether segments, leading to a shift in solvation preferences from two-chain solvation to single-chain solvation. This shift is expected to reduce the long-range transport of Li^+ by suppressing inter-chain hopping. When the shift is due to a temperature increase, its adverse effect on Li^+ transport is offset by a significant increase in segmental dynamics. However, if the shift is caused by the dilution of ether segments at fixed segmental dynamics, a reduction in the rate of Li^+ hopping is expected, especially inter-chain hopping.

6.4.4 The Impact on Li+ Hopping Mechanisms

To further characterize how the presence of O=(carbonate) in a coordination shell affects Li^+ transport, we calculated the coordination autocorrelation function (CACF), which quantifies how fast a Li^+ escapes from its current coordination environment[216,219]. It is defined as

$$\mathrm{CACF}(t) = \left\langle \frac{|S(t) \cap S(0)|}{|S(0)|} \right\rangle, \tag{6.1}$$

where S(0), S(t) denote the sets of atoms present in the first solvation shell of a Li^+ at a starting time point and at a future time point t, respectively. ∩ is the intersection operator, |…| is the cardinality of the set, and á…ñ denotes an ensemble average over time origins and Li^+ instances. The CACF defined here is an intermittent correlation function, since the set of solvating oxygens is compared at the two ends of the time interval of interest. Figure 6.6A compares CACFs contributed by different oxygen types, which are determined as follows. The CACF for O=(carbonate) considers the decorrelation when the solvation shell at either time point contains O=(carbonate). The CACF of O(ether) considers the decorrelation when the solvation shells at both time points contain only O(ether). Our results show that the overall decorrelation in PGCMA-r-POEM is mostly due to the decorrelation from O(ether) solvation shells, while the decorrelation from O(carbonate) solvation shells is extremely fast and does not contribute much to the overall decorrelation. This is caused by the lower Li^+-O=(carbonate) coordination number compared to Li^+-O(ether), leading to frequent replacement of the Li^+-carbonate coordination, while the majority of the solvation shell, *i.e.* Li^+-O(ether) coordination, remains unchanged. The small contribution of the carbonate CACF to the total CACF supports the idea that the replacement of O=(carbonate) in a solvation shell does not lead to Li^+ displacement via hopping, but instead Li^+ movement relies on the slower replacement of O(ether), which is rate-limiting. The rate-limiting decorrelation of the Li^+-O(ether) solvation shell is due to both interchain and intrachain hopping. Figure 6.6B

compares CACFs contributed by each mechanism in POEM and in PGCMA-r-POEM. The CACF of interchain hopping considers the decorrelation when the set of side chains involved in S(t) is different from that involved in S(0). In both systems, the first coordination shell members appear to be fully decorrelated after 30 ns. The total CACF decay is largely due to the decay of the interchain CACF, while the intrachain hopping contribution is small; a Li^+ that is typically solvated by five O(ether) along a side chain can only hop by a maximum of four O(ether) units on the same side chain. We find that the total decorrelation is faster in POEM compared to PGCMA-r-POEM, and this difference in total CACF mainly results from the difference in interchain hopping rates.

To summarize, the analysis of the CACF indicates that Li^+ solvation by carbonate is transient and does not impact the overall CACF. Instead, the slower decay of the overall CACF in PGCMA-r-POEM is due to suppressed interchain hopping among O(ether) solvation sites.

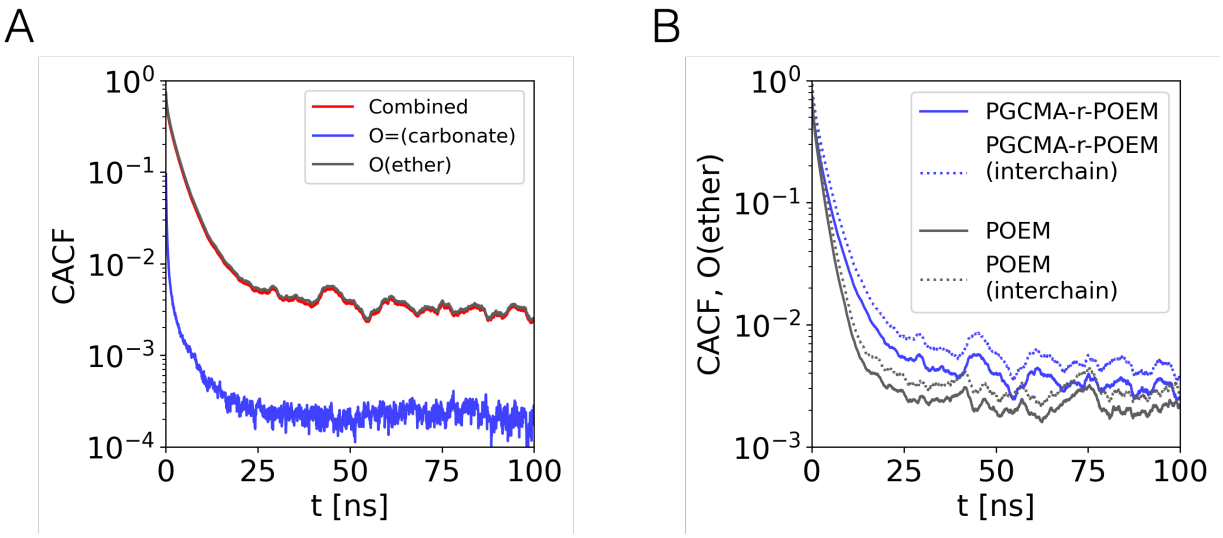

Figure 6.6. Coordination autocorrelation functions at T-Tf = 250 K. (A) The total CACF and its breakdown into O(ether) contribution and O=(carbonate) contribution in PGCMA-r-POEM. (B) Total CACF by O(ether) and their interchain O(ether) contribution in PGCMA-r-POEM and POEM. The total autocorrelation function considers both intra-side chain and inter-side chain changes in the Li^+ first solvation shell members. The interchain autocorrelation functions only consider replacements of Li^+ first solvation shell members by oxygens from different side chains.

6.4.5 Hybrid Solvation Sites Facilitate Their Network Percolation

The concept of solvation site connectivity, introduced in recent studies, describes the concentration and spatial arrangement of Li^+-solvating units in SPEs and provides a useful tool to connect the molecular structure of the SPE and its ability to transport Li^+[77,257]. Past reports have shown that differences in conductivity can be explained by differences in connectivity, provided that differences in segmental mobility are accounted for[77,219,256]. In what follows we rely on solvation site connectivity to quantify the diluting effects of the added PGCMA on Li^+ transport. We begin our analysis by identifying viable solvation sites according to previously reported protocols[77,219,256]. Our calculations include all oxygen types in the polymer that participate in the first Li^+ solvation shell, including O=(carbonate). In Figure 6.7A-B, representative snapshots of identified solvation sites illustrate that the number density of solvation sites is lower in PGCMA-*r*-POEM than in POEM. Both systems, however, exhibit viable solvation sites that are distributed evenly throughout the simulation box. The corresponding connectivity κ is $(3.94 \pm 0.89) \times 10^{-4}$ in PGCMA-*r*-POEM, half of that of POEM $(7.85 \pm 1.15) \times 10^{-4}$. This ratio is consistent with the reported two-fold difference in conductivity observed in experiments[260].

To further probe how Li^+ transport occurs in mixed SPEs, we extend our investigation to include the block copolymer PGCMA-*b*-POEM, which exhibits near identical segmental dynamics to those of the random copolymer but lower miscibility between POEM and PGCMA units. The idea of varying degrees of miscibility has been employed in a recent study to probe Li^+ transport in PEO/PMMA mixture electrolytes, because in those materials the PEO and PMMA segments coexist in a single phase macroscopically, while their local concentrations fluctuate depending on the degree of miscibility[259]. That study reported that an increased degree of miscibility worsens the conductivity by encouraging the solvation sites to group into isolated clusters at a critical length

scale of 5-15 Å. In this study, the random and block copolymers exhibit pronounced differences in interchain packing at the same length scale, with the random copolymer being better mixed (Figure 6.14). In contrast to that study, for the PGCMA/POEM pair examined here, experiments find an opposite trend in conductivity: the more mixed random copolymer PGCMA-*r*-POEM exhibits higher conductivity than the block copolymer PGCMA-*b*-POEM[260]. Since local mixing leads to an inhomogeneous distribution of Li^+ solvation sites, characterizing Li^+ transport in mixed SPE requires an analysis that goes beyond solvation site connectivity.

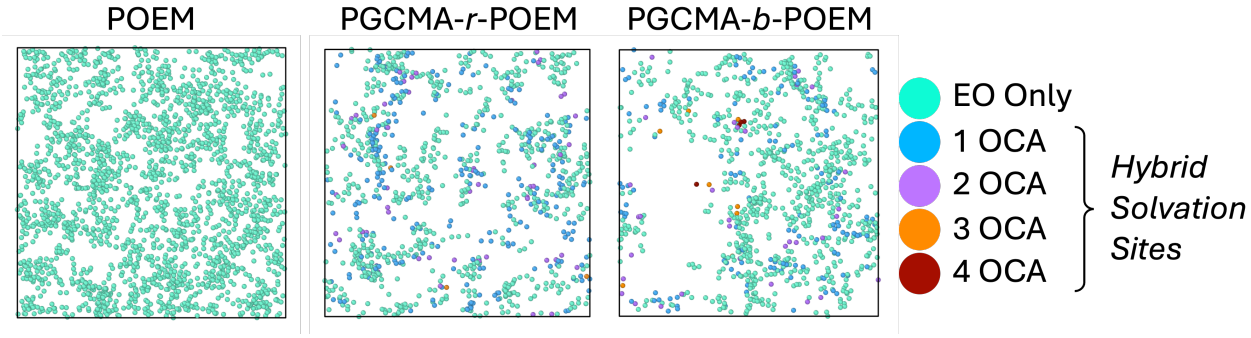

Figure 6.7. Visualization of viable solvation sites in (A) POEM, (B) PGCMA-*r*-POEM, and (C) PGCMA-*b*-POEM. The simulations are at T- T_f = 150 K. In (A), the viable solvation sites are colored by O=(carbonate) composition: cyan sites are O(ether) only; blue, purple, orange, and red sites are hybrid sites containing one, two, three, and four O=(carbonate), respectively.

The viable solvation sites can be further categorized based on their compositions of O(ether) and O=(carbonate), to highlight the relative contribution of each. Figure 6.7B indicates that in PGCMA-*r*-POEM, the PGCMA and POEM units mix to form hybrid viable solvation sites that include both O=(carbonate) and O(ether) over a wide range of compositions, as revealed by an abundance of blue, purple, and orange sites in the figure. This suggests that the solvation site network in PGCMA-*r*-POEM can percolate through a mixture of O(ether)-only sites and hybrid sites. In contrast, Figure 6.7C shows that in PGCMA-*b*-PMMA, the viable solvation sites are found to be either O(ether) only (cyan sites) or contain many O=(carbonate) (orange and red sites), whereas hybrid sites that contain only one or two O=(carbonate) are less frequent. In contrast,

Figure 6.7C shows that in PGCMA-*b*-PMMA, the majority of the identified viable solvation sites contain zero or only one O=(carbonate), whereas hybrid sites are rare. Visually, the distribution of these solvation sites also reflects a greater contrast of the local concentration in the block copolymers, where the ether-dominant sites tend to be in certain regions, while other areas are nearly void of solvation sites. Even in domains rich in PGCMA, few 4-carbonate solvation sites are found, possibly due to a higher steric hindrance associated with forming the all-carbonate solvation sites, despite the fact that sufficient O=(carbonate) are present. These isolated sites are possibly unreachable by the Li^+ from other solvation sites. Because patches of PGCMA-rich domains in the block copolymer do not help with Li^+ solvation or transport, the overall solvation network is no longer connected. This is different from what is observed in liquid electrolytes, where Li^+ solvation by four carbonate units is common due to minimal steric hindrance. Finally, these results also reveal the critical role of interfacial sharpness in the formation and arrangement of viable solvation sites in the materials considered here. A diffuse interface between PGCMA-rich and POEM-rich domains allows O=(carbonate) to join the formation of hybrid solvation sites and leads to an overall denser and interconnected network, whereas a sharp interface effectively restricts the participation of O=(carbonate) in Li^+ solvation.

The trends outlined above for the composition of viable solvation sites is consistent with the population distribution of Li^+ coordination motifs discussed earlier. The two concepts differ slightly in that viable solvation sites are geometric centroids of groups of solvating oxygens that could host Li^+, whereas the coordination motifs correspond to the actual first solvation shells formed with Li^+. Figure 6.15 and Figure 6.5A report the population of the five most abundant Li^+ coordination motifs in the block and random copolymers, respectively. A comparison between them shows that the population distribution of the top three motifs is nearly identical. However,

the hybrid coordination motif 401-2, which involves four O(ether) from a POEM side chain and one O=(carbonate), is less frequent in the block copolymer than in the random copolymer. In the block copolymer, this hybrid motif is overtaken by the all-O(ether) motif 600-2. To further quantify the utilization of Li^+-solvating oxygens for solvation and transport, we compare the participation rates of O(ether) and O=(carbonate) in forming viable solvation sites. In PGCMA-*r*-POEM, 85 ± 1% of the total O(ether) population and 41 ± 3% of the total O=(carbonate) population are expected to form viable solvation sites. In PGCMA-*b*-POEM, the participation rates are 83 ± 1% and 27 ± 3% for O(ether) and O=(carbonate), respectively. For reference, in POEM the participation rate for O(ether) is 90 ± 1%. While the participation rate for O(ether) is consistently high across the three materials, there is a statistically significant reduction in O=(carbonate) participation in the block compared to the random copolymer. It is important to note that small-angle X-ray scattering data for the block copolymer indicates a characteristic length scale of 20 Å for local concentration fluctuations[260], suggesting that simulations over larger length scales and timescales could provide better comparisons between the block and the random copolymer. Nonetheless, the results reported here provide a coherent physical picture of Li^+ solvation in the random versus the block copolymers, and helps explain their underlying conductivity differences.

6.5 Conclusion

Atomistic simulations have been used to investigate Li^+ solvation and transport in POEM homopolymers and its copolymers with PGCMA. The simulated ion mobilities are in agreement with experimental findings[260] and show that the reduction in Li^+ diffusivity in the copolymer persists even after accounting for segmental mobility T_g effects.

We find that entropic penalties govern the solvation tendency in copolymers of mixed polarity; Li^+-O(ether) solvation is preferred over that by the highly polar O=(carbonate). As the

presence of PGCMA dilutes the concentration of O(ether), the solvation preference is shifted towards single-chain solvation, thereby decreasing interchain hopping. In addition to a change of the hopping mechanism, a disruption of the solvation site network also contributes to reduced Li^+ diffusivity. In particular, the solvation site connectivity decreases by 50% in the random copolymer compared to the homopolymer, consistent with the experimentally measured reduction in conductivity[260]. By further extending the analysis to random and block copolymers of PGCMA and POEM, we find that PGCMA units and ether segments can form hybrid solvation sites at diffuse nanoscopic interfaces. In the well-mixed random copolymer, these hybrid solvation sites create a percolating Li^+ transport network. In contrast, in the less-mixed block copolymer, regions that are enriched with PGCMA and depleted of POEM are transiently unavailable for Li^+ transport, as the formation of an all-carbonate solvation site is entropically unfavorable. Experimental conductivity differences between the random and the block copolymer can therefore be explained through a difference in solvation site percolation due to different degrees of mixing.

6.6 Supporting Information

Methods and Force Field Parameters for Molecular Dynamics Simulations

In this study, the TraPPE-UA force field[202–204] is used for all inter- and intramolecular interactions between polymer atoms. Instead of rigid bonds used in the TraPPE-UA force field, the generalized CHARMM bonding spring constants are used[277]. Partial charges of the polymer interaction sites are refined through ab initio calculations using the B3LYP functional and the 6-31G(d,p) basis set, performed with GAUSSIAN 09 program[266]. The charge fitting uses the ChElPG calculation scheme[267]. Compatible all-atom parameters for LiTFSI are adapted from a previous simulation study[59,206]. An additional charge scaling of 0.7 is applied to Li+ and TFSI-[268]. Figure 6.8 provides reference labels for polymer atom types used in the force field.

The simulations were performed using the LAMMPS package[208]. For all MD simulations, a cutoff radius of 12 Å with Van der Waals tail correction was used for short-range Lennard-Jones (LJ) interactions. Long-range non-bonded interactions were cut off at a radius of 12 Å and were handled using the Particle-particle particle-mesh solver with 10–4 accuracy[207]. The trajectories were integrated using the velocity-Verlet algorithm with a 1 fs timestep. For NVT simulations, the Nosé-Hoover thermostat with a damping parameter of 100 fs was used. For NPT simulations, the Nosé-Hoover barostat with a damping parameter of 1000 fs was applied in addition to the thermostat.

United Atom Model: Terminal Groups, Tacticity, and Atom Type Assignments

The numbers of chains and numbers of repeat units for each system are summarized in Table 6.1. The salt concentration for all simulations is $r = [Li^+]/([EO]+[OCOO]) = 0.05$, where [OCOO] refers to the carbonyl oxygen in the cyclic carbonate group. The termini for the polymethacrylate backbone are CH3, which are connected to the CT interaction sites. All polymer chains in this study are atactic. When generating the initial configuration, the stereochemistry of each chiral center is randomly chosen as S or R with equal probability.

Table 6.1. Summary table of POEM homopolymer, PGCMA-r-POEM, and PGCMA-b-POEM simulation systems: system composition, polymer chain lengths, and fictive temperature

System	Number of Chains	Number of Repeat Units	POEM wt.%	T_f
POEM	1 POEM	300	100	239 ± 5 K
PGCMA-*r*-POEM	1 PGCMA-*r*-POEM	432 (PGCMA)-*r*-168 (POEM)	50.3	276 ± 4 K
PGCMA-*b*-POEM	16 PGCMA-*b*-POEM	26 (PGCMA)-*b*-10 (POEM)	50.6	274 ± 3 K

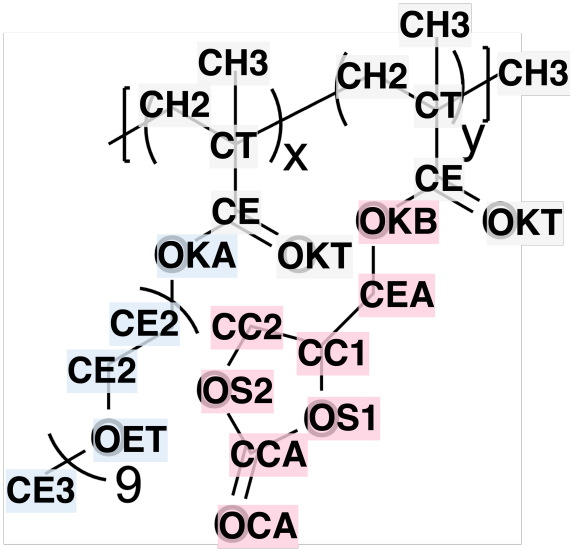

Figure 6.8. Reference labels for atom types in force field parameters.

Non-bonded Interaction Parameters

The nonbonded interactions include Lennard-Jones interactions and Coulombic interactions. For united atoms i and j, their nonbonded interaction is:

$$u_{nb}(r_{ij}) = 4\varepsilon_{ij}\left[\left(\frac{\sigma_{ij}}{r_{ij}}\right)^{12} - \left(\frac{\sigma_{ij}}{r_{ij}}\right)^{6}\right] + \frac{q_i q_j}{4\pi\epsilon_0 r_{ij}}, \tag{6.2}$$

where r_{ij} is the separation distance between atoms i and j, σ_{ij} is the Lennard-Jones diameter, ε_{ij} is the Lennard-Jones interaction strength, ϵ_0 is the vacuum permittivity. q_i and q_j are the partial charges of atoms i and j.

LJ interactions are computed with Lorentz-Berthelot mixing rules. For 1-2, 1-3, and 1-4 bonded interaction sites, the Lennard-Jones interactions are turned off. Coulomb interactions are turned off for 1-2 and 1-3 bonded interaction sites and scaled by 0.5 for 1-4 bonded interactions. The non-bonded interaction parameters are listed in Table 6.2. The partial charges on chain termini are slightly adjusted to ensure charge neutrality.

Table 6.2. Nonbonded interaction potential parameters for polymer atoms

atom	m (amu)	σ_{ii} (Å)	ϵ_{ii} ($\frac{\text{kcal}}{\text{mol}}$)	q (e)
CH2	14.027	3.95	0.091411	-0.0765
CH3	15.035	3.75	0.194746	-0.066
CT	12.011	6.4	0.000994	0.1826
CE	12.011	3.82	0.079488	0.6593
OKT	15.9994	3.05	0.156989	-0.514
OKA	15.9994	2.8	0.109296	-0.435
OET	15.9994	2.85	0.109296	-0.4757
CE2	14.027	3.95	0.091411	0.2413
CE3	15.035	3.75	0.194746	0.1875
OKB	15.9994	2.8	0.109296	-0.2887
CEA	14.027	3.95	0.091411	0.1015
CC1	13.019	4.33	0.01987	0.2193
CC2	14.027	3.95	0.091411	0.3004
OS1	15.9994	2.85	0.109296	-0.4153
OS2	15.9994	2.85	0.109296	-0.424
OCA	15.9994	3.05	0.156989	-0.5105
CCA	12.011	3.75	0.105	0.8319

Bonding Potential Parameters

1-2 bonded united atoms interact via a harmonic bonding potential in the form:

$$u_{bond}(r_{ij}) = k_{bond}(r_{ij} - {r_{ij}}^{(0)})^2, \tag{6.3}$$

where r_{ij} is the separation distance between atoms i and j, k_{bond} is the force constant and ${r_{ij}}^{(0)}$ is the equilibrium bond length. The bonding interaction parameters are listed in Table 6.3.

Table 6.3. Bonding potential parameters for polymer atoms

bond	k_{bond} ($\frac{\text{kcal}}{\text{mol·Å}^2}$)	${r_{ij}}^{(0)}$ (Å)	bond	k_{bond} ($\frac{\text{kcal}}{\text{mol·Å}^2}$)	${r_{ij}}^{(0)}$ (Å)
CE2-CE2	225	1.540	CH2-CH2	225	1.540
CE2-OET	360	1.410	OCA-CCA	360	1.229
CE3-OET	360	1.410	CCA-OS1	360	1.344
CH3-CT	225	1.540	CCA-OS2	360	1.344
CH2-CT	225	1.540	OS1-CC1	360	1.410
CEA-OKB	360	1.410	OS2-CC2	360	1.410
CE2-OKA	360	1.410	CC2-CC1	225	1.540
CE-CT	200	1.520	CC1-CEA	225	1.540
CE-OKT	360	1.200	CE-OKB	360	1.344
CE-OKA	360	1.344			

Bending Potential Parameters

1-2-3 bonded united atoms interact via a harmonic bending potential in the form:

$$u_{bend}(\theta_{ijk}) = k_{bend}\left(\theta_{ijk} - {\theta_{ijk}}^{(0)}\right)^2, \tag{6.4}$$

where k_{bend} is the force constant, θ_{ijk} is the angle between united atoms i, j, and k, and ${\theta_{ijk}}^{(0)}$ is the equilibrium angle. The bending interaction parameters are listed in Table 6.4.

Table 6.4. Bending potential parameters for polymer atoms

bend	k_{bend} ($\frac{\text{kcal}}{\text{mol·rad}^2}$)	${\theta_{ijk}}^{(0)}$ (Å)	bend	k_{bend} ($\frac{\text{kcal}}{\text{mol·rad}^2}$)	${\theta_{ijk}}^{(0)}$ (Å)
CE2-OET-CE2	60.0136	112.0	CH3-CT-CH3	62.1000	109.5
CE2-OET-CE3	60.0136	112.0	OKA-CE2-CE2	49.9782	112.0
CE2-CE2-OET	49.9782	112.0	OKB-CEA-CC1	49.9782	112.0
CH2-CT-CH2	62.1000	109.5	OCA-CCA-OS1	40.0600	123.0

Table 6.4. Bending potential parameters for polymer atoms, continued.

CH3-CT-CH2	62.1000	109.5	OCA-CCA-OS2	40.0600	123.0
CT-CH2-CT	62.1000	114.0	CCA-OS2-CC2	62.1000	115.0
CE-OKB-CEA	62.1000	115.0	CCA-OS1-CC1	62.1000	115.0
CE-OKA-CE2	62.1000	115.0	OS1-CCA-OS2	72.4000	110.0
OKT-CE-OKA	62.1000	125.0	OS2-CC2-CC1	59.9400	112.0
OKT-CE2-C2	49.9782	112.0	OS1-CC1-CC2	59.9400	112.0
CH2-CT-CE	62.1000	109.5	OS1-CC1-CEA	59.9400	112.0
CT-CE-OKT	62.1000	125.0	CC2-CC1-CEA	62.1000	112.0
CT-CE-OKA	70.1483	110.0	OKT-CE-OKB	62.1000	125.0
CH3-CT-CE	62.1000	109.5	CT-CE-OKB	70.1483	110.0

Torsional Potential Parameters

The torsional potentials for 1-2-3-4 bonded united atoms take the form:

$$u_{tors}(\phi_{ijkl}) = \frac{K_1}{2}\left[1 + \cos(\phi_{ijkl})\right] + \frac{K_2}{2}\left[1 - \cos(2\phi_{ijkl})\right] + \frac{K_3}{2}\left[1 + \cos(3\phi_{ijkl})\right] + \frac{K_4}{2}\left[1 - \cos(4\phi_{ijkl})\right], \quad (6.5)$$

where c_1, c_2, and c_3 are coefficients and ϕ_{ijkl} is the dihedral angle defined by atoms i, j, k, and l. The torsional interaction parameters are listed in Table 6.5.

Table 6.5. Torsional potential parameters for polymer atoms

torsion	K_1 $(\frac{\text{kcal}}{\text{mol}})$	K_2 $(\frac{\text{kcal}}{\text{mol}})$	K_3 $(\frac{\text{kcal}}{\text{mol}})$	K_4 $(\frac{\text{kcal}}{\text{mol}})$
OKA-CE2-CE2-OET	1.888000	-1.888000	0.000000	0.000000
OET-CE2-CE2-OET	1.888000	-1.888000	0.000000	0.000000
CE2-CE2-OET-CE2	2.882840	-0.650809	2.218510	0.000000

Table 6.5. Torsional potential parameters for polymer atoms, continued.

CE2-CE2-OET-CE3	2.882840	-0.650809	2.218510	0.000000
CH3-CT-CH2-CT	0.000000	0.000000	1.833350	0.000000
CH2-CT-CH2-CT	0.000000	0.000000	1.833350	0.000000
CT-CH2-CT-CE	0.000000	0.000000	1.833350	0.000000
CH3-CT-CE-OKT	-0.919280	0.229880	-0.609280	0.000000
CH2-CT-CE-OKT	-0.919280	0.229880	-0.609280	0.000000
CH3-CT-CE-OKA	0.915310	0.216840	0.609670	0.000000
CH2-CT-CE-OKA	0.915310	0.216840	0.609670	0.000000
CT-CE-OKB-CEA	9.689610	7.678560	1.387070	0.000000
CT-CE-OKA-CE2	9.689610	7.678560	1.387070	0.000000
CE-OKA-CE2-CE2	-2.988080	2.142010	-0.087834	0.203768
OKT-CE-OKB-CEA	-9.669740	7.376500	-1.045270	0.000000
OKT-CE-OKA-CE2	-9.669740	7.376500	-1.045270	0.000000
OCA-CCA-OS2-CC2	-0.636000	6.488000	0.870000	0.000000
OCA-CCA-OS1-CC1	-0.636000	6.488000	0.870000	0.000000
CCA-OS2-CC2-CC1	-0.404000	4.748000	2.418000	0.000000
CCA-OS1-CC1-CC2	-0.404000	4.748000	2.418000	0.000000
OS1-CCA-OS2-CC2	0.000000	9.000000	0.000000	0.000000
OS2-CCA-OS1-CC1	0.000000	9.000000	0.000000	0.000000
OS2-CC2-CC1-OS1	0.574000	-0.422000	4.562000	0.000000
OS2-CC2-CC1-CEA	0.702000	-0.212000	3.060000	0.000000
CE-OKB-CEA-CC1	-2.988080	2.142010	-0.087834	0.203768
OKB-CEA-CC1-OS1	1.888000	-1.888000	0.000000	0.000000
CCA-OS1-CC1-CEA	-0.404000	4.748000	2.418000	0.000000
CC2-CC1-CEA-OKB	0.702000	-0.212000	3.060000	0.000000

Table 6.5. Torsional potential parameters for polymer atoms, continued.

CH3-CT-CE-OKB	0.915310	0.216840	0.609670	0.000000
CH2-CT-CE-OKB	0.915310	0.216840	0.609670	0.000000

Simulation Protocol

To prepare the starting configuration, the polymer chains are initiated with random positions and orientations in a large box. The polymer chains are first relaxed under the NVT ensemble at 500 K for 30 ns. Then a 40 ns NPT equilibration at 500 K and 1 bar is performed for polymer chains to equilibrate and to ensure the bulk density does not drift. The process of introduction of Li^+ is as follows: Li^+ and $TFSI^-$ ions are introduced at random positions in the equilibrated neat polymer at the designated ratio of $r = 0.05$. To remove any steric clashes in the simulation cell, the system is relaxed under the NVE ensemble for 10,000 steps, where the maximum displacement of an atom is limited to 0.1 Å per step.

To perform each production simulation, the salt-doped polymer is equilibrated at the designated temperature under the NPT ensemble for 40 ns. Then the system is further equilibrated for 10 ns under the NVT ensemble. At the beginning of this NVT equilibration, the box size is scaled to reflect the ensemble average density during the last 10 ns of the NPT equilibration. Then, the trajectory for analysis is collected from a 150-ns production simulation under the NVT ensemble.

Fictive Temperature Determination

To determine the fictive temperature, equilibrated configurations at a high temperature are continuously cooled at a cooling rate of 10 K/ns at 1 bar. For POEM, the system is cooled from 400 K to 50 K. For PGCMA-*r*-POEM and PGCMA-*b*-POEM, the system is cooled from 500 K to 50 K. The density is plotted as a function of temperature under the NPT ensemble. Two linear

segments are fitted for the glass and liquid regions respectively. The T_f is determined as the intercept of the extrapolated linear fit lines. This procedure to calculate T_f is sensitive to the fitting range of the two segments. Therefore, the endpoints of the fitting segments are systematically sampled in the following manner. The starting point of the glassy segment was fixed at 50 K, while the endpoint of the glassy segment was randomly sampled between 100 K and 150 K. Similarly, the starting point of the liquid segment was fixed at the starting temperature, 400 K and 500 K for POEM and the copolymers, respectively. The endpoint of the liquid segment was sampled between 300 K and 350 K for POEM. For the copolymers, the endpoint of the liquid segment was sampled between 350 K and 400 K. The fitting intervals for the glassy segment and the liquid segment are randomly drawn within the sampling interval defined above, the intersections between which yield a set of T_f values. Only T_f values that fall between the endpoints of fitting segments are kept. The T_f calculation described above was repeated for another independent sample. For each sample, combinations of glassy and liquid fitting ranges are generated 10,000 times. The mean and standard deviation of the set of T_f values collected from both samples are reported. Figure 6.9 includes the cooling curve and the distribution of resulting T_f values collected.

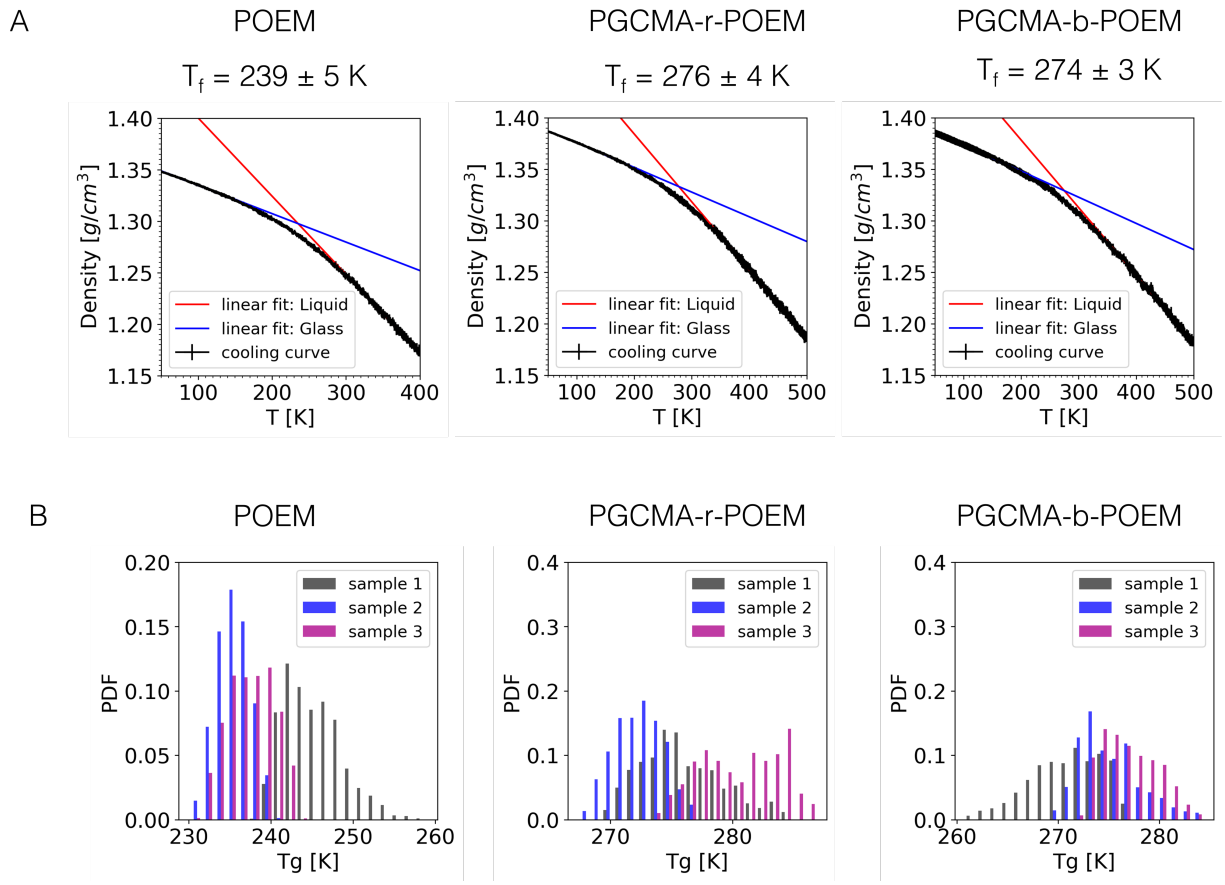

Figure 6.9. Fictive temperatures in simulations. (A) Density as a function of temperature for POEM homopolymer, PGCMA-r-POEM, and PGCMA-b-POEM copolymers, respectively. Example fitting lines for liquid and glassy regions are shown in red and blue, respectively. The error bars of the cooling curve arise from three independent runs. (B) Normalized histograms of collected T_f values. Histograms from three independent samples are plotted in different colors.

Calculation of Functional Group Dipole Moments

The dipole moments of the cyclic carbonate fragment and the C-O-C ethylene oxide fragment are obtained based on the following geometry:

(A)

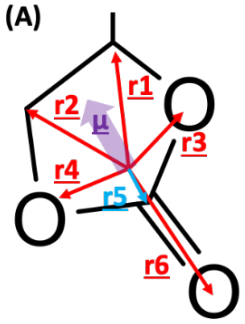

Average distance r_i from center of mass [Å]	
r1	1.57
r2	1.60
r3	1.13
r4	1.10
r5	0.72
r6	1.93

Average Angle between r_i and μ	
r1	32°
r2	26°
r3	90°
r4	84°
r5	169°
r6	175°

(B)

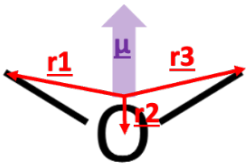

Average distance r_i from center of mass [Å]	
r1	1.20
r2	0.51
r3	1.20

Average Angle between r_i and μ	
r1	76°
r2	180°
r3	76°

Figure 6.10. (A) Average geometry for a GCMA fragment. (B) Average geometry for a C-O-C fragment along the POEM side chain. The results are obtained from MD simulation at 150K above T_f and are found to be independent of temperature.

Calculation of Dielectric Constant

The dielectric constant ε is computed based on the fluctuation of permanent dipole (Eq. 5),

$$\varepsilon = 1 + \frac{4\pi[\langle \boldsymbol{M}^2 \rangle - \langle \boldsymbol{M} \rangle^2]}{3kTV} \tag{6.6}$$

where k is Boltzmann's constant, T is temperature, V is the box volume. The ensemble averages are defined as

$$\langle \boldsymbol{M}^2 \rangle = \frac{1}{N_s}\sum_{i=1}^{N_s} \boldsymbol{M}^2(t_i) \quad \text{and} \quad \langle \boldsymbol{M} \rangle^2 = \left[\frac{1}{N_s}\sum_{i=1}^{N_s} \boldsymbol{M}(t_i)\right]^2. \tag{6.7}$$

where $\boldsymbol{M}(t) = \frac{e}{\sqrt{4\pi\epsilon_0}}\sum_{i=1}^{N} z_i \boldsymbol{r}_i(t)$ is the instantaneous dipole moment at time t. To correctly compute ε, no bonded atoms are allowed to cross the periodic boundary. This means that the molecules are unwrapped and made "whole", and their centers of mass are contained in the {0,0,0} box image.

Effects of Alternative Partial Charge Assignment on Li^+ Coordination

To test the robustness of the entropy argument on the Li^+ solvation trend, two sets of additional simulations were performed, where the partial charges are assigned based on different rationales, and all other parameters are kept identical. The original model used for the rest of the work is referred to as model 1. In model 2, the partial charges for Li^+ and $TFSI^-$ from ref. 206 are used as-is without rescaling. In model 3, the polymer partial charges are adapted directly from ref.204,205 for POEM and ref.264 for PGCMA. The partial charges for Li^+ and $TFSI^-$ in model 3 are unscaled. Table 6.6 lists the partial charges on the polymer interaction sites adapted from ref.204,205. The readers are referred to the original work for parameters of Li^+ and $TFSI^-$.

Table 6.6. Partial charges assigned on polymer interaction sites in model 3. The partial charges on chain termini are slightly adjusted to ensure charge neutrality.

atom	q (e)	atom	q (e)
CH2	0.00	OKB	-0.40
CH3	0.00	CEA	0.25
CT	0.00	CC1	0.2227
CE	0.55	CC2	0.229
OKT	-0.45	OS1	-0.4314
OKA	-0.40	OS2	-0.4314
OET	-0.50	OCA	-0.6378
CE2	0.25	CCA	1.0489
CE3	0.25		

The three models cover all possible cases of relative polarity among the three competing Li^+-solvating units: O(ether), O=(carbonate), and O(TFSI). While O=(carbonate) stays more polar than O(ether) in all three models, the polarity of O(TFSI), relative to the other two oxygen types,

ranks as lowest in model 1, highest in model 2, and between them in model 3. To probe the Li^+ solvation environment under models 2 and 3, radial distribution functions and coordination numbers shown in Figure 6.4 are replicated below using the alternative models. Since the three models only differ in the partial charges, the size of the solvation shell varies minimally across them. Consistent with Figure 6.4, the first solvation shell is comprised of O(ether), O=(carbonate), and O(TFSI), whereas O(ester) and O(carbonyl) from the backbone, despite being more polar than O(ether) are absent. Similar to the findings from Figure 6.4, Figure 6.10 shows that the relative contribution to Li^+ first solvation shell from O(TFSI) and O=(carbonate) relates closely to their polarity rank. Such polarity argument again does not apply to O(ether), which is always the predominant Li^+-solvating unit regardless of the polarity rank. Figure 6.4 and Figure 6.11 combine to reinforce that while the polarity argument is generally applicable, it is not sufficient to describe the preferential Li^+ solvation by O(ether).

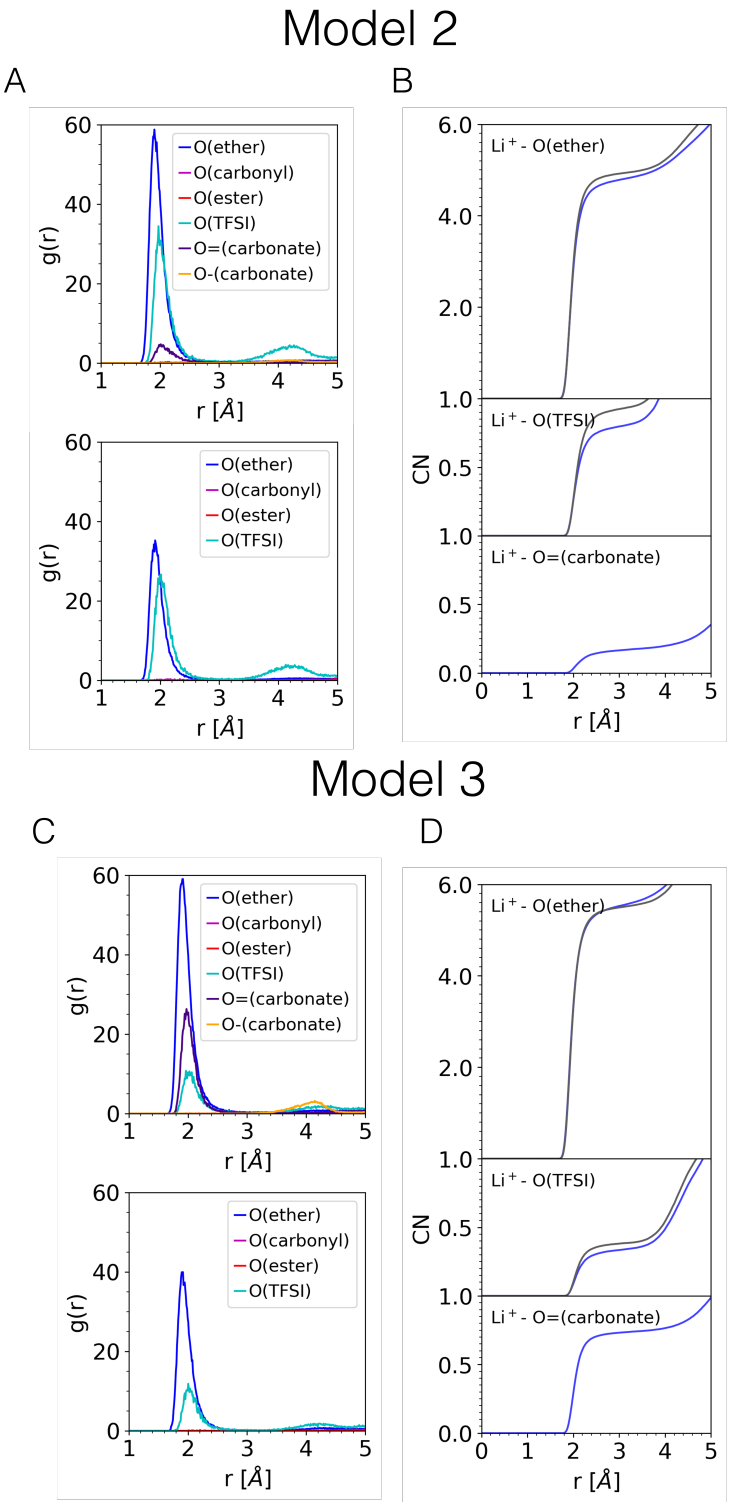

Figure 6.11. (A, C) Radial distribution functions between Li^+ and oxygen atoms in POEM (top) and PGCMA-r-POEM (bottom). (B, D) Coordination numbers CNij(r) in POEM and PGCMA-r-POEM between Li^+ and O(ether) (top), O(TFSI) (center), and O=(carbonate) (bottom). The results are obtained at 150 K above Tf using (A-B) model 2 and (C-D) model 3.

Degrees of Independent Ion Motions in POEM and in PGCMA-r-POEM

The degree of independent ion motions, α, is defined as the ratio of correlated MSD to the self MSD (Eq. 7). In a simulation, obtaining long-time valid statistics for α is often difficult, so the value of α is commonly estimated over the sub-diffusive regime at short timescales and extrapolated to longer timescales[51,177]. Here we compute α as a function of time and report the averaged value over the first 10 ns.

$$\alpha = \lim_{t\to\infty} \frac{\sum_{i=1}^{N_{ion}} \sum_{j=1}^{N_{ion}} z_i z_j \langle [\boldsymbol{r}_i(t) - \boldsymbol{r}_i(0)] \cdot [\boldsymbol{r}_j(t) - \boldsymbol{r}_j(0)] \rangle}{\sum_{i=1}^{N_{ion}} z_i^2 \langle \|\boldsymbol{r}_i(t) - \boldsymbol{r}_i(0)\|^2 \rangle} \tag{6.8}$$

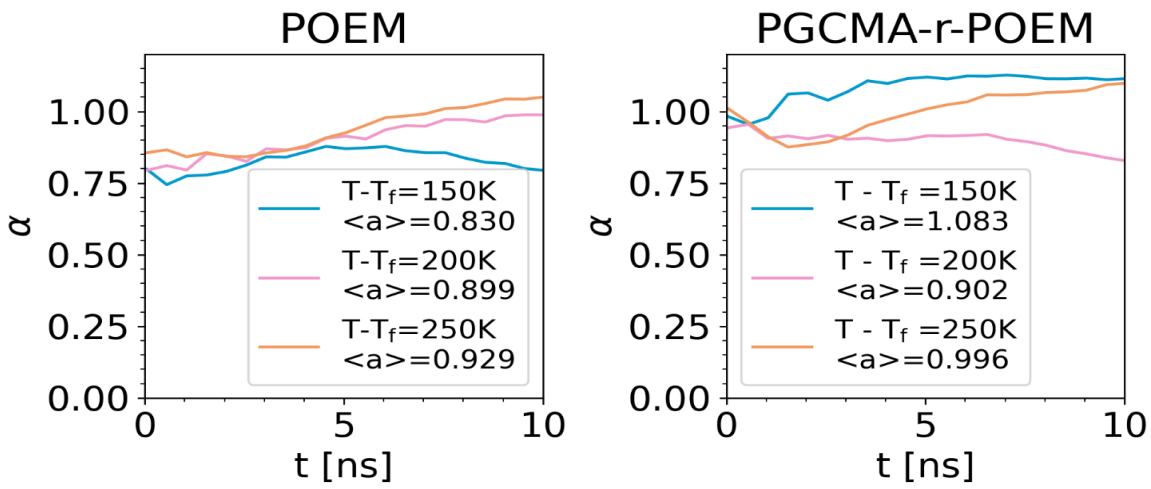

Figure 6.12. α as a function of correlation time for POEM and PGCMA-r-POEM. The averaged values for α are reported in the legend accordingly. The results show that ion motions are reasonably uncorrelated in both materials under the simulation conditions.

Binding Probability of O(ether) to Li^+ Along POEM Side Chains in POEM and PGCMA-*r*-POEM

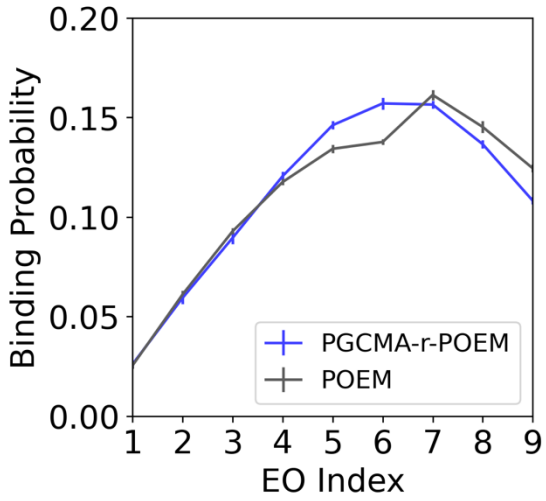

Figure 6.13. Binding probability of O(ether) to Li^+ as a function of the position along a POEM side chain. The trends in the two materials are highly similar. Li^+ are found to be primarily solvated by O(ether) at positions 4-8 along the side chain. The side chains are split into five independent sets to obtain estimates of error.

Decay of Effective Concentration in PGCMA-*r*-POEM and PGCMA-*b*-POEM

To demonstrate the degree of miscibility, we probe the interchain packing of POEM in PGCMA-b-POEM (BCP) versus in PGCMA-*r*-POEM (RCP) in terms of the decay of effective concentration. As described in ref. 278 and 239, the normalized effective concentration of a component decays from unity to zero and indicates how closely a chain packs with other chains of the same species. The plot shows that the normalized effective concentration of POEM decays faster in the RCP, revealing a higher degree of intermixing in the RCP.

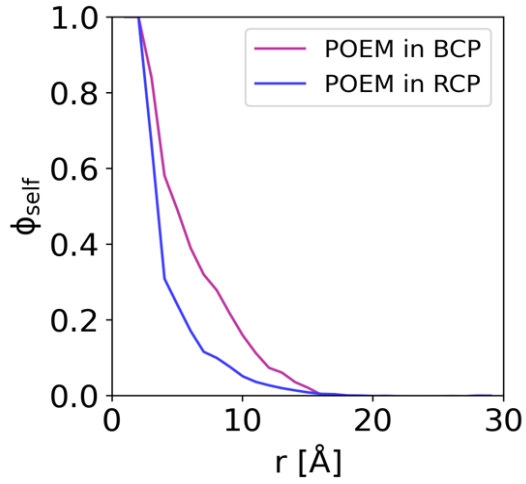

Figure 6.14. Normalized decay of the self-effective concentration of the POEM component in PGCMA-*r*-POEM and PGCMA-*b*-POEM.

Population of Coordination Motifs in PGCMA-b-POEM

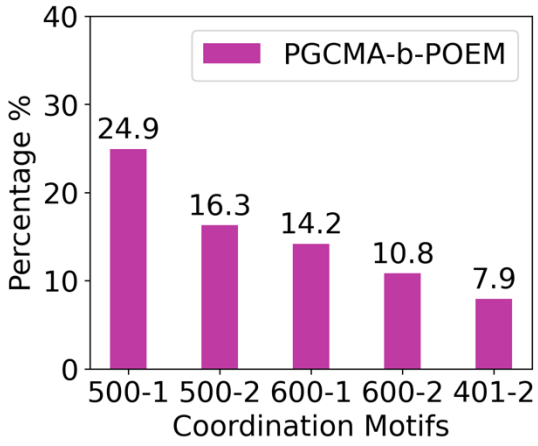

Figure 6.15. Population of five most abundant Li^+ coordination motifs in PGCMA-*b*-POEM at T-T_f = 150 K. The plot uses the identical notation rule for coordination motifs as for PGCMA-*r*-POEM, as described in Figure 6.5.

CHAPTER 7

CONCLUSIONS

7.1 Summary of contributions

This dissertation put forward two soft material platforms that interact with ions. These materials are intentionally designed for versatile, precise synthesizability, enable vast freedom in the design of sequence, architecture, and nanostructure. The primary contribution of this work is to condense the design space into a set of fundamental principles. In each system, we consider design factors such as building block sequence, molecular architecture, and nanostructure. An extensive toolkit is employed, including simulation, free energy methods, statistical analysis, and network analysis to systematically investigate their effects on the dynamic and thermodynamic properties of these materials.

In the field of biomimetic material, this work provides valuable design insights into repurposing protein binding functions for stimuli-responsive absorbent materials. Rather than the conventional use of PAs to target large biomolecules, our focus is on the sequestration of small molecules such as ions. Through two consecutive studies, we demonstrate that (1) functional segments of protein can be extracted and repurposed into synthetic material, (2) these materials can utilize adaptive, flexible binding mechanisms, different from traditional protein binding mechanisms. Although our material design initially centered on protein-derived peptide sequences, simulations revealed that this material utilizes distinct binding principles that are not accessible to conformationally constrained protein. This somewhat unexpected finding prompt us to view the design of this material as a polyelectrolyte study rather than a protein-inspired sequence optimization. While paving the way for engineering biomimetic absorbent materials utilizing *de*

novo sequences, this also suggests that future research should reevaluate the balance between entropic binding and specificity.

In the field of polymer electrolyte material, this work broadens our understanding of lithium-ion solvation and transport to inform the design of multicomponent SPEs. We have evaluated essential design factors such as architecture, monomeric mixing, and sequence, which inevitably come into play when incorporating multiple functionalities and nanostructures into material design. Instead of examining their combined effects in a number of example systems, we have methodically designed controlled comparisons to investigate the role of each factor individually. For each of these factors, our research has provided quantitative characterization of Li^+ solvation trends, explanations for their thermodynamic origins, and insights into how they both short-range and long-range Li^+ transport. The use of network analysis has added a new dimension to the concept of solvation site connectivity, effectively addressing the clustering features of solvation sites resulting from heterogeneity.

Juxtaposing two material systems that are similar in their high-level construct but different in other aspects, this work showcases that common underlying thermodynamic principles and research approaches can be applied to both questions. We demonstrate that population statistics of binding motifs can effectively describe the ion sequestration behavior by polymer chains and by peptide amphiphile molecules, successfully uncovering binding mechanisms and thermodynamics in both contexts. It is reasonable to anticipate the extension of other characterization analyses, such as ion hopping, ion dynamics, and free energy calculations, from one study to another, thereby gaining further insights into these systems.

This work also exemplifies how simulations and experiments collaborate to offer a thorough and convincing understanding that might otherwise be overlooked when conducted in

isolation. Throughout the research, computational studies have been informed and validated by realistic characterization from experiments. In turn, fundamental insights from simulations have offered molecular-level insights that can explain and guide experiments.

7.2 Future directions

Building upon the findings from this dissertation, future work can explore several paths, into fundamental investigations, expanded applications, and advanced computation methodologies.

The current studies have demonstrated the feasibility of engineering a protein-derived synthetic material for phosphate capture. The newly identified adaptive, flexible binding mechanism paves the way for *de novo* designs of these materials, providing the following opportunities for future studies. First, there are opportunities for computational investigations regarding the binding selectivity of these materials. The entropic-driven multi-chain binding mechanism identified in PAMs brings up the intriguing question about the retained selectivity. It is worthwhile to reevaluate the relative significance between entropic-driven binding and bio-inspired specific binding, by simulating the material in the presence of other types of ions. Second, there is room for sequence design to achieve a desired balance between entropic binding and specific binding. In contrast to the intricate protein-derived sequence design, we have a design space with multiple components but relatively simplistic sequences. Starting with educated selections, one can uncover initial trends in sequence design, such as the impacts of glycine spacer length, the location and number of lysine residues. The gathered data can subsequently inform the exploration into actively learned sequences, ultimately leading to a data-driven optimization of this multi-component system. Finally, beyond ion sequestration, this material has the potential for alternative applications. For example, the dynamics of micelle-bound phosphate remains uncharacterized and poses an intriguing research question. After thorough characterization of

micelle-bound phosphate dynamics and phosphate binding kinetics, this material presents the potential for tunable ion mobility triggered by pH changes, which can be strategically targeted for gating. Through sequence design discussed above, this potential can be extended to other ionic species beyond phosphates.

Modelling charge-containing PA materials demands high accuracy and access to long time and length scales. While the current simulation methods of the PA material find a balance between accuracy and efficiency, there is room for improvement in several aspects. First, modelling condensed weak electrolytes must take into account the speciation of protonatable groups as a function of pH. This can be achieved through constant pH simulations or estimated from single-chain-in-mean-field (SCMF) calculations. Second, when dealing with highly polarizable molecular ions, the modelling of ionic binding can achieve the required accuracy through the use of polarizable force fields. Finally, emerging methodologies have enabled chemistry-informed coarse-graining from atomistic to field representation[279] and backwards.[280] Future studies of these systems can implement these toolkits alongside the methods discussed earlier.

The design practical, high-performance polymer electrolytes is a multi-objective problem and has thus gathered massive research efforts. While this dissertation has focused exclusively on salt-doped, poly (ethylene oxide)-based polymer electrolytes with relatively low salt concentrations, numerous studies have sought to explore alternative designs. These include alternative chemistries, charged or zwitterionic functional groups, highly branched or crosslinked architectures, ceramic and nanoparticle composite, to name a few. Many of these studies have also considered materials under extended operating conditions, including high salt concentrations and high voltages. Since abundant molecular designs, characterization, and design insights have become available in the literature, there is an urgent need for a tool to featurize those designs and

summarize their trends. Future studies aiming to develop efficient discovery tools can consider the following directions. First, the emerging field of material informatics addresses structure-property relation directly. Existing works have showcased efficient polymer featurization,[281] demonstrating data-informed discovery for polymer electrolytes[282] and fuel cell polymer membranes.[283] Future efforts in this area are encouraged to go beyond the chemistry space and incorporate other complex design factors and operating conditions. Second, machine learning tools can harness the abundant data from molecular dynamics simulations. Instead of collecting long-time statistics to extract ion dynamics, machine learning can be leveraged to accelerate the time evolution or to predict long-time dynamics from short simulations, by learning behaviors[284] and/or coarse-graining.[285] While developing methods in this regard, one must cautiously interrogate for data quality, embedded physics, and method robustness. Finally, the study of ion-containing materials can benefit from accurate description of intermolecular interaction. While existing classical all-atom MD simulations have offer valuable physical insights, they are plagued with sluggish ion dynamics due to the lack of appropriate treatment for polarization effect.[286] Machine-learned force fields[287,288] and polarizable force fields have aid in to resolve this issue. Although these methods demand relatively high computational cost, rapid advances in computational power will broaden their application in this field.

REFERENCES

(1) Elias, M.; Wellner, A.; Goldin-Azulay, K.; Chabriere, E.; Vorholt, J. A.; Erb, T. J.; Tawfik, D. S. The Molecular Basis of Phosphate Discrimination in Arsenate-Rich Environments. *Nature* **2012**, *491* (7422), 134–137.

(2) Bianchi, A.; Giorgi, C.; Ruzza, P.; Toniolo, C.; Milner-White, E. J. A Synthetic Hexapeptide Designed to Resemble a Proteinaceous P-Loop Nest Is Shown to Bind Inorganic Phosphate. *Proteins: Structure, Function and Bioinformatics* **2012**, *80* (5), 1418–1424.

(3) Gros, M.; Petrović, M.; Ginebreda, A.; Barceló, D. Removal of Pharmaceuticals during Wastewater Treatment and Environmental Risk Assessment Using Hazard Indexes. *Environ Int* **2010**, *36* (1), 15–26.

(4) Liu, C.; Hsu, P. C.; Xie, J.; Zhao, J.; Wu, T.; Wang, H.; Liu, W.; Zhang, J.; Chu, S.; Cui, Y. A Half-Wave Rectified Alternating Current Electrochemical Method for Uranium Extraction from Seawater. *Nature Energy 2017 2:4* **2017**, *2* (4), 1–8.

(5) UNESCO World Water Assessment Programme. *The United Nations World Water Development Report, 2017: Wastewater: The Untapped Resource*; Paris, 2017.

(6) van Loosdrecht, M. C. M.; Brdjanovic, D. Anticipating the next Century of Wastewater Treatment. *Science (1979)* **2014**, *344* (6191), 1452–1453.

(7) Mo, W.; Zhang, Q. Energy–Nutrients–Water Nexus: Integrated Resource Recovery in Municipal Wastewater Treatment Plants. *J Environ Manage* **2013**, *127*, 255–267.

(8) Cisse, L.; Mrabet, T.; Abdelkader, R.; Mazini, A. World Phosphate Production : Overview and Prospects Abstract , However , Is Always Phosphate Rock for Direct Processing and Direct Application Was Estimated to 125. **2004**, *15*, 21–25.

(9) Cordell, D.; Drangert, J.-O.; White, S. The Story of Phosphorus: Global Food Security and Food for Thought. *Global Environmental Change* **2009**, *19* (2), 292–305.

(10) Cordell, D.; Rosemarin, A.; Schröder, J. J.; Smit, A. L. Towards Global Phosphorus Security: A Systems Framework for Phosphorus Recovery and Reuse Options. *Chemosphere* **2011**, *84* (6), 747–758.

(11) Smith, V. H.; Schindler, D. W. Eutrophication Science: Where Do We Go from Here? *Trends Ecol Evol* **2009**, *24* (4), 201–207.

(12) Saraste, M.; Sibbald, P. R.; Wittinghofer, A. The P-Loop — a Common Motif in ATP- and GTP-Binding Proteins. *Trends Biochem Sci* **1990**, *15* (11), 430–434.

(13) Watson, J. D.; Milner-White, E. J. A Novel Main-Chain Anion-Binding Site in Proteins: The Nest. A Particular Combination of φ,ψ Values in Successive Residues Gives Rise to

Anion-Binding Sites That Occur Commonly and Are Found Often at Functionally Important Regions 1 1Edited by J. Thornton. *J Mol Biol* **2002**, *315* (2), 171–182.

(14) Milner-White, E. J.; Russell, M. J. Sites for Phosphates and Iron-Sulfur Thiolates in the First Membranes: 3 to 6 Residue Anion-Binding Motifs (Nests). *Origins of Life and Evolution of the Biosphere* **2005**, *35* (1), 19–27.

(15) Romero Romero, M. L.; Yang, F.; Lin, Y.-R.; Toth-Petroczy, A.; Berezovsky, I. N.; Goncearenco, A.; Yang, W.; Wellner, A.; Kumar-Deshmukh, F.; Sharon, M.; Baker, D.; Varani, G.; Tawfik, D. S. Simple yet Functional Phosphate-Loop Proteins. *Proceedings of the National Academy of Sciences* **2018**, *115* (51).

(16) Cui, H.; Webber, M. J.; Stupp, S. I. Self-Assembly of Peptide Amphiphiles: From Molecules ToNanostructures to Biomaterials. *Peptide Science* **2010**, *94*, 1–18.

(17) Löwik, D. W. P. M.; Van Hest, J. C. M. Peptide Based Amphiphiles. *Chem Soc Rev* **2004**, *33* (4), 234–245.

(18) Dehsorkhi, A.; Castelletto, V.; Hamley, I. W. Self-Assembling Amphiphilic Peptides. *Journal of Peptide Science* **2014**, *20* (7), 453–467.

(19) Trent, A.; Marullo, R.; Lin, B.; Black, M.; Tirrell, M. Structural Properties of Soluble Peptide Amphiphile Micelles. *Soft Matter* **2011**, *7* (20), 9572.

(20) Israelachvili, J. N.; Mitchell, D. J.; Ninham, B. W. Theory of Self-Assembly of Hydrocarbon Amphiphiles into Micelles and Bilayers. *Journal of the Chemical Society, Faraday Transactions 2* **1976**, *72*, 1525.

(21) Velichko, Y. S.; Stupp, S. I.; De La Cruz, M. O. Molecular Simulation Study of Peptide Amphiphile Self-Assembly. *Journal of Physical Chemistry B* **2008**, *112* (8), 2326–2334.

(22) Paramonov, S. E.; Jun, H.-W.; Hartgerink, J. D. Self-Assembly of Peptide−Amphiphile Nanofibers: The Roles of Hydrogen Bonding and Amphiphilic Packing. *J Am Chem Soc* **2006**, *128* (22), 7291–7298.

(23) Tu, R. S.; Tirrell, M. Bottom-up Design of Biomimetic Assemblies. *Adv Drug Deliv Rev* **2004**, *56* (11), 1537–1563.

(24) Priya, R.; Kumar, A.; Manimekalai, M. S. S.; Grüber, G. Conserved Glycine Residues in the P-Loop of ATP Synthases Form a Doorframe for Nucleotide Entrance. *J Mol Biol* **2011**, *413* (3), 657–666.

(25) Gruber, M.; Greisen, P.; Junker, C. M.; Hélix-Nielsen, C. Phosphorus Binding Sites in Proteins: Structural Preorganization and Coordination. *J Phys Chem B* **2014**, *118* (5), 1207–1215.

(26) Gruber, M. F.; Wood, E.; Truelsen, S.; Østergaard, T.; Hélix-Nielsen, C. Computational Design of Biomimetic Phosphate Scavengers. *Environ Sci Technol* **2015**, *49* (16), 9469–9478.

(27) Watson, J. D.; Milner-White, E. J. The Conformations of Polypeptide Chains Where the Main-Chain Parts of Successive Residues Are Enantiomeric. Their Occurrence in Cation and Anion-Binding Regions of Proteins. *J Mol Biol* **2002**, *315* (2), 183–191.

(28) Chang, C. E. A.; Chen, W.; Gilson, M. K. Ligand Configurational Entropy and Protein Binding. *Proc Natl Acad Sci U S A* **2007**, *104* (5), 1534–1539.

(29) Du, X.; Li, Y.; Xia, Y. L.; Ai, S. M.; Liang, J.; Sang, P.; Ji, X. L.; Liu, S. Q. Insights into Protein–Ligand Interactions: Mechanisms, Models, and Methods. *Int J Mol Sci* **2016**, *17* (2), 1–34.

(30) Chodera, J. D.; Mobley, D. L. Entropy-Enthalpy Compensation: Role and Ramifications in Biomolecular Ligand Recognition and Design. *Annu Rev Biophys* **2013**, *42* (1), 121–142.

(31) Rohrdanz, M. A.; Zheng, W.; Clementi, C. Discovering Mountain Passes via Torchlight: Methods for the Definition of Reaction Coordinates and Pathways in Complex Macromolecular Reactions. *Annu Rev Phys Chem* **2013**, *64* (1), 295–316.

(32) Hénin, J.; Fiorin, G.; Chipot, C.; Klein, M. L. Exploring Multidimensional Free Energy Landscapes Using Time-Dependent Biases on Collective Variables. *J Chem Theory Comput* **2010**, *6* (1), 35–47.

(33) Comer, J.; Gumbart, J. C.; Hénin, J.; Lelievre, T.; Pohorille, A.; Chipot, C. The Adaptive Biasing Force Method: Everything You Always Wanted to Know but Were Afraid to Ask. *Journal of Physical Chemistry B* **2015**, *119* (3), 1129–1151.

(34) Yuan, F.; Wang, S.; Larson, R. G. Potentials of Mean Force and Escape Times of Surfactants from Micelles and Hydrophobic Surfaces Using Molecular Dynamics Simulations. *Langmuir* **2015**, *31* (4), 1336–1343.

(35) Gumbart, J. C.; Roux, B.; Chipot, C. Standard Binding Free Energies from Computer Simulations: What Is the Best Strategy? *J Chem Theory Comput* **2013**, *9* (1), 794–802.

(36) Kumar, S.; Rosenberg, J. M.; Bouzida, D.; Swendsen, R. H.; Kollman, P. A. THE Weighted Histogram Analysis Method for Free-Energy Calculations on Biomolecules. I. The Method. *J Comput Chem* **1992**, *13* (8), 1011–1021.

(37) Bartels, C. Analyzing Biased Monte Carlo and Molecular Dynamics Simulations. *Chem Phys Lett* **2000**, *331* (5–6), 446–454.

(38) Li, Q.; Chen, J.; Fan, L.; Kong, X.; Lu, Y. Progress in Electrolytes for Rechargeable Li-Based Batteries and Beyond. *Green Energy and Environment* **2016**, *1* (1), 18–42.

(39) Duffner, F.; Kronemeyer, N.; Tübke, J.; Leker, J.; Winter, M.; Schmuch, R. Post-Lithium-Ion Battery Cell Production and Its Compatibility with Lithium-Ion Cell Production Infrastructure. *Nature Energy 2021 6:2* **2021**, *6* (2), 123–134.

(40) Lopez, J.; Mackanic, D. G. Designing Polymers for Advanced Battery Chemistries. *Nat Rev Mater* **2019**, *4* (mAY).

(41) Tikekar, M. D.; Choudhury, S.; Tu, Z.; Archer, L. A. Design Principles for Electrolytes and Interfaces for Stable Lithium-Metal Batteries. *Nat Energy* **2016**, *1* (9), 1–7.

(42) Schaefer, J. L.; Lu, Y.; Moganty, S. S.; Agarwal, P.; Jayaprakash, N.; Archer, L. A. Electrolytes for High-Energy Lithium Batteries. *Applied Nanoscience (Switzerland)* **2012**, *2* (2), 91–109.

(43) Albertus, P.; Babinec, S.; Litzelman, S.; Newman, A. Status and Challenges in Enabling the Lithium Metal Electrode for High-Energy and Low-Cost Rechargeable Batteries. *NAture eNergy* | **2018**, *3*.

(44) Barai, P.; Higa, K.; Srinivasan, V. Lithium Dendrite Growth Mechanisms in Polymer Electrolytes and Prevention Strategies. *Physical Chemistry Chemical Physics* **2017**, *19* (31), 20493–20505.

(45) Fenton, D. E.; Parker, J. M.; Wright, P. V. Complexes of Alkali Metal Ions with Poly(Ethylene Oxide). *Polymer (Guildf)* **1973**, *14* (11), 589.

(46) Meyer, B. W. H. Polymer Electrolytes for Lithium-Ion Batteries. *Advanced Materials* **1998**, *10* (6), 439–448.

(47) Hallinan, D. T.; Balsara, N. P. Polymer Electrolytes. *Annu Rev Mater Res* **2013**, *43* (1), 503–525.

(48) Golodnitsky, D.; Strauss, E.; Peled, E.; Greenbaum, S. Review—On Order and Disorder in Polymer Electrolytes. *J Electrochem Soc* **2015**, *162* (14), A2551–A2566.

(49) Ketkar, P. M.; Shen, K.-H.; Hall, L. M.; Epps, T. H. Charging toward Improved Lithium-Ion Polymer Electrolytes: Exploiting Synergistic Experimental and Computational Approaches to Facilitate Materials Design. *Mol Syst Des Eng* **2019**, *4* (2), 223–238.

(50) Borodin, O.; Smith, G. D. Molecular Dynamics Simulations of Poly(Ethylene Oxide)/LiI Melts. 1. Structural and Conformational Properties. *Macromolecules* **1998**, *31* (23), 8396–8406.

(51) Wheatle, B. K.; Keith, J. R.; Mogurampelly, S.; Lynd, N. A.; Ganesan, V. Influence of Dielectric Constant on Ionic Transport in Polyether-Based Electrolytes. *ACS Macro Lett* **2017**, *6* (12), 1362–1367.

(52) Shen, K.-H.; Hall, L. M. Effects of Ion Size and Dielectric Constant on Ion Transport and Transference Number in Polymer Electrolytes. *Macromolecules* **2020**, *53* (22), 10086–10096.

(53) Borodin, O.; Smith, G. D. Molecular Dynamics Simulations of Poly(Ethylene Oxide)/LiI Melts. 2. Dynamic Properties. *Macromolecules* **2000**, *33* (6), 2273–2283.

(54) Diddens, D.; Heuer, A.; Borodin, O. Understanding the Lithium Transport within a Rouse-Based Model for a PEO/LiTFSI Polymer Electrolyte. *Macromolecules* **2010**, *43* (4), 2028–2036.

(55) Webb, M. A.; Yamamoto, U.; Savoie, B. M.; Wang, Z.-G.; Miller, T. F. Globally Suppressed Dynamics in Ion-Doped Polymers. *ACS Macro Lett* **2018**, *7* (6), 734–738.

(56) Mongcopa, K. I. S.; Tyagi, M.; Mailoa, J. P.; Samsonidze, G.; Kozinsky, B.; Mullin, S. A.; Gribble, D. A.; Watanabe, H.; Balsara, N. P. Relationship between Segmental Dynamics Measured by Quasi-Elastic Neutron Scattering and Conductivity in Polymer Electrolytes. *ACS Macro Lett* **2018**, *7* (4), 504–508.

(57) Borodin, O.; D. Smith, G. Development of Many−Body Polarizable Force Fields for Li-Battery Applications: 2. LiTFSI-Doped Oligoether, Polyether, and Carbonate-Based Electrolytes. *J Phys Chem B* **2006**, *110* (12), 6293–6299.

(58) Teran, A. A.; Tang, M. H.; Mullin, S. A.; Balsara, N. P. Effect of Molecular Weight on Conductivity of Polymer Electrolytes. *Solid State Ion* **2011**, *203* (1), 18–21.

(59) Wu, H.; Wick, C. D. Computational Investigation on the Role of Plasticizers on Ion Conductivity in Poly(Ethylene Oxide) LiTFSI Electrolytes. *Macromolecules* **2010**, *43* (7), 3502–3510.

(60) Fullerton-Shirey, S. K.; Maranas, J. K. Structure and Mobility of PEO/LiClO 4 Solid Polymer Electrolytes Filled with Al 2 O 3 Nanoparticles. *The Journal of Physical Chemistry C* **2010**, *114* (20), 9196–9206.

(61) Croce, F.; Persi, L.; Scrosati, B.; Serraino-Fiory, F.; Plichta, E.; Hendrickson, M. A. Role of the Ceramic Fillers in Enhancing the Transport Properties of Composite Polymer Electrolytes. *Electrochim Acta* **2001**, *46* (16), 2457–2461.

(62) Nithya, H.; Selvasekarapandian, S.; Arun Kumar, D.; Sakunthala, A.; Hema, M.; Christopherselvin, P.; Kawamura, J.; Baskaran, R.; Sanjeeviraja, C. Thermal and Dielectric Studies of Polymer Electrolyte Based on P(ECH-EO). *Mater Chem Phys* **2011**, *126* (1–2), 404–408.

(63) Deng, Y.; Ding, J.; Yu, G.; Mobbs, R. H.; Heatley, F.; Price, C.; Booth, C. Preparation and Properties of Stat-Copoly-(Oxyethylene-Oxypropylene)-Block-Poly (Oxyethylene): 1. Use of Crown Ether in the Anionic Copolymerization of Propylene Oxide and Ethylene Oxide. *Polymer (Guildf)* **1992**, *33* (9), 1959–1962.

(64) Ruzette, A.-V. G.; Soo, P. P.; Sadoway, D. R.; Mayes, A. M. Melt-Formable Block Copolymer Electrolytes for Lithium Rechargeable Batteries. *J Electrochem Soc* **2001**, *148* (6), A537.

(65) Sadoway, D. R. Block and Graft Copolymer Electrolytes for High-Performance, Solid-State, Lithium Batteries. *J Power Sources* **2004**, *129* (1), 1–3.

(66) Borodin, O.; Smith, G. D. Molecular Dynamics Simulations of Comb-Branched Poly(Epoxide Ether)-Based Polymer Electrolytes. *Macromolecules* **2007**, *40* (4), 1252–1258.

(67) Mackanic, D. G.; Michaels, W.; Lee, M.; Feng, D.; Lopez, J.; Qin, J.; Cui, Y.; Bao, Z. Crosslinked Poly(Tetrahydrofuran) as a Loosely Coordinating Polymer Electrolyte. *Adv Energy Mater* **2018**, *8* (25), 1–11.

(68) Tominaga, Y. Ion-Conductive Polymer Electrolytes Based on Poly(Ethylene Carbonate) and Its Derivatives. *Polym J* **2017**, *49* (3), 291–299.

(69) Hooper, R.; Lyons, L.; Moline, D.; West, R. Novel Siloxane Polymers as Polymer Electrolytes for High Energy Density Lithium Batteries. *Silicon Chemistry* **2002**, *1* (2), 121–128.

(70) Yu, X.; J. Hoffman, Z.; Lee, J.; Fang, C.; A. Gido, L.; Patel, V.; B. Eitouni, H.; Wang, R.; P. Balsara, N. A Practical Polymer Electrolyte for Lithium and Sodium Batteries: Poly(Pentyl Malonate). *ACS Energy Lett* **2022**, *7* (11), 3791–3797.

(71) Pesko, D. M.; Jung, Y.; Hasan, A. L.; Webb, M. A.; Coates, G. W.; Miller, T. F.; Balsara, N. P. Effect of Monomer Structure on Ionic Conductivity in a Systematic Set of Polyester Electrolytes. *Solid State Ion* **2016**, *289*, 118–124.

(72) Webb, M. A.; Jung, Y.; Pesko, D. M.; Savoie, B. M.; Yamamoto, U.; Coates, G. W.; Balsara, N. P.; Wang, Z.-G.; Miller, T. F. Systematic Computational and Experimental Investigation of Lithium-Ion Transport Mechanisms in Polyester-Based Polymer Electrolytes. *ACS Cent Sci* **2015**, *1* (4), 198–205.

(73) Jones, S. D.; Bamford, J.; Fredrickson, G. H.; Segalman, R. A. Decoupling Ion Transport and Matrix Dynamics to Make High Performance Solid Polymer Electrolytes. *ACS Polymers Au* **2022**, *2* (6), 430–448.

(74) Schauser, N. S.; Seshadri, R.; Segalman, R. A. Multivalent Ion Conduction in Solid Polymer Systems. *Mol Syst Des Eng* **2019**, *4* (2), 263–279.

(75) Savoie, B. M.; Webb, M. A.; Miller, T. F. Enhancing Cation Diffusion and Suppressing Anion Diffusion via Lewis-Acidic Polymer Electrolytes. *J Phys Chem Lett* **2017**, *8* (3), 641–646.

(76) Chen, S.; Li, Y.; Wang, Y.; Li, Z.; Peng, C.; Feng, Y.; Feng, W. Cross-Linked Single-Ion Solid Polymer Electrolytes with Alternately Distributed Lithium Sources and Ion-Conducting Segments for Lithium Metal Batteries. *Macromolecules* **2021**, *54* (19), 9135–9144.

(77) Pesko, D. M.; Webb, M. A.; Jung, Y.; Zheng, Q.; Miller, T. F.; Coates, G. W.; Balsara, N. P. Universal Relationship between Conductivity and Solvation-Site Connectivity in Ether-Based Polymer Electrolytes. *Macromolecules* **2016**, *49* (14), 5244–5255.

(78) Bennington, P.; Sánchez-Leija, R. J.; Deng, C.; Sharon, D.; de Pablo, J. J.; Patel, S. N.; Nealey, P. F. Mixed-Polarity Copolymers Based on Ethylene Oxide and Cyclic Carbonate: Insights into Li-Ion Solvation and Conductivity. *Macromolecules* **2023**, *56* (11), 4244–4255.

(79) Soo, P. P.; Huang, B.; Jang, Y. I. I.; Chiang, Y. M.; Sadoway, D. R.; Mayes, A. M. Rubbery Block Copolymer Electrolytes for Solid-State Rechargeable Lithium Batteries. *J Electrochem Soc* **1999**, *146* (1), 32–37.

(80) Kuan, W.-F.; Remy, R.; Mackay, M. E.; Epps, III, T. H. Controlled Ionic Conductivity via Tapered Block Polymer Electrolytes. *RSC Adv* **2015**, *5* (17), 12597–12604.

(81) Rolland, J.; Brassinne, J.; Bourgeois, J.-P.; Poggi, E.; Vlad, A.; Gohy, J.-F. Chemically Anchored Liquid-PEO Based Block Copolymer Electrolytes for Solid-State Lithium-Ion Batteries. *J. Mater. Chem. A* **2014**, *2* (30), 11839–11846.

(82) Shim, J.; Bates, F. S.; Lodge, T. P. Superlattice by Charged Block Copolymer Self-Assembly. *Nat Commun* **2019**, *10* (1), 2108.

(83) Bates, C. M.; Chang, A. B.; Jones, S. C.; Grubbs, R. H. ABA Triblock Brush Polymers: Synthesis, Self-Assembly, Conductivity, and Rheological Properties. **2015**.

(84) Shibuya, Y.; Tatara, R.; Jiang, Y.; Shao-Horn, Y.; Johnson, J. A. Brush-First ROMP of Poly(Ethylene Oxide) Macromonomers of Varied Length: Impact of Polymer Architecture on Thermal Behavior and Li+ Conductivity. *J Polym Sci A Polym Chem* **2019**, *57* (3), 448–455.

(85) Guo, M.; Zhang, M.; He, D.; Hu, J.; Wang, X.; Gong, C.; Xie, X.; Xue, Z. Comb-like Solid Polymer Electrolyte Based on Polyethylene Glycol-Grafted Sulfonated Polyether Ether Ketone. *Electrochim Acta* **2017**, *255*, 396–404.

(86) Bouchet, R.; Maria, S.; Meziane, R.; Aboulaich, A.; Lienafa, L.; Bonnet, J.-P.; Phan, T. N. T.; Bertin, D.; Gigmes, D.; Devaux, D.; Denoyel, R.; Armand, M. Single-Ion BAB Triblock Copolymers as Highly Efficient Electrolytes for Lithium-Metal Batteries. *Nat Mater* **2013**, *12* (5), 452–457.

(87) Young, W.-S.; Kuan, W.-F.; Epps, T. H. Block Copolymer Electrolytes for Rechargeable Lithium Batteries. *J Polym Sci B Polym Phys* **2014**, *52* (1), 1–16.

(88) Bates, F. S.; Fredrickson, G. H. BLOCK COPOLYMERS—DESIGNER SOFT MATERIALS. *Phys Today* **1999**, *52* (2), 32–38.

(89) Sethuraman, V.; Mogurampelly, S.; Ganesan, V. Ion Transport Mechanisms in Lamellar Phases of Salt-Doped PS–PEO Block Copolymer Electrolytes. *Soft Matter* **2017**, *13* (42), 7793–7803.

(90) Sethuraman, V.; Mogurampelly, S.; Ganesan, V. Multiscale Simulations of Lamellar PS–PEO Block Copolymers Doped with LiPF 6 Ions. *Macromolecules* **2017**, *50* (11), 4542–4554.

(91) Nakamura, I.; Wang, Z. Thermodynamics of Salt-Doped Block Copolymers. *ACS Macro Lett* **2014**, *3*, 708–711.

(92) Morris, M. A.; Gartner, T. E.; Epps, T. H. Tuning Block Polymer Structure, Properties, and Processability for the Design of Efficient Nanostructured Materials Systems. *Macromol Chem Phys* **2017**, *218* (5), 1600513.

(93) Luo, M.; Brown, J. R.; Remy, R. A.; Scott, D. M.; Mackay, M. E.; Hall, L. M.; Epps, T. H. Determination of Interfacial Mixing in Tapered Block Polymer Thin Films: Experimental and Theoretical Investigations. *Macromolecules* **2016**, *49* (14), 5213–5222.

(94) Sharon, D.; Bennington, P.; Webb, M. A.; Deng, C.; de Pablo, J. J.; Patel, S. N.; Nealey, P. F. Molecular Level Differences in Ionic Solvation and Transport Behavior in Ethylene Oxide-Based Homopolymer and Block Copolymer Electrolytes. *J Am Chem Soc* **2021**, *143* (8), 3180–3190.

(95) Nakamura, I.; Wang, Z.-G. Salt-Doped Block Copolymers: Ion Distribution, Domain Spacing and Effective χ Parameter. *Soft Matter* **2012**, *8* (36), 9356.

(96) Sethuraman, V.; Ganesan, V. Segmental Dynamics in Lamellar Phases of Tapered Copolymers. *Soft Matter* **2016**, *12* (37), 7818–7823.

(97) Grant, S. B.; Saphores, J.-D.; Feldman, D. L.; Hamilton, A. J.; Fletcher, T. D.; Cook, P. L. M.; Stewardson, M.; Sanders, B. F.; Levin, L. A.; Ambrose, R. F.; Deletic, A.; Brown, R.; Jiang, S. C.; Rosso, D.; Cooper, W. J.; Marusic, I. Taking the "Waste" Out of "Wastewater" for Human Water Security and Ecosystem Sustainability. *Science (1979)* **2012**, *337* (6095), 681–686.

(98) de-Bashan, L. E.; Bashan, Y. Recent Advances in Removing Phosphorus from Wastewater and Its Future Use as Fertilizer (1997–2003). *Water Res* **2004**, *38* (19), 4222–4246.

(99) Kolpin, D. W.; Furlong, E. T.; Meyer, M. T.; Thurman, E. M.; Zaugg, S. D.; Barber, L. B.; Buxton, H. T. Pharmaceuticals, Hormones, and Other Organic Wastewater Contaminants in U.S. Streams, 1999−2000: A National Reconnaissance. *Environ Sci Technol* **2002**, *36* (6), 1202–1211.

(100) Puyol, D.; Batstone, D. J.; Hülsen, T.; Astals, S.; Peces, M.; Krömer, J. O. Resource Recovery from Wastewater by Biological Technologies: Opportunities, Challenges, and Prospects. *Front Microbiol* **2017**, *7*.

(101) Mehta, C. M.; Khunjar, W. O.; Nguyen, V.; Tait, S.; Batstone, D. J. Technologies to Recover Nutrients from Waste Streams: A Critical Review. *Crit Rev Environ Sci Technol* **2015**, *45* (4), 385–427.

(102) Cai, T.; Park, S. Y.; Li, Y. Nutrient Recovery from Wastewater Streams by Microalgae: Status and Prospects. *Renewable and Sustainable Energy Reviews* **2013**, *19*, 360–369.

(103) Yuan, Z.; Pratt, S.; Batstone, D. J. Phosphorus Recovery from Wastewater through Microbial Processes. *Curr Opin Biotechnol* **2012**, *23* (6), 878–883.

(104) Le Corre, K.; Valsami-Jones, E.; Hobbs, P.; S, P. Phosphorous Recovery from Waste Water by Struvite Crysatllisation: A Review. *Crit Rev Environ Sci Technol* **2009**, *39* (6), 433–477.

(105) Lee, C. G.; Alvarez, P. J. J.; Kim, H. G.; Jeong, S.; Lee, S.; Lee, K. B.; Lee, S. H.; Choi, J. W. Phosphorous Recovery from Sewage Sludge Using Calcium Silicate Hydrates. *Chemosphere* **2018**, *193*, 1087–1093.

(106) Harris, S. M.; Nguyen, J. T.; Pailloux, S. L.; Mansergh, J. P.; Dresel, M. J.; Swanholm, T. B.; Gao, T.; Pierre, V. C. Gadolinium Complex for the Catch and Release of Phosphate from Water. *Environ Sci Technol* **2017**, *51* (8), 4549–4558.

(107) Su, Z.; Hostert, J. D.; Renner, J. N. Phosphate Recovery by a Surface-Immobilized Cerium Affinity Peptide. *ACS ES&T Water* **2021**, *1* (1), 58–67.

(108) Desmidt, E.; Ghyselbrecht, K.; Zhang, Y.; Pinoy, L.; Van der Bruggen, B.; Verstraete, W.; Rabaey, K.; Meesschaert, B. Global Phosphorus Scarcity and Full-Scale P-Recovery Techniques: A Review. *Crit Rev Environ Sci Technol* **2015**, *45* (4), 336–384.

(109) CISSE, L.; MRABET, T. World Phosphate Production: Overview and Prospects. *Phosphorus Research Bulletin* **2004**, *15* (0), 21–25.

(110) Zhu, H.; Wang, H.; Shi, B.; Shangguan, L.; Tong, W.; Yu, G.; Mao, Z.; Huang, F. Supramolecular Peptide Constructed by Molecular Lego Allowing Programmable Self-Assembly for Photodynamic Therapy. *Nat Commun* **2019**, *10* (1), 2412.

(111) Hartgerink, J. D.; Beniash, E.; Stupp, S. I. Self-Assembly and Mineralization of Peptide-Amphiphile Nanofibers. *Science (1979)* **2001**, *294* (5547), 1684–1688.

(112) Missirlis, D.; Chworos, A.; Fu, C. J.; Khant, H. A.; Krogstad, D. V.; Tirrell, M. Effect of the Peptide Secondary Structure on the Peptide Amphiphile Supramolecular Structure and Interactions. *Langmuir* **2011**, *27* (10), 6163–6170.

(113) Peters, D.; Kastantin, M.; Kotamraju, V. R.; Karmali, P. P.; Gujraty, K.; Tirrell, M.; Ruoslahti, E. Targeting Atherosclerosis by Using Modular, Multifunctional Micelles. *Proceedings of the National Academy of Sciences* **2009**, *106* (24), 9815–9819.

(114) Chung, E. J.; Cheng, Y.; Morshed, R.; Nord, K.; Han, Y.; Wegscheid, M. L.; Auffinger, B.; Wainwright, D. A.; Lesniak, M. S.; Tirrell, M. V. Fibrin-Binding, Peptide Amphiphile Micelles for Targeting Glioblastoma. *Biomaterials* **2014**, *35* (4), 1249–1256.

(115) Ananthanarayanan, B.; Little, L.; Schaffer, D. V.; Healy, K. E.; Tirrell, M. Neural Stem Cell Adhesion and Proliferation on Phospholipid Bilayers Functionalized with RGD Peptides. *Biomaterials* **2010**, *31* (33), 8706–8715.

(116) Li, Y.; Lock, L. L.; Mills, J.; Ou, B. S.; Morrow, M.; Stern, D.; Wang, H.; Anderson, C. F.; Xu, X.; Ghose, S.; Li, Z. J.; Cui, H. Selective Capture and Recovery of Monoclonal Antibodies by Self-Assembling Supramolecular Polymers of High Affinity for Protein Binding. *Nano Lett* **2020**, *20* (10), 6957–6965.

(117) Yang, Q.; Zhu, Y.; Luo, B.; Lan, F.; Wu, Y.; Gu, Z. PH-Responsive Magnetic Metal–Organic Framework Nanocomposites for Selective Capture and Release of Glycoproteins. *Nanoscale* **2017**, *9* (2), 527–532.

(118) Chen, Y.; Li, P.; Modica, J. A.; Drout, R. J.; Farha, O. K. Acid-Resistant Mesoporous Metal–Organic Framework toward Oral Insulin Delivery: Protein Encapsulation, Protection, and Release. *J Am Chem Soc* **2018**, *140* (17), 5678–5681.

(119) Hasan, Z.; Jhung, S. H. Removal of Hazardous Organics from Water Using Metal-Organic Frameworks (MOFs): Plausible Mechanisms for Selective Adsorptions. *J Hazard Mater* **2015**, *283*, 329–339.

(120) Nagul, E. A.; McKelvie, I. D.; Worsfold, P.; Kolev, S. D. The Molybdenum Blue Reaction for the Determination of Orthophosphate Revisited: Opening the Black Box. *Anal Chim Acta* **2015**, *890*, 60–82.

(121) Ganesh, S.; Khan, F.; Ahmed, M. K.; Velavendan, P.; Pandey, N. K.; Kamachi Mudali, U. Spectrophotometric Determination of Trace Amounts of Phosphate in Water and Soil. *Water Science and Technology* **2012**, *66* (12), 2653–2658.

(122) Abraham, M. J.; Murtola, T.; Schulz, R.; Páll, S.; Smith, J. C.; Hess, B.; Lindahl, E. GROMACS: High Performance Molecular Simulations through Multi-Level Parallelism from Laptops to Supercomputers. *SoftwareX* **2015**, *1–2*, 19–25.

(123) Sidky, H.; Colón, Y. J.; Helfferich, J.; Sikora, B. J.; Bezik, C.; Chu, W.; Giberti, F.; Guo, A. Z.; Jiang, X.; Lequieu, J.; Li, J.; Moller, J.; Quevillon, M. J.; Rahimi, M.; Ramezani-Dakhel, H.; Rathee, V. S.; Reid, D. R.; Sevgen, E.; Thapar, V.; Webb, M. A.; Whitmer, J. K.; de Pablo, J. J. SSAGES: Software Suite for Advanced General Ensemble Simulations. *J Chem Phys* **2018**, *148* (4).

(124) Vanommeslaeghe, K.; Hatcher, E.; Acharya, C.; Kundu, S.; Zhong, S.; Shim, J.; Darian, E.; Guvench, O.; Lopes, P.; Vorobyov, I.; Mackerell, A. D. CHARMM General Force Field: A Force Field for Drug-like Molecules Compatible with the CHARMM All-Atom Additive Biological Force Fields. *J Comput Chem* **2009**, *31*, NA-NA.

(125) Jorgensen, W. L.; Chandrasekhar, J.; Madura, J. D.; Impey, R. W.; Klein, M. L. Comparison of Simple Potential Functions for Simulating Liquid Water. *J Chem Phys* **1983**, *79* (2), 926–935.

(126) Essmann, U.; Perera, L.; Berkowitz, M. L.; Darden, T.; Lee, H.; Pedersen, L. G. A Smooth Particle Mesh Ewald Method. *J Chem Phys* **1995**, *103* (19), 8577–8593.

(127) Hess, B.; Bekker, H.; Berendsen, H. J. C.; Fraaije, J. G. E. M. LINCS: A Linear Constraint Solver for Molecular Simulations. *J Comput Chem* **1997**, *18* (12), 1463–1472.

(128) Daura, X.; Gademann, K.; Jaun, B.; Seebach, D.; van Gunsteren, W. F.; Mark, A. E. Peptide Folding: When Simulation Meets Experiment. *Angewandte Chemie International Edition* **1999**, *38* (1/2), 236–240.

(129) Lee, O.-S.; Stupp, S. I.; Schatz, G. C. Atomistic Molecular Dynamics Simulations of Peptide Amphiphile Self-Assembly into Cylindrical Nanofibers. *J Am Chem Soc* **2011**, *133* (10), 3677–3683.

(130) Eisenhaber, F.; Lijnzaad, P.; Argos, P.; Sander, C.; Scharf, M. The Double Cubic Lattice Method: Efficient Approaches to Numerical Integration of Surface Area and Volume and to Dot Surface Contouring of Molecular Assemblies. *J Comput Chem* **1995**, *16* (3), 273–284.

(131) THAYER, A. M. MAKING PEPTIDES AT LARGE SCALE. *Chemical & Engineering News Archive* **2011**, *89* (22), 21–25.

(132) Zhai, H.; Qin, L.; Zhang, W.; Putnis, C. V.; Wang, L. Dynamics and Molecular Mechanism of Phosphate Binding to a Biomimetic Hexapeptide. *Environ Sci Technol* **2018**, *52* (18), 10472–10479.

(133) Lin, B. F.; Megley, K. A.; Viswanathan, N.; Krogstad, D. V.; Drews, L. B.; Kade, M. J.; Qian, Y.; Tirrell, M. V. PH-Responsive Branched Peptide Amphiphile Hydrogel Designed for Applications in Regenerative Medicine with Potential as Injectable Tissue Scaffolds. *J Mater Chem* **2012**, *22* (37), 19447.

(134) Schneider, C. A.; Rasband, W. S.; Eliceiri, K. W. NIH Image to ImageJ: 25 Years of Image Analysis. *Nat Methods* **2012**, *9* (7), 671–675.

(135) Ghosh, A.; Haverick, M.; Stump, K.; Yang, X.; Tweedle, M. F.; Goldberger, J. E. Fine-Tuning the PH Trigger of Self-Assembly. *J Am Chem Soc* **2012**, *134* (8), 3647–3650.

(136) Gebhardt, K. E.; Ahn, S.; Venkatachalam, G.; Savin, D. A. Rod-Sphere Transition in Polybutadiene−Poly(<scp>l</Scp> -Lysine) Block Copolymer Assemblies. *Langmuir* **2007**, *23* (5), 2851–2856.

(137) Bunce, J. T.; Ndam, E.; Ofiteru, I. D.; Moore, A.; Graham, D. W. A Review of Phosphorus Removal Technologies and Their Applicability to Small-Scale Domestic Wastewater Treatment Systems. *Front Environ Sci* **2018**, *6*.

(138) Chouyyok, W.; Wiacek, R. J.; Pattamakomsan, K.; Sangvanich, T.; Grudzien, R. M.; Fryxell, G. E.; Yantasee, W. Phosphate Removal by Anion Binding on Functionalized Nanoporous Sorbents. *Environ Sci Technol* **2010**, *44* (8), 3073–3078.

(139) Liu, H.; Sun, X.; Yin, C.; Hu, C. Removal of Phosphate by Mesoporous ZrO2. *J Hazard Mater* **2008**, *151* (2–3), 616–622.

(140) Zeng, L.; Li, X.; Liu, J. Adsorptive Removal of Phosphate from Aqueous Solutions Using Iron Oxide Tailings. *Water Res* **2004**, *38* (5), 1318–1326.

(141) Dimarco, R. L.; Heilshorn, S. C. Multifunctional Materials through Modular Protein Engineering. *Advanced Materials*. 2012.

(142) Tamerler, C.; Sarikaya, M. Genetically Designed Peptide-Based Molecular Materials. *ACS Nano* **2009**, *3* (7), 1606–1615.

(143) Hamley, I. W. Small Bioactive Peptides for Biomaterials Design and Therapeutics. *Chem Rev* **2017**, *117* (24), 14015–14041.

(144) Acar, H.; Ting, J. M.; Srivastava, S.; LaBelle, J. L.; Tirrell, M. V. Molecular Engineering Solutions for Therapeutic Peptide Delivery. *Chem Soc Rev* **2017**, *46* (21), 6553–6569.

(145) Black, K. A.; Lin, B. F.; Wonder, E. A.; Desai, S. S.; Chung, E. J.; Ulery, B. D.; Katari, R. S.; Tirrell, M. V. Biocompatibility and Characterization of a Peptide Amphiphile Hydrogel for Applications in Peripheral Nerve Regeneration. *Tissue Eng Part A* **2015**, *21* (7–8), 1333–1342.

(146) Knight, A. S.; Zhou, E. Y.; Francis, M. B. Development of Peptoid-Based Ligands for the Removal of Cadmium from Biological Media. *Chem Sci* **2015**, *6* (7), 4042–4048.

(147) Pizzi, A.; Pigliacelli, C.; Bergamaschi, G.; Gori, A.; Metrangolo, P. Biomimetic Engineering of the Molecular Recognition and Self-Assembly of Peptides and Proteins via Halogenation. *Coord Chem Rev* **2020**, *411*, 213242.

(148) Zhong, H.; Yuan, C.; He, J.; Yu, Y.; Jin, Y.; Huang, Y.; Zhao, R. Engineering Peptide-Functionalized Biomimetic Nanointerfaces for Synergetic Capture of Circulating Tumor Cells in an EpCAM-Independent Manner. *Anal Chem* **2021**, *93* (28), 9778–9787.

(149) Knight, A. S.; Zhou, E. Y.; Pelton, J. G.; Francis, M. B. Selective Chromium(VI) Ligands Identified Using Combinatorial Peptoid Libraries. *J Am Chem Soc* **2013**, *135* (46), 17488–17493.

(150) Zhou, L.; Bosscher, M.; Zhang, C.; Özçubukçu, S.; Zhang, L.; Zhang, W.; Li, C. J.; Liu, J.; Jensen, M. P.; Lai, L.; He, C. A Protein Engineered to Bind Uranyl Selectively and with Femtomolar Affinity. *Nat Chem* **2014**, *6* (3), 236–241.

(151) Walker, J. E.; Saraste, M.; Runswick, M. J.; Gay, N. J. Distantly Related Sequences in the Alpha- and Beta-Subunits of ATP Synthase, Myosin, Kinases and Other ATP-Requiring Enzymes and a Common Nucleotide Binding Fold. *EMBO J* **1982**, *1* (8), 945–951.

(152) Leipe, D. D.; Wolf, Y. I.; Koonin, E. V; Aravind, L. Classification and Evolution of P-Loop GTPases and Related ATPases. *J Mol Biol* **2002**, *317* (1), 41–72.

(153) Denessiouk, K. A.; Johnson, M. S.; Denesyuk, A. I. Novel CαNN Structural Motif for Protein Recognition of Phosphate Ions. *J Mol Biol* **2005**, *345* (3), 611–629.

(154) Milner-White, E. J.; Nissink, J. W. M.; Allen, F. H.; Duddy, W. J. Recurring Main-Chain Anion-Binding Motifs in Short Polypeptides: Nests. *Acta Crystallogr D Biol Crystallogr* **2004**, *60* (11), 1935–1942.

(155) Mapare, S. V.; Yu, P.-L.; Sarkar, A.; Mukhopadhyay, S. C. A Review of Sensor Technology for In-Field Phosphate Monitoring. In *2013 Seventh International Conference on Sensing Technology (ICST)*; IEEE, 2013; pp 411–418.

(156) Bellasi, A.; Kooienga, L.; Block, G. A. Phosphate Binders: New Products and Challenges. *Hemodialysis International* **2006**, *10* (3), 225–234.

(157) Hendricks, M. P.; Sato, K.; Palmer, L. C.; Stupp, S. I. Supramolecular Assembly of Peptide Amphiphiles. *Acc Chem Res* **2017**, *50* (10), 2440–2448.

(158) Behanna, H. A.; Donners, J. J. J. M.; Gordon, A. C.; Stupp, S. I. Coassembly of Amphiphiles with Opposite Peptide Polarities into Nanofibers. *J Am Chem Soc* **2005**, *127* (4), 1193–1200.

(159) Raspa, A.; Saracino, G. A. A.; Pugliese, R.; Silva, D.; Cigognini, D.; Vescovi, A.; Gelain, F. Complementary Co-Assembling Peptides: From In Silico Studies to In Vivo Application. *Adv Funct Mater* **2014**, *24* (40), 6317–6328.

(160) Shimada, T.; Lee, S.; Bates, F. S.; Hotta, A.; Tirrell, M. Wormlike Micelle Formation in Peptide-Lipid Conjugates Driven by Secondary Structure Transformation of the Headgroups. *J Phys Chem B* **2009**, *113* (42), 13711–13714.

(161) Missirlis, D.; Farine, M.; Kastantin, M.; Ananthanarayanan, B.; Neumann, T.; Tirrell, M. Linker Chemistry Determines Secondary Structure of P53 $_{14–29}$ in Peptide Amphiphile Micelles. *Bioconjug Chem* **2010**, *21* (3), 465–475.

(162) Fowler, W. C.; Deng, C.; Griffen, G. M.; Teodoro, T.; Guo, A. Z.; Zaiden, M.; Gottlieb, M.; de Pablo, J. J.; Tirrell, M. V. Harnessing Peptide Binding to Capture and Reclaim Phosphate. *J Am Chem Soc* **2021**, *143* (11), 4440–4450.

(163) Luecke, H.; Quiocho, F. A. High Specificity of a Phosphate Transport Protein Determined by Hydrogen Bonds. *Nature* **1990**, *347* (6291), 402–406.

(164) Sarkhel, S.; Desiraju, G. R. N□H…O, O□H…O, and C□H…O Hydrogen Bonds in Protein-Ligand Complexes: Strong and Weak Interactions in Molecular Recognition. *Proteins: Structure, Function, and Bioinformatics* **2003**, *54* (2), 247–259.

(165) Copley, R. R.; Barton, G. J. A Structural Analysis of Phosphate and Sulphate Binding Sites in Proteins. *J Mol Biol* **1994**, *242* (4), 321–329.

(166) Afzal, A. M.; Al-Shubailly, F.; Leader, D. P.; Milner-White, E. J. Bridging of Anions by Hydrogen Bonds in Nest Motifs and Its Significance for Schellman Loops and Other Larger Motifs within Proteins. *Proteins: Structure, Function, and Bioinformatics* **2014**, *82* (11), 3023–3031.

(167) Hossain, Md. A.; Işıklan, M.; Pramanik, A.; Saeed, M. A.; Fronczek, F. R. Anion Cluster: Assembly of Dihydrogen Phosphates for the Formation of a Cyclic Anion Octamer. *Cryst Growth Des* **2012**, *12* (2), 567–571.

(168) Choi, T. S.; Tezcan, F. A. Overcoming Universal Restrictions on Metal Selectivity by Protein Design. *Nature* **2022**, *603* (7901), 522–527.

(169) Wan, W.-Y.; Milner-White, E. J. A Natural Grouping of Motifs with an Aspartate or Asparagine Residue Forming Two Hydrogen Bonds to Residues Ahead in Sequence: Their Occurrence at α-Helical N Termini and in Other Situations. *J Mol Biol* **1999**, *286* (5), 1633–1649.

(170) Humphrey, W.; Dalke, A.; Schulten, K. VMD: Visual Molecular Dynamics. *J Mol Graph* **1996**, *14* (1), 33–38.

(171) Cheng, S.; Smith, D. M.; Li, C. Y. How Does Nanoscale Crystalline Structure Affect Ion Transport in Solid Polymer Electrolytes? *Macromolecules* **2014**, *47* (12), 3978–3986.

(172) Siqueira, L. J. A.; Ribeiro, M. C. C. Molecular Dynamics Simulation of the Polymer Electrolyte Poly(Ethyleneoxide)/LiClO4. I. Structural Properties. *J Chem Phys* **2005**, *122* (19), 194911.

(173) Siqueira, L. J. A.; Ribeiro, M. C. C. Molecular Dynamics Simulation of the Polymer Electrolyte Poly(Ethylene Oxide)/LiClO4. II. Dynamical Properties. *J Chem Phys* **2006**, *125* (21), 214903.

(174) Duan, Y.; Halley, J. W.; Curtiss, L.; Redfern, P. Mechanisms of Lithium Transport in Amorphous Polyethylene Oxide. *J Chem Phys* **2005**, *122* (5), 054702.

(175) Molinari, N.; Mailoa, J. P.; Kozinsky, B. Effect of Salt Concentration on Ion Clustering and Transport in Polymer Solid Electrolytes: A Molecular Dynamics Study of PEO–LiTFSI. *Chemistry of Materials* **2018**, *30* (18), 6298–6306.

(176) Brooks, D. J.; Merinov, B. V.; Goddard, W. A.; Kozinsky, B.; Mailoa, J. Atomistic Description of Ionic Diffusion in PEO–LiTFSI: Effect of Temperature, Molecular Weight, and Ionic Concentration. *Macromolecules* **2018**, *51* (21), 8987–8995.

(177) Borodin, O.; Smith, G. D. Mechanism of Ion Transport in Amorphous Poly(Ethylene Oxide)/LiTFSI from Molecular Dynamics Simulations. *Macromolecules* **2006**, *39* (4), 1620–1629.

(178) Karo, J.; Brandell, D. A Molecular Dynamics Study of the Influence of Side-Chain Length and Spacing on Lithium Mobility in Non-Crystalline LiPF6·PEOx; X=10 and 30. *Solid State Ion* **2009**, *180* (23–25), 1272–1284.

(179) Webb, M. A.; Savoie, B. M.; Wang, Z.-G.; Miller III, T. F. Chemically Specific Dynamic Bond Percolation Model for Ion Transport in Polymer Electrolytes. *Macromolecules* **2015**, *48* (19), 7346–7358.

(180) Müller-Plathe, F.; van Gunsteren, W. F. Computer Simulation of a Polymer Electrolyte: Lithium Iodide in Amorphous Poly(Ethylene Oxide). *J Chem Phys* **1995**, *103* (11), 4745–4756.

(181) Maitra, A.; Heuer, A. Cation Transport in Polymer Electrolytes: A Microscopic Approach. *Phys Rev Lett* **2007**, *98* (22), 227802.

(182) Zheng, Q.; Pesko, D. M.; Savoie, B. M.; Timachova, K.; Hasan, A. L.; Smith, M. C.; Miller, T. F.; Coates, G. W.; Balsara, N. P. Optimizing Ion Transport in Polyether-Based Electrolytes for Lithium Batteries. *Macromolecules* **2018**, *51* (8), 2847–2858.

(183) Tripathi, B. P.; Shahi, V. K. Organic–Inorganic Nanocomposite Polymer Electrolyte Membranes for Fuel Cell Applications. *Prog Polym Sci* **2011**, *36* (7), 945–979.

(184) Hanson, B.; Pryamitsyn, V.; Ganesan, V. Mechanisms Underlying Ionic Mobilities in Nanocomposite Polymer Electrolytes. *ACS Macro Lett* **2013**, *2* (11), 1001–1005.

(185) Chattoraj, J.; Diddens, D.; Heuer, A. Effects of Ionic Liquids on Cation Dynamics in Amorphous Polyethylene Oxide Electrolytes. *J Chem Phys* **2014**, *140* (2), 024906.

(186) Bannister, D. J.; Davies, G. R.; Ward, I. M.; McIntyre, J. E. Ionic Conductivities of Poly(Methoxy Polyethylene Glycol Monomethacrylate) Complexes with LiSO3CH3. *Polymer (Guildf)* **1984**, *25* (11), 1600–1602.

(187) Itoh, T. Effect of Branching in Base Polymer on Ionic Conductivity in Hyperbranched Polymer Electrolytes. *Solid State Ion* **2002**, *150* (3–4), 337–345.

(188) Hou, W.-H.; Chen, C.-Y. Studies on Comb-like Polymer Electrolyte with a Nitrile Group. *Electrochim Acta* **2004**, *49* (13), 2105–2112.

(189) Marchese, L.; Andrei, M.; Roggero, A.; Passerini, S.; Prosperi, P.; Scrosati, B. A New Class of Polymer Electrolytes Based on Chain-Extended Polyepoxides and LiClO4. *Electrochim Acta* **1992**, *37* (9), 1559–1564.

(190) Blonsky, P. M.; Shriver, D. F.; Austin, P.; Allcock, H. R. Polyphosphazene Solid Electrolytes. *J Am Chem Soc* **1984**, *106* (22), 6854–6855.

(191) Dong, S.; Qi, L.; Zhao, F.; Wang, M. Properties of a Nanocomposite Polymer Electrolyte from an Amorphous Comb-Branch Polymer and Nanoparticles. *Journal of Solid State Electrochemistry* **2004**, *8* (5), 283–289.

(192) Zhang, R. K.; Sun, Z.; Xie, H. H.; Wu, X.; Liang, M.; Xue, S. A New Comb-like Copolymer and Its Blend with Poly(Ethylene Oxide) for Solid Electrolytes and Application in Dye-Sensitized Solar Cells. *Solar Energy* **2012**, *86* (9), 2346–2353.

(193) Yoshizawa, M.; Ogihara, W.; Ohno, H. Novel Polymer Electrolytes Prepared by Copolymerization of Ionic Liquid Monomers. *Polym Adv Technol* **2002**, *13* (8), 589–594.

(194) Cowie, J. Effect of Side Chain Length and Crosslinking on the Ac Conductivity of Oligo (Ethyleneoxide) Comb-Branch Polymer-Salt Mixtures. *Solid State Ion* **1990**, *42* (3–4), 243–249.

(195) Snyder, J. F.; Ratner, M. A.; Shriver, D. F. Ion Conductivity of Comb Polysiloxane Polyelectrolytes Containing Oligoether and Perfluoroether Sidechains. *J Electrochem Soc* **2003**, *150* (8), A1090.

(196) Ikeda, Y.; Masui, H.; Syoji, S.; Sakashita, T.; Matoba, Y.; Kohjiya, S. Comb-Shaped High Molecular Weight Polyether Consisting of Oxyethylene Units for Polymer Solid Electrolyte. *Polym Int* **1997**, *43* (3), 269–273.

(197) Cowie, J. Novel Single Ion, Comb-Branched Polymer Electrolytes. *Solid State Ion* **1999**, *123* (1–4), 233–242.

(198) Herzberger, J.; Niederer, K.; Pohlit, H.; Seiwert, J.; Worm, M.; Wurm, F. R.; Frey, H. Polymerization of Ethylene Oxide, Propylene Oxide, and Other Alkylene Oxides: Synthesis, Novel Polymer Architectures, and Bioconjugation. *Chem Rev* **2016**, *116* (4), 2170–2243.

(199) Brandell, D.; Priimägi, P.; Kasemägi, H.; Aabloo, A. Branched Polyethylene/Poly(Ethylene Oxide) as a Host Matrix for Li-Ion Battery Electrolytes: A Molecular Dynamics Study. *Electrochim Acta* **2011**, *57*, 228–236.

(200) Hussain, H.; Mya, K. Y.; He, C. Self-Assembly of Brush-like Poly[Poly(Ethylene Glycol) Methyl Ether Methacrylate] Synthesized via Aqueous Atom Transfer Radical Polymerization. *Langmuir* **2008**, *24* (23), 13279–13286.

(201) Sharon, D.; Bennington, P.; Liu, C.; Kambe, Y.; Dong, B. X.; Burnett, V. F.; Dolejsi, M.; Grocke, G.; Patel, S. N.; Nealey, P. F. Interrogation of Electrochemical Properties of Polymer Electrolyte Thin Films with Interdigitated Electrodes. *J Electrochem Soc* **2018**, *165* (16), H1028–H1039.

(202) Martin, M. G.; Siepmann, J. I. Transferable Potentials for Phase Equilibria. 1. United-Atom Description of n-Alkanes. *Journal of Physical Chemistry B* **1998**, *102* (14), 2569–2577.

(203) Stubbs, J. M.; Potoff, J. J.; Siepmann, J. I. Transferable Potentials for Phase Equilibria. 6. United-Atom Description for Ethers, Glycols, Ketones, and Aldehydes. *J Phys Chem B* **2004**, *108* (45), 17596–17605.

(204) Maerzke, K. A.; Schultz, N. E.; Ross, R. B.; Siepmann, J. I. TraPPE-UA Force Field for Acrylates and Monte Carlo Simulations for Their Mixtures with Alkanes and Alcohols. *J Phys Chem B* **2009**, *113* (18), 6415–6425.

(205) Wick, C. D.; Theodorou, D. N. Connectivity-Altering Monte Carlo Simulations of the End Group Effects on Volumetric Properties for Poly(Ethylene Oxide). *Macromolecules* **2004**, *37* (18), 7026–7033.

(206) Canongia Lopes, J. N.; Pádua, A. A. H. Molecular Force Field for Ionic Liquids Composed of Triflate or Bistriflylimide Anions. *J Phys Chem B* **2004**, *108* (43), 16893–16898.

(207) Brown, W. M.; Kohlmeyer, A.; Plimpton, S. J.; Tharrington, A. N. Implementing Molecular Dynamics on Hybrid High Performance Computers – Particle–Particle Particle-Mesh. *Comput Phys Commun* **2012**, *183* (3), 449–459.

(208) Plimpton, S. Fast Parallel Algorithms for Short-Range Molecular Dynamics. *J Comput Phys* **1995**, *117* (1), 1–19.

(209) McIntosh, L. D.; Kubo, T.; Lodge, T. P. Morphology, Modulus, and Conductivity of a Triblock Terpolymer/Ionic Liquid Electrolyte Membrane. *Macromolecules* **2014**, *47* (3), 1090–1098.

(210) Barteau, K. P.; Wolffs, M.; Lynd, N. A.; Fredrickson, G. H.; Kramer, E. J.; Hawker, C. J. Allyl Glycidyl Ether-Based Polymer Electrolytes for Room Temperature Lithium Batteries. *Macromolecules* **2013**, *46* (22), 8988–8994.

(211) Miller, T. F.; Wang, Z.-G.; Coates, G. W.; Balsara, N. P. Designing Polymer Electrolytes for Safe and High Capacity Rechargeable Lithium Batteries. *Acc Chem Res* **2017**, *50* (3), 590–593.

(212) Porter, C. E.; Blum, F. D. Thermal Characterization of PMMA Thin Films Using Modulated Differential Scanning Calorimetry. *Macromolecules* **2000**, *33* (19), 7016–7020.

(213) Molinari, N.; Mailoa, J. P.; Kozinsky, B. General Trend of a Negative Li Effective Charge in Ionic Liquid Electrolytes. *J Phys Chem Lett* **2019**, *10* (10), 2313–2319.

(214) Molinari, N.; Mailoa, J. P.; Craig, N.; Christensen, J.; Kozinsky, B. Transport Anomalies Emerging from Strong Correlation in Ionic Liquid Electrolytes. *J Power Sources* **2019**, *428*, 27–36.

(215) Molinari, N.; Sutton, A. P.; Mostofi, A. A. Mechanisms of Reinforcement in Polymer Nanocomposites. *Physical Chemistry Chemical Physics* **2018**, *20* (35), 23085–23094.

(216) Chu, W.; Webb, M. A.; Deng, C.; Colón, Y. J.; Kambe, Y.; Krishnan, S.; Nealey, P. F.; de Pablo, J. J. Understanding Ion Mobility in P2VP/NMP $^{+}$ I $^{-}$ Polymer Electrolytes: A Combined Simulation and Experimental Study. *Macromolecules* **2020**, *53* (8), 2783–2792.

(217) Xue, Z.; He, D.; Xie, X. Poly(Ethylene Oxide)-Based Electrolytes for Lithium-Ion Batteries. *J Mater Chem A Mater* **2015**, *3* (38), 19218–19253.

(218) Bennington, P.; Deng, C.; Sharon, D.; Webb, M. A.; de Pablo, J. J.; Nealey, P. F.; Patel, S. N. Role of Solvation Site Segmental Dynamics on Ion Transport in Ethylene-Oxide Based Side-Chain Polymer Electrolytes. *J Mater Chem A Mater* **2021**, *9* (15), 9937–9951.

(219) Deng, C.; Webb, M. A.; Bennington, P.; Sharon, D.; Nealey, P. F.; Patel, S. N.; de Pablo, J. J. Role of Molecular Architecture on Ion Transport in Ethylene Oxide-Based Polymer Electrolytes. *Macromolecules* **2021**, *54* (5), 2266–2276.

(220) Lascaud, S.; Perrier, M.; Vallee, A.; Besner, S.; Prud'homme, J.; Armand, M. Phase Diagrams and Conductivity Behavior of Poly(Ethylene Oxide)-Molten Salt Rubbery Electrolytes. *Macromolecules* **1994**, *27* (25), 7469–7477.

(221) Abdul Halim, S. I.; Chan, C. H.; Kressler, J. Effects on the Properties after Addition of Lithium Salt in Poly(Ethylene Oxide)/Poly(Methyl Acrylate) Blends. *Polymers (Basel)* **2020**, *12* (12), 2963.

(222) Yap, Y. L.; You, A. H.; Teo, L. L. Preparation and Characterization Studies of PMMA–PEO-Blend Solid Polymer Electrolytes with SiO2 Filler and Plasticizer for Lithium Ion Battery. *Ionics (Kiel)* **2019**, *25* (7), 3087–3098.

(223) Tao, C.; Gao, M. H.; Yin, B. H.; Li, B.; Huang, Y. P.; Xu, G.; Bao, J. J. A Promising TPU/PEO Blend Polymer Electrolyte for All-Solid-State Lithium Ion Batteries. *Electrochim Acta* **2017**, *257*, 31–39.

(224) Jeddi, K.; Qazvini, N. T.; Jafari, S. H.; Khonakdar, H. A. L. I. Enhanced Ionic Conductivity in PEO / PMMA Glassy Miscible Blends : Role of Nano-Confinement of Minority Component Chains. **2010**, *48*, 2065–2071.

(225) Osman, Z.; Ansor, N. M.; Chew, K. W.; Kamarulzaman, N. Infrared and Conductivity Studies on Blends of PMMA/PEO Based Polymer Electrolytes. *Ionics (Kiel)* **2005**, *11* (5–6), 431–435.

(226) Florjańczyk, Z.; Such, K.; Wieczorek, W. Effect of Tacticity of Poly(Methyl Methacrylate) on Conductivity of Poly(Ethylene Oxide)-Poly(Methyl Methacrylate) Blend-Based Polymeric Electrolytest. *Journal of Macromolecular Science, Part A* **1992**, *29* (10), 853–863.

(227) Floriańczyk, Z.; Such, K.; Wieczorek, W.; Wasiucionek, M. Highly Conductive Poly(Ethylene Oxide)-Poly(Methyl Methacrylate) Blends Complexed with Alkali Metal Salts. *Polymer (Guildf)* **1991**, *32* (18), 3422–3425.

(228) Young, W.-S.; Albert, J. N. L.; Schantz, A. B.; Epps, T. H. Mixed-Salt Effects on the Ionic Conductivity of Lithium-Doped PEO-Containing Block Copolymers. *Macromolecules* **2011**, *44* (20), 8116–8123.

(229) Maslyn, J. A.; Frenck, L.; Loo, W. S.; Parkinson, D. Y.; Balsara, N. P. Extended Cycling through Rigid Block Copolymer Electrolytes Enabled by Reducing Impurities in Lithium Metal Electrodes. *ACS Appl Energy Mater* **2019**, *2*, 8197–8206.

(230) Chintapalli, M.; Chen, X. C.; Thelen, J. L.; Teran, A. A.; Wang, X.; Garetz, B. A.; Balsara, N. P. Effect of Grain Size on the Ionic Conductivity of a Block Copolymer Electrolyte. *Macromolecules* **2014**, *47* (15), 5424–5431.

(231) Schauser, N. S.; Harry, K. J.; Parkinson, D. Y.; Watanabe, H.; Balsara, N. P. Lithium Dendrite Growth in Glassy and Rubbery Nanostructured Block Copolymer Electrolytes. *J Electrochem Soc* **2015**, *162* (3), A398–A405.

(232) Irwin, M. T.; Hickey, R. J.; Xie, S.; So, S.; Bates, F. S.; Lodge, T. P. Structure–Conductivity Relationships in Ordered and Disordered Salt-Doped Diblock Copolymer/Homopolymer Blends. *Macromolecules* **2016**, *49* (18), 6928–6939.

(233) Xie, S.; Meyer, D. J.; Wang, E.; Bates, F. S.; Lodge, T. P. Structure and Properties of Bicontinuous Microemulsions from Salt-Doped Ternary Polymer Blends. *Macromolecules* **2019**, *52* (24), 9693–9702.

(234) Bouchet, R.; Phan, T. N. T.; Beaudoin, E.; Devaux, D.; Davidson, P.; Bertin, D.; Denoyel, R. Charge Transport in Nanostructured PS–PEO–PS Triblock Copolymer Electrolytes. *Macromolecules* **2014**, *47* (8), 2659–2665.

(235) Sharon, D.; Bennington, P.; Dolejsi, M.; Webb, M. A.; Dong, B. X.; de Pablo, J. J.; Nealey, P. F.; Patel, S. N. Intrinsic Ion Transport Properties of Block Copolymer Electrolytes. *ACS Nano* **2020**, *14* (7), 8902–8914.

(236) Glynos, E.; Petropoulou, P.; Mygiakis, E.; Nega, A. D.; Pan, W.; Papoutsakis, L.; Giannelis, E. P.; Sakellariou, G.; Anastasiadis, S. H. Leveraging Molecular Architecture To Design New, All-Polymer Solid Electrolytes with Simultaneous Enhancement in Modulus and Ionic Conductivity. *Macromolecules* **2018**, *51* (7), 2542–2550.

(237) Mu, D.; Huang, X.-R.; Lu, Z.-Y.; Sun, C.-C. Computer Simulation Study on the Compatibility of Poly(Ethylene Oxide)/Poly(Methyl Methacrylate) Blends. *Chem Phys* **2008**, *348* (1–3), 122–129.

(238) Dionísio, M.; Fernandes, A. C.; Mano, J. F.; Correia, N. T.; Sousa, R. C. Relaxation Studies in PEO/PMMA Blends. *Macromolecules* **2000**, *33* (3), 1002–1011.

(239) Sacristan, J.; Chen, C.; Maranas, J. K. Role of Effective Composition on Dynamics of PEO−PMMA Blends. *Macromolecules* **2008**, *41* (14), 5466–5476.

(240) Huynh, T. V.; Messinger, R. J.; Sarou-Kanian, V.; Fayon, F.; Bouchet, R.; Deschamps, M. Restricted Lithium Ion Dynamics in PEO-Based Block Copolymer Electrolytes Measured by High-Field Nuclear Magnetic Resonance Relaxation. *J Chem Phys* **2017**, *147* (13).

(241) Lodge, T. P.; McLeish, T. C. B. Self-Concentrations and Effective Glass Transition Temperatures in Polymer Blends. *Macromolecules* **2000**, *33* (14), 5278–5284.

(242) Gaikwad, A. N.; Wood, E. R.; Ngai, T.; Lodge, T. P. Two Calorimetric Glass Transitions in Miscible Blends Containing Poly(Ethylene Oxide). *Macromolecules* **2008**, *41* (7), 2502–2508.

(243) Zawada, J. A.; Ylitalo, C. M.; Fuller, G. G.; Colby, R. H.; Long, T. E. Component Relaxation Dynamics in a Miscible Polymer Blend: Poly(Ethylene Oxide)/Poly(Methyl Methacrylate). *Macromolecules* **1992**, *25* (11), 2896–2902.

(244) Zeroni, I.; Ozair, S.; Lodge, T. P. Component Terminal Dynamics in Poly(Ethylene Oxide)/Poly(Methyl Methacrylate) Blends. *Macromolecules* **2008**, *41* (13), 5033–5041.

(245) Chiu, C.-Y.; Chen, H.-W.; Kuo, S.-W.; Huang, C.-F.; Chang, F.-C. Investigating the Effect of Miscibility on the Ionic Conductivity of $LiClO_4$ /PEO/PCL Ternary Blends. *Macromolecules* **2004**, *37* (22), 8424–8430.

(246) Ravindar Reddy, M.; Subrahmanyam, A. R.; Maheshwar Reddy, M.; Siva Kumar, J.; Kamalaker, V.; Jaipal Reddy, M. X-RD, SEM, FT-IR, DSC Studies of Polymer Blend Films of PMMA and PEO. *Mater Today Proc* **2016**, *3* (10), 3713–3718.

(247) Pfefferkorn, D.; Kyerematen, S. O.; Busse, K.; Kammer, H.-W.; Thurn-Albrecht, T.; Kressler, J. Crystallization and Melting of Poly(Ethylene Oxide) in Blends and Diblock Copolymers with Poly(Methyl Acrylate). *Macromolecules* **2011**, *44* (8), 2953–2963.

(248) Abutalib, M. M.; Rajeh, A. Influence of Fe3O4 Nanoparticles on the Optical, Magnetic and Electrical Properties of PMMA/PEO Composites: Combined FT-IR/DFT for Electrochemical Applications. *J Organomet Chem* **2020**, *920*, 121348.

(249) Jackson, N. E.; Savoie, B. M.; Chen, L. X.; Ratner, M. A. A Simple Index for Characterizing Charge Transport in Molecular Materials. *J Phys Chem Lett* **2015**, *6* (6), 1018–1021.

(250) Patel, S. N. 100th Anniversary of Macromolecular Science Viewpoint: Solid Polymer Electrolytes in Cathode Electrodes for Lithium Batteries. Current Challenges and Future Opportunities. *ACS Macro Lett* **2021**, *10* (1), 141–153.

(251) Hallinan, D. T.; Balsara, N. P. Polymer Electrolytes. *Annu Rev Mater Res* **2013**, *43* (1), 503–525.

(252) Gomez, E. D.; Panday, A.; Feng, E. H.; Chen, V.; Stone, G. M.; Minor, A. M.; Kisielowski, C.; Downing, K. H.; Borodin, O.; Smith, G. D.; Balsara, N. P. Effect of Ion Distribution on Conductivity of Block Copolymer Electrolytes. *Nano Lett* **2009**, *9* (3), 1212–1216.

(253) Xu, K. Nonaqueous Liquid Electrolytes for Lithium-Based Rechargeable Batteries. *Chem Rev* **2004**, *104* (10), 4303–4418.

(254) Wheatle, B. K.; Lynd, N. A.; Ganesan, V. Effect of Polymer Polarity on Ion Transport: A Competition between Ion Aggregation and Polymer Segmental Dynamics. *ACS Macro Lett* **2018**, *7* (10), 1149–1154.

(255) Sharon, D.; Bennington, P.; Webb, M. A.; Deng, C.; de Pablo, J. J.; Patel, S. N.; Nealey, P. F. Molecular Level Differences in Ionic Solvation and Transport Behavior in Ethylene Oxide-Based Homopolymer and Block Copolymer Electrolytes. *J Am Chem Soc* **2021**, *143* (8), 3180–3190.

(256) Bennington, P.; Deng, C.; Sharon, D.; Webb, M. A.; de Pablo, J. J.; Nealey, P. F.; Patel, S. N. Role of Solvation Site Segmental Dynamics on Ion Transport in Ethylene-Oxide Based Side-Chain Polymer Electrolytes. *J. Mater. Chem. A* **2021**, *9* (15), 9937–9951.

(257) Webb, M. A.; Savoie, B. M.; Wang, Z.-G.; Miller III, T. F. Chemically Specific Dynamic Bond Percolation Model for Ion Transport in Polymer Electrolytes. *Macromolecules* **2015**, *48* (19), 7346–7358.

(258) Tobishima, S.; Morimoto, H.; Aoki, M.; Saito, Y.; Inose, T.; Fukumoto, T.; Kuryu, T. Glyme-Based Nonaqueous Electrolytes for Rechargeable Lithium Cells. *Electrochim Acta* **2004**, *49* (6), 979–987.

(259) Sharon, D.; Deng, C.; Bennington, P.; Webb, M. A.; Patel, S. N.; de Pablo, J. J.; Nealey, P. F. Critical Percolation Threshold for Solvation-Site Connectivity in Polymer Electrolyte Mixtures. *Macromolecules* **2022**, *55* (16), 7212–7221.

(260) Bennington, P.; Sánchez-Leija, R. J.; Deng, C.; Sharon, D.; de Pablo, J. J.; Patel, S. N.; Nealey, P. F. Mixed-Polarity Copolymers Based on Ethylene Oxide and Cyclic Carbonate: Insights into Li-Ion Solvation and Conductivity. *Macromolecules* **2023**, *56* (11), 4244–4255.

(261) Canongia Lopes, J. N.; Pádua, A. A. H. Molecular Force Field for Ionic Liquids Composed of Triflate or Bistriflylimide Anions. *J Phys Chem B* **2004**, *108* (43), 16893–16898.

(262) Kamath, G.; Robinson, J.; Potoff, J. J. Application of TraPPE-UA Force Field for Determination of Vapor–Liquid Equilibria of Carboxylate Esters. *Fluid Phase Equilib* **2006**, *240* (1), 46–55.

(263) Wick, C. D.; Martin, M. G.; Siepmann, J. I. Transferable Potentials for Phase Equilibria. 4. United-Atom Description of Linear and Branched Alkenes and Alkylbenzenes. *J Phys Chem B* **2000**, *104* (33), 8008–8016.

(264) Soetens, J.-C.; Millot, C.; Maigret, B.; Bakó, I. Molecular Dynamics Simulation and X—Ray Diffraction Studies of Ethylene Carbonate, Propylene Carbonate and Dimethyl Carbonate in Liquid Phase. *J Mol Liq* **2001**, *92* (3), 201–216.

(265) Chaudhari, M. I.; Nair, J. R.; Pratt, L. R.; Soto, F. A.; Balbuena, P. B.; Rempe, S. B. Scaling Atomic Partial Charges of Carbonate Solvents for Lithium Ion Solvation and Diffusion. *J Chem Theory Comput* **2016**, *12* (12), 5709–5718.

(266) M. J. Frisch, G. W. Trucks, H. B. Schlegel, G. E. Scuseria, M. A. Robb, J. R. Cheeseman, G. Scalmani, V. Barone, G. A. Petersson, H. Nakatsuji, X. Li, M. Caricato, A. Marenich, J. Bloino, B. G. Janesko, R. Gomperts, B. Mennucci, H. P. Hratchian, J. V. Ort, and D. J. F. Gaussian 09, Revision A.02. Gaussian, Inc.: Wallingford CT 2016.

(267) Breneman, C. M.; Wiberg, K. B. Determining Atom-Centered Monopoles from Molecular Electrostatic Potentials. The Need for High Sampling Density in Formamide Conformational Analysis. *J Comput Chem* **1990**, *11* (3), 361–373.

(268) Brooks, D. J.; Merinov, B. V.; Goddard, W. A.; Kozinsky, B.; Mailoa, J. Atomistic Description of Ionic Diffusion in PEO–LiTFSI: Effect of Temperature, Molecular Weight, and Ionic Concentration. *Macromolecules* **2018**, *51* (21), 8987–8995.

(269) Dahbi, M.; Ghamouss, F.; Tran-Van, F.; Lemordant, D.; Anouti, M. Comparative Study of EC/DMC LiTFSI and LiPF6 Electrolytes for Electrochemical Storage. *J Power Sources* **2011**, *196* (22), 9743–9750.

(270) Wheatle, B. K.; Keith, J. R.; Mogurampelly, S.; Lynd, N. A.; Ganesan, V. Influence of Dielectric Constant on Ionic Transport in Polyether-Based Electrolytes. *ACS Macro Lett* **2017**, *6* (12), 1362–1367.

(271) Flory, P. J. Thermodynamics of High Polymer Solutions. *J Chem Phys* **1942**, *10* (1), 51–61.

(272) Schantz, S. On the Ion Association at Low Salt Concentrations in Polymer Electrolytes; a Raman Study of NaCF3SO3 and LiClO4 Dissolved in Poly(Propylene Oxide). *J Chem Phys* **1991**, *94* (9), 6296–6306.

(273) Zhang, C.; Ueno, K.; Yamazaki, A.; Yoshida, K.; Moon, H.; Mandai, T.; Umebayashi, Y.; Dokko, K.; Watanabe, M. Chelate Effects in Glyme/Lithium Bis(Trifluoromethanesulfonyl)Amide Solvate Ionic Liquids. I. Stability of Solvate Cations and Correlation with Electrolyte Properties. *J Phys Chem B* **2014**, *118* (19), 5144–5153.

(274) Willner, L.; Poppe, A.; Allgaier, J.; Monkenbusch, M.; Lindner, P.; Richter, D. Micellization of Amphiphilic Diblock Copolymers: Corona Shape and Mean-Field to Scaling Crossover. *Europhysics Letters (EPL)* **2000**, *51* (6), 628–634.

(275) Morioka, T.; Nakano, K.; Tominaga, Y. Ion-Conductive Properties of a Polymer Electrolyte Based on Ethylene Carbonate/Ethylene Oxide Random Copolymer. *Macromol Rapid Commun* **2017**, *38* (8), 1600652.

(276) Tillmann, S. D.; Isken, P.; Lex-Balducci, A. Lithium Coordination in Cyclic-Carbonate-Based Gel Polymer Electrolyte. *The Journal of Physical Chemistry C* **2015**, *119* (27), 14873–14878.

(277) Vanommeslaeghe, K.; Hatcher, E.; Acharya, C.; Kundu, S.; Zhong, S.; Shim, J.; Darian, E.; Guvench, O.; Lopes, P.; Vorobyov, I.; Mackerell, A. D. CHARMM General Force Field: A Force Field for Drug-like Molecules Compatible with the CHARMM All-Atom Additive Biological Force Fields. *J Comput Chem* **2010**, *31* (4), 671–690.

(278) Sharon, D.; Deng, C.; Bennington, P.; Webb, M. A.; Patel, S. N.; de Pablo, J. J.; Nealey, P. F. Critical Percolation Threshold for Solvation-Site Connectivity in Polymer Electrolyte Mixtures. *Macromolecules* **2022**, *55* (16), 7212–7221.

(279) Shen, K.; Nguyen, M.; Sherck, N.; Yoo, B.; Köhler, S.; Speros, J.; Delaney, K. T.; Shell, M. S.; Fredrickson, G. H. Predicting Surfactant Phase Behavior with a Molecularly Informed Field Theory. *J Colloid Interface Sci* **2023**, *638*, 84–98.

(280) Lequieu, J. Combining Particle and Field-Theoretic Polymer Models with Multi-Representation Simulations. *J Chem Phys* **2023**, *158* (24).

(281) Kim, C.; Chandrasekaran, A.; Doan Huan, T.; Das, D.; Ramprasad, R. Polymer Genome: A Data-Powered Polymer Informatics Platform for Property Predictions. *The Journal of Physical Chemistry C* **2018**, *122* (31), 17575–17585.

(282) Bradford, G.; Lopez, J.; Ruza, J.; A. Stolberg, M.; Osterude, R.; A. Johnson, J.; Gomez-Bombarelli, R.; Shao-Horn, Y. Chemistry-Informed Machine Learning for Polymer Electrolyte Discovery. *ACS Cent Sci* **2023**, *9* (2), 206–216.

(283) Tran, H.; Shen, K.-H.; Shukla, S.; Kwon, H.-K.; Ramprasad, R. Informatics-Driven Selection of Polymers for Fuel-Cell Applications. *The Journal of Physical Chemistry C* **2023**, *127* (2), 977–986.

(284) Khajeh, A.; Schweigert, D.; B. Torrisi, S.; Hung, L.; D. Storey, B.; Kwon, H.-K. Early Prediction of Ion Transport Properties in Solid Polymer Electrolytes Using Machine Learning and System Behavior-Based Descriptors of Molecular Dynamics Simulations. *Macromolecules* **2023**, *56* (13), 4787–4799.

(285) Fu, X.; Xie, T.; Rebello, N. J.; Olsen, B. D.; Jaakkola, T. Simulate Time-Integrated Coarse-Grained Molecular Dynamics with Multi-Scale Graph Networks. **2022**.

(286) Bedrov, D.; Piquemal, J.-P.; Borodin, O.; MacKerell, A. D.; Roux, B.; Schröder, C. Molecular Dynamics Simulations of Ionic Liquids and Electrolytes Using Polarizable Force Fields. *Chem Rev* **2019**, *119* (13), 7940–7995.

(287) Park, C. W.; Kornbluth, M.; Vandermause, J.; Wolverton, C.; Kozinsky, B.; Mailoa, J. P. Accurate and Scalable Graph Neural Network Force Field and Molecular Dynamics with Direct Force Architecture. *NPJ Comput Mater* **2021**, *7* (1).

(288) Borodin, O. Polarizable Force Field Development and Molecular Dynamics Simulations of Ionic Liquids. *J Phys Chem B* **2009**, *113* (33), 11463–11478.